

Fluid Mechanics of Nano-textured Coalescing Filters

BY

RAKESH PRASAD SAHU
B.M.E., Jadavpur University, Kolkata, India, 2010

THESIS

Submitted as a partial fulfillment of the requirements
for the degree of Doctor of Philosophy in Mechanical Engineering
in the Graduate College of the
University of Illinois at Chicago, 2014

Chicago, Illinois

Defense Committee

Alexander L. Yarin,	Chair and Advisor
Farzad Mashayek,	Mechanical and Industrial Engineering
Kenneth Brezensky,	Mechanical and Industrial Engineering
Eduard Karpov,	Civil and Materials Engineering
Suman Sinha-Ray,	Mechanical and Industrial Engineering.

I dedicate this thesis to my mother Smt. Bela Devi and my father Sri Mahendra Sahu, without whose love and support it would never has been accomplished.

ACKNOWLEDGEMENTS

I would like to express my deepest gratitude to my Doctoral advisor, Professor Yarin, for the spirit of adventure in the field of research and excitement in regards of teaching. I sincerely thank him for not getting tired and impatient with multiple questions asked several times. I am also thankful for all those wonderful historical and scientific stories and discussions that he shared with me. Without his consistent help this dissertation would not have been possible. I would like to use this opportunity to thank all the great teachers since my primary school who has significantly contributed to the success of my career so far.

I would like to thank my thesis committee members for their suggestions, support and assistance, which helped me in achieving my goals.

I would like to thank my parents for their unceasing support and encouragement to be the best. It is because of them I am here in the first place. I am thankful to them for being great mentors in my life and shaping my thoughts and aspirations. I would like to thank my siblings Mukesh, Punam and Priti for their continuous support and encouragement during all these years spent in fulfilling my dream. I am blessed to have them all in my life.

I am extremely grateful to Dr. Suman Sinha-Ray for his support and inspiration in my research. I would like to thank my roommates, lab mates and all my friends who directly or indirectly have lent their helping hand in this venture.

In addition, I also thank the undergraduate students Bryan Whittington, Cristine Wiesner, Vadim Drozd and Benjamin Erickson, who helped me sincerely in the research work. I wish to express my sincere thanks to David Mecha, Tom Bruzan and Eric Schmidt for their significant contributions in making my experiments successful.

R.P.S

Portions of this thesis have been published in peer reviewed journals. Sections 2.1 and 3.1, as well as Chapter 4 were published in Soft Matter by the Royal Society of Chemistry (Sahu, R. P., Sinha-Ray, S., Yarin, A. L., & Pourdeyehimi, B. (2012). Drop impacts on electrospun nanofiber membranes. Soft Matter, 8(14), 3957-3970). Sections 2.2 and 3.2, as well as Chapter 5, were published in Soft Matter by the Royal Society of Chemistry (Sahu, R. P., Sinha-Ray, S., Yarin, A. L., & Pourdeyehimi, B. (2013). Blowing drops off a filament. Soft Matter, 9(26), 6053-6071). Permission letters given by the publisher are in the Appendix.

CONTRIBUTION OF AUTHORS

The work on drop impact on porous membranes in Section 2.1, Section 3.1, and Chapter 4 represents a published manuscript [Sahu et al. (2012)] for which I was the primary author and conducted all the experiments. Dr. Sinha-Ray contributed in the design of the experimental setup and took the SEM images of the porous membranes. Dr. Sinha-Ray also assisted in writing of the manuscript. The work on blowing of drops in Section 2.2, Section 3.2, and Chapter 5 represents a published manuscript [Sahu et al. (2013)] for which I am the primary author, designer of the apparatus, and conductor of experiments. In all published works my advisor, Dr. Yarin, contributed to the writing of the manuscript. Dr. Pourdeyhimi also assisted in writing of the manuscript. Chapter 6 is the unpublished experiments directed at looking at the depth of penetration of liquid drops inside porous membranes. Chapter 7 is also the series of unpublished experiments done to look at the change in the orientation of nanofibers during liquid evaporation from the nanofiber mats. I anticipate that these works will be published as manuscript in peer reviewed journals in the future. Chapter 8 summarizes the overall conclusions of the presented research in the thesis.

TABLE OF CONTENTS

<u>CHAPTER</u>	<u>PAGE</u>
1. INTRODUCTION	1
1.1 History of nanofibers	1
1.2 Nanofibers in filter media	2
1.3 Coalescing filters	3
1.4 Thesis objectives	5
2. BACKGROUND AND LITERATURE REVIEW	6
2.1 Drop impacts onto membranes.....	6
2.2 Motion of drops along and across a filament	9
2.3 Penetration of drops into porous membranes	14
2.4 Drop evaporation	18
3. RESEARCH OUTLINE	21
3.1 Drop impacts onto nano-textured porous membranes	21
3.2 Drop motion under the action of air blowing	22
3.3 Liquid penetration into non-wettable fibrous filter media	23
3.4 Mechanical strength of nanofiber filter media	23
4. DROP IMPACTS ONTO ELECTROSPUN NANOFIBER MEMBRANES	24
4.1 Introduction	24
4.2 Experimental materials and methods	25
4.2.1 Materials	25
4.2.2 Preparation of Solutions	25
4.2.3 Electrospinning	27
4.2.4 Contact angle	28
4.2.5 Preparation of teflon-coated nylon grids	28
4.2.6 Drop impact experiments	28
4.2.7 Microscopy	30
4.3 Results and discussion	31
4.3.1 Water drop impacts onto bare nylon grids	31
4.3.2 Water drop impacts onto teflon-coated nylon grids	34
4.3.3 FC 7500 drop impacts onto bare nylon grids and grids coated with teflon	42
4.3.4 Impact of hexane drops onto bare nylon grids and grids coated with Teflon	48
4.3.5 Drop impact onto electrospun PAN nanofiber mats supported by bare nylon grids	50

TABLE OF CONTENTS (continued)

<u>CHAPTER</u>		<u>PAGE</u>
4.3.6	Water drop impact onto electrospun Nylon 6/6 nanofiber mats onto bare nylon grids	61
4.3.7	Water drop impact onto electrospun PCL nanofiber mats supported on bare nylon grids	63
4.3.8	Water drop impact onto electrospun teflon nanofiber mats supported on bare nylon grids	65
4.4	Theoretical model	70
4.5	Conclusion	72
 5.	 BLOWING DROPS OFF A FILAMENT.....	 74
5.1	Introduction	74
5.2	Experimental materials and methods	75
5.2.1	Materials	75
5.2.2	Experimental setup	75
5.3	Experimental results	77
5.3.1	Dynamics of drop motion along the filament	78
5.3.2	Instability of thin film and recoil motion of drops along the Filament	91
5.3.3	Stick-slip motion of drops on filament	97
5.3.4	Drops on filament in cross-flow	100
5.3.5	Drop hopping across filaments	114
5.4	Theoretical model	117
5.4.1	Dynamics of drop motion along the filament	117
5.4.2	Tail formation and instability; recoil motion of drops	121
5.5	Conclusion	123
 6.	 IMPACT OF AQUEOUS SUSPENSION DROPS ONTO NON-WETTABLE POROUS MEMBRANES: HYDRODYNAMIC FOCUSING AND PENETRATION OF NANOPARTICLES	 124
6.1	Introduction	124
6.2	Materials and methods	125
6.2.1	Materials	125
6.2.2	Experimental setups	127
6.3	Experimental results: penetration into pores	130
6.4	Theoretical model	143
6.4.1	Drop impact and penetration into a single pore	143
6.4.2	Forced liquid filtration inside membrane	151
6.5	Discussion: theory versus experiment	157
6.5.1	Penetration fronts	157

TABLE OF CONTENTS (continued)

<u>CHAPTER</u>		<u>PAGE</u>
6.5.2	Viscous dissipation inside pores and the critical thickness of PTFE membrane	158
6.6	Conclusion	161
7.	EFFECT OF DROP EVAPORATION ON SUSPENDED NANOFIBER MAT	163
7.1	Introduction	163
7.2	Experimental materials and methods	163
7.2.1	Materials	163
7.2.2	Experimental method and setup	163
7.3	Results and discussions	165
7.3.1	Evaporation of a sessile drop	165
7.3.2	Void formation during evaporation on nanofiber mat	171
7.3.3	Effect on porosity of nanofiber mat	175
7.3.4	Theoretical Model	177
7.4	Conclusion	183
8.	CONCLUSION	184
9.	CITED LITERATURE	186
10.	APPENDIX	198
11.	CURRICULUM VITAE	200

LIST OF TABLES

<u>TABLE</u>	<u>PAGE</u>
4.1 Properties of Teflon AF and the solvents tested for its electrospinning	27
4.2 Electrospinning parameters.....	27
4.3 Static contact angle of water on cast polymer films	28
5.1 The average (over several trials) values of the capillary number of different silicone oil drops at various blowing speeds.....	92
5.2 Oscillation frequencies of silicone oil and water drops in the direction of blowing. The experimental frequencies are an average taken over several trials.....	102
6.1 Spread factor measured for drop impact onto the glass fiber membrane at different impact velocities. The experimental results listed in the table are the averages of two duplicate experiments.....	142

LIST OF FIGURES

<u>FIGURE</u>	<u>PAGE</u>
4.1 Schematic of the experimental setup	30
4.2 SEM image of: (a) bare Nylon grid, (b) Teflon-coated Nylon grid. The image shows some blocked pores (the white areas), which were very infrequent. The blockage is due to a thin Teflon film. The majority of the pores are always open (the dark areas).....	31
4.3 Impact of a water drop onto a bare nylon grid with a low impact velocity of 1 m/s. The panels correspond to: (a) $t = 0$ ms, (b) $t = 6$ ms, (c) $t = 12$ ms, (d) $t = 18$ ms, (e) $t = 24$ ms and (f) $t = 30$ ms. Scale bars, 1mm	32
4.4 Water drop impact on bare nylon grid in 2 ms after the impacts. The impact velocities are: (a) 2.23 m/s, (b) 2.44 m/s, (c) 2.64 m/s, (d) 2.82 m/s, (e) 3.0 m/s, (f) 3.16 m/s, (g) 3.31 m/s and (h) 3.46 m/s. Scale bars, 1mm.....	33
4.5 Water drop impact with the impact velocity of 2.23 m/s at the time moments: (a) $t = 2$ ms and (b) $t = 4$ ms. Water drop impact with the impact velocity of 3.46 m/s at the time moments: (c) $t = 2$ ms and (d) $t = 4$ ms. The comparison of panels (a) and (c) shows how the amount of water penetrating through Nylon grid increases with an increase in the impact velocity. Panel (b) show that at a lower impact velocity, the surface tension is capable of retracting almost all penetrated water, whereas panel (d) shows that at a higher impact velocity, the surface tension is incapable to prevent full penetration of a significant part of the impacting drop. Scale bars, 1mm.....	34
4.6 Static contact angle of water drops on (a) a bare nylon grid and (b) on a Teflon-coated nylon grid. The images show that Teflon coating changed the partially wettable nylon grids into rather hydrophobic ones under static conditions. Scale bars, 1mm.....	35
4.7 Water drop impact onto a Teflon-coated nylon grid with a low impact velocity of 1 m/s at (a) $t = 0$ ms, (b) $t = 4$ ms, (c) $t = 8$ ms, (d) $t = 12$ ms, (e) $t = 16$ ms and (f) $t = 20$ ms. Scale bars, 1mm.....	37
4.8 Water drop impact onto Teflon-coated nylon grid 2 ms after the first contact. The impacts velocities are (a) 2.64 m/s, (b) 2.82 m/s, (c) 3.0 m/s, (d) 3.16 m/s, (e) 3.31 m/s and (f) 3.46 m/s. Scale bars, 1mm.....	38

LIST OF FIGURES (continued)

<u>FIGURE</u>	<u>PAGE</u>
4.9 Water drop impact onto Teflon-coated nylon grid with the impact velocity of 2.64 m/s at (a) $t = 2$ ms and (b) $t = 8$ ms. An impact with the impact velocity of 3.46 m/s at (c) $t = 2$ ms and (d) $t = 4$ ms. The comparison of panels (a) and (c) shows how the amount of water penetrating through the grid increases with the increase in the impact velocity. Panel (b) shows that at a lower velocity, surface tension is capable of stopping and uplifting almost all the penetrated water behind the rear side of the grid. On the other hand, panel (d) shows that at a higher impact velocity no “lift-up” is possible anymore and a significant part of water fully detaches from the rear side of the grid. Scale bars, 1mm.....	39
4.10 Fractions of water drops which penetrated through micropores after drop impact onto bare nylon or Teflon-coated nylon grids. The data were obtained using the images recorded 2 ms after drop impact. In the case of nylon grids, there is no water penetration at the impact velocities below 2.23 m/s, in the case of Teflon-coated nylon grids there is no water penetration at the impact velocities below 2.64 m/s.....	41
4.11 Drop of FC 7500 impacting onto a bare nylon grid with the impact velocity of 1 m/s at (a) $t = 0$ ms, (b) $t = 2$ ms, (c) $t = 4$ ms, (d) $t = 6$ ms after the impact. Scale bars, 1mm.....	42
4.12 Drop of FC 7500 impacting onto a bare nylon grid with the impact velocity of 2.64 m/s. Scale bars, 1mm.....	43
4.13 Impact of FC 7500 drop onto bare Nylon grid from a height of 60 cm (3.46 m/s). Scale bars, 1mm.....	44
4.14 Effect of the impact velocity on the penetration pattern of drops of FC 7500 liquid impacting onto a bare nylon grid. The impact velocities are: (a) 1.0 m/s, (b) 1.41 m/s, (c) 1.73 m/s, (d) 2.0 m/s, (e) 2.23 m/s, (f) 2.44 m/s, (g) 2.64 m/s, (h) 2.82 m/s, (i) 3.0 m/s, (j) 3.16 m/s, (k) 3.31 m/s and (l) 3.46 m/s. All the images correspond to 2 ms after drop impact. Scale bars, 1mm.....	45
4.15 Effect of the impact velocity on the penetration pattern of the FC 7500 drops onto Teflon-coated nylon grid. (a) 1.0 m/s, (b) 1.41 m/s, (c) 1.73 m/s, (d) 2.0 m/s, (e) 2.23 m/s, (f) 2.44 m/s, (g) 2.64 m/s, (h) 2.82 m/s, (i) 3.0 m/s, (j) 3.16 m/s, (k) 3.31 m/s and (l) 3.46 m/s. All the images correspond to 2 ms after drop impact. Scale bars, 1mm.....	47

LIST OF FIGURES (continued)

<u>FIGURE</u>	<u>PAGE</u>
4.16 Hexane drop impact onto bare nylon grid at different impact velocities. The sequence of the images for each velocity value corresponds to the time span from 0 ms (the moment just before the impact) to 8 ms. Scale bars, 1mm.....	49
4.17 Hexane drop impact onto Teflon-coated nylon grid at the impact velocities of $V = 1$ m/s and $V = 3.46$ m/s. Scale bars, 1mm.....	50
4.18 SEM image of electrospun PAN nanofibers deposited onto bare Nylon grid for 60 s. (a) The overall view, (b) a zoomed-in view over an opening in the grid.....	52
4.19 Panels (a) and (b) show PAN nanofibers electrospun onto a nylon grid for 20 s (two different locations). Panels (c) and (d) show PAN nanofibers electrospun onto nylon grid for 60 s (two different locations). It can be seen from the images that a longer electrospinning time reduced the pore size significantly, while the mat thickness can stay approximately the same (see Fig. 4.20). This can be explained as follows. The nylon grid, which is dielectric, is kept on a copper electrode during electrospinning. As polymer nanofibers are deposited onto the grid, they are attracted to the still open domains of the copper electrode. Moreover, the residual electric charge in the polymer nanofibers also tends to repel the oncoming polymer jet. This repels the oncoming nanofiber loops toward the still open domains of the copper electrode, which diminishes pore size even more.....	53
4.20 Thickness of electrospun PAN nanofiber mat on bare nylon grids versus the electrospinning time. There is no pronounced dependence of the mat thickness on the electrospinning time.....	54
4.21 Impacts of the identical water drops onto PAN nanofiber mats electrospun onto nylon grids for different time t . The impact velocity was 3.46 m/s, the initial drop diameter was 2 mm. The electrospinning time t values were: (a) $t=5$ s, (b) $t=10$ s, (c) $t=15$ s, (d) $t=20$ s, (e) $t=25$ s, (f) $t=30$ s, (g) $t=35$ s, (h) $t=40$ s, (i) $t=45$ s, (j) $t=50$ s, (k) $t=55$ s and (l) $t=60$ s. The images correspond to 2 ms after the moment when the drops touched the target. Scale bars, 1mm.....	56
4.22 The critical velocity for water penetration after drop impact versus the electrospinning time of PAN nanofiber mats onto nylon grids. The square symbols correspond to the experiments where water penetration was observed, whereas the triangular ones correspond to the experiments without water penetration after drop impact. The initial drop diameter was 2 mm.....	57
4.23 Magnified optical images showing the same place of the nanofiber mat deposited over a nylon grid before [in (a)] and after [in (b)] drop impact. The deposition time of the nanofiber mat was 60 s and the drop impact velocity was 3.46 m/s. Scale bars, 10 μ m.....	58

LIST OF FIGURES (continued)

<u>FIGURE</u>	<u>PAGE</u>
4.24 Optical images of electrospun PAN nanofiber mat on a nylon grid. (a) Before drop impact, (b) after 4 impacts, (c) after 6 impacts, and (d) after 8 impacts of 1 mm drop of FC 7300. This liquid has a relatively low surface tension, which diminishes nanofiber rearrangement when samples are dried after drop impact prior to the observations.....	60
4.25 SEM images of nylon 6/6 nanofibers collected over a bare nylon grid. (a) The overall view, and (b) a zoomed-in image.....	61
4.26 Water drop impact onto electrospun nylon 6/6 nanofiber mats on a bare nylon grid at different velocities: (a) $V = 1$ m/s, (b) $V = 2.64$ m/s and (c) $V = 3.46$ m/s. The images correspond to different time instants from the moment of impact (approximately at $t = 0$ ms). Scale bars, 1mm.....	63
4.27 Penetration chart for PCL and PAN nanofiber mats on bare nylon grids. The solid line corresponds to PCL and the dashed line to PAN.....	65
4.28 Static contact angle of water drop on (a) cast Teflon on the glass slide and (b) on electropsun Teflon nanofiber mat collected on a nylon grid. Scale bars, 1mm....	66
4.29 SEM images of the electrospun Teflon nanofiber mat collected on the nylon grid. The pore size of the nylon grid is $20\text{ }\mu\text{m}$ and the collected nanofibers effectively reduce the pore size of the substrate to $3\text{--}6\text{ }\mu\text{m}$. The thickness of the nanofiber mat is of the order of $5\text{--}8\text{ }\mu\text{m}$. (a) The overall view. (b) Teflon fibers over a pore of the nylon grid. SEM images of the electrospun Teflon nanofiber mat before (a) and after (c) drop impact at the impact location. The comparison of panels (a) and (c) does not show any visible damage to the mat caused by drop impact.....	67
4.30 Two frames from the movie (S1) demonstrating superhydrophobicity of the Teflon nanofiber mat when water jet impacts onto it a velocity of 1-2 m/s. (a) Water jet is repelled from Teflon nanofiber mat on a Nylon grid. (b) Drops are blown off from the Teflon nanofiber mat. Scale bars, 1mm.....	68
4.31 Water drop impact onto electrospun Teflon nanofiber mat on nylon grid. The impact velocity $V = 3.46$ m/s. Scale bars, 1mm.....	70

LIST OF FIGURES (continued)

<u>FIGURE</u>	<u>PAGE</u>
5.1 Sketch of the experimental setup. (a) Compressed air is supplied through the air inlet, its flow is regulated by a pressure regulator. Then, air flows through the high- pressure tubing, controlled by a three-way solenoid valve (on/off), and is issued out through an outlet which can be co-axial with a thin filament suspended under light tension (cf. Fig. 5.2). The schematics of the filament supports in different cases are shown for: (b) blowing in parallel to the filament; (c) blowing perpendicular to a single filament; and (d) blowing perpendicular to a series of parallel filaments.....	76
5.2 An enlarged sketch of a filament co-axial to the air outlet (in the case of blowing parallel to the filament).....	77
5.3 Typical displacement and velocity curves for three different drops of 100 cst silicone oil at the blowing speed of 8.9 m/s. (a-b) $Ri = 0.052$ cm, (c-d) $Ri = 0.042$ cm and (e-f) $Ri = 0.040$ cm. The insets show the drops on the filament for the respective trials. In the insets in panels (a), (c) and (e) scale bars are 0.5 mm.....	78
5.4 Typical experimental data for the displacement curves of different 100 cst silicone drops depicted in the insets which were submitted to the blowing speed of 8.9 m/s. Scale bars, 0.5 mm.....	80
5.5 Displacement and velocity curves for three different drops of 100 cst silicone oil at the blowing speed of 6.5 m/s. (a-b) $Ri = 0.05$ cm; (c-d) $Ri = 0.047$ cm; (e-f) $Ri = 0.038$ cm. Scale bars in the insets in panels (a), (c) and (e) are 0.5 mm.....	83
5.6 Snapshots of 100 cst silicone oil drop with (a) $Ri = 0.038$ cm, and (b) $Ri = 0.047$ cm moving along the filament at different time moments. The drops are moving due to air blowing with the speed of 6.5 m/s. Scale bars, 0.5 mm.....	84
5.7 Measured displacement curves of 100 cst silicone oil drops subjected to the blowing speed of 6.5 m/s.....	85
5.8 Displacement curves for two 100 cst silicone oil drops of different size at the blowing speed of 3.3 m/s. (a) $Ri = 0.05$ cm: in the range $5 \text{ s} < t < 20 \text{ s}$ the drop moves in a stick-slip manner; (b) $Ri = 0.055$ cm: in the range $2.5 \text{ s} < t < 13 \text{ s}$ the drop moves in a stick-slip manner.....	85
5.9 Comparison of the maximum velocity of the 100 cst silicone oil drops obtained experimentally and predicted theoretically for different drop radii and different blowing speeds: (a) $V_{\max} = 8.9$ m/s, (b) $V_{\max} = 6.5$ m/s and (c) $V_{\max} = 3.3$ m/s.....	86

LIST OF FIGURES (continued)

<u>FIGURE</u>	<u>PAGE</u>
5.10 Typical displacement and velocity curves for three 50 cst silicone oil drops of different sizes at the blowing speed of 8.9 m/s. (a and b) $Ri = 0.045$ cm, (c and d) $Ri = 0.042$ cm, and (e and f) $Ri = 0.040$ cm. The insets show the drops on the filament. The scale bars are 0.5 mm.....	87
5.11 Typical displacement and velocity curves for two 50 cst silicone oil drops of different sizes at the blowing speed of 6.5 m/s. (a and b) $Ri = 0.041$ cm, and (c and d) $Ri = 0.037$ cm. The insets show the drops on the filament. The scale bars are 0.5 mm.....	88
5.12 Typical displacement and velocity curves for three 20 cst silicone oil drops of different sizes at the blowing speed of 8.9 m/s. (a and b) $Ri = 0.047$ cm, (c and d) $Ri = 0.045$ cm, and (e and f) $Ri = 0.038$ cm. The insets show several snapshots of the drops on the filament; the scale bars are 0.5 mm.....	89
5.13 Displacement and velocity curves for three 20 cst silicone oil drops of different sizes at the blowing speed of 6.5 m/s. (a and b) $Ri = 0.044$ cm, (c and d) $Ri = 0.041$ cm, and (e and f) $Ri = 0.037$ cm. The insets show the drops on the filament. Scale bars are 0.5 mm.....	90
5.14 Snapshots of a 20 cst silicone oil drop of $Ri = 0.045$ cm on a filament at different time moments. The drop is moving due to air blowing at the speed of 8.9 m/s. Scale bars are 0.5 mm.	90
5.15 Development of the capillary instability of thin liquid film withdrawn from a drop moving along the filament. The drop of 100 cst silicone oil is subjected to blowing at the speed of 8.9 m/s at the nozzle exit. Blowing is from left to right. Scale bars are 0.5mm.....	93
5.16 (a) Recoil motion of a 20 cst silicone oil drop after the cessation of air blowing. (b) Recoil motion of a 20 cst silicone oil drop. Air blowing was ceased earlier than in panel (a), and the drop recoils to a further distance, closer towards the nozzle. Scale bars, 1mm; $t=0$ corresponds to the moments of the cessation of air blowing.....	95
5.17 Recoil motion of three different 20 cst silicone oil drops along the filament. The experimental data are traced with dashed lines, the theoretical prediction is shown by solid line. The slopes of the linear fit to the recoil path were: 0.017 cm/s in trial 1, 0.024 cm/s in trial 2 and 0.03 cm/s in trial 3.....	97
5.18 An instantaneous flow pattern in air issued from the nozzle at 3.3 m/s. The intermittency sets in at a distance of 2.7 cm from the nozzle. Flow visualization is done with smoke. Scale bar, 5mm.....	98

LIST OF FIGURES (continued)

<u>FIGURE</u>	<u>PAGE</u>
5.19 (a) Oscillations in the lateral displacement of water drop apex, and (b) the corresponding Fourier coefficients. The drop is positioned at a distance of 4.5 cm from the nozzle exit and the air blowing speed is 7.2 m/s. The standard deviation of the apex displacement measurement is about 0.0004 cm, i.e. close to 10% of the measured amplitude.....	99
5.20 Frequency of lateral oscillations of water drop at different Reynolds numbers.....	100
5.21 Position of the drop with respect to the filament and the nozzle exit. Panel (a) corresponds to the viewing direction A-A in Fig. 5.1c, and panels (b) and (c) correspond to the viewing direction B-B in Fig. 5.1c. The position and volume of the drop on the filament before and after blowing is illustrated in panels (c) and (d), respectively.....	101
5.22 Several snapshots of drop blowing off in the vibrational type breakup of type V1. Silicone oil drop at $We = 2.8$ and $Oh = 0.07$ at different time moments. The direction of blowing is from left to right. The drop volume-equivalent diameter $2Ri = 0.9$ mm. Scale bars, 1 mm.....	103
5.23 Several snapshots of drop blowing off corresponding to the vibrational breakup of type V2. Silicone oil drop at $We = 6.19$ and $Oh = 0.07$ at different time moments. The direction of blowing is from left to right. The volume-equivalent initial drop diameter $2Ri = 0.88$ mm. Scale bars, 1 mm.....	104
5.24 Several snapshots corresponding to the vibrational breakup of type V3. Silicone oil drop at $We = 7.39$ and $Oh = 0.07$ at different time moments. The direction of blowing is from left to right and the volume-equivalent initial drop diameter $2Ri = 1.1$ mm. Scale bars, 1 mm.....	105
5.25 Snapshots of the bag-stamen type breakup of a silicone oil drop at $We = 11.67$ and $Oh = 0.07$ at different time moments. The blowing direction is from left to right and the volume-equivalent diameter of the initial drop $2Ri = 0.94$ mm. Scale bars, 1 mm.....	106
5.26 Snapshots of the bag type breakup of a silicone oil drop at $We = 17.17$ and $Oh = 0.07$ at different time moments. The direction of blowing is from left to right and the volume-equivalent diameter of the initial drop $2Ri = 1$ mm. No stamen is visible here. Scale bars, 1 mm.....	107

LIST OF FIGURES (continued)

<u>FIGURE</u>	<u>PAGE</u>
5.27 The vibrational breakup of type V2 of a silicone oil drop at $We = 17.73$ and $Oh = 0.13$ at different time moments. The direction of blowing is from left to right and the volume-equivalent diameter of the initial droplet $2R_i = 1$ mm. Scale bars, 1 mm.....	108
5.28 The breakup of 1 wt% aqueous solution of PEO ($M_w = 2000$ kDa) at $We = 7.5$ and $Oh = 0.25$ at different time moments. The direction of blowing is from left to right and the volume-equivalent diameter of the initial drop $2R_i = 1$ mm. Scale bars, 1 mm.....	109
5.29 The We - Oh with the domains corresponding to different types of breakup of Newtonian liquid drops on filament in cross-flow: I- vibrational breakup of type V1; II- vibrational breakup of type V2; III- vibrational breakup of type V3; IV- bag-stamen type breakup; V- bag type breakup.....	110
5.30 Breakup time versus the Weber number for different viscosities of silicone oils.....	111
5.31 Probability density function of the size of the residual droplet left on the filament. (a) The blowing velocity $V_0 = 11.14$ m/s, (b) $V_0 = 14.43$ m/s, (c) $V_0 = 17.46$ m/s, (d) $V_0 = 20.13$ m/s. The lines spanning the bar charts are the corresponding normal distributions.....	112
5.32 Normalized volume-equivalent radius of the residual droplet left on the filament versus the normalized air blowing velocity. Here the blowing velocity is rendered dimensionless by $V^* = 1$ m/s. Symbols represent the experimental data (the average taken over 20 trials for each point) spanned by a power-law fit written in each panel. (a) $\mu = 10$ cst, (b) $\mu = 20$ cst, (c) $\mu = 50$ cst, (d) $\mu = 100$ cst.....	113
5.33 A 10 cst silicone oil drop hopping across parallel filaments which are perpendicular to the air blowing direction. The inter-filament distance is 2 mm. The blowing is from bottom to top of the image. $V_0 = 11.14$ m/s. Scale bars, 1 mm.....	115
5.34 A 10 cst silicone oil drop hoping across parallel filaments which are perpendicular to the air blowing direction. The inter-filament distance is 2 mm. The blowing is from bottom to top of the image. $V_0 = 14.43$ m/s. Scale bars, 1 mm.....	116
5.35 A 10 cst silicone oil drop hoping across parallel filaments which are perpendicular to the air flow. The inter-filament distance is 2 mm. The blowing direction is from bottom to top of the image. $V = 17.46$ m/s. Scale bars, 1 mm.....	116

LIST OF FIGURES (continued)

<u>FIGURE</u>	<u>PAGE</u>
5.36 A 10 cst silicone oil drop bridging the filaments placed parallel to each other and perpendicular to the air flow. The inter-filament distance is 1 mm. The blowing direction is from bottom to top of the image. $V = 17.46$ m/s. Scale bars, 1 mm.....	117
5.37 Schematic of the drop shape on a filament before blowing and during blowing.....	119
5.38 Schematic of the drop deformation in the process of tail formation due to the filament motion along the x-axis.....	121
6.1 Optical microscope images of glass fiber filter (a-c) and PTFE membrane (d-f) showing the fibers and the pore sizes.....	126
6.2 Contact angle of water drop on the PTFE membrane.....	127
6.3 Schematic of the experimental setup used to drip nanoparticle suspension drops onto porous membranes.....	128
6.4 Schematic of the experimental setup for cutting sample membranes to detect nanoparticles embedded inside (if any).....	130
6.5 Top views of the glass fiber membrane after drop impact at 1.4 m/s [panel (a)] and 3.49 m/s [panel (b)]: the final domains of the nanoparticle deposition at the membrane surface. The impact velocities were measured at the impact moment. Drops were formed using a 14G needle. Scale bars: 1cm. (c) The side view of the cut cross-section of the membrane corresponding to the maximum penetration depth of a drop which impacted at 1.4 m/s: the nanoparticle distribution in depth. The lower boundary of the deposition domain is traced by the red line. Scale bar: 1mm. In all the images the membrane domains with no nanoparticles deposited look white, while those with the deposited nanoparticles look black. In panel (c) the dark strip under the membrane is the supporting Aluminum plate.	132
6.6 Sequence of images of drops of aqueous suspensions of nanoparticles impacting onto: (a) PTFE membrane, and (b) glass fiber membrane. The drops were issued from a 14G needle at the height of 180 cm, and had the impact velocity of 5.32 m/s (measured at the impact moment). Scale bar is 1cm.....	134

LIST OF FIGURES (continued)

<u>FIGURE</u>	<u>PAGE</u>
6.7 The side view of the cut cross-section of PTFE depth membranes at the locations corresponding to the maximal penetration depth. Panel (a) corresponds to the case when the membrane was cut beginning from the surface where the drop impact took place, whereas panel (b) shows the cut done in the opposite direction. The drops were issued from a 14G needle from the height of 180 cm, and had the impact velocity of 5.32 m/s (measured at the impact moment). The boundaries of the nanoparticle domains are traced by the red lines. Scale bars are 1 mm.....	135
6.8 (a) The experimentally measured ultimate penetration front into PTFE depth membrane is shown by symbols with the error bars corresponding to variance within different samples. (b) The predicted penetration front corresponding to the dimensionless time $t=0.6$. The drops were issued from a 14G needle. The impact height was 180 cm and the corresponding impact velocity was 5.32 m/s. The coordinates are rendered dimensionless using the membrane thickness h . As discussed in detail in section 6.5, time is rendered dimensionless by h/U_p ; (this value of b corresponds to a 26 μl drop impacting onto a membrane of thickness $h=0.1$ cm, with liquid penetrating with)......	136
6.9 The ultimate point of nanoparticle deposition corresponding to the results of Fig. 8 is shown by the symbol (PTFE depth membrane). The predicted locations of the tip of the water propagating front are shown by line, which is extended beyond the visible ultimate deposition of nanoparticles. Time is rendered dimensionless by h/U_p	137
6.10 Three-dimensional reconstruction of the penetration domain in PTFE membrane seeded by nanoparticles using data acquired from different sections of the drop impact surface. The drops were issued from a 14G needle, and cuts were done from the drop impact surface. The impact height was 180 cm and the corresponding impact velocity was 5.32 m/s. The inset shows a sketch of the cuts used in the reconstruction. The colors signify the depth at various points and correspond to the y -axis.....	138
6.11 Sketch of drop impact onto a single pore.....	144
6.12 Conformal mapping onto the upper half-plane.....	146
6.13 Potential distribution at the moment of impact. (a) , (b) , (c) (remind that here a stands for the dimensionless \bar{a}).....	149
6.14 Impact of a drop of Fluorinert fluid FC 7500 onto a Nylon membrane with the impact velocity of 2.64 m/s. Scale bars, 1mm.....	150

LIST OF FIGURES (continued)

<u>FIGURE</u>	<u>PAGE</u>
6.15 Velocity distribution at the drop bottom for a pore with . The red part corresponds to the pore, the green and blue parts – to the wall.....	151
6.16 Sketch of the membrane which is impacted by a drop from below. The bottom of the spread-out drop corresponds to $-b \leq x \leq b$, $y = 0$. The coordinates x and y , as well as b are rendered dimensionless by the membrane thickness h . This means, in particular, that the dimensionless effective penetration width of liquid after drop impact $2a$ of subsection 6.4.1 now becomes $2b = \bar{a}(D/h)$	153
6.17 Filtration front configurations at the dimensionless time moments shown in the inset. Time shown in the inset is rendered dimensionless by h/U_p . In the present case $b=0.8$	157
6.18 Normalized penetration depth Ω versus the Weber number. Straight lines are the linear fits according to Eq. (6.41). Panel (a) corresponds to the case where the PTFE membrane was cut beginning from the drop impact surface, whereas panel (b) corresponds to the case where the PTFE membrane was cut in the opposite direction. The value of C for panel (a) is 0.864 and for panel (b) is 0.791.....	161
7.1 Schematic of the collector used to form suspended nanofiber mats.....	164
7.2 Water drops gently deposited onto: (a) polycarbonate sheet, (b) PTFE sheet, and (c) suspended PAN nanofiber mat. Time $t = 0$, i.e. the images correspond to the deposition moment	165
7.3 Drop parameters during evaporation on a polycarbonate sheet. (a) Change in the contact angle and the dimensionless height. The height is rendered dimensionless by the initial height of the drop at $t=0$. (b) Change in the dimensionless contact diameter of the drop during evaporation. The contact diameter was rendered dimensionless by the initial contact diameter at $t=0$. The encircled area corresponds to the regime of constant area at the first stage of drop evaporation	167
7.4 Drop parameters during evaporation on the PTFE sheet. (a) Change in the contact angle and the dimensionless height. The height is rendered dimensionless by the initial height of the drop at $t=0$. (b) Change in the dimensionless contact diameter of the drop during evaporation. The contact diameter was rendered dimensionless by the initial contact diameter at $t=0$. The encircled area corresponds to the regime of constant area at the first stage of drop evaporation.....	168
7.5 Different stages of drop evaporation observed on the solid surfaces.....	169

LIST OF FIGURES (continued)

<u>FIGURE</u>	<u>PAGE</u>
7.6 Drop parameters during evaporation on the PAN nanofiber mat. (a) Change in the contact angle and the dimensionless height. The height is rendered dimensionless by the initial height of the drop at $t=0$. (b) Change in the dimensionless contact diameter of the drop during evaporation. The contact diameter was rendered dimensionless by the initial contact diameter at $t=0$. The encircled area corresponds to the regime of constant area at the first stage of drop evaporation.....	170
7.7 Water drop evaporation on a rarefied PAN nanofiber mat. The nanofibers surrounding the triple contact line are pulled and deformed by liquid. The time interval between two neighboring images is 1s	172
7.8 Superimposed images of the same nanofibers which were initially surrounding the contact line of a residual of an evaporating drop (dark fibers) and their locations after evaporation had been finished (light fibers). The arrows indicate displacement of the individual fiber elements.....	172
7.9 Relocation of nanofibers inside the wetted area of a denser nanofiber mat. The fibers adjacent to the contact line do not move.....	173
7.10 Thin and thick nanofiber mat collected on the aluminium plates for different times of electrospinning. The images are taken before the drop evaporation.....	174
7.11 Thin and thick nanofiber mat collected on the aluminium plates for different times of electrospinning. The images are taken after the drop evaporation.....	175
7.12 Frequency distribution of void sizes: (a) before, and (b) after drop evaporation.....	176
7.13 Schematic of the fiber deformation due to the evaporation of water film spanning the fibers. (a) Bending of nanofibers by the attached film and (b) different possible film configurations that might arise as a result of fiber bending	177
7.14 Probability density function versus θ_0 constructed using data acquired for four different nanofiber samples. Panel (a) corresponds to the results before drop evaporation, and panel (b) - after drop evaporation. The probability density function of each sample is an average of ten different images taken over the area where the footprint of a gently deposited drop was located. The encircled area in panel (b) shows formation of large pores, which is expressed by an increase in their frequency.....	180
7.15 Threshold transition described by the renormalization group theory in 2D .	181

LIST OF FIGURES (continued)

<u>FIGURE</u>	<u>PAGE</u>
7.16 Probability p of hole formation as a result of water evaporation and shrinkage of water films spanning neighboring nanofibers	182

SUMMARY

The goal of this work is to elucidate different physical mechanisms associated with the applications of coalescing filter media. Different stages of filtration of liquid drops impinging onto coalescing filters are separated into several fundamental problems each of them being discussed in a separate chapter. The first stage of filtration in a coalescing filter is associated with the encounter of a liquid drop delivered by an air flux onto the front surface of the fibrous filter media. The first fundamental question which arises is whether the drop penetrates into the layered fibrous media or not? What are the parameters that affect drop penetration through the fibrous layered media. As the drop penetrates into filter media it is intercepted by the fibers inside the filter. The next fundamental question which arises is how does the drop intercepted by the fibers inside the filter move due to the continuous air blowing? What factors affect drop motion on the fibers? As the drop moves into the depth of the filter media the next important question which arises is to what depth can liquid penetrate into the filter membrane? This work answers all the questions raised above both experimentally and theoretically.

The first part of this thesis demonstrates the outcomes of drop impacts of both polar (water) and non-polar (FC 7500 and hexane) liquids onto various porous substrates and elucidates what happens when a drop impacts onto a nano-textured coalescing filter. Nylon grid was used as a supportive membrane and nanofibers were electrospun from different polymer solutions of different wettability onto the same Nylon grid. At the first stage of the research work, drop impacts onto the Nylon grid and Teflon-coated Nylon grid revealed that the drop penetrates into nano-textured porous membranes above a relatively low threshold

velocity of about 2 m/s irrespective of the surface wettability. Drop impacts onto Nylon grids coated with electrospun nanofiber mat of thickness of 8-10 μm and pore sizes of 3-6 μm revealed penetration of a portion of the primary drop at a slightly higher than the threshold velocity (still less than in many practical cases, e.g. 3 m/s). Theoretical evaluation of the critical nanofiber mat thickness associated with viscous dissipation inside porous membrane is studied as the later part of the penetration process, first theoretically, and then corroborated by the experimental data. The work nixes wide-spread expectations that an ideal water repellant filter media can fully eliminate water penetration into the filter. The results achieved in this part form foundations for design of effective nano-textured coalescing filter media.

The second part of the thesis elucidates the motion of oil drops on silicone filaments at two different orientations i.e., when air blowing happens along the filament or across the filament. Motion of a single drop on a single fiber under the effect of air blowing is an important model situation to understand the behavior of the entire filter medium. Fibers inside a non-woven fibrous filter media are arranged randomly in different directions. The two extreme cases of the fiber orientation with respect to the blowing direction is 0° and 90° studied in detail in the part of the work. First, motion of a single oil drop on a single filament is studied for different viscosities of oil and different air blowing velocities. Several important findings include formation of a thin film on the windward side of the drop, capillary instability of the thin film, stick-slip motion of the drop and oscillations of the drop. These experimental findings were also described in the framework of theoretical models developed in this work. Second, different breakup patterns a drop on a filament in cross-flow were studied experimentally and delineated on the plane of the dimensionless Weber and

Ohnesorge numbers. This non-dimensional Weber and Ohnesorge number plane elucidates understanding of the final drop under different blowing conditions. The hopping of a single drop across several fibers aligned parallel to each other was also observed in this part of the work.

To visualize drop penetration into fibrous medium a special experimental setup was designed. Suspensions of Titanium nanoparticles were used as tracer particles for the observation purposes. The experimental data and the theoretical model developed in this part revealed hydrodynamic focusing of liquid through smaller pores and easy water penetration into non-wettable PTFE membranes.

The addition of nanofibers to a filter media increases the filtration efficiency. Evaporation of drops and thin liquid films from the nanofiber surface is inevitable during the filtration operation. The unbonded nanofibers undergo deflections as a result of evaporation. The evaporation of a drop on a suspended nanofiber mat was studied and the change in the network formed by the nanofibers was elucidated.

1. INTRODUCTION

1.1 History of nanofibers

Formation of fibers from a solution subjected to electric field was first demonstrated in 1902 [Cooley (1902)]. Nanofibers from polymer solution were obtained in practice by A. Formhals in Germany in 1934 [Formhals (1934)]. Fine fiber production in the presence of electrostatic fields open a way for improving the production of filter materials; in the former USSR such filters were named after the inventor Petryanov-Sokolov as PF (Petryanov's filters) [Lushnikov (1997)]. The PF materials were used to protect the environment from radioactive aerosols. Major research on nanofiber forming was conducted at Karpov's Scientific Research Institute of Physics and Chemistry (Moscow), which is summarized in the following monograph [Filatov et al. (2007)]. An instrument for producing patterned ultra-thin and ultra-light nanofiber fabrics was patented by Harold L. Simons in 1966. Nanofiber formation was revived in the age of nanotechnology due to the works of P.K. Baumgartner, D.H. Reneker and A.L. Yarin [Yarin et al. (2014)]

Nanofibers were first introduced into advanced commercial applications in the US by Donaldson, one of the leading companies in the filter media industry. A European company Freudenberg then became the leader of the industrial applications of nanofibers in the Old World. Today, several other leading companies (e.g. DuPont) are seriously interested in nanofibers and nanofiber-containing filter media. The recent advances in electrospinning result in the improved nanofibers and their wider applications.

1.2 Nanofibers in filter media

Nanofibers are used in a wide variety of filtration-related applications, such as high efficiency air filtration media, filter media for pulse-clean cartridges in dust collection, coalescence-promoting filter media, anti-microbial wound healing applications, cigarette filters, engine air filtration, biocatalytic filtering media, ion exchange filter media, and many more. Pure water and clean gas supply have become a necessity for several major industries, like pharmaceutical, semiconductor, manufacturing and processing, and biotechnology [Barhate and Ramakrishna (2007)]. Liquid and solid aerosols of a wide range of sizes are formed in processing or in the equipment operation due to fluid shear, splashing, evaporation-condensation, interfacial and frictional forces. These mists need to be removed from the fluid stream as they might pose environmental risks. The different mechanisms of particle capture in the filter are direct interception, inertial impaction, Brownian diffusion, electrostatic interaction and gravity settling. The total efficiency of a filter is related to the collective contribution of the individual efficiencies of the mechanisms listed above. Particles of sizes below $0.3\ \mu\text{m}$ undergo Brownian motion and thus move randomly with a higher probability of being captured by the fibers of the coalescing filter. Particles of sizes between $0.3\ \mu\text{m}$ and $1\ \mu\text{m}$ follow the fluid flow practically without any deviation from the fluid elements trajectories, and thus can be directly intercepted by the fibers on head-on or tangential collisions. Particles in the range between $1\ \mu\text{m}$ and $10\ \mu\text{m}$ deviate from the fluid flow due to inertia and can be intercepted when colliding with a fiber in a filter. Particles larger than $10\ \mu\text{m}$ are heavy enough to settle down due to gravity.

The nanofiber filter media have several advantages over the existing filter media such as small pore sizes, lower weight, and high specific surface area, which could be used to improve and enhance the filtration efficiency compared to the existing filter media. Moreover, the ease at which the nanofiber surface could be actively functionalized, results in the extensive use of nanofibers in both air and liquid filtration. The particles of the size of 0.3 μm and above could be successfully filtered using the existing high efficiency air filters but the smaller particles cannot be caught effectively by the standard filter media. The challenge for the filtration industry is in removal of particles smaller than 0.3 μm , as well as in the adsorption of the toxic gases.

1.3 Coalescing filters

A process in which liquid aerosols are caused to agglomerate into larger droplets as they pass through a filter medium is the key element of coalescing filters. The agglomerated droplets eventually form a merger drop large enough to be gravitationally drained away. There are two types of filtration technique: surface filtration where the particles or droplets are intercepted on the incoming side of the filter surface and do not necessarily pass through the depth of the filter, and the deep-bed filtration where the particles or droplets penetrate inside the thickness of the filter with the continuous phase and are intercepted within it. Removal of water in oil emulsions in engine and other applications, removal of oil mists from the air streams for compressed gas cleaning, engine crankcase ventilation, cutting and machining operations, removal of water droplets from the air stream in HVAC (Heating ventilation and air conditioning), capture of soot particles from the air stream in Diesel engine crankcase ventilation comprise a set of industrially important applications where

coalescing filters are used. For example, in order to avoid the risk to the environment and human health, removal of oil mists is very important. Recently separation of water-oil emulsions has received significant attention in the petroleum and chemical industries due to the safety, product quality, ecological and economic reasons [Shin et al. (2005); Shin et al. (2004); Agarwal et al. (2013); Hunter et al. (2014)]. It should be emphasized that it is very difficult to separate dispersions of drop sizes of less than 100 μm .

In emulsion separation several groups of parameters play a significant role, such as filter properties (fiber diameter, permeability, pore size, surface wettability, roughness, thickness), dispersed and continuous phase properties (viscosity and interfacial tension, density difference between the phases, presence of surfactants, droplet or particle sizes), and operating conditions (flow rate, pressure drop, filter orientation, emulsion concentration) [Shin et al. (2004)]. Coalescing filters have different porosity varying in the thickness, with the larger fibers on both outer surfaces and smaller fibers in-between inside the filter. The following elements of the coalescence process within a coalescing filter should be mentioned: capturing of water droplets by the fibrous bed, coalescence of the collected drops on the fibers, and finally the release of the merger drops and their migration from the fiber surfaces. An intermediate wettability of the fiber material results in the best performance [Voyutskii et al. (1953)]. The fiber material should be hydrophilic enough to facilitate coalescence of water drops rather than super-hydrophilic, which might result in an excessive clogging by accumulated water drops. The coalescence efficiency was found to be independent of the wettability of the continuous phase. Low flow rates, increased thickness and high specific surface area of the filter result in an increased coalescence filtration efficiency. Coalescing filters can also be used to capture solid contaminants being operated

as particulate filters. Soot in oil systems showed propensity to increase pressure drop compared to liquid aerosol because of an increase in the effective viscosity due to the presence of solid particles and deposition of soot on the fibrous filter [Hunter et al. (2012)]. The addition of recycled polystyrene nanofibers to glass-fiber coalescing filters significantly improves the coalescence efficiency at the expense of an increase in pressure drop within the filter [Shin et al. (2005)]. Layered filter media of different wettability were used to study the effect of layered structures on the filter performance [Kulkarni et al. (2012)].

1.4 Thesis objectives

Even though the fibrous filter media are being used for decades, the basic physical mechanisms governing the filtration process are still not purely understood. Super-hydrophobic water-repellant porous surfaces are used without a prior knowledge of the dynamics of drop impact onto the filter surface. Sufficiently thick filter media are used to avoid liquid penetration at the cost of an increased pressure drop. The research aims of this research work are as follows: to elucidate the outcomes of liquid drop impacts of various fluids onto fibrous membranes; to evaluate the critical filter membrane thickness, which completely avoids liquid penetration through it. Chapter 4 aims at the investigation of liquid drop penetration through thin nanofiber mats of different wettability. Motion of a drop on a single filament is discussed in chapter 5. Several different modes of drop breakup are also uncovered. Chapter 6 studies the ultimate penetration fronts of water drops in non-wettable PTFE membranes. Drop evaporation on suspended nanofiber membranes and the related nanofiber network distortions are discussed in chapter 7.

2. BACKGROUND AND LITERATURE REVIEW

2.1 Drop impacts onto membranes

(This section has been previously published in Sahu et al. (2012)).

Questions on penetration of liquid drops into porous media arise in relation to filtration through porous nonwoven membranes, coalescence filters and ordered fibrous media with fiber diameters from several tens of micron down to electrospun nanofibers [Yarin et al. (2006); Sherony et al. (1978); Pich (1966); Tien (1989); Brown (1993); Sareen et al. (1966); Spielman and Goren (1972); Bitten (1970); Rosenfeld and Wasan (1974)]. Single collector capture mechanisms intercept a single drop per event, at one point on a fiber or at the pore surface. Multi-fiber capture mechanisms such as straining, pore bridging, and pore blocking are also present in practice. Various physical mechanisms of drop interception and drainage are discussed in the above-mentioned references. Some approaches to the development of novel coalescence filters were triggered by the development of a number of the so-called superhydrophobic materials with high static contact angles of more than 150-160°, in particular, those mimicking the lotus effect [Marmur (2007); Jiang et al. (2004); Gao and McCarthy (2009)]. Drop impacts on porous nonwovens are characteristic not only of coalescence filtration but also of protective clothes used as a barrier for warfare liquid aerosols, e.g. such nerve agents as VX [Reneker et al. (2007)].

Nonwovens are used not only to intercept impacting drops but also to deliver them to a surface on which they are deposited as a coating, as in the recently introduced method of cooling of high-heat-flux electronic devices and server rooms through electrospun nanofiber mats [Srikar et al. (2009)]. The latter work, as well as the accompanying works [Lembach et

al. (2010); Sinha-Ray et al. (2011); Weickgenannt et al. (2011a) and Weickgenannt et al. (2011b)], in fact, demonstrated that the concept of hydrophobic micro- and nano-textured filters and porous coatings might be intrinsically vulnerable, since it is based on a misconception of static hydrophobicity. For example, in Lembach et al. (2010) it was shown that a millimeter-sized water drop softly deposited on a nonwoven electrospun nanofiber mat produced from PAN stayed almost spherical for several minutes. A completely different outcome was observed when a water drop of 2 mm in diameter impacted onto the same nanofiber mat at a speed of 2 m/s. In the latter case, the drop first rapidly spreads on a nanofiber mat surface as on a dry, rigid substrate and then remains pinned in the spread-out configuration and does not recede or bounce, as on a completely wettable substrate. Pinning of spread-out drops after the spreading stage of impact was used in Srikar et al. (2009), Lembach et al. (2010), Sinha-Ray et al. (2011), Weickgenannt et al. (2011a) and Weickgenannt et al. (2011b) to facilitate drop cooling of hot surfaces coated with nanofiber mats – a paradoxical situation where cooling was intensified by putting an insulation-like "furry overcoat" on a hot surface.

The observations with the help of high-speed cameras revealed many intriguing features of drop impacts on solid and liquid surfaces and significantly facilitated our understanding of these fascinating phenomena [Yarin (2006) and Thoroddsen et al. (2008)]. A recent ramification of such investigations encompassed drop impacts onto nano-textured porous surfaces [Srikar et al. (2009); Lembach et al. (2010); Sinha-Ray et al. (2011); Weickgenannt et al. (2011a); Weickgenannt et al. (2011b); Liu and Guo (2007); Tsai et al. (2009); Han and Steckl (2009); Tsai et al. (2010); Nguyen et al. (2010); Lee and Lee (2011)]. Such impacts are accompanied by non-trivial physical effects, which require their

understanding. In addition to the interesting physical aspects, the attention to drop impacts onto nano-textured porous surfaces was fueled by the interest in developing novel water-repelling surfaces with electrospun Teflon nanofiber mats being a natural candidate [Han and Steckl (2009)]. On the other hand, drop impacts onto nanofiber mats (both electrospun or not) revealed that under certain conditions they promote dynamic wettability rather than repelling water [Srikar et al. (2009); Lembach et al. (2010); Sinha-Ray et al. (2011); Weickgenannt et al. (2011a); Weickgenannt et al. (2011b); Tsai et al. (2009); Lee and Lee (2011)]. Moreover, it was recognized that due to the large disparity between the drop and the inter-fiber pore sizes (the drop diameter D of the order of 1 mm and the pore size d of the order of 1-10 μm), liquid accumulates the kinetic energy at the pore entrances and protrudes into them with a speed of the order of $(D/d)V \approx 100V$ where V is the impact velocity. This effect is reminiscent of the mechanism of formation of shaped-charge (Munroe) jets and is kindred to the widely-known way of opening of wine bottles by a sufficiently strong palm hit onto their bottom. Above the threshold impact velocity, in the dynamic wettability domain, such high speeds of liquid penetration and short times involved (on the scale of several milliseconds) preclude any manifestations of wettability-related effects such as the time dependence of the retention force observed on the scale of 10 min [Tadmor (2011) and Tadmor et al. (2009)]. A possible directionality of wettability-driven liquid spreading on nonuniform electrospun mats [Lembach et al. (2010)] or slanted nanohairs [Kim and Suh (2009); Kwak et al. (2010)] is a slow phenomenon (on the scale of 10 s), which is immaterial in the domain of the dynamic wettability (on the scale of a few milliseconds).

The idea that it might be possible to achieve an ultimate fluid repellent coalescence filter made of electrospun Teflon or other superhydrophobic nanofibers is of significant

interest, sounds attractive and is widely discussed. However, as the above-mentioned results on drop impact on electrospun nanofiber mats show, static hydrophobicity of such mats does not characterize dynamic behavior under the conditions of drop impact, and cannot prevent water penetration into these nanofiber mats. The latter means that dynamic transition from the Cassie-Baxter to Wenzel state is possible for such systems, even though the static one is not. This effect precludes development of ideal, absolutely water repellent filter media, or their front layers, but maybe such highly hydrophobic materials as Teflon-coated nanofibers [Han and Steckl (2009)] hold potential? The answer to this question will be negative according to the results described below

2.2 Motion of drops along and across a filament

(This section has been previously published in Sahu et al. (2013)).

Blowing drops off thin filaments by gas flow represents itself a complex fluid mechanical phenomenon which did not attract much attention so far, even though it is quite common and non-trivial, as well as is associated with such important applications as coalescence filters, printing and coating. Drop motion on filament networks can result in coalescence, division, atomization, and encapsulation of tiny particles intercepted by a filter. Liquid-gas coalescers are of great importance in separating water and oil drops from the gas streams, whereas liquid-liquid coalescers are used in the oil refining industry. It was found that as drops move along the filaments, they can coat them with a thin liquid film. This phenomenon plays an important role in drop motion along filaments. There are three possible scenarios: (i) liquid film on a filament which breaks into smaller droplets due to the capillary instability; (ii) formation of the axisymmetric barrel-shaped drops connected by liquid films;

and (iii) formation of the asymmetric clamshell-shaped drops [Kumar and Hartland (1988); McHale and Newton (2002); Carroll (1986); Chou et al. (2011)]. Stability of drops on filaments and transition of barrel-shaped to clamshell-shaped drops depend on the drop volume, filament radius, and surface/interfacial tension. Numerical and semi-analytical approaches were developed to establish stability criteria for drops of different conformations on filaments [McHale et al. (2001); Wu and Dzenis (2006)]. The capillary instability of thin liquid films on filaments is due to surface tension and kindred to the capillary breakup of liquid jets studied by Lord Rayleigh [Rayleigh (1878)]. In the case of capillary instability of thin liquid films on filaments this problem was studied in Goren (1962); Johnson et al. (1991); Yarin et al. (1993) and Quere (1999).

Some additional effects associated with drop motion on thin filaments were studied. Motion of drops on filaments due to temperature gradient [Yarin et al. (2002)], gradient of cross-sectional radius of the filament [Lorenceau and Quere (2004)], and surrounding air flow [Dawar et al. (2006)] were studied. Characterization of the capture efficiency and the dynamics of drops impacting onto horizontal filaments were discussed [Lorenceau et al. (2004)]. Filament-based microfluidic devices and biochemical microreactions can incorporate elements with drop motion on vertical filaments and networks under the action of gravity and viscous friction [Gilet et al. (2009); Gilet et al. (2010); Link et al. (2004) and Song et al. (2006)]. Viscous drag coefficient for drops moving on filaments was experimentally found in Dawar et al. (2006). The study of an individual drop motion on a filament is important for controlling filter coalescence performance in mist filters. The flow resistance of fibrous filter operating under wet conditions increases and approaches saturation. Performance of wet filters was characterized using resistance correlations for

different packing density and liquids [Liew and Conder (1985); Raynor and Deith (2000)]. The optimum orientation of filaments in wet filters for maximum self-cleaning was demonstrated in Mullins et al. (2004). To evaluate the particle capture efficiency of wet filters, a mathematical model was proposed to predict the barrel and clamshell drop oscillations on a filament [Mullins et al. (2005) and Mullins et al. (2006)].

Vertical vibrations of sessile drops on flat horizontal substrates were reported in Noblin et al. (2004) and Noblin et al. (2009) and two different oscillation modes were recognized: (i) oscillations with pinned contact line and changing contact angle, and (ii) simultaneous oscillations of the contact line position and the contact angle. The stick-slip behavior was observed at certain oscillation amplitudes. The stick-slip phenomenon was attributed to the effect of the contact angle hysteresis. Sharp et al. (2011) studied the dependence of the contact angle of small water drops on substrates of different wettability on the resonant frequencies considering standing wave profiles along the drop surface. It was observed that a certain finite contact angle hysteresis was essential to break the periodic symmetry and cause the drop to drift [Mettu and Chaudhury (2011)]. Strouhal et al. (1878) showed that the frequency of vibrations of cylindrical threads subjected to air cross-flow depends on the relative velocity of air which is attributed to the von Karman vortex street shed from the thread into its aerodynamic wake. Similar vibrations also exist for spheres. The wakes of cylinders and spheres can sustain regular or irregular vortex patterns in a wide range of the Reynolds number Re [Roshko (1953)]. The flows past a sphere in a wide range of the Reynolds number were studied experimentally [Taneda (1956)]. The Strouhal number, which is the dimensionless sphere vibration frequency, was studied in the range $10^3 < Re < 4 \cdot 10^4$. Two different levels of the Strouhal number in this range of Re were found. The high

level (the high-frequency vibrations of a sphere) is associated with the small-scale instability of the shear layer, whereas the low level of the Strouhal number (the low-frequency vibrations) is due to the large-scale eddies in the wake behind the sphere [Sakamoto and Haniu (1990); Kim and Durbin (1988)]. At relatively low Reynolds numbers about 300, the large-scale eddies represent the only source of the fluctuations in the wake.

Blowing of drops across the filaments by a cross-flow differs significantly from blowing along the filament. It is kindred to some extent to disintegration of free drops falling in air at rest or in the air flow in a wind tunnel or a shock tube which were studied in relation to such widespread applications as fuel injectors, chemical reactors, chemical separators, pesticide atomization, meteorology, medicine, spray drying and food processing. Generally speaking, the atomization process of free liquid drops is subdivided into primary and secondary atomization. The larger drops produced at the primary stage are unstable and undergo further secondary disintegration into smaller drops. The physical parameters which affect the atomization process, as well as blowing of drops off a filament by cross-flow are density, viscosity, pressure and temperature of both liquid drop and gas, the surface tension of the liquid drop and the relative velocity of the gas flow. In the framework of the dimensional analysis, the following dimensionless groups are of primary importance in this case: the Weber number and the Ohnesorge number where ρ_a is the gas (e.g. air) density, ρ_l is the liquid density, σ the surface tension, μ is the liquid viscosity, $2R_i$ is the volume-equivalent diameter of the primary drop, and V is the relative air velocity. The Weber number represents the ratio of the dynamic pressure of the air flow to the capillary pressure in the drop, whereas the Ohnesorge number represents the effect of the viscous stresses. Several breakup modes of drops in high-speed gas flows were reported. These include the

vibrational mode, bag mode, bag and stamen mode, chaotic mode, stripping mode and catastrophic mode (note that the terminology varies). The transition from one breakup mode to another is controlled by both Weber and Ohnesorge numbers. The effect of liquid viscosity on the breakup mode is sufficiently small when the Ohnesorge number is of the order of 10^{-3} .

The disintegration of free drops by gas flow was studied both theoretically and experimentally [Ranger and Nicholls (1969); Hinze (1955); Krzeczkowski (1980); Hirahara and Kawahashi (1992); Pilch and Erdman (1987)], in particular, using shock tubes or continuous gas jets. There is a critical Weber number below which the drop atomization does not occur. This critical value signifies the threshold of the bag type breakup mode. The empirical correlations for the critical Weber number and the breakup time for both low and high viscosity drops are available [Hirahara and Kawahashi (1992); Pilch and Erdman (1987); Cao et al. (2007) and Zhao et al. (2011)]. It is emphasized that there are significant differences between values of the critical Weber number reported in different works [Wierzbna (1990)]. The liquid viscosity has a significant effect on the transition boundaries between different regimes of drop atomization [Birouk et al. (2003)]. It was shown that the atomization of free drops occurs according to the Rayleigh-Taylor piercing mechanism in the range $10 < We < 10^2$, whereas the shear-induced entrainment is responsible for the atomization in the range $We > 10^3$ (Theofanus and Li (2008)). The physical mechanisms of different modes of drop atomization for Newtonian and non-Newtonian liquids were discussed [Arcoumanis et al. (1996); Guildenbecher et al. (2009); Chou and Faeth (1998); Liu and Reitz (1997); Wilcox et al. (1961); Joseph et al. (2002); Faeth et al. (1995); Hoyt and Taylor (1977)]. The vortices formed in the drop wake in gas cross-flow were visualized using PIV, and generation of alternate vortices and symmetrical twin vortices was found to be

responsible for the bag type and bag-stamen type atomization [Inamura et al. (2009)]. An empirical correlation for the drag coefficient for drops detaching from a filament due to gas flow was reported [Dawar and Chase (2010)].

2.3 Penetration of drops into porous membranes

Drop impact and spreading on impermeable solid surfaces and porous media are characteristic of numerous applications and are a part of our everyday experience [Yarin (2006)]. The observations made with the help of high-speed cameras revealed many intriguing features of drop impact onto solid, liquid and porous surfaces [Yarin (2006); Thoroddsen et al. (2008); Srikar et al. (2009); Lembach et al. (2010); Sahu et al. (2012); Sinha-Ray et al. (2011); Weickgenannt et al. (2011a) and Weickgenannt et al. (2011b)]. Recently it was shown that drop impacts at about 3.5 m/s onto nano-textured electrospun membranes can result in water penetration even through hydrophobic Teflon nanofiber mats, i.e. the dynamic focusing effects can fully dominate the wettability effects [Sahu et al. (2012)]. During hydrodynamic focusing the kinetic energy brought by a drop which impacts a wall with a very small opening compared to the drop size is focused into the opening, which results in very high speeds of flow into it. This effect is related to the well-known formation of shaped-charge jets (the Munroe jets or Neumann effect) due to focusing of the kinetic energy delivered by an explosion to a ductile metal (a liner on the explosive conical cavity which collapses), when the metal flows with very high speed like an inviscid liquid through a tiny opening [Birkhoff et al. (1948)]. A similar hydrodynamic focusing in the form of jetting (an ejecta sheet) was predicted in the neck between an impacting droplet and the target liquid surface [Weiss and Yarin (1999)], which was confirmed in the experiments in

the subsequent work [Thoroddsen (2002)]. Due to the hydrodynamic focusing, the initial velocity of liquid penetration into individual pores $U_p \approx (D/d)V_0$ is several orders of magnitude higher than the drop impact velocity V_0 , since the drop size D , which is of the order of 1 mm, is much larger than the pore size d , which is of the order of 1 μm [Lembach et al. (2010) and Weickgenannt et al. (2011a)]. During the hydrodynamic focusing, the initial penetration velocity U_p is also much larger than the Lucas-Washburn velocity corresponding to the wettability-driven imbibition, which makes the latter immaterial, while water drops are penetrating into Teflon electrospun nanofiber mats [Sahu et al. (2012)]. Moreover, the hydrodynamic focusing resulting in dynamic penetration happens well below the static penetration threshold, i.e. at $\rho V_0^2 < 4\sigma/d$ (with ρ and σ being the liquid density and surface tension), already at $\rho V_0^2 / (4\sigma/d) \approx 0.025$, in distinction from the case when drops and orifices are of the same order of magnitude [Lorenceanu and Quere (2003)]. The hydrodynamic focusing and penetration of drops into electrospun nanofiber mats has already been used to enhance cooling of high-heat flux surfaces [Sinha-Ray et al. (2011)], and in particular, to prevent the Leidenfrost effect even at such high surface temperatures as 300 °C [Weickgenannt et al. (2011a) and Weickgenannt et al. (2011b)]. The effect of surface roughness of the impermeable non-porous media on drop impact is clearly distinct from the phenomena observed in drop impacts onto permeable porous nano-textured surfaces [Yarin (2006); Weickgenannt et al. (2011b) and Sivakumar et al. (2005)].

Liquid flow on porous substrates in some cases depends on the liquid/solid wetting properties. Much work has been done on liquid drop spreading on porous substrates in the creeping flow regimes at low Reynolds number $Re < 1$, where the spreading and pore

imbibition are governed by the contact line motion, capillary pressure and wettability. Magnetic Resonance Imaging or X-ray could be possible options for the observations inside porous media, albeit they are either too slow or do not provide enough resolution to observe the evolution of the liquid penetration front. Significant research efforts were directed at the low Reynolds number spreading and wettability-driven imbibition, which was studied experimentally, analytically and numerically [Alleborn et al. (2004); Borhan and Rungta (1993); Denesuk et al. (1993); Pezron et al. (1995); Marmur and Cohen (1997); Starov et al. (2003); Kumar et al. (2006)]. These sources provide a wider context for the present work which aims at the observations of liquid penetration front into porous media following drop impact. It should be emphasized that drop impact onto nonwoven membranes comprised of multiple fibers encompassing the inter-fiber pores involves simultaneous interaction of liquid with multiple fibers and thus, involves different phenomena compared to those in drop impact onto individual fibers [Lorenceanu et al. (2004); Piroird et al. (2009)], since in the latter case dynamic focusing is impossible.

Modeling of flow within porous media can be quite challenging, particularly in the case of multi-phase (liquid, gas and/or vapor) flows [Barenblatt et al. (1989)]. Properly depicting the pore topology is essential for such simulations. Among various methods available for the observations of pore structures, micro-CT (micro-computed tomography) imaging technique is the most recent. It provides a direct visualization of the pore geometry [Gunde et al. (2010)]. On the other hand, numerical modeling of forced impregnation of a single or a few capillaries tackled only the regimes with $\rho V_0^2 \gg 4\sigma/d$ and is irrelevant in the present context, as discussed below.

Forced penetration of a single liquid drop through both hydrophilic and hydrophobic capillaries has been experimentally observed to delineate different impregnation regimes [Delbos et al. (2010)]. The drop diameter corresponding to the maximum spreading is very important because it elucidates the conditions under which the penetration process begins [Asai et al. (1993)]. Refractive index matching technique was used to track the kinetics of drop penetration into porous medium [Lembach et al. (2010)]. One of the main parameters governing liquid penetration into pores under the almost static conditions is the capillary pressure based on the pore size and wettability [Lorenceanu and Quere (2003)]. The rate of imbibition of porous media and spreading over the surface was estimated by measuring the change in the contact radius and height of the drop [Clarke et al. (2002)].

Coalescence filters are an example of porous media collecting drops from an oncoming gas or liquid flow [Filatov et al. (2007); Contal et al. (2004) and Frising et al. (2005)]. Drops penetrate the filter membrane and accumulate inside. As a result, filter permeability decreases, whereas the pressure drop in gas which is required to sustain the flow increases. Some groups expressed expectations that a hydrophobic filter medium will prevent water drops from penetrating inside, thus facilitating water collection and removal at the front surface. The hydrodynamic focusing, however, is expected to overcome hydrophobicity and let the impacting water drops to penetrate into hydrophobic media [Lembach et al. (2010); Sahu et al. (2012); Sinha-Ray et al. (2011); Weickgenannt et al. (2011a) and Weickgenannt et al. (2011b)]. In the present work this is directly demonstrated using the entrainment of seeding particles. In a broader context, the entrainment of seeding particles is not merely an observation tool but is of interest by itself in such applications as inkjet printing on smart textiles [Park et al. (2012)].

2.4 Drop evaporation

Evaporation of spherical droplets is characteristic of spraying of pesticides, ink-jet printing, spotting of DNA microarray data, and many more. The evaporation of free spherical droplets is accurately described by the well-known d^2 -law [Spalding (1953)] but the evaporation of non-spherical interacting with solid surfaces complicates the situation. The substrate affects the drop shape and thus affects its evaporation. The sessile drop evaporation can be found in numerous applications in micro-nano-fabrication, coating processes, spraying of pesticides, evaporative cooling, biochemical assays, etc. Droplet interactions with fibers are becoming more and more important in several processes such as filtration, textile fabrication, coating applications, coalescing media, ink-jet printing, etc.

Drop evaporation on surfaces attracted attention for many years [Langmuir (1918); Maxwell (1890)]. The dynamics of drop during evaporation is quantified in terms of the contact diameter, drop volume, drop height, shape of the drop and variation of the contact angle. The evaporation of sessile drops on smooth polymer surfaces (PMMA and PET) was studied to determine the receding contact angle by monitoring the contact diameter and contact angle using video microscopy [Erbil et al. (1999)]. This method of measurement resulted in less scattering data than the other standard techniques, such as needle-syringe and the inclined plane methods. Different stages of droplet evaporation have been observed, such as the stage where the contact angle is constant, or the stage where the contact radius is constant, or the stick-slip mode. The theoretical model for constant contact angle stage and constant contact area stage of evaporation has been developed and compared with the experimental data [Picknett and Bexon (1977); Schönfeld et al. (2008)]. The rate of evaporation from a sessile drop was found to be proportional to the contact radii as the

contact angle changes during the evaporation process [Birdi et al. (1989)]. The constant contact angle mode of evaporation on PTFE surface was observed for drops with an initial contact angle of less than 90° [Erbil et al. (2002)]. Water drop evaporation on PMMA surfaces was studied in the regime of constant contact radius [Rowan et al. (1995)]. Droplet evaporation on superhydrophobic surface has been studied, and the wetting behavior along with the transition from the Cassie-Baxter state to the Wenzel state was observed and discussed [McHale et al. (2005); Jung and Bhushan (2008); Shin et al. (2009); Shin et al. (2010); Nguyen et al. (2012)]. The rate of droplet evaporation is faster on hydrophilic surfaces as the contact area is relatively large during the entire process. Dynamics of the triple line during evaporation on both strongly and weakly pinning surfaces were observed and discussed [Bormashenko et al. (2011)]. The effect of the ambient atmosphere (either saturated or not) was studied and the evolution of the contact angle and contact diameter on different polymer surfaces was elucidated [Shanahan and Bourges (1994)]. The motion of the triple line was attributed to the surface morphology on different polymeric surfaces and the pinning and depinning effects were discussed [Pittoni et al. (2013)]. The effect of nanoparticles suspended in liquid drops on the evaporation mechanism was experimentally investigated as well [Moffat et al. (2009)].

Drop evaporation on fibers with different contact angle hysteresis was studied, and both the constant contact angle and the constant contact area modes were observed [Funk et al. (2014)]. Drops on fibers can acquire three possible shapes: (i) to form of a thin liquid film on a filament; (ii) to form an axisymmetric barrel-shaped body; and (iii) to form an asymmetric clamshell-shaped body [Kumar and Hartland (1988); McHale and Newton (2002); Carroll (1986); Chou et al. (2011); Sahu et al. (2013)]. Different factors such as

filament radius, surface/interfacial tension and drop volume affect the stability of drops on filaments and the transition from the barrel-shaped to clamshell-shaped configurations. Several numerical and semi-analytical approaches were developed to establish stability criteria for drops of different configurations on filaments [McHale et al. (2001); Wu and Dzenis (2006)].

Wetting of fibrous nonwovens is of importance in filter media, tissue scaffolding and drug delivery, where interaction between fibers and liquid is important. The evaporation from the nonwovens can affect their morphology. The high surface area to volume ratio of micro- and nanofibers determine their incorporation into such nonwovens as tissue templates, paper products, gas and fluid filters, fibrous reinforcement, thermal and sound insulators, chemical carriers, etc. The elastic stiffness of the planar fiber network has been modeled accounting for the microscopic deformations of fiber segments of all possible lengths and orientations [Wu and Dzenis (2005)]. The collapse of two nanofibers at different orientations induced by adhesion has been also studied [Wu and Dzenis (2007)]. The effect of solvent evaporation on porosity and fiber deformation of meltspun polyethylene membranes has been studied and investigated [Kamo et al. (1992)]. The change in the membrane porosity was observed as a result of evaporation. Wetting and evaporation of liquid drops between two parallel fibers (relatively rigid or flexible) were studied for different aspect ratio of a fiber [Duprat et al. (2013); Duprat et al. (2012)]. Evaporation of drops located on a porous nonwoven membrane might results in shrinkage or even collapse of the membrane.

3. RESEARCH OUTLINE

3.1 Drop impacts on nano-textured porous membranes

(This section has been previously published in Sahu et al. (2012)).

Drop impact on solid surfaces both smooth and rough, dry or covered by liquid layers attracted significant attention in the past. Only a few works addressed drop impact onto porous surfaces, and all of them dealt with the regime of static penetration. This work aims at the dynamic penetration (hydrodynamic focusing) resulting from drop impact onto porous membranes, the topic of significant interest in view of coalescing filters.

The aim of the present work is to elucidate the outcomes of drop impacts of polar and non-polar fluids onto electrospun nanofiber membranes with different degrees of wettability. The approach and results are absolutely novel, since none of the above-mentioned works dealt with nanofiber membranes, as well as the dynamic penetration mechanisms overbearing wettability were not fully demonstrated so far, as to our knowledge. The questions explored in the present work need to be resolved, first of all, to address the following general scientific issues. (i) Can hydrophobicity prevent water penetration through a layer of porous medium, and especially through a layer of a nanotextured porous medium? (ii) Under what conditions hydrophobicity or hydrophilicity become secondary, and water penetration is fully dominated by the dynamic effects? (iii) Does hydrophobicity of the skeleton of a porous medium with interconnected pores shed any light on its interaction with the impacting drops? (iv) Can superhydrophobicity of the skeleton prevent water penetration due to drop impact? (v) What is the role of liquid viscosity under the conditions of the dynamic penetration? In addition, to these basic scientific questions, it is emphasized that the answers to them are of significant importance for applications such as

drop and spray cooling of high-heat-flux microelectronic, optoelectronic and radiological devices, as well as server rooms, coalescence filter media, membranes and nonwovens.

3.2 Drop motion under the action of air blowing

(This section has been previously published in Sahu et al. (2013)).

The present work deals with drops on filaments subjected to air blowing along and across the filament. Our aim is to demonstrate the mechanisms of drop entrainment by air flow, and dynamics of their motion on the filament. The rate of drop motion on filaments is significantly affected by the mutual orientation of the filament and the surrounding air flow. A novel setup had to be designed to study drop motion both along and across a filament. The present study covers the two limiting orientations of the filament with respect to the air flow: the parallel and perpendicular one. The focus is on different regimes of drop motion and breakup on a filament due to the surrounding gas flow. Several new observations phenomena were discovered as a result. The breakup regimes and disintegration patterns of drops on filaments in cross-flow of the surrounding gas have not been studied so far, as to our knowledge. The air velocity in the present study ranges from 7.23 m/s to 22.7 m/s. The Weber number varies from 2 to 40 and the Ohnesorge number ranges from 0.07 to 0.8. In spray and drop atomization the critical Weber number at which the bag type breakup is observed is of primary importance. In the coalescence and drainage of drops in the filter media the Weber number at which a drop falls off the filament is equally important. The lower and upper critical Weber number are introduced in this study to distinguish between the following two cases: one in which the drop starts breaking off the filament and the other one in which the bag-stamen breakup begins.

3.3 Liquid penetration into non-wettable fibrous filter media

There are several techniques, such as Magnetic Resonance Imaging and X-ray tomography, that were used to observe phenomena in porous media. However, they are very slow and also do not have enough resolution to visualize liquid penetration front resulting from drop impact onto a porous membrane. This motivates the aim of the present work to develop a novel setup and theory to elucidate liquid penetration fronts within porous membranes. The aim of the present work is in the experimental and theoretical investigation of dynamic liquid penetration due to hydrodynamic focusing, and the entrainment and deposition of nanoparticles suspended in drops impinging onto a porous filter membrane. In Section 6.2 the experimental details are given. Then, in Section 6.3 the experimental results are presented. The theoretical framework is described in Section 6.4. The discussion and comparison of the predictions with the experimental data are presented in Section 6.5. Conclusions are drawn in Section 6.6.

3.4 Mechanical strength of nanofiber filter media

Nanofiber membranes are very compliant when they are subjected to air and water flow. In order to prevent rupture of nanofiber membranes, they are normally bonded or sandwiched over meltblown supportive fibrous media thus enhancing their mechanical strength. The substrates not only provide the mechanical support but also facilitates mechanical strength of compound filters, their durability, pleating and cleaning. An additional thermal bonding of nanofiber webs improves the interfiber bonding making it more rigid. In the present work we aim at studying droplet evaporation on suspended nanofiber mats. The objective is to elucidate the effect of droplet evaporation on the porosity and morphology of the nanofiber mat.

4. DROP IMPACTS ON ELECTROSPUN NANOFIBER MEMBRANES

This chapter has been previously published in Sahu et al. (2012).

4.1 Introduction

This work reports a systematic study of the impacts of drops of polar and non-polar liquids onto different electrospun nanofiber membranes (of 8-10 μm thickness and pore sizes of 3-6 μm) with the increasing degree of hydrophobicity. The membranes were deposited onto rigid Nylon grids which eliminated vibrations and possessed much larger pores of 20 μm and the inter-pore distances of about 40 and 60 μm , with the hydraulic resistance negligible compared to that of the nanofiber mats. The liquids studied were water, FC 7500 (Fluorinert fluid) and hexane. The nanofibers used were electrospun from Polyacrylonitrile (PAN), Nylon 6/6, Polycaprolactone (PCL) and Teflon. The outcomes of drop impacts were recorded by using a high speed CCD camera. It was found that for any liquid/fiber pair there exist a threshold impact velocity ($\sim 1.5\text{-}3\text{ m/s}$) above which water penetrates membranes irrespective of their hydrophobicity. The other liquids (FC 7500 and hexane) penetrate membranes even easier. Low surface tension liquid FC 7500 left the rear side of sufficiently thin membranes as a millipede-like system of tiny jets protruding through a number of pores. For high surface tension water such jets immediately merged into a single bigger jet, which formed secondary spherical drops due to capillary instability. No mechanical damage to the nanofiber mats after liquid perforation was observed. A theoretical estimate of the critical membrane thickness sufficient for complete viscous dissipation of the kinetic energy of penetrating liquid is given and corroborated with by the experimental data.

4.2. Experimental materials and methods

4.2.1 Materials

Polyacrylonitrile (PAN-molecular weight – 150 kDa) was obtained from Polymer Inc. N-N, Dimethyl Formamide (DMF) anhydrous 99.8%, Dichloromethane anhydrous 99.8% (MC), Polycaprolactone (PCL-molecular weight- 80kDa), Formic Acid and Nylon 6/6 (molecular weight - 22 KDa) were obtained from Sigma Aldrich. 1 wt% Teflon AF 2400 was obtained from DuPont. Teflon AF 1600 in powder form was generously donated by DuPont. FC 40 (also termed Fluorinert Fluid), FC 7100, FC 7200, FC 7300, FC 7500 and FC 7600 (also termed Novec Engineered Fluids were generously donated by 3M Company. FC-40 was used to dissolve Teflon solutions. Nylon grids (a filter medium) of 20 μm average pore size, with a pitch of 40 μm and 60 μm in orthogonal directions and 34 μm in thickness, which was used as a substrate for the electrospun nanofiber mats to prevent vibrations after drop impact was obtained from “Small Parts”. The Nylon grids thus received were rinsed with de-ionized water and dried prior to use to remove ethylene oxide with which they were treated by the manufacturer.

4.2.2 Preparation of solutions

Polymer solutions used for electrospinning of PAN nanofiber mats were prepared from 8 wt% PAN dissolved in DMF. Polymer solutions used to electrospin Nylon 6/6 were prepared from 23 wt% Nylon 6/6 dissolved in Formic Acid. Solution of 13 wt% PCL was prepared by dissolving PCL in DMF and MC in the ratio of 75/25 by weight.

The difficulty with electrospinning of Teflon is associated with its low dielectric constant and boiling point of its best solvent, FC 40. As recommended in Scheffler et al. (2010) FC 40 was blended with the other Novec Engineered fluids to increase the dielectric constant of solvent. The relative dielectric permittivity and boiling point of different Novec Engineered, Fluorinert fluids and Teflon AF 1600 are listed in Table 4.1 according to the values provided by the supplier. Different Teflon solutions were prepared by dissolution in blends of 20% of FC 40 and 80% of different Novec Engineered fluids. The Teflon solutions were prepared at 45 °C overnight under agitation until a uniform solution was obtained. It was found that the solutions containing FC 7100 and FC 7200 dried at the tip of the electrospinning needle. This can be attributed to the fact that these fluids have low boiling points, which results in a high evaporation rate at a given temperature. It was also found that although FC 7600 had a comparatively higher boiling point, the solution made by using FC 7600 was not a homogenous one. In addition, this solution started precipitating within 30-40 min after being removed from the hotplate. Therefore, only solutions based on FC 7300 (whose boiling point is close to that of water) worked properly in electrospinning. The dielectric permittivity of FC 7300 is slightly lower than that of FC 7100. However, the use of FC 7300 was preferable to prevent the accumulation and drying at the tip of the electrospinning nozzle in order to have a robust electrospinning process. Therefore, for electrospinning, 5 wt% solution of Teflon AF 1600 was prepared by dissolving Teflon in a solvent comprised of 20 wt% FC 40 and 80 wt% FC 7300.

Table 4.1 Properties of Teflon AF and the solvents tested for its electrospinning

	Teflon AF 1600	FC 40	FC 7100	FC 7200	FC 7300	FC 7600
Dielectric permittivity	1.93	1.9	7.4	7.3	6.1	6.4
Boiling point (°C)	-	155	61	76	98	131

4.2.3 Electrospinning

All the solutions were electrospun directly onto square sized bare nylon grids of 1"×1". Electrospinning was carried out using a standard single nozzle setup. Different parameters used for electrospinning of different polymer solutions are listed in Table 4.2.

Table 4.2 Electrospinning parameters

Polymer solution	Concentration (wt%)	Flow rate (ml/h)	Electric field strength (kV/cm)	Inter-electrode distance (cm)	Needle
PAN	8	0.7	1	15	18G
Nylon 6/6	23	0.3	1.5	10	25G
PCL	13	0.8	1	15	18G
Teflon AF 1600	5	0.2	2	8	18G

4.2.4 Contact angle

Contact angles of water drops on cast samples of different polymers on a glass slide were measured and listed in Table 4.3. The polymers used in this study span the partially wettable to hydrophobic regime.

Table 4.3 Static contact angle of water on cast polymer films

Polymer	Nylon 6/6	PAN	PCL	Teflon AF 1600
Contact angle	30°- 40°	40°- 45°	95°- 105°	115°- 120°

4.2.5 Preparation of teflon-coated nylon grids

To prepare nylon grids coated with Teflon, the following procedure was implemented. An original 1 wt% Teflon AF 2400 solution in FC 40 was diluted to 0.1 wt% using FC 40 solvent. Then, a bare nylon grid was dipped into the diluted Teflon solution. After that, the grid was wiped gently to avoid the formation of a thick Teflon film that might block the pores. The dried Teflon-coated nylon grid was then subjected to air blowing to ensure the pore size to be the same as in the bare nylon grids.

4.2.6 Drop impact experiments

Electrospun nanofiber membranes deposited onto nylon grids were installed in the experimental setup schematically shown in Fig. 4.1. It consisted of an adjustable platform, a syringe pump, a high speed CCD camera (RedLake Motion Pro Camera), an external light source, a computer and a stand assembly. Samples were placed centrally on the adjustable

platform which can be moved in the X-Y direction (in the horizontal plane). The supporting grids prevented any visible vibrations following drop impact onto the electrospun mats. On the other hand, the grids could not affect liquid penetration, since the hydraulic resistance of the grids was much lower than that of the mats. The high speed CCD camera recorded the dynamics of drop impact onto the nanofiber mats supported by nylon grids at 500 fps with a shutter speed of 1/6000 s. To ensure reproducibility of drop sizes, liquids were delivered by syringe pump with a constant flow rate of 5 ml/hr. A 25G needle was used to form water drops by gravity-driven dripping, whereas an 18G needle was used to form FC 7500 and hexane drops. The images recorded by the CCD camera were processed by using ImageJ, Matlab and Adobe Photoshop CS2. In all the experiments the drop size was close to 1 mm in diameter and remained unchanged. Drops were dripped from different heights in the range 5–60 cm, which is equivalent to increasing the drop impact velocity from 1 m/s to 3.46 m/s in each of the 8 cases described in the following paragraph.

The experiments were done in the following succession: (i) hydrophilic bare nylon grids were used as membranes, while water drops impacted onto them. (ii) Hydrophobic Teflon-coated grids were used as membranes, while water drops impacted onto them. Note, that water is a polar, high surface tension fluid. (iii) Drops of a non-polar, low surface tension Fluorinert fluid FC 7500 impacted onto bare nylon grids and Teflon-coated grids. (iv) Drops of another non-polar, relatively low surface tension fluid, hexane were impacted onto bare nylon grids and Teflon-coated grids. (v) Water drops were impacted onto partially wettable electrospun PAN nanofiber mats, (vi) Water drops were impacted onto partially wettable electrospun Nylon 6/6 nanofiber mats, (vii) Water drops were impacted onto hydrophobic electrospun PCL nanofiber mats. (viii) Water drops were impacted onto superhydrophobic

Teflon nanofiber mats. This succession of experiments was chosen to explore the effect of the grid wettability (partially hydrophilic/superhydrophobic), of the liquid properties (in particular, high/low surface tension, polar/non-polar), and of the nanofiber mat wettability (partially hydrophilic/ hydrophobic/ superhydrophobic) on the drop impact outcome. In all cases the impact velocity was gradually increased, until a threshold velocity was reached, above which the liquid penetrated through the membrane irrespective of its wettability.

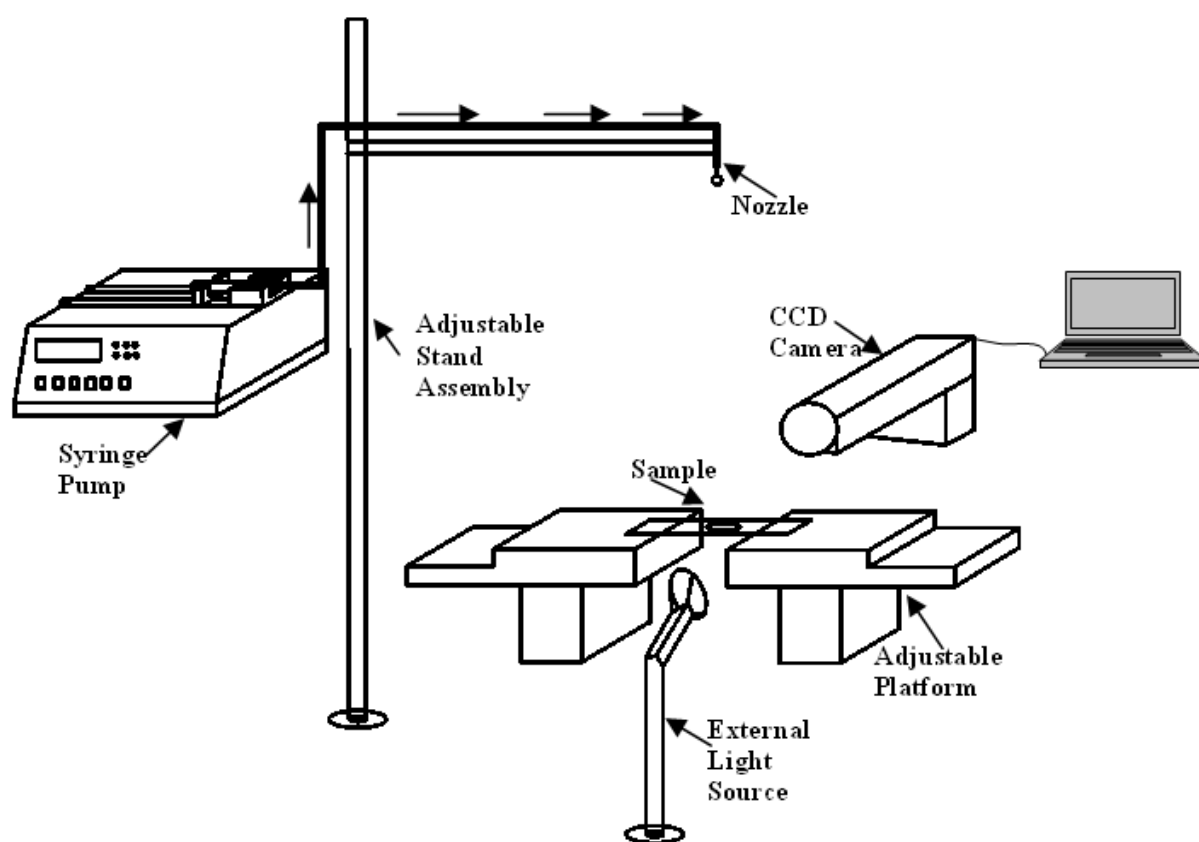


Figure 4.1. Schematic of the experimental setup.

4.2.7 Microscopy

Microscopic images were obtained using Scanning Electron Microscope (SEM) JEOL-JSM 6320F Scanning Electron Microscope (SEM).

4.3. Results and discussion

4.3.1 Water drop impacts onto bare nylon grids

In the experiments with drop impact onto bare nylon grids, the SEM image of one of which is shown in Fig. 4.2a, it was found that at low impact velocities (1-2 m/s) there was no visible penetration of water drops into the other side of the grid (Fig. 4.3). However, it can be seen from Fig. 4.3b-f that although there was no penetration to the other side, water drop did not retract, but rather was pinned, similarly to the observations of drop impacts onto nanofiber mats in Lembach et al. (2010), Sinha-Ray et al. (2011) and Weickgenannt et al. (2011).

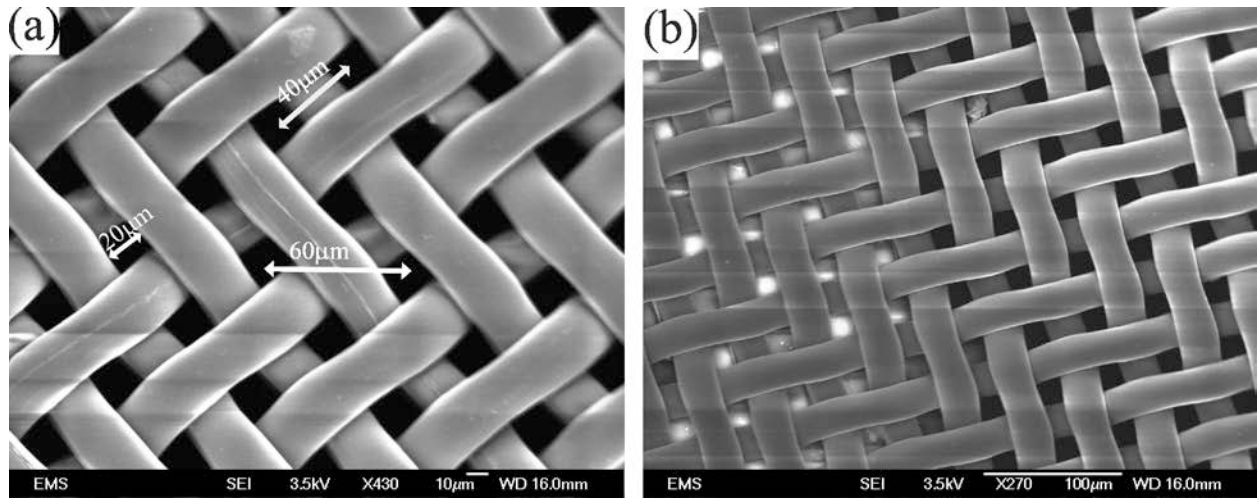


Fig. 4.2. SEM image of: (a) bare Nylon grid, (b) Teflon-coated Nylon grid. The image shows some blocked pores (the white areas), which were very infrequent. The blockage is due to a thin Teflon film. The majority of the pores are always open (the dark areas).

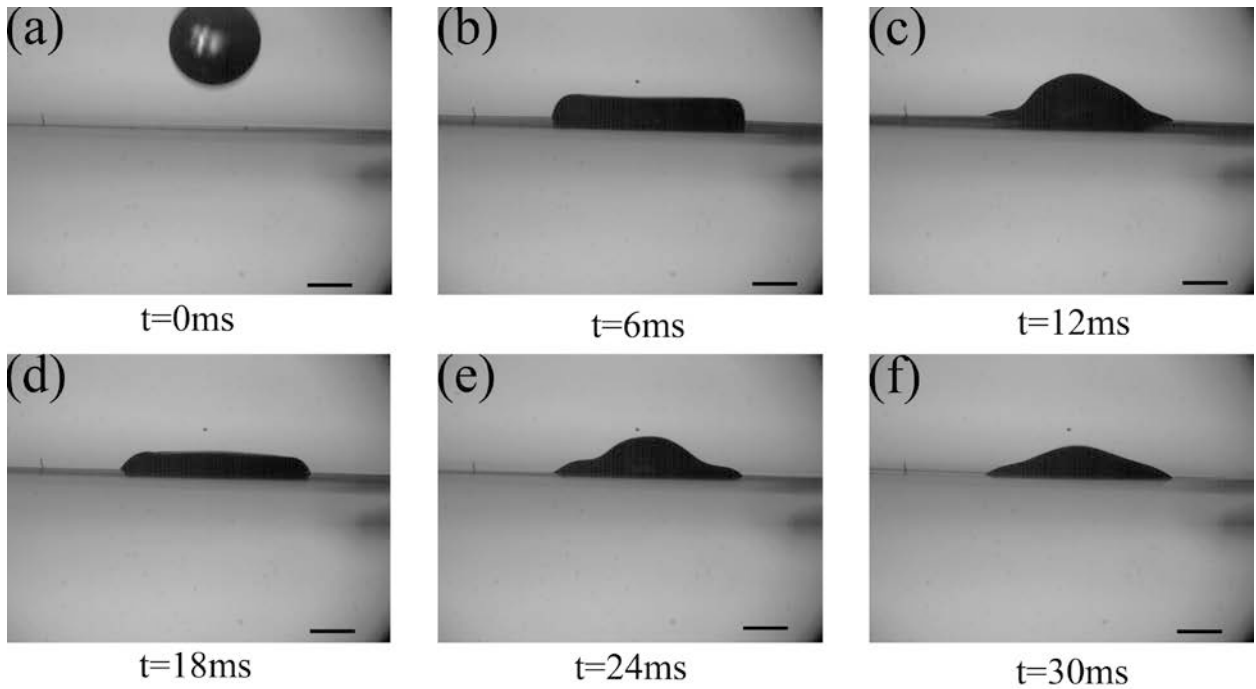


Figure 4.3. Impact of a water drop onto a bare nylon grid with a low impact velocity of 1 m/s. The panels correspond to: (a) $t = 0\text{ ms}$, (b) $t = 6\text{ ms}$, (c) $t = 12\text{ ms}$, (d) $t = 18\text{ ms}$, (e) $t = 24\text{ ms}$ and (f) $t = 30\text{ ms}$. Scale bars, 1mm.

When the drop impact velocity was increased above 2 m/s, visible penetration of water through bare nylon grids was observed (Fig. 4.4). However, it was also observed that at lower impact velocities (2-3 m/s) after the water drop has penetrated through the nylon grid, it mostly retracted back presumably due to the effect of the surface tension (Fig. 4.5a and b). At a higher impact velocity (3.46 m/s), a part of the water drop that penetrated through the nylon grid did not retract back and dripped down as smaller drops (Fig. 4.5c and d). It is clear that in the latter case water still had enough kinetic energy to overbear surface tension.

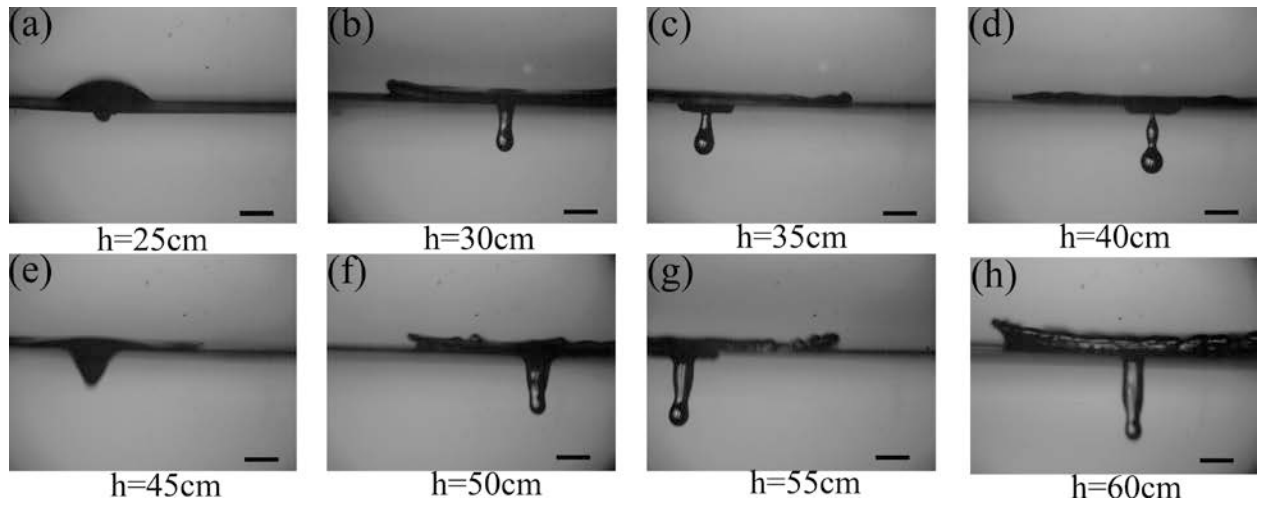


Figure 4.4 Water drop impact on bare nylon grid in 2 ms after the impacts. The impact velocities are: (a) 2.23 m/s, (b) 2.44 m/s, (c) 2.64 m/s, (d) 2.82 m/s, (e) 3.0 m/s, (f) 3.16 m/s, (g) 3.31 m/s and (h) 3.46 m/s. Scale bars, 1mm.

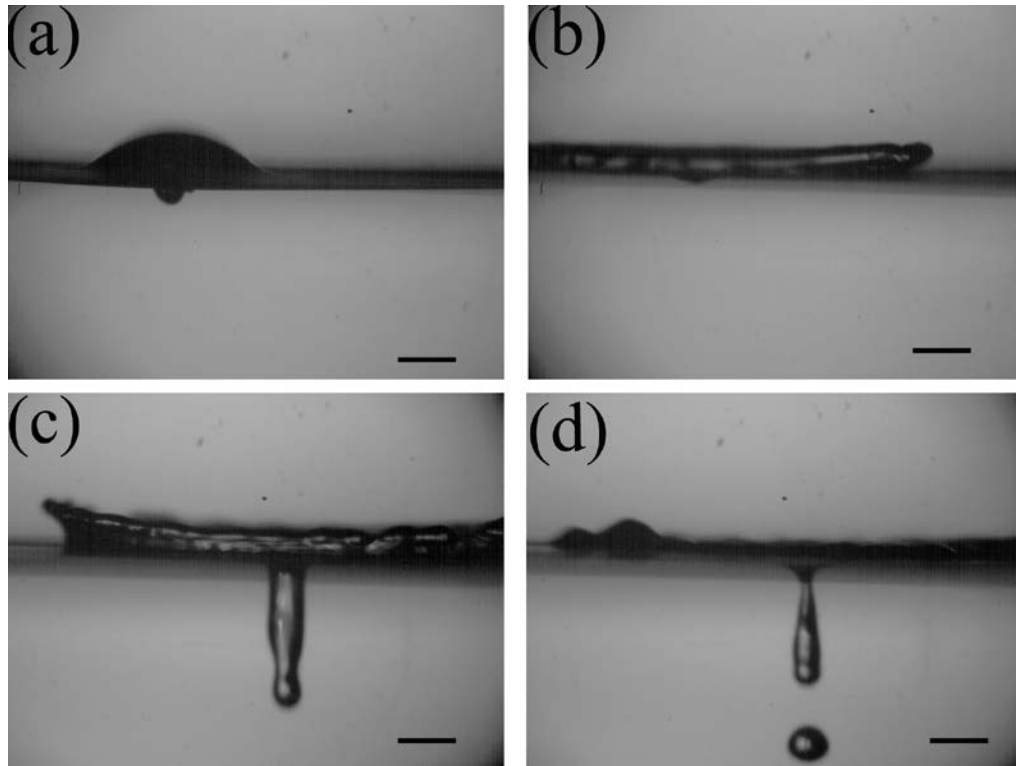


Figure 4.5. Water drop impact with the impact velocity of 2.23 m/s at the time moments: (a) $t = 2\text{ ms}$ and (b) $t = 4\text{ ms}$. Water drop impact with the impact velocity of 3.46 m/s at the time moments: (c) $t = 2\text{ ms}$ and (d) $t = 4\text{ ms}$. The comparison of panels (a) and (c) shows how the amount of water penetrating through Nylon grid increases with an increase in the impact velocity. Panel (b) show that at a lower impact velocity, the surface tension is capable of retracting almost all penetrated water, whereas panel (d) shows that at a higher impact velocity, the surface tension is incapable to prevent full penetration of a significant part of the impacting drop. Scale bars, 1mm.

4.3.2 Water drop impacts onto teflon-coated nylon grids

The SEM image of a Teflon-coated nylon grid is shown in Fig. 4.2b. Even though the grid has some blocked pores (the white areas) due to a thin clogging film of Teflon, the occurrence of such blockage was very rare. The majority of the pores are always open (the

dark areas). Generally, the dip coating of Teflon over nylon grids was successfully conducted without pore blockage.

The difference in wettability of bare nylon grids and Teflon-coated nylon grids was evaluated as follows. Water drops were gently put on each of these two types of grids at different places, and their contact angles observed. Two representative images are depicted in Fig. 4.6. It is seen that bare nylon grids were partially wettable with water, with the static contact angle varying in the range of 55° - 65° . On the other hand, the Teflon-coated nylon grids were rather non-wettable, with the static contact angle varying in the range of 125° - 140° .

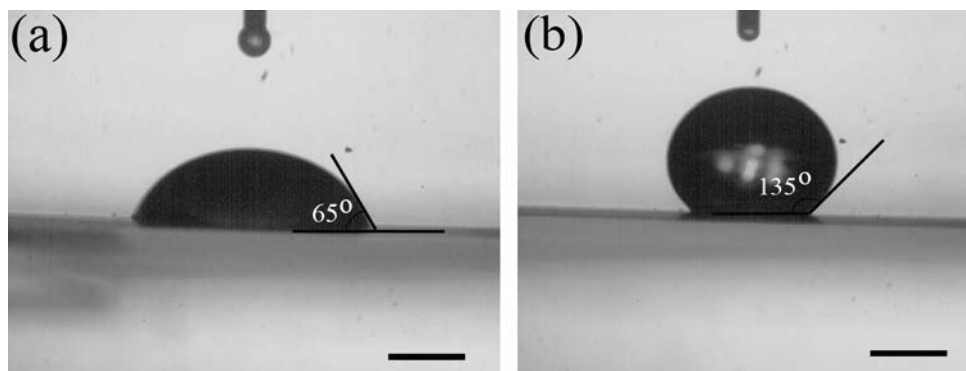


Figure 4.6. Static contact angle of water drops on (a) a bare nylon grid and (b) on a Teflon-coated nylon grid. The images show that Teflon coating changed the partially wettable nylon grids into rather hydrophobic ones under static conditions. Scale bars, 1mm.

The low velocity (1 m/s) impact of a water drop dripped onto a Teflon-coated nylon grid is shown in Fig. 4.7. It is seen that after an initial spreading, the water drop recedes under the action of surface tension and even tends to bounce back from the grid, albeit the lower part of it remains in contact. No visible water penetration through such grids was found

at such low impact velocities (up to 2.44 m/s). This is different from the observations described in the previous subsection for bare nylon grids. However, for drop impact with the impact velocities of 2.64m/s and beyond, there is visible penetration into the other side of the Teflon-coated nylon grids resembling that for bare nylon grids (Fig. 4.8). Sometimes, it was found that the upper part of a penetrating water drop splashes and breaks up into smaller drops, as is characteristic of receding splashes on hydrophobic surfaces [Yarin (2006)]. Still, a part of the penetrated drop (the impact velocity of 2.64 m/s) can be lifted back to the rear side of Teflon-coated nylon grid due to the surface tension effect (Fig. 4.9a and b). For drop impacts with the impact velocity of 3.46 m/s onto Teflon-coated nylon grid, no “lift-up” was found and some part of the penetrated drop detached from the parent drop (Fig. 4.9) similar to the higher-speed impacts onto bare nylon grids (Fig. 4.5d).

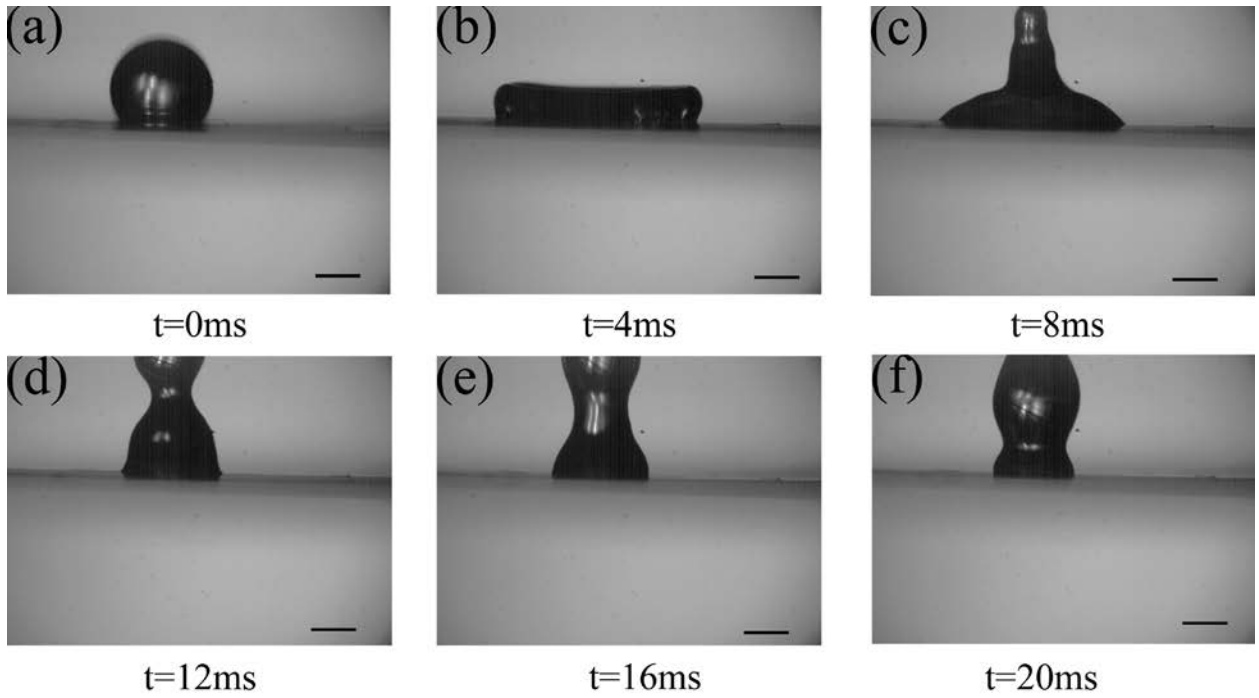


Figure 4.7. Water drop impact onto a Teflon-coated nylon grid with a low impact velocity of 1 m/s at (a) $t = 0\text{ ms}$, (b) $t = 4\text{ ms}$, (c) $t = 8\text{ ms}$, (d) $t = 12\text{ ms}$, (e) $t = 16\text{ ms}$ and (f) $t = 20\text{ ms}$. Scale bars, 1mm.

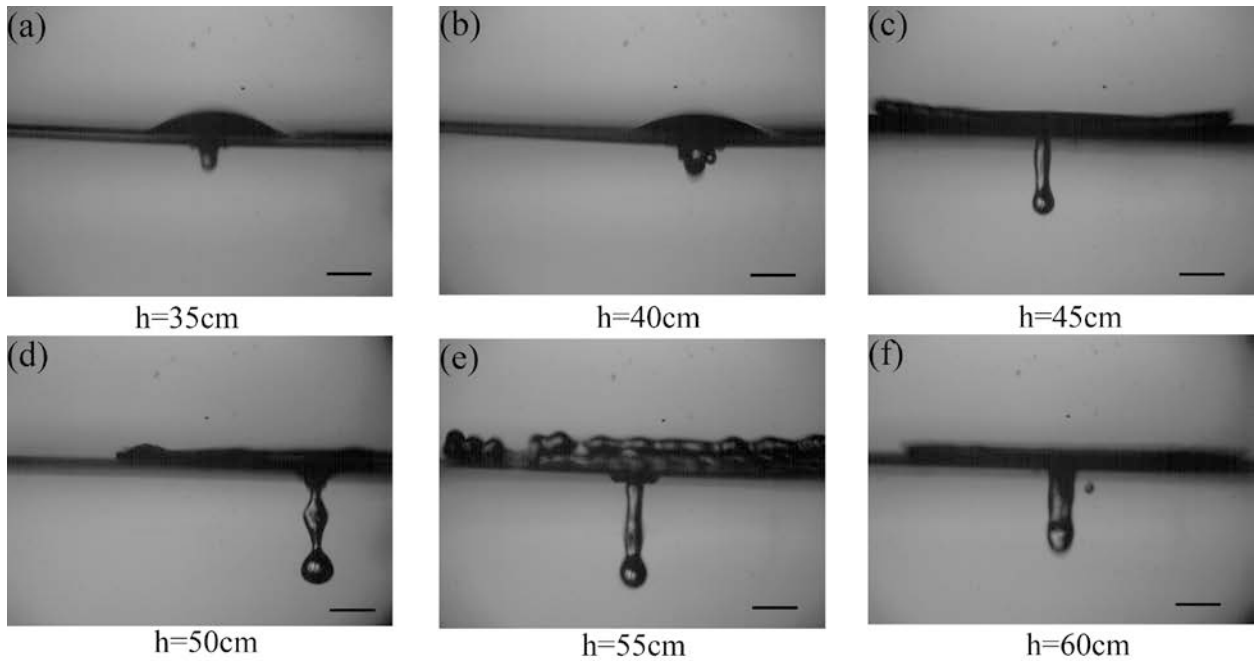


Figure 4.8. Water drop impact onto Teflon-coated nylon grid 2 ms after the first contact. The impacts velocities are (a) 2.64 m/s, (b) 2.82 m/s, (c) 3.0 m/s, (d) 3.16 m/s, (e) 3.31 m/s and (f) 3.46 m/s. Scale bars, 1mm.

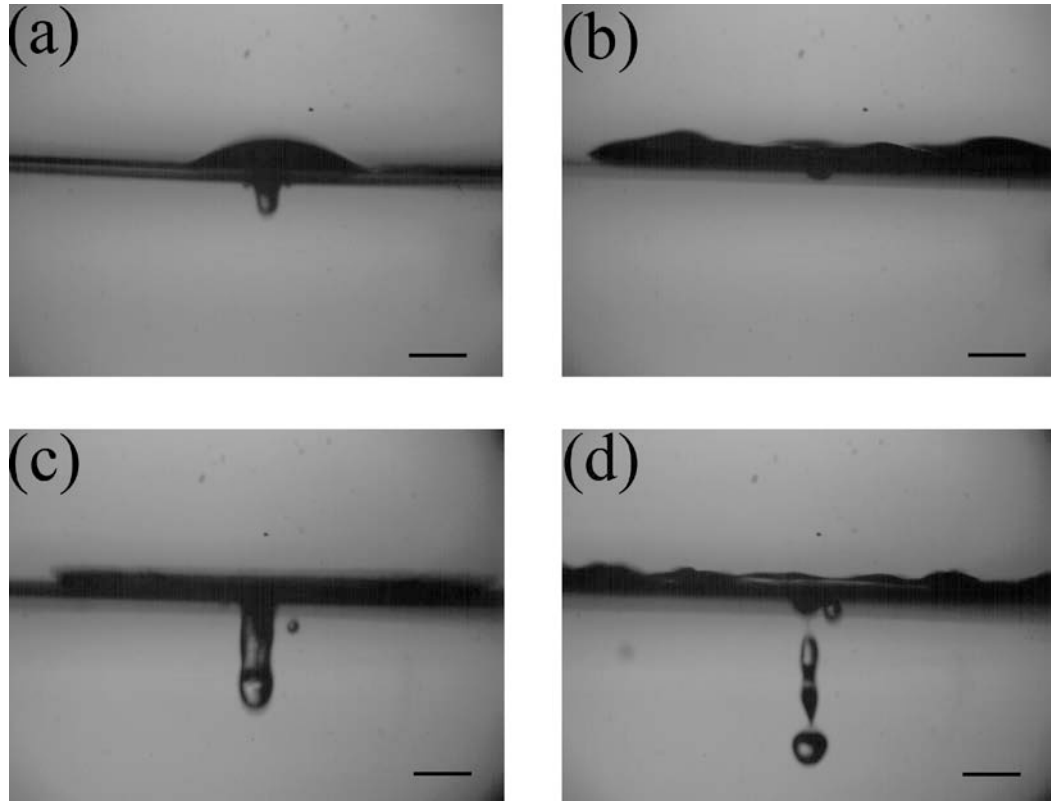


Figure 4.9. Water drop impact onto Teflon-coated nylon grid with the impact velocity of 2.64 m/s at (a) $t = 2 \text{ ms}$ and (b) $t = 8 \text{ ms}$. An impact with the impact velocity of 3.46 m/s at (c) $t = 2 \text{ ms}$ and (d) $t = 4 \text{ ms}$. The comparison of panels (a) and (c) shows how the amount of water penetrating through the grid increases with the increase in the impact velocity. Panel (b) shows that at a lower velocity, surface tension is capable of stopping and uplifting almost all the penetrated water behind the rear side of the grid. On the other hand, panel (d) shows that at a higher impact velocity no “lift-up” is possible anymore and a significant part of water fully detaches from the rear side of the grid. Scale bars, 1mm.

The inspection of the images in Fig. 4.3 – 4.5, 4.8 and 4.9 shows that penetrating water jets have diameters of about 0.01 to 0.05 cm. Given the distance of about 40-60 μm between the pores in the grid, these values recast into simultaneous penetration of water through 4-100 pores.

Volume fractions of the impacting drops which penetrate through the grid were evaluated using images taken 2 ms after the impact. It was assumed that water visible below the rear surface of the grid forms a body of revolution, which allows the evaluation of volume fraction based on two-dimensional images. Fig. 4.10 shows the penetrated fraction of water drop versus the impact height of the initial drop for the two cases: bare nylon grids and Teflon-coated nylon grids. It is instructive to see that at lower impact velocities the Teflon coating diminishes the penetrated volume fraction. However, as the impact velocity increases up to 3.31 m/s, the penetrated volume fractions in both cases (bare nylon grid and Teflon-coated grid) become the same, and the grid wettability has no effect on the penetration process. At higher impact velocities penetration becomes fully dynamic, as predicted in Lembach et al. (2010) and Weickgenannt et al. (2011).

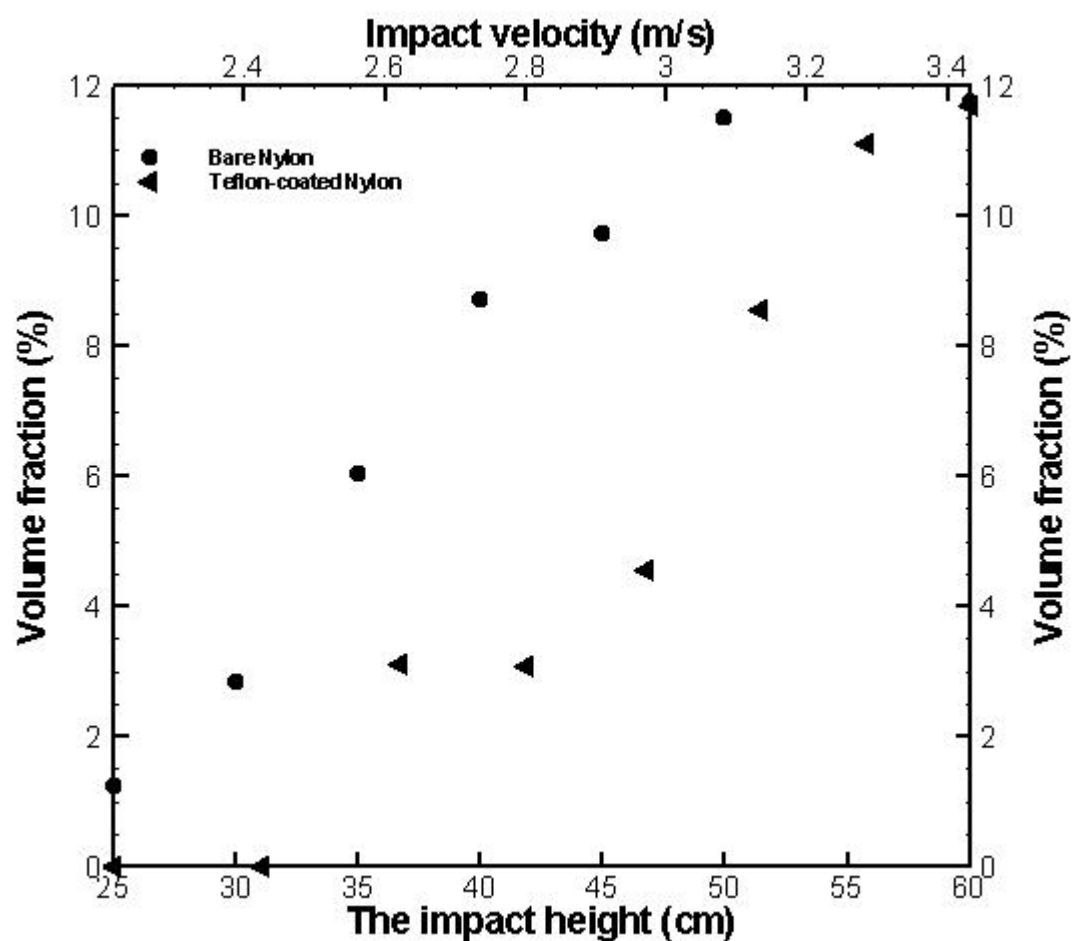


Figure 4.10. Fractions of water drops which penetrated through micropores after drop impact onto bare nylon or Teflon-coated nylon grids. The data were obtained using the images recorded 2 ms after drop impact. In the case of nylon grids, there is no water penetration at the impact velocities below 2.23 m/s, in the case of Teflon-coated nylon grids there is no water penetration at the impact velocities below 2.64 m/s.

4.3.3 FC 7500 drop impacts onto bare nylon grids and grids coated with teflon

Figure 4.11 shows the sequence of images for the drop of FC 7500 [Bhardwaj et al. (2007)] (the surface tension and kinematic viscosity are 16 mN/m and 0.77 cSt, respectively) for the impact velocity of 1 m/s onto a bare nylon grid. It can be seen that the liquid penetrates through the grid even at such a low impact velocity (compared with the threshold velocity of 2.23 m/s for water penetration through such grids). This can be attributed to the fact that for the penetration through nanofiber mat of thickness h , the impact velocity needed for the full penetration is of the order of $V = \nu h / \delta^2$ (cf. the theoretical section 4.4), where ν is the kinematic viscosity and δ is the pore size. An impact with such velocity can overbear viscous dissipation in the pores and deliver the liquid entering the pores to the rear side of the grid. The kinematic viscosity of FC 7500 is 0.77 cSt, which is less than that of water, which explains the reason for easier penetration of FC 7500 (compared to that of water) through the entire nylon grid mat thickness at lower impacting velocities.

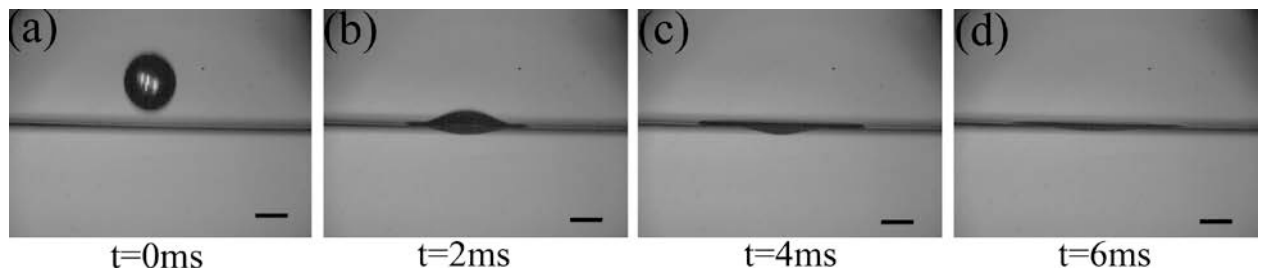


Figure 4.11. Drop of FC 7500 impacting onto a bare nylon grid with the impact velocity of 1 m/s at (a) $t = 0$ ms, (b) $t = 2$ ms, (c) $t = 4$ ms, (d) $t = 6$ ms after the impact. Scale bars, 1mm.

An important observation can be made for impacts of FC 7500 drops onto bare nylon grids. At a certain threshold velocity of about 2 m/s, FC 7500 had started emerging after penetration as separate tiny jets originating from the pores of the Nylon grid, as seen in Fig. 4.12a. The leading parts of these tiny jets then break up into tiny droplets (presumably due to the Rayleigh capillary instability), whereas the residual parts then coalesce to form a single jet, similar to the one accompanying water drop impact, as can be seen in Fig. 4.12b and c. The merger jet, in turn, breaks into bigger secondary droplets, again due to the action of surface tension (the capillary instability).

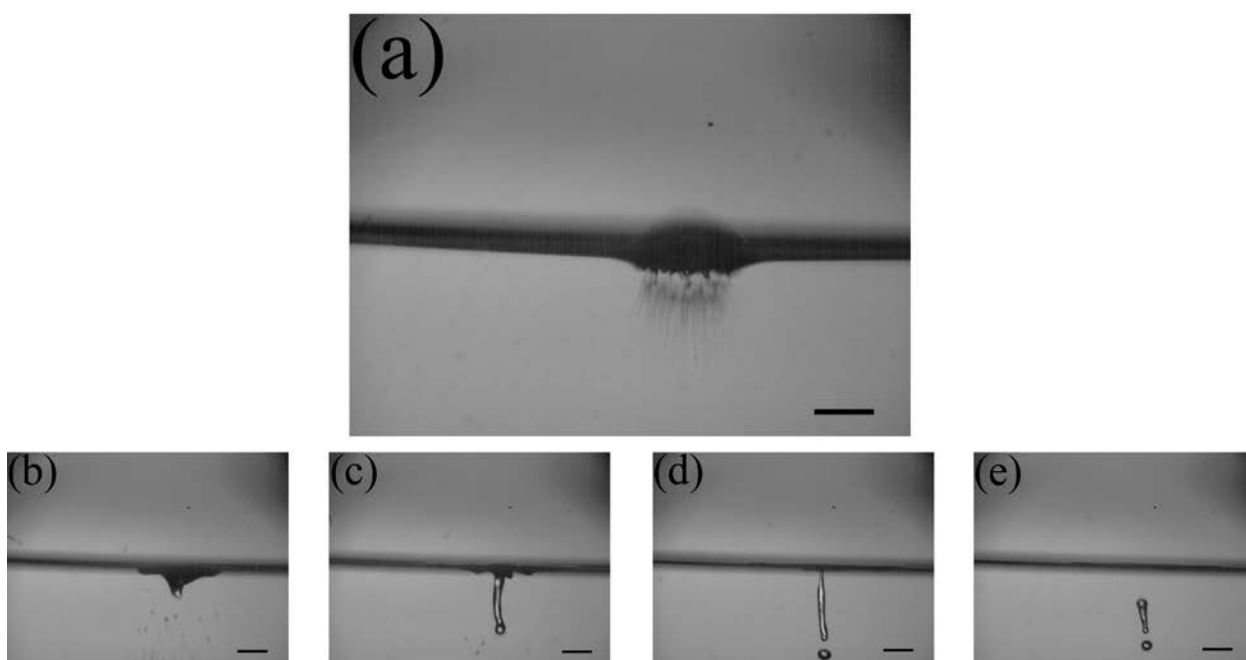


Figure 4.12. Drop of FC 7500 impacting onto a bare nylon grid with the impact velocity of 2.64 m/s. Scale bars, 1mm.

Figure 4.13 shows the sequence of images for the FC 7500 drop impact with the impact velocity of 3.46 m/s). The appearance of tiny jets is also apparent in this case: cf. Fig. 4.13 which depicts the processes of penetration, coalescence and jet breakup similar to those of Fig. 4.12. The tiny jets are rather blurred in Fig. 4.13a, which is due to the high impact speed of the drop.

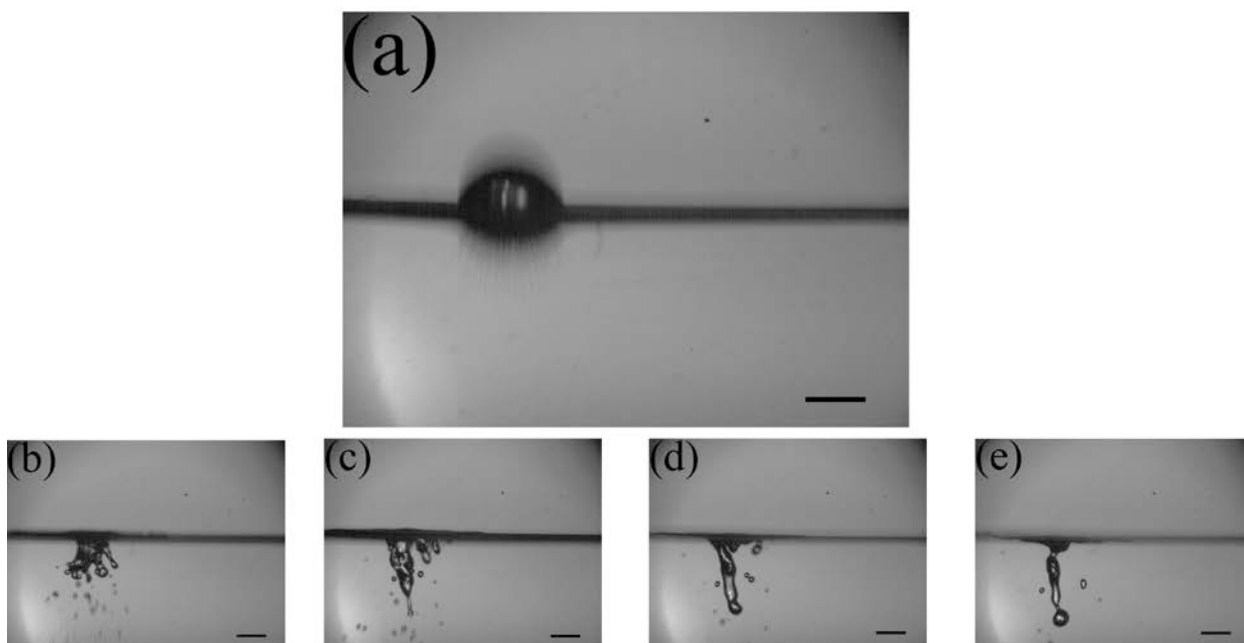


Figure 4.13. Impact of FC 7500 drop onto bare Nylon grid from a height of 60 cm (3.46 m/s). Scale bars, 1mm.

The effect of the impact height on the outcome of the FC 7500 drop impact is illustrated in Fig. 4.14. The penetration patterns for this liquid corresponding to various heights can be clearly distinguished.

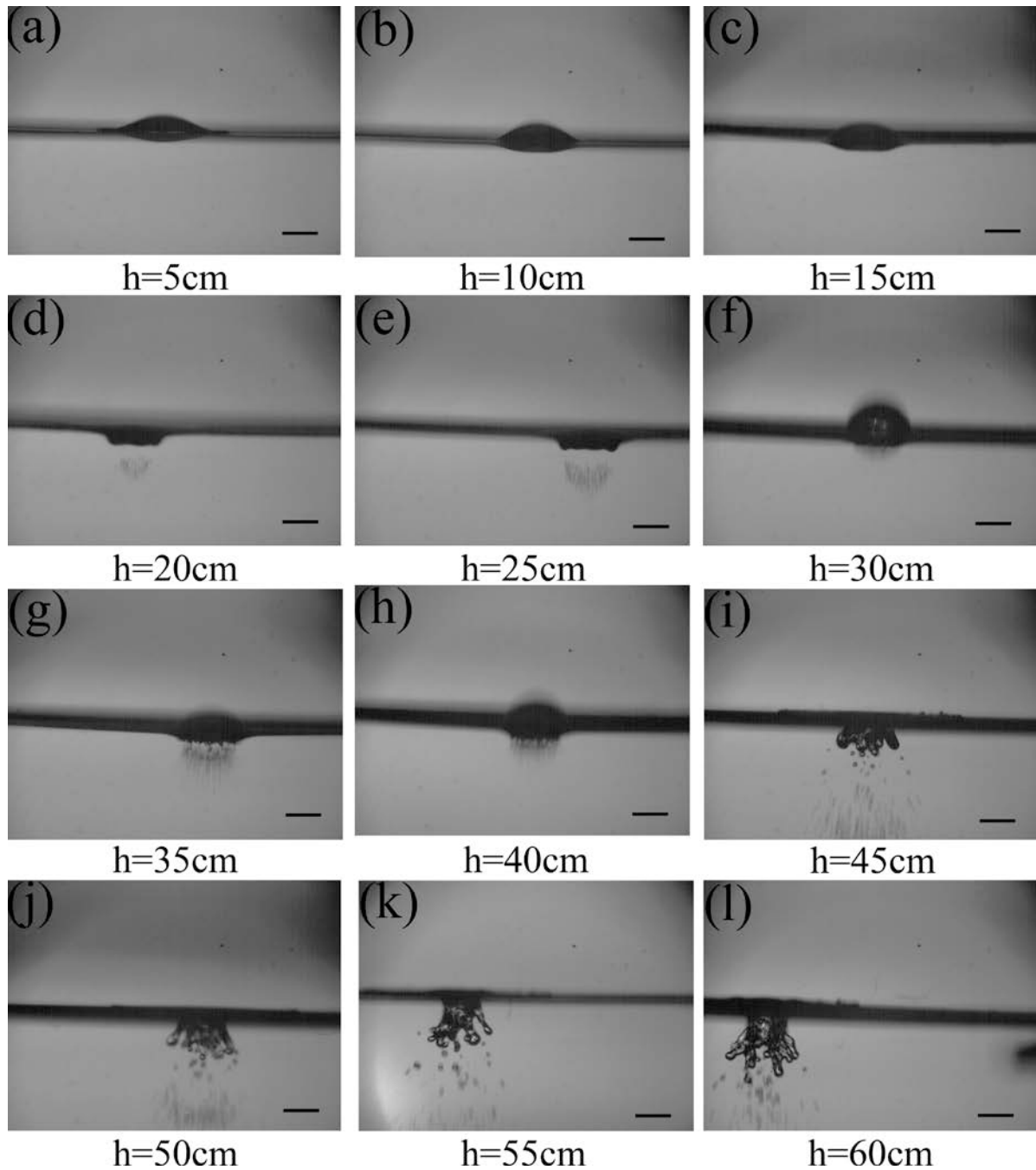


Figure 4.14. Effect of the impact velocity on the penetration pattern of drops of FC 7500 liquid impacting onto a bare nylon grid. The impact velocities are: (a) 1.0 m/s, (b) 1.41 m/s, (c) 1.73 m/s, (d) 2.0 m/s, (e) 2.23 m/s, (f) 2.44 m/s, (g) 2.64 m/s, (h) 2.82 m/s, (i) 3.0 m/s, (j) 3.16 m/s, (k) 3.31 m/s and (l) 3.46 m/s. All the images correspond to 2 ms after drop impact. Scale bars, 1mm.

Similar experiments were conducted with the FC 7500 drop impacts onto Teflon-coated nylon grids. The experiments showed no visible difference in the penetration pattern of drops of FC 7500 through Teflon-coated grids compared to those for the bare nylon grids. Fig. 4.15 shows (in comparison with Fig. 4.14) that the presence of the Teflon coating on the grid practically does not affect the FC 7500 penetration process after drop impact.

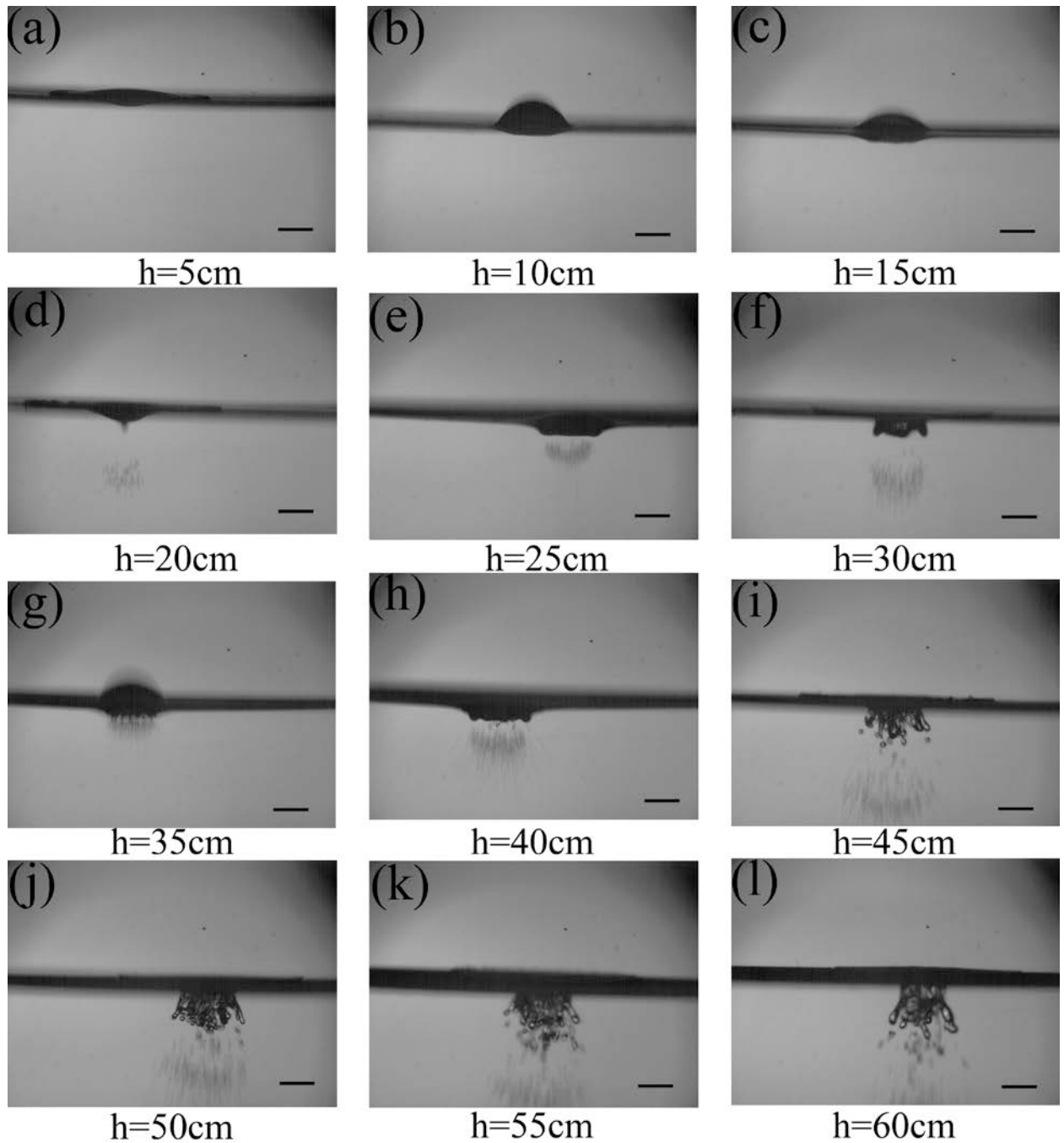


Figure 4.15. Effect of the impact velocity on the penetration pattern of the FC 7500 drops onto Teflon-coated nylon grid. (a) 1.0 m/s, (b) 1.41 m/s, (c) 1.73 m/s, (d) 2.0 m/s, (e) 2.23 m/s, (f) 2.44 m/s, (g) 2.64 m/s, (h) 2.82 m/s, (i) 3.0 m/s, (j) 3.16 m/s, (k) 3.31 m/s and (l) 3.46 m/s. All the images correspond to 2 ms after drop impact. Scale bars, 1mm.

4.3.4 Drop impact of hexane drops onto bare nylon grids and grids coated with teflon

Hexane has kinematic viscosity of 0.45 cSt, which is even lower than that of FC 7500. The results for the hexane drop impacts onto a bare nylon grid are shown in Fig. 4.16 for three impact velocity values: $V = 1$ m/s, $V = 1.4$ m/s, and $V = 3.46$ m/s. It is seen that hexane drops fully penetrate through bare nylon grids at very low velocity of 1 m/s compared to that of water drops for which the first penetration was observed at 2.23 m/s. This can be attributed to a much lower kinematic viscosity of hexane, and thus the reduced dissipation of kinetic energy inside pores. After penetrating at the impact speed of 1 m/s, hexane blob retracts back to the rear surface of nylon grid under the action of surface tension. Hexane drop impact at a high speed of 3.46 m/s results in separate jets coming out of several micropores of the nylon grid as is seen in Fig. 4.16. The relatively low surface tension of hexane (18.43 mN/m) compared to that of water is insufficient to merge the multiple jets after penetration (cf. Fig. 4.16 and 4.4).

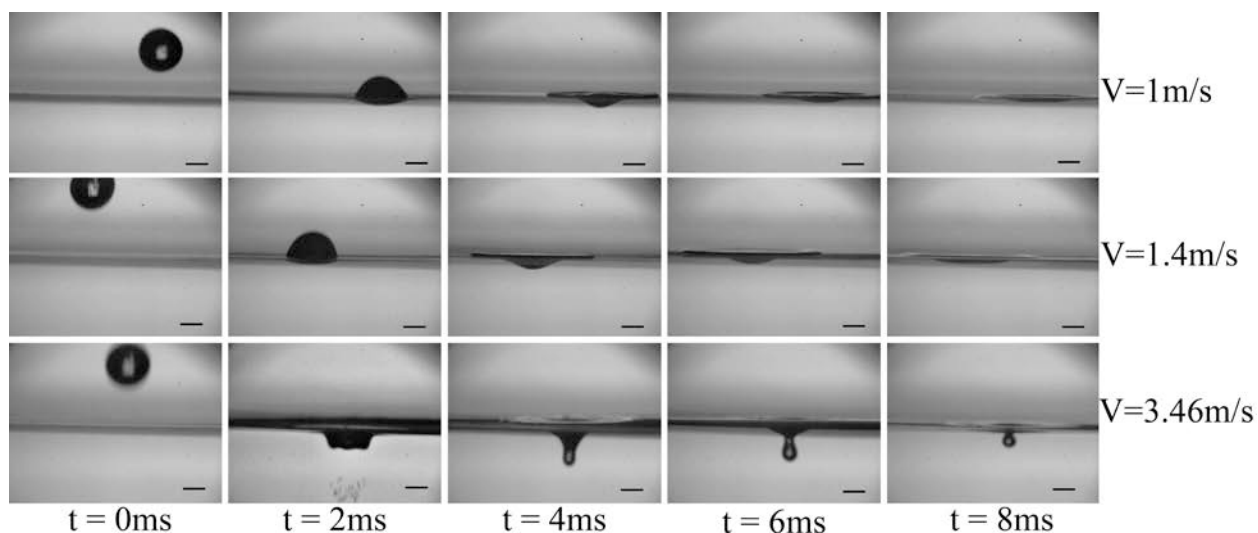


Figure 4.16 Hexane drop impact onto bare nylon grid at different impact velocities. The sequence of the images for each velocity value corresponds to the time span from 0 ms (the moment just before the impact) to 8 ms. Scale bars, 1mm.

The impacts of hexane drops onto Teflon-coated nylon grid at low and high impact velocity ($V = 1 \text{ m/s}$ and $V = 3.46 \text{ m/s}$, respectively) is depicted in Fig. 4.17. The outcomes look similar to those for bare nylon grid. At low velocity a blob which penetrated through the grid retracts back to the rear surface, whereas at high impact velocity separate jets are visible behind the nylon grid.

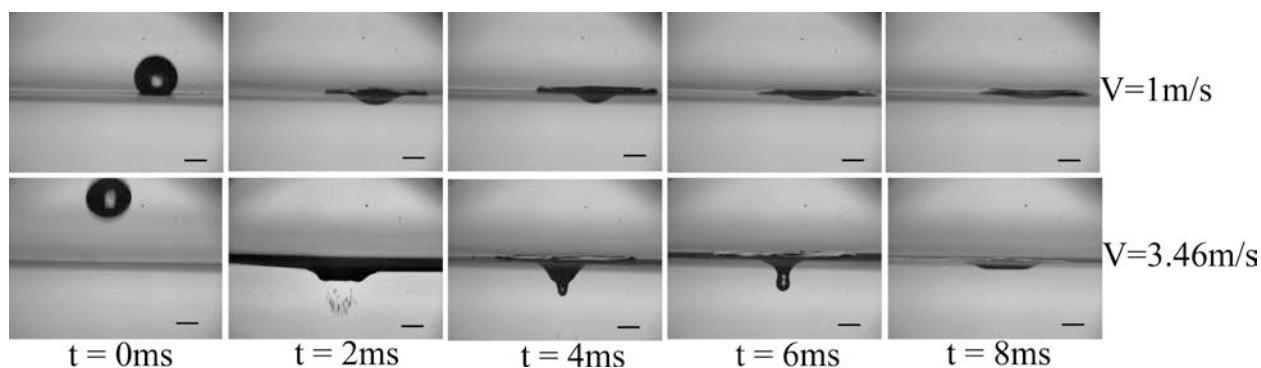


Figure 4.17. Hexane drop impact onto Teflon-coated nylon grid at the impact velocities of $V = 1 \text{ m/s}$ and $V = 3.46 \text{ m/s}$. Scale bars, 1mm.

The results for the FC 7500 and hexane drops show that tiny jets behind the grid break into tiny secondary droplets presumably due to the capillary instability. That makes it extremely difficult to evaluate the amount of liquid penetrated through the grid. Therefore, the results similar to those for water in Fig. 4.10 are unavailable for FC 7500 and hexane. It is emphasized that for both these low surface tension and low viscosity liquids, FC 7500 and hexane, penetration through pores was much easier (at a lower impact velocity) than that for water. Therefore, the experiments described in the following subsections were conducted for water drops alone.

4.3.5 Drop impact onto electrospun PAN nanofiber mats supported by bare nylon grids

An 8 wt% PAN solution in DMF was electrospun onto bare nylon grids for different time. A representative SEM image of PAN nanofiber mat on a grid is shown in Fig. 4.18. Fig. 4.18a shows the overall view, whereas Fig. 4.18b shows a zoomed-in image of the PAN nanofibers suspended over the grid openings. It can be seen that due to the presence of nanofibers, the pore sizes are reduced to the order of 1-10 μm . It is emphasized that the pore

size and the thickness of the nanofiber mat are determined by the duration of electrospinning (Fig. 4.19) and the relative humidity of the surrounding atmosphere. During electrospinning of PAN nanofiber mats onto bare nylon grids the relative humidity was within the range of 20-30% and the electrospinning duration was from 5 to 60 s. The thickness of the deposited PAN nanofiber mats was measured using the Olympus BX-51 Optical Microscope. The microscope was focused at the bottom layer of nanofibers, and after that, on the top layer. The difference between the corresponding two focus lengths was attributed to the mat thickness (Fig. 4.20). It can be seen from Fig. 4.20 that the fiber mat thickness does not possess any visible trend versus the deposition time. However, it was observed that while the mat thickness can stay constant or even decrease, the pore size decreases at longer deposition times, indicating a more dense packing of nanofibers. It should also be mentioned that attempts were made to measure the pore size of nanofiber mats deposited onto bare nylon grids by using mercury porosimetry. However, the results reflected only the pore size of about 20 μm , whereas Fig. 4.18 shows that the pore size is in the range of 1-10 μm . The disagreement can be attributed to the fact that in such experiments mercury emerged through the nylon grid, probably after delaminating the more flexible nanofibers, which made mercury porosimetry results unreliable. Therefore, in the discussion below the electrospinning time is chosen as the mat characteristic.

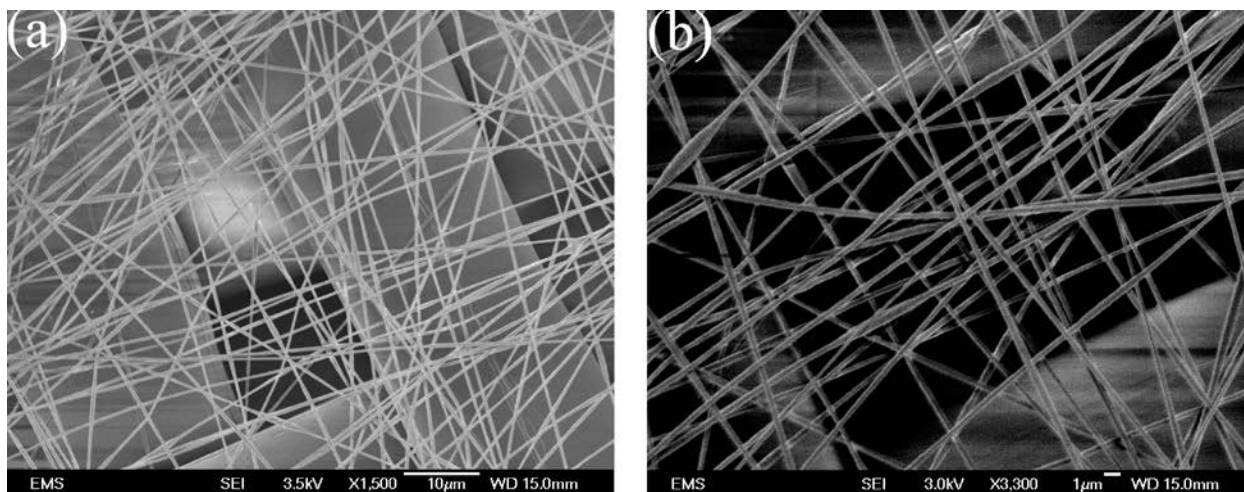


Figure 4.18. SEM image of electrospun PAN nanofibers deposited onto bare Nylon grid for 60 s. (a) The overall view, (b) a zoomed-in view over an opening in the grid.

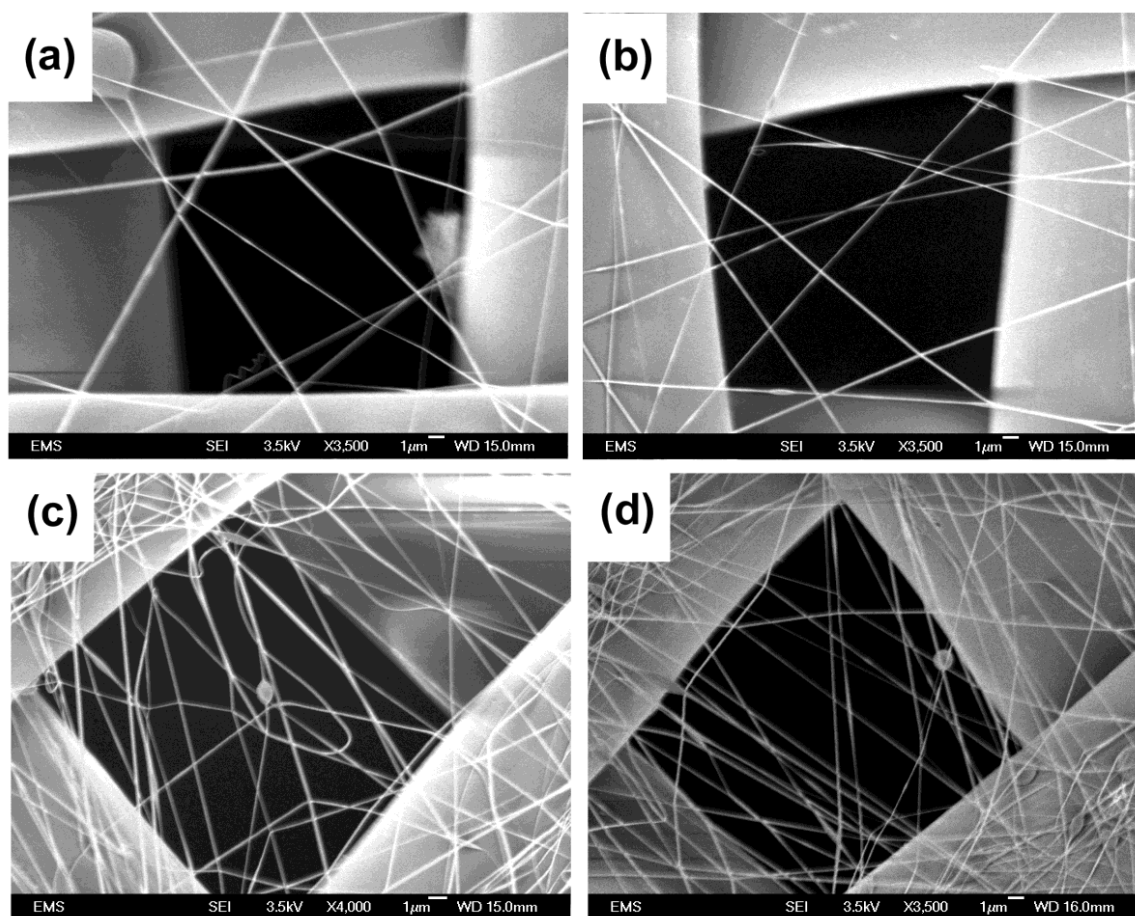


Figure 4.19. Panels (a) and (b) show PAN nanofibers electrospun onto a nylon grid for 20 s (two different locations). Panels (c) and (d) show PAN nanofibers electrospun onto nylon grid for 60 s (two different locations). It can be seen from the images that a longer electrospinning time reduced the pore size significantly, while the mat thickness can stay approximately the same (see Fig. 4.20). This can be explained as follows. The nylon grid, which is dielectric, is kept on a copper electrode during electrospinning. As polymer nanofibers are deposited onto the grid, they are attracted to the still open domains of the copper electrode. Moreover, the residual electric charge in the polymer nanofibers also tends to repel the oncoming polymer jet. This repels the oncoming nanofiber loops toward the still open domains of the copper electrode, which diminishes pore size even more.

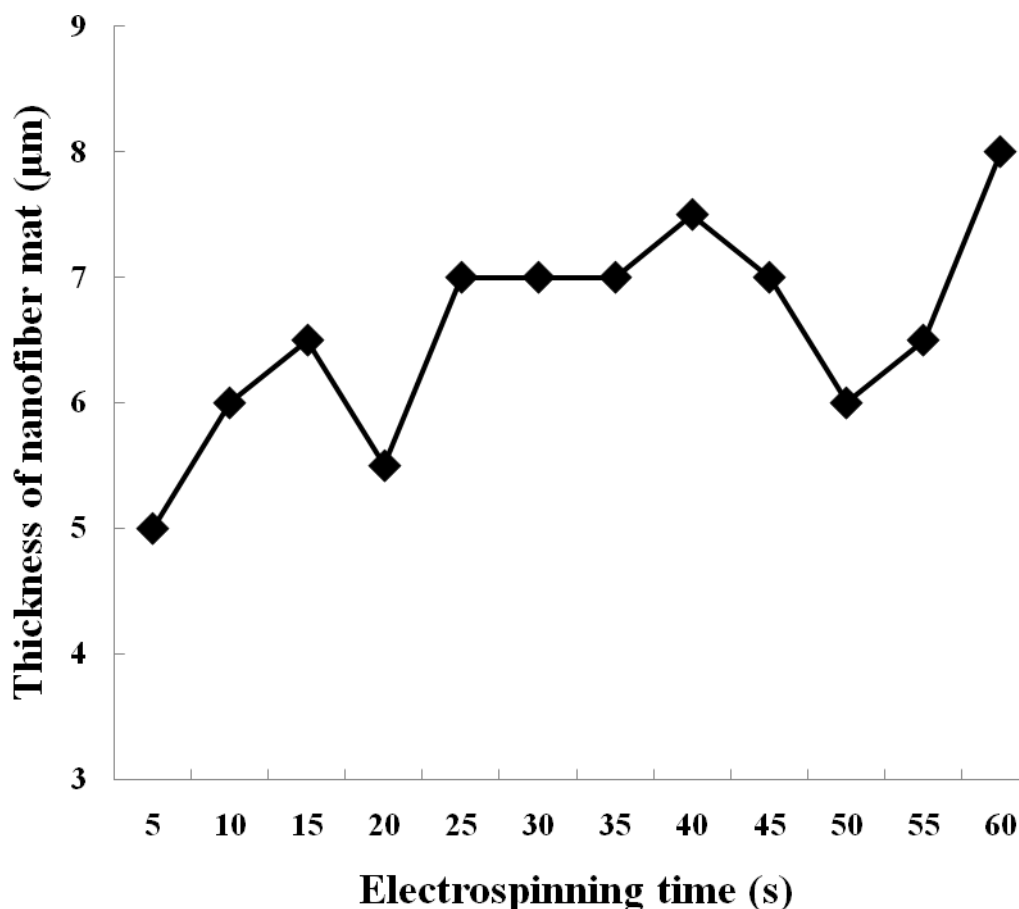


Figure 4.20. Thickness of electrospun PAN nanofiber mat on bare nylon grids versus the electrospinning time. There is no pronounced dependence of the mat thickness on the electrospinning time.

Drop impact with the impact velocity of 3.46 m/s onto nylon grids coated with PAN nanofibers electrospun for 5-60 s are shown in the images in Fig. 4.21. It was found that the threshold velocity for water penetration through the nanofiber-coated nylon grid (with the mat deposited for 5 s) was 2.43 m/s. This value is higher than that of the corresponding threshold value of 2.23 m/s for bare Nylon grids. Therefore, nanofiber mats deposited on

nylon grids significantly reduce permeability. Water penetration through the first layer of pores at the nanofiber mat surface is hardly expected to be diminished by the fact that pores in the mats are an order of magnitude smaller than that in bare nylon grids [Lembach et al. (2010)]. However, the presence of nanofibers results in a significant increase in viscous dissipation during water flow inside the pores, as discussed in the theoretical section 4.4 below. The latter factor determines the thickness of nanofiber mat which can be fully penetrated at a given impact velocity. Alternatively, viscous dissipation determines a higher critical impact velocity for a full penetration of a given mat thickness in comparison with that for the bare nylon grid underneath. It is emphasized that water penetration after drop impact onto a nanofiber mat deposited on a grid is mostly determined by the mat permeability, whereas the grid permeability effect is negligible since the grid is much more permeable than the mat. Indeed, pores in the mat are of the order of 1-10 μm (cf. Fig. 4.18), while those in the grid are of the order of 20 μm , and the permeability depends on the pore size squared.

Figure 4.22 depicts the critical threshold velocity of drop impact needed for the full water penetration through nanofiber mats on nylon grid electrospun for different times. The critical velocity linearly increases with the deposition time in the range studied.

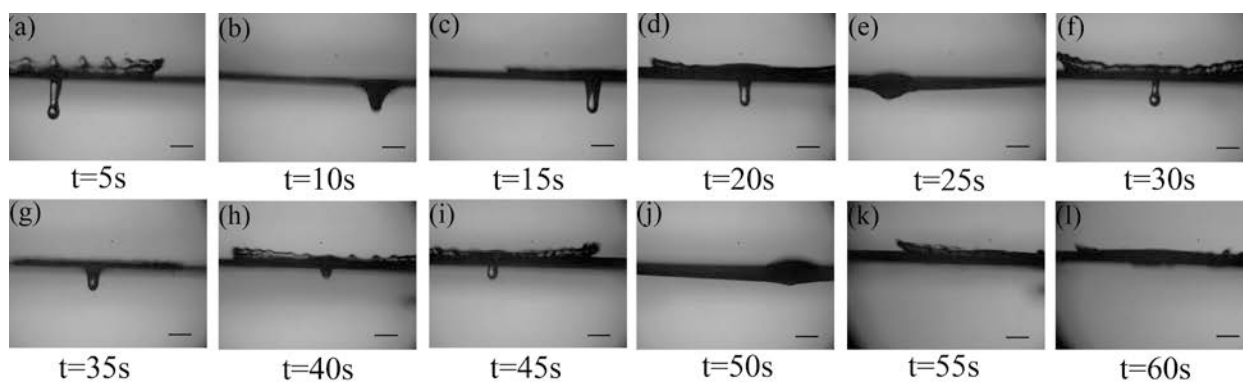


Figure 4.21. Impacts of the identical water drops onto PAN nanofiber mats electrospun onto nylon grids for different time t . The impact velocity was 3.46 m/s, the initial drop diameter was 2 mm. The electrospinning time t values were: (a) $t=5$ s, (b) $t=10$ s, (c) $t=15$ s, (d) $t=20$ s, (e) $t=25$ s, (f) $t=30$ s, (g) $t=35$ s, (h) $t=40$ s, (i) $t=45$ s, (j) $t=50$ s, (k) $t=55$ s and (l) $t=60$ s. The images correspond to 2 ms after the moment when the drops touched the target. Scale bars, 1mm.

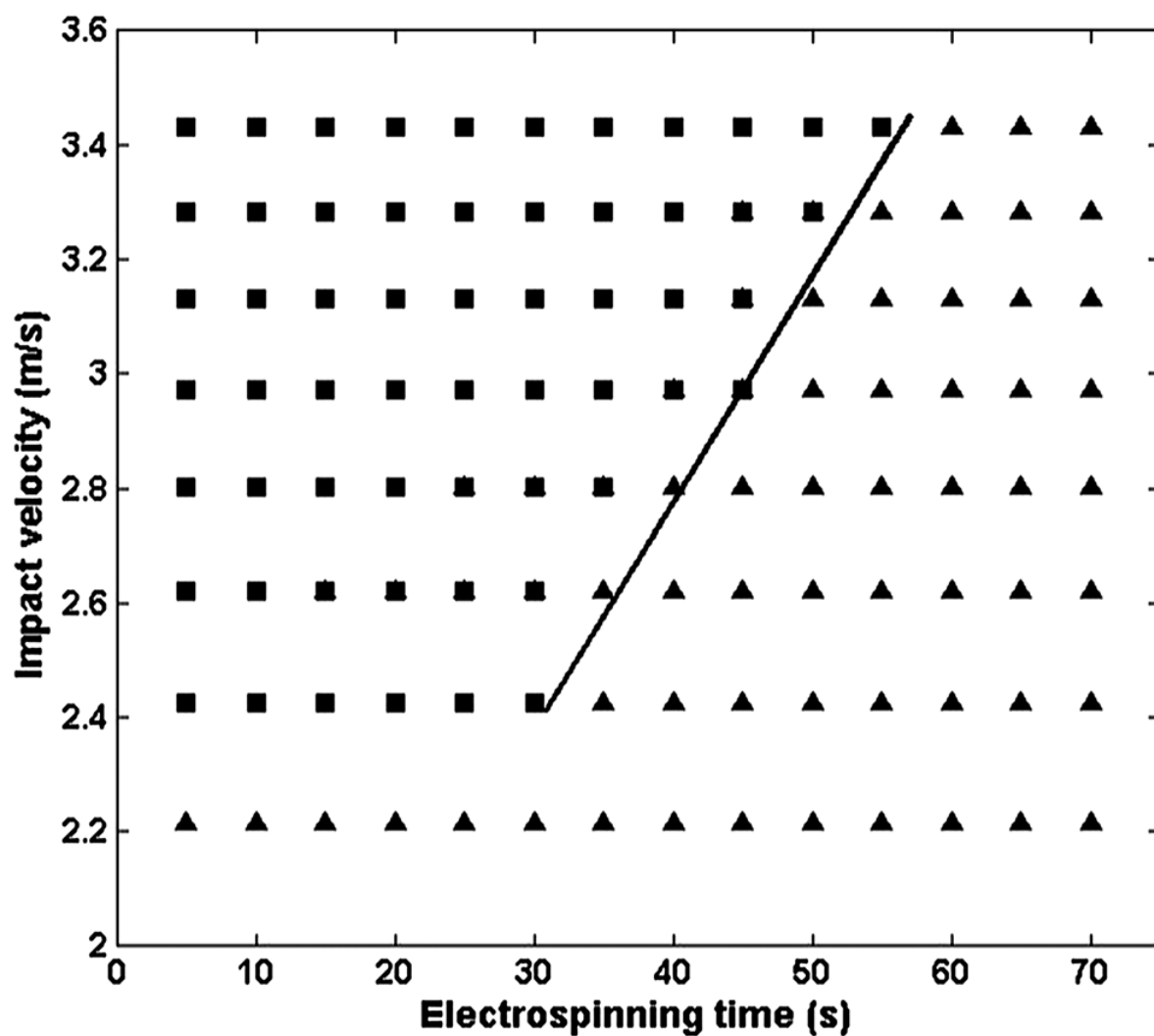


Figure 4.22. The critical velocity for water penetration after drop impact versus the electrospinning time of PAN nanofiber mats onto nylon grids. The square symbols correspond to the experiments where water penetration was observed, whereas the triangular ones correspond to the experiments without water penetration after drop impact. The initial drop diameter was 2 mm.

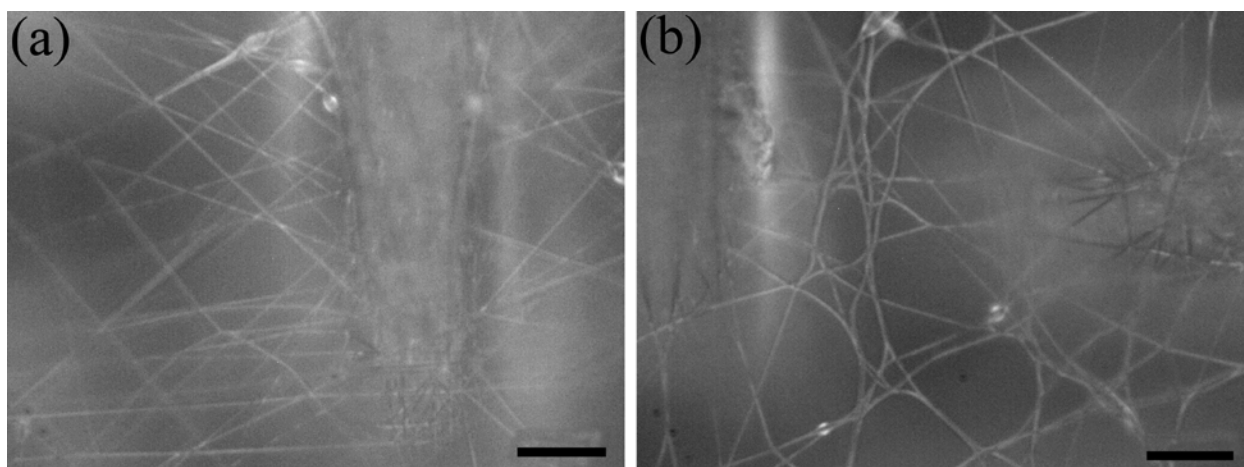


Figure 4.23. Magnified optical images showing the same place of the nanofiber mat deposited over a nylon grid before [in (a)] and after [in (b)] drop impact. The deposition time of the nanofiber mat was 60 s and the drop impact velocity was 3.46 m/s. Scale bars, 10 μm .

The nanofiber mats deposited over nylon grids were inspected before and after drop impacts to corroborate that no big holes in the mats were created by drops, and water penetration was indeed associated with the initial mat porosity. The surface of the nanofiber mat deposited over a nylon grid shown in Fig. 4.23 (a) had the average pore size of about 10 μm . The same location was inspected in Fig. 22 (b) after drop impact and complete water drying. In the latter case several different nanofiber layers visible in the image look as they were compressed together by drop impact (or water drying). On the other hand, it is also evident that the drop impact did not create any holes in the nanofiber mat as the pore size and the overall mat morphology still remain approximately the same. It is emphasized that the drop was on the scale of 1 mm, and the entire area of the nanofiber mat seen in Fig. 4.23 was subjected to the impact. In addition, the effect of multiple drop impacts at the same place of nanofiber mats was studied. PAN nanofibers were electrospun on a bare nylon grid. Then, FC7300 drops (1mm in diameter) impacted the same spot with an impact velocity of 3.31m/s

eight times in succession. The images of the nanofiber mat before the first impact, and after the 4th, 6th and 8th impacts taken using an Olympus BX51 microscope are shown in Fig. 4.24 a–d, respectively. It can be seen from the images that no big holes appear even after the 8th impact, albeit some local nanofiber rearrangement could happen. Note that FC 7300 possesses a relatively low surface tension, which diminishes nanofiber rearrangement when samples are dried after drop impact prior to the observations.

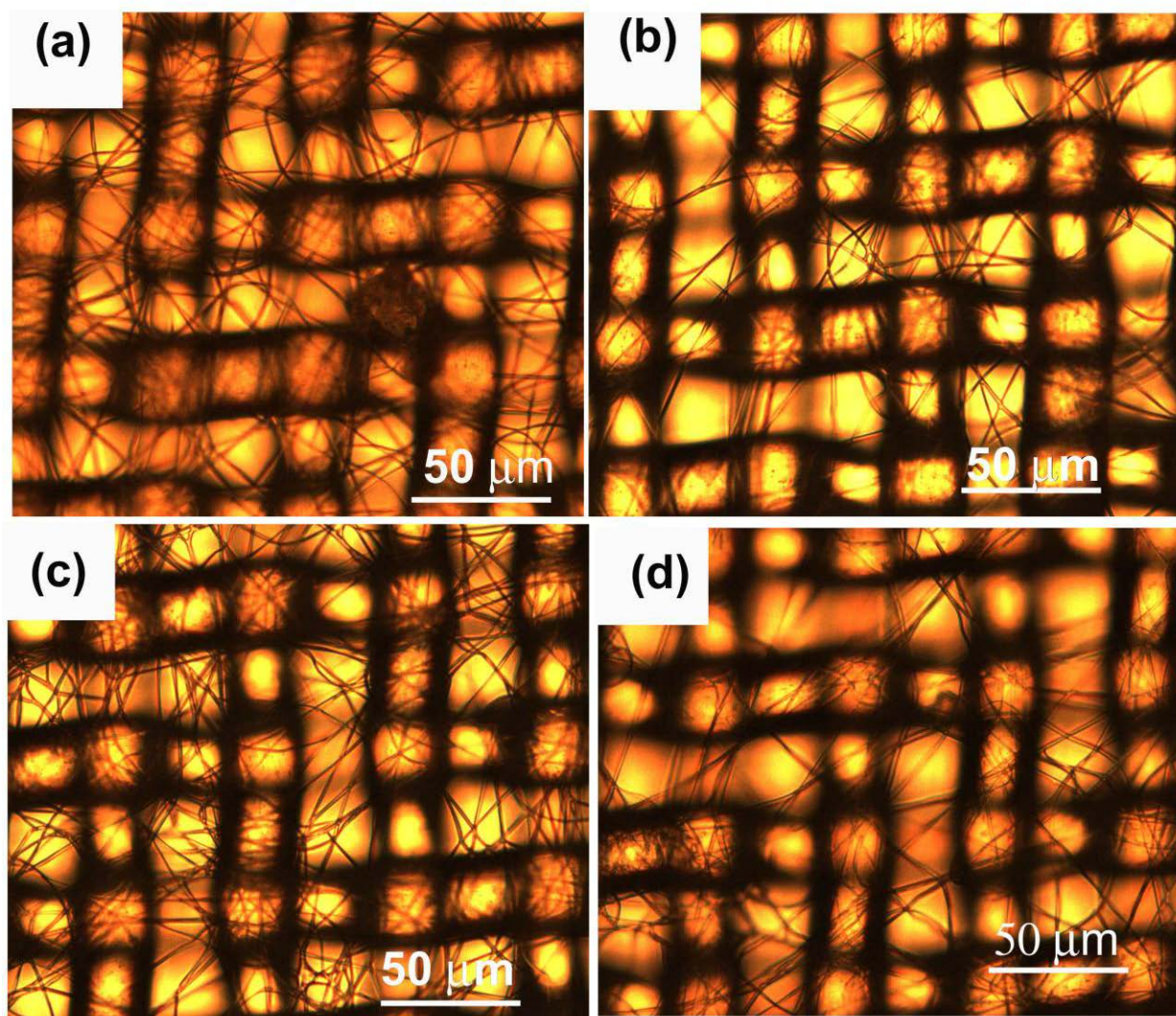


Figure 4.24. Optical images of electrospun PAN nanofiber mat on a nylon grid. (a) Before drop impact, (b) after 4 impacts, (c) after 6 impacts, and (d) after 8 impacts of 1 mm drop of FC 7300. This liquid has a relatively low surface tension, which diminishes nanofiber rearrangement when samples are dried after drop impact prior to the observations.

4.3.6 Water drop impact onto electrospun nylon 6/6 nanofiber mats on bare nylon grids

Nylon 6/6 nanofibers were electrospun over bare nylon grids for a few seconds. The rate of Nylon 6/6 nanofiber deposition was very rapid compared to that of PAN nanofibers. The accumulation of Nylon 6/6 nanofibers beyond 10 s would result in very thick nanofiber mats, which exceed the critical nanofiber mat thickness, estimated theoretically (cf. the theoretical part 4.4) and also significantly reduce the pore size to 2-4 μm . Therefore, nylon 6/6 nanofibers were collected for 5 s. The thickness of the collected nylon 6/6 nanofiber mats was in the range of 8-10 μm . Numerous (10-12) samples of nylon 6/6 nanofiber mats were collected and used in water drop impact experiments. Fig. 4.25a shows SEM image of a bare nylon grid with electrospun nylon 6/6 nanofibers supported by it. Fig. 4.25b shows a zoomed-in image of nylon 6/6 nanofibers collected over a pore in the nylon grid. The pore size in the mat is of the order of 1-4 μm .

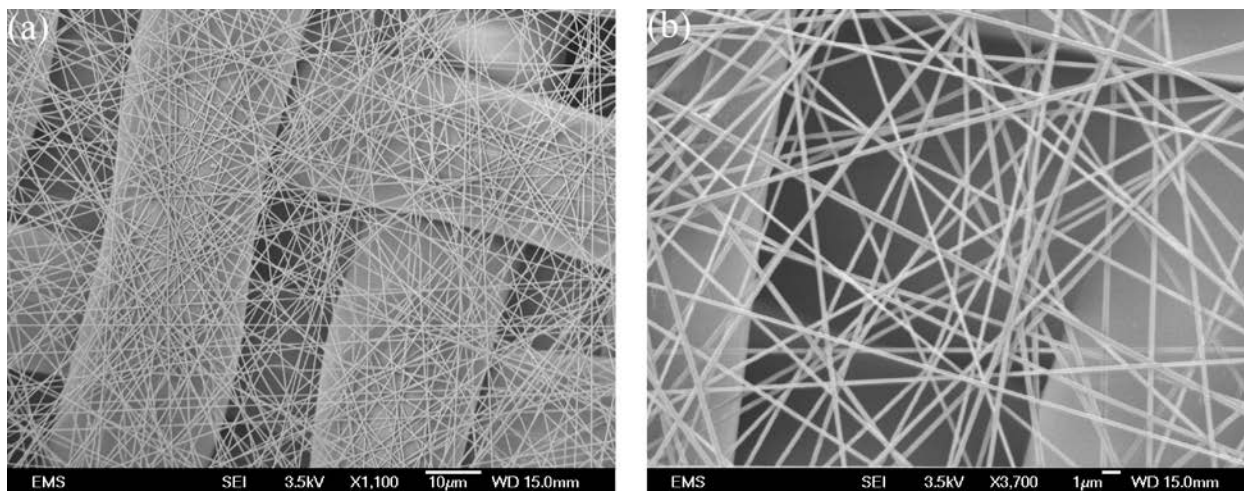


Figure 4.25. SEM images of nylon 6/6 nanofibers collected over a bare nylon grid. (a) The overall view, and (b) a zoomed-in image.

Figure 4.26 shows a sequence of images illustrating water drop impact onto nylon 6/6 nanofiber mat electrospun over a bare nylon grid. At a low impact velocity the scenario is similar to the impact onto PAN nanofiber mats, where water drop spreads after impact and its contact line becomes pinned with no visible penetration through the mat. An increase in the impact velocity to $V = 2.64$ m/s results in water drop corona splash after the impact. The wettability of cast PAN and nylon 6/6 are approximately the same, which is evident from the contact angle measurement results shown in Table 4.3 and the thickness of these nanofiber mats was also approximately the same. However, full water penetration in the case of nylon 6/6 begins from the impact velocity of 3 m/s, compared to the impact velocity of 2.44 m/s in the case of PAN. This is attributed to the reduced pore size of the nylon 6/6 nanofiber mat compared to that of PAN, which results in a higher viscous dissipation of kinetic energy inside the pores in the case of nylon 6/6. At the impact velocity of 3.46 m/s the water drop fully penetrates through the nylon 6/6 nanofiber mat on a bare Nylon grid. The penetrated water drop can either retract back to the rear side of the grid under the action of surface tension, or break off as a merged jet and smaller secondary droplets resulting from the capillary instability.

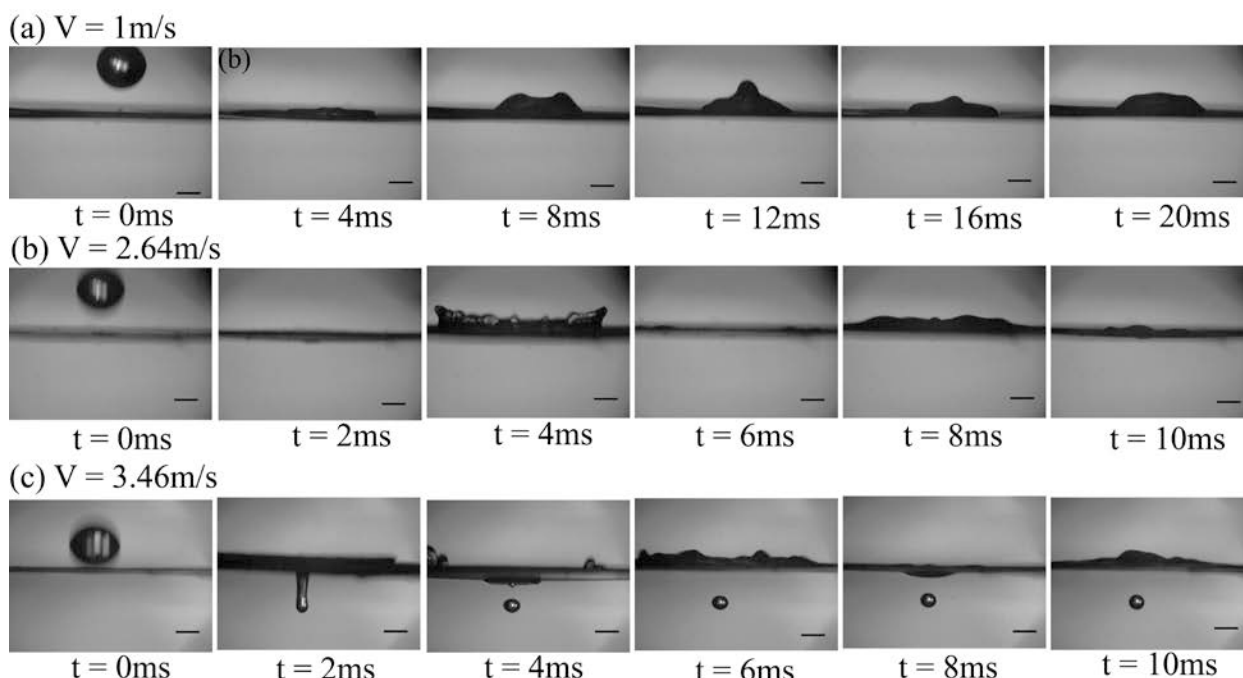


Figure 4.26. Water drop impact onto electrospun nylon 6/6 nanofiber mats on a bare nylon grid at different velocities: (a) $V = 1 \text{ m/s}$, (b) $V = 2.64 \text{ m/s}$ and (c) $V = 3.46 \text{ m/s}$. The images correspond to different time instants from the moment of impact (approximately at $t = 0 \text{ ms}$). Scale bars, 1mm.

4.3.7 Water drop impact onto electrospun PCL nanofiber mats supported on bare nylon grids

PCL nanofibers were electrospun onto bare nylon grids for different time in the range of 10 to 120 s. These supported nanofiber mats were subjected to water drop impacts with velocities in the range 1 m/s to 3.46 m/s. As mentioned before, deposition of PAN nanofibers onto bare nylon grids was dependent on the relative humidity in the surrounding air. During electrospinning of PCL nanofibers the relative humidity was within the range of 50-60%, which is higher than that for the PAN nanofibers discussed above (20-30%). Therefore, for

the sake of comparison with PCL, electrospun PAN nanofiber mats were also prepared at the higher humidity and with thickness comparable to that of the electrospun PCL mats. The penetration charts for both PAN and PCL nanofiber mats obtained in the water drop impact experiments were superimposed and presented in Fig. 4.27. Each point in the penetration chart corresponds to a certain combination of the impact velocity and the electrospinning time. The square symbols correspond to the penetration events, whereas the triangular symbols correspond to the non-penetration ones (for PCL nanofibers). The threshold velocity corresponding to the same time of deposition during electrospinning appears to be different for the PAN and PCL, namely it is higher for PCL mats compared to that for PAN. This can be attributed to the interplay of the difference in the thickness and different pore sizes in the mats, and different wettability of PCL and PAN (much lower for the former). However, the penetration chart in Fig. 4.27 shows that for any wettability, after a threshold velocity is surpassed, water penetration inevitably happens.

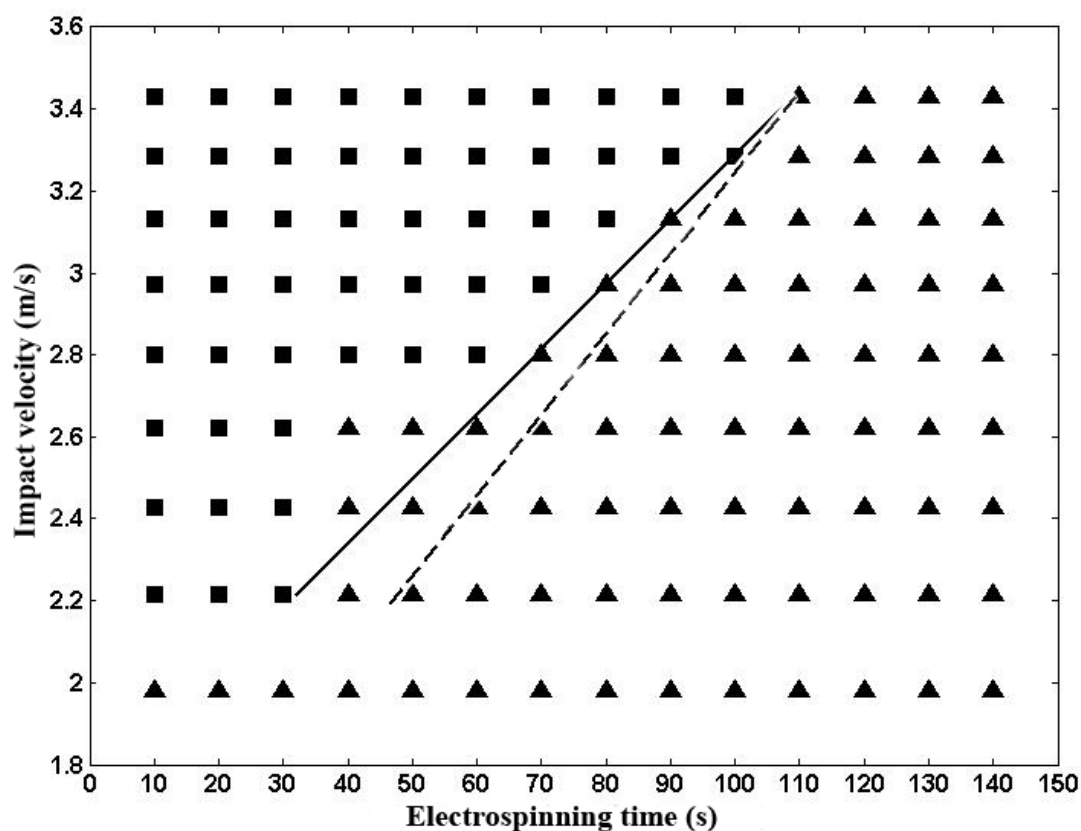


Figure 4.27. Penetration chart for PCL and PAN nanofiber mats on bare nylon grids. The solid line corresponds to PCL and the dashed line to PAN.

4.3.8 Water drop impact onto electrospun teflon nanofiber mats supported on bare nylon grids

The static contact angle of water drops on cast Teflon was measured as 115-120° (Fig. 4.28a), whereas the static contact angle of water drops on the electrospun Teflon membrane on a nylon grid was in the range 140-150° (Fig. 4.28b).

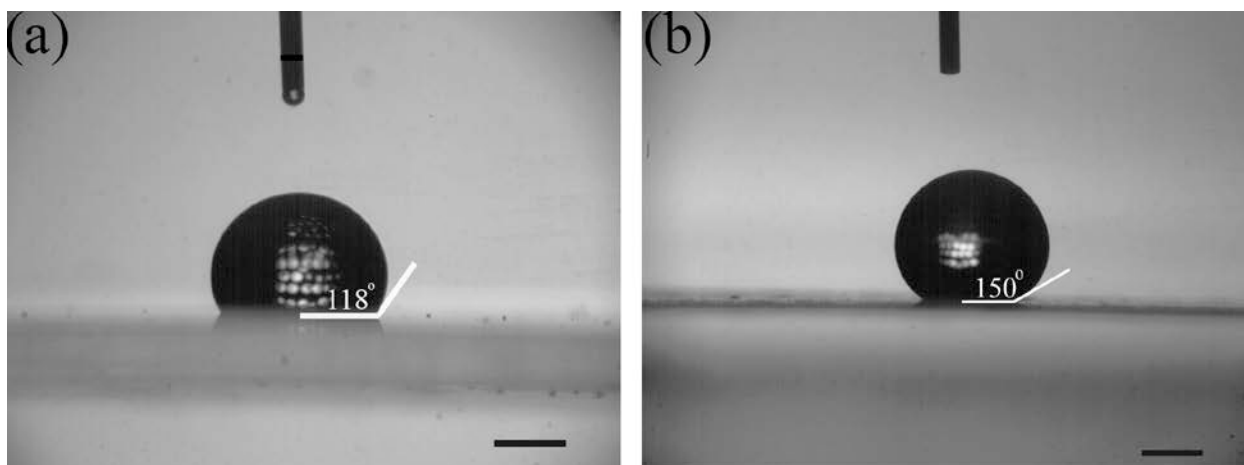


Figure 4.28. Static contact angle of water drop on (a) cast Teflon on the glass slide and (b) on electrosun Teflon nanofiber mat collected on a nylon grid. Scale bars, 1mm.

Figure 4.29 shows the SEM micrograph of the electrospun 5 wt% Teflon AF 1600 nanofibers collected on a nylon grid. The fiber cross-sectional diameter ranges from 400 nm to 1 μm . It can also be seen from the SEM image in Fig.4. 29a and b that at some places the fibers flattened and ribbon-like structures appeared. The flattened structures could probably be merged nanofiber bundles which result from fibers landing at the counter-electrode while still wet due to an incomplete solvent evaporation.

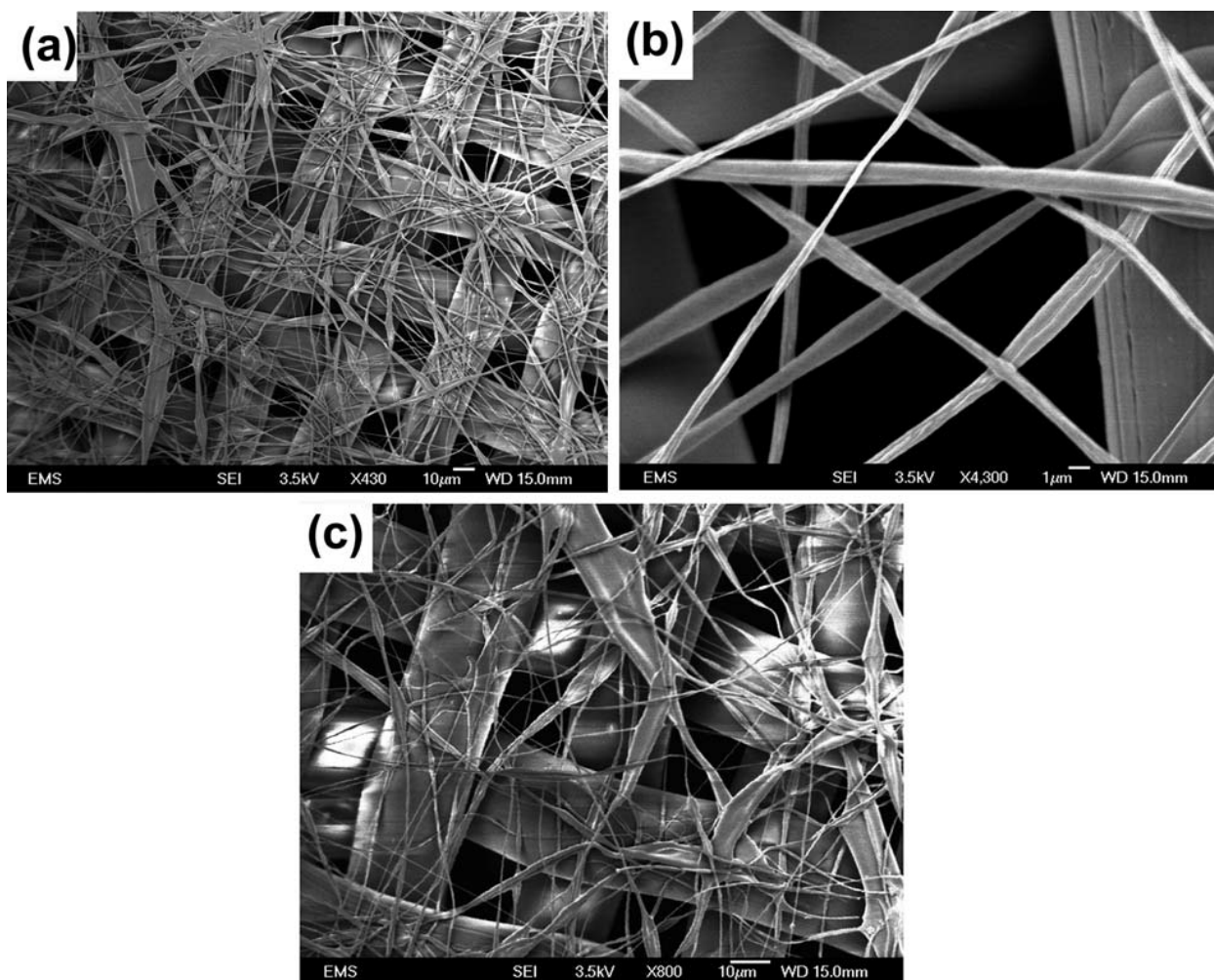


Figure 4.29. SEM images of the electrospun Teflon nanofiber mat collected on the nylon grid. The pore size of the nylon grid is 20 μm and the collected nanofibers effectively reduce the pore size of the substrate to 3–6 μm . The thickness of the nanofiber mat is of the order of 5–8 μm . (a) The overall view. (b) Teflon fibers over a pore of the nylon grid. SEM images of the electrospun Teflon nanofiber mat before (a) and after (c) drop impact at the impact location. The comparison of panels (a) and (c) does not show any visible damage to the mat caused by drop impact.

SEM images of Teflon nanofibers collected on a nylon grid are shown in Fig. 4.29a. It can be seen that the pores in the grid were not entirely blocked by the nanofibers but rather diminished to the level of 3-6 μm when a 5-8 μm thick mat was electrospun. The mat is superhydrophobic as shown in Fig. 4.30. Superhydrophobicity of Teflon nanofiber mats is also illustrated in Fig. 4.30a where a water jet impacts obliquely at a relatively low velocity of 1-2 m/s on the mat. It is seen that the jet is bounced back from the mat. Fig. 4.30b shows blowing off of drops from the mat surface by low speed air blowing.

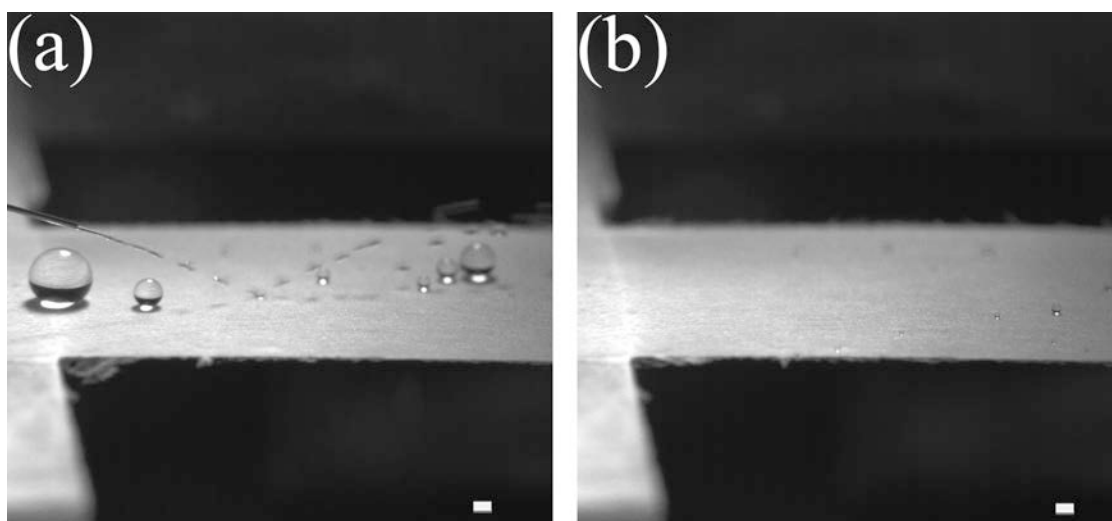


Figure 4.30. Two frames from the movie (S1) demonstrating superhydrophobicity of the Teflon nanofiber mat when water jet impacts onto it a velocity of 1-2 m/s. (a) Water jet is repelled from Teflon nanofiber mat on a Nylon grid. (b) Drops are blown off from the Teflon nanofiber mat. Scale bars, 1mm.

Significant water repellency of Teflon nanofiber mats visible in Fig. 4.30 does not necessarily mean that such mats are impenetrable to water under dynamic conditions of drop impact. On the contrary, the mechanism of the accumulation of the kinetic energy of drop

impact [Lembach et al. (2010; Sinha-Ray et al. (2011) and Weickgenannt et al. (2011)] should inevitably result in water penetration if the impact velocity is sufficiently high. In the following experiments, water drops impacted onto Teflon nanofiber mats of thickness in the range of 5-7 μm deposited on nylon grids. Drops had the impact velocity of 2.82 m/s, and water penetration through the mat and grid was observed. Fig. 4.31 shows the images of water drop impact onto Teflon mats at the impact velocity of $V = 3.46$ m/s. It is seen that the water drop partially penetrated through the Teflon nanofiber mat. After the impact the penetrated portion of water drop might retract back to the surface of the supporting nylon grid or break off as a jet or individual secondary droplets (as in Fig. 4.31). The penetration patterns depended on the impact velocity and thickness of the nanofiber mat. After the impact the portion of a water drop remaining on the nanofiber mat surface retracts and completely rebounds from the surface. The inspection of the nanofiber mat after drop penetration showed that no damage was caused to the nanofibers and that the porous structure after penetration resembles the one before the penetration which is evident from Fig. 4.29a and c. The portion of the nanofiber mat shown in Fig. 4.29a and c corresponds to the impact location. It only covers an area of $0.2 \text{ mm} \times 0.2 \text{ mm}$. Some fibers are seen slightly re-oriented either by drop impact or water drying. However, it can be seen that no significant damage (big holes) was observed.

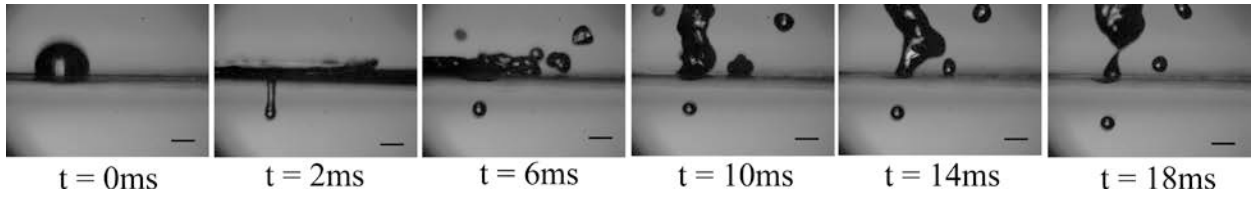


Figure 4.31. Water drop impact onto electrospun Teflon nanofiber mat on nylon grid. The impact velocity $V = 3.46$ m/s. Scale bars, 1mm.

4.4 Theoretical model

In Lembach et al. (2010) and Weickgenannt et al. (2011) it was shown that liquid penetration into pores of size δ after drop impact of size D at velocity V proceeds with the entering velocity U , where

$$U \approx V \frac{D}{\delta} \quad (4.1)$$

which is much higher than V in the cases where $D/\delta \gg 1$. In particular, in the present case $D \approx 0.1$ cm, whereas $\delta \approx 10^{-3}$ cm for the grids used, and $\delta \approx 10^{-4}$ cm for the nanofiber mats on them. Given $V \approx 1$ m/s, the accumulation of the kinetic energy due to drop impact in flow into the pores [Lembach et al. (2010) and Weickgenannt et al. (2011)] can result in the initial penetration velocities of the order of $U \approx 100$ m/s. This analysis can be extended, in principle, to the case when the drop penetrates into several pores simultaneously, which will diminish the value of U .

The entire kinetic energy brought by the penetrating water drop into the pores will be rapidly dissipated by viscous friction at the pore walls. As a result, a critical mat thickness should exist which corresponds to the total dissipation of the initial kinetic energy. The following estimate demonstrates that. The kinetic energy E_k brought by a water drop penetrating into the pores can be evaluated as

$$E_k \approx \rho U^2 D^3 \approx \rho \left(V \frac{D}{\delta} \right)^2 D^3 \quad (4.2)$$

In the dynamic penetration the surface tension effects are negligible, and the only resistance to flow in the pores arises from viscous friction at the pore walls. The viscous shear stress σ is estimated as

$$\sigma \approx \mu \frac{U}{\delta} \approx \frac{\mu}{\delta} \left(V \frac{D}{\delta} \right) \quad (4.3)$$

The length of a tortuous pore is assumed to be of the order of the size of an impacting drop D . Then, the pore surface area is of the order of δD , and the viscous friction force acting on liquid in a single pore is estimated as $\sigma \delta D$. On the other hand, the number of pores through which liquid is penetrating is of the order of $(D/\delta)^3$, which makes the total viscous force of the order of $\sigma \delta D (D/\delta)^3$. The estimate of the number of pores takes into consideration the through pores and the pores leading sideways. Correspondingly, the work done by viscous forces while liquid has penetrated a mat of the thickness h is of the order of $\sigma \delta D (D/\delta)^3 h$, which represents itself the total viscous dissipation E_d . Using Eq. (4.3), we find that

$$E_d \approx \frac{\mu}{\delta} \left(V \frac{D}{\delta} \right) \delta D \left(\frac{D}{\delta} \right)^3 h \quad (4.4)$$

In the mat of the critical thickness, the entire kinetic energy brought by a drop is fully dissipated by viscous forces, i.e. $E_k \approx E_d$. As a result, Eqs. (4.2) and (4.4) yield the critical mat thickness of the order of

$$h = \frac{\rho V \delta^2}{\mu} \quad (4.5)$$

It is instructive to see that the critical mat thickness does not depend on the impacting drop size. Taking for the estimates the pores of the order of $\delta \approx 10^{-3}$ cm and the impact velocity of the order of $V \approx 1$ m/s, we obtain from Eq. (4.5) for water the critical mat thickness $h \approx 100$ μm . According to Fig. 4.20, all PAN nanofiber mats which were fully penetrated by water had thicknesses of the order of 10 μm , since they were deposited for less than 70 s. This experimental result is within the range of the theoretical estimate. It is emphasized that the theoretical analysis of this section, and in particular, its result, Eq (4.5), is novel, to our knowledge.

4.5. Conclusion

Drop impacts of a single liquid drop in a range of the impact velocities from 1 m/s to 3.46 m/s were studied experimentally. The experiments employed impacts onto bare nylon grids (partially wettable), Teflon-coated nylon grids, nylon grids covered with electrospun polyacrylonitrile (PAN), nylon 6/6, polycaprolactone (PCL) and Teflon nanofiber mats, which covers a wide wettability range (from partially wettable to superhydrophobic). It was found experimentally that there exists a relatively low threshold velocity at which water drops fully penetrate (i.e. some water is disconnected from the rear side) through any of these micro-porous and nano-textured membranes irrespective of their wettability. It shows that after the threshold velocity has been surpassed, the static wettability plays only a secondary role in water penetration, which is mainly a dynamic process. In particular, it was shown that in the case of bare nylon grids, water penetration happens at the impact velocities above the threshold value of 2.23 m/s. In the case of bare Teflon-coated nylon grids there is water penetration at the impact velocities above the threshold value of 2.64 m/s. The other liquids

studied (Fluorinert fluid FC 7500 and hexane) penetrated through the grids much more easily than water, which possesses a higher surface tension and kinematic viscosity.

It was also shown that the threshold impact velocity for water penetration exists for the impacts onto electrospun nanofiber mats of PAN, nylon 6/6, PCL and Teflon, which practically encompass the entire wettability range. This shows that water penetration (the dynamic wettability) always sets in above a relatively low threshold impact velocity, and an ultimate water repellent fibrous medium is hardly possible. The less wettable the membrane is, the higher is the threshold velocity, however, it still stays below 3.5 m/s. An especially non-trivial result is that superhydrophobicity of the porous nano-textured Teflon skeleton with the interconnected pores is incapable of preventing water penetration due to drop impact, even at relatively low impact velocities close to $V = 3.46$ m/s. It is also emphasized that electrospun nano-textured Teflon membranes, which represent themselves as relatively new nano-textured, superhydrophobic materials obtained two years ago, which possess very low hydraulic permeability, are shown to be incapable of fully repelling water under the dynamic conditions corresponding to drop impact.

A theoretical estimate is developed to evaluate the critical thickness of the nanofiber mat capable to fully dissipate droplet kinetic energy of penetrating liquid. The critical thickness is close to 100 μm . It was found from the experiments that the data are within the range of the theoretical estimate.

5. BLOWING DROPS OFF A FILAMENT

This chapter has been previously published in Sahu et al. (2013).

5.1 Introduction

The first part of this work is devoted to the experimental study of oil drop motion along a filament due to the parallel air jet blowing. The drop displacement and velocity along the filament are measured. A number of accompanying phenomena are observed. These include drop stick-slip motion and shape oscillations, shedding of a tail along the filament, the tail capillary instability and drop recoil motion. The experimental observations are rationalized in the framework of several simplified models, and the origin of several observed phenomena is elucidated.

In the second part of this work experiments with cross-flow of the surrounding gas relative to the filament with an oil drop on it are conducted with the gas velocity being in the range 7.23 to 22.7 m/s. The Weber number varied from 2 to 40 and the Ohnesorge number was in the range 0.07 to 0.8. The lower and upper critical Weber numbers were introduced to distinguish between the beginning of drop blowing off the filament and the onset of the bag-stamen drop breakup. The range of the Weber number between these two critical values is filled with consequent three types of vibrational breakup: V1 (balloon-like drop being blown off), V2 (a drop on a single stamen being blown off), and V3 (a drop on a double stamen being blown off). At still higher values of the Weber number the bag-stamen breakup can be replaced by the bag type of breakup depending on a slight difference in the blowing speed, or the former and the latter can become intermittent depending on the drop asymmetry relative to the filament. The Weber number/Ohnesorge number plane was delineated into domains

corresponding to different breakup regimes, the statistics of residual liquid portion left on a filament was established and drop hopping across neighboring filaments was studied.

5.2 Experimental materials and methods

5.2.1 Materials

Flexible fused silica capillary tubings of 90 μm in diameter, which were used as filaments, were donated by Polymicro Technologies. Silicone oils of different viscosities (10 cst, 20 cst, 50 cst and 100 cst) were purchased from Clearco Products. Poly (ethylene oxide), PEO, with molecular weight $M_w = 2000$ kDa was supplied by Sigma-Aldrich. The capillary tubings have an outer polyamide coating stable against organic solvents which allows usage in multiple experiments.

5.2.2 Experimental setup

The schematic of the experimental setup used in the present study of blowing drops off a filament due to a parallel gas flow or cross-flow is shown in Fig. 5.1. The setup consists of a high-pressure air line connected to a pressure regulator valve, high pressure tubing and a three-way solenoid valve. The high velocity of air flow issued from the high-pressure air line was reduced inside the high-pressure tubing shown in Fig. 5.1a due to friction losses. The outlet of the three-way solenoid valve was supported on the filament support. The outlet and the filament were coaxial if the air stream should be parallel to the filament. The volumetric flow rate through the outlet was calibrated for different pressure reading of the regulator using a digital flow meter (Omega FMA-5610). Drop motion was recorded using a High speed CCD camera (Phantom Miro 4). A 30G needle was used to deposit silicone oil drops

onto the filament at any desired position. The images recorded by the CCD camera were processed by using ImageJ, Matlab and Adobe Photoshop CS2. An enlarged sketch of the air stream outlet with the coaxial filament is shown in Fig. 5.2.

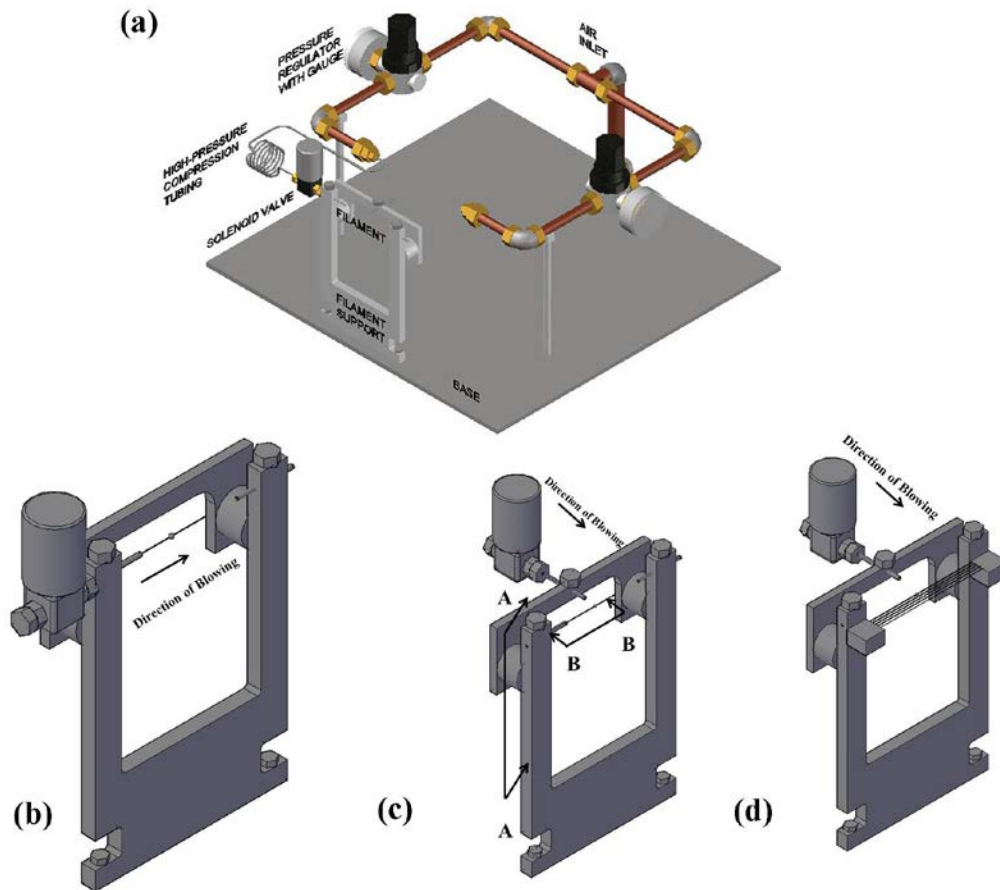


Figure 5.1. Sketch of the experimental setup. (a) Compressed air is supplied through the air inlet, its flow is regulated by a pressure regulator. Then, air flows through the high- pressure tubing, controlled by a three-way solenoid valve (on/off), and is issued out through an outlet which can be co-axial with a thin filament suspended under light tension (cf. Fig. 5.2). The schematics of the filament supports in different cases are shown for: (b) blowing in parallel to the filament; (c) blowing perpendicular to a single filament; and (d) blowing perpendicular to a series of parallel filaments.

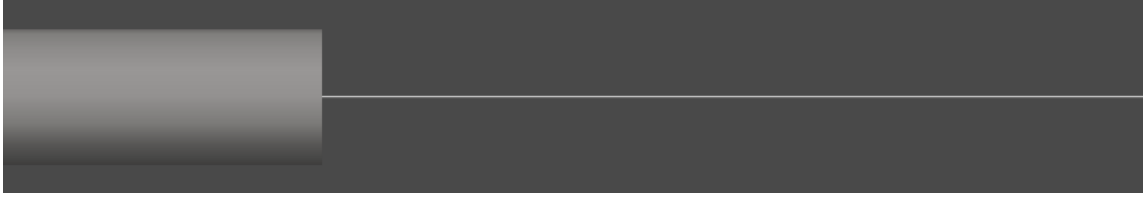


Figure 5.2. An enlarged sketch of a filament co-axial to the air outlet (in the case of blowing parallel to the filament).

After depositing an oil drop onto a filament at a certain position, the solenoid valve was turned on, issuing air with a known velocity. As a result, the drop starts moving along the filament in the case of the parallel blowing, or is blown off the filament in cross-flow. Drop motion and deformation were recorded by the CCD camera at various frame rates (50 fps, 100 fps and 500 fps) depending on the viscosity of the liquid drop and the air velocity.

5.3 Experimental results

Drops on filaments in parallel gas flow are considered first in subsections 5.3.1 – 5.3.3. Then, in subsection 5.3.4 drops on filaments subjected to gas cross-flow are studied, and finally, in subsection 5.3.5 drop hopping from filament to filament is investigated.

In the case of parallel gas flow, a drop on a filament could either be shaped as an axisymmetric barrel, or possess an asymmetric clamshell shape depending on the filament wettability, radius and the drop volume. These factors determine the stability and transition from one drop shape to another [Chou et al. (2011) and Eral et al. (2012)]. To avoid the clamshell drop shape, silicone oil was used as the working fluid, as it sufficiently wets the capillary tubing used as a filament. The drop was placed over the filament using a 30G needle in each trial, which also ensured smaller drop sizes to avoid clamshell shapes.

5.3.1 Dynamics of drop motion along the filament

The experiments were conducted for three pressure levels to sustain air blowing, namely, 5 psi, 10 psi and 15 psi corresponding to the maximum velocity of the air stream at the nozzle exit of 3.3 m/s, 6.5 m/s and 8.9 m/s, respectively. Drops of different volumes were used for each velocity value. The experimentally obtained displacement and velocity of drops were also compared to the theoretically predicted ones using the theory exposed in theoretical section 5.4.1. Figure 5.3 shows the displacement and velocity curves for 100 cst silicone oil drops of three different volume-equivalent radii subjected to a blowing speed of 8.9 m/s (pressure of 15 psi) at the nozzle exit.

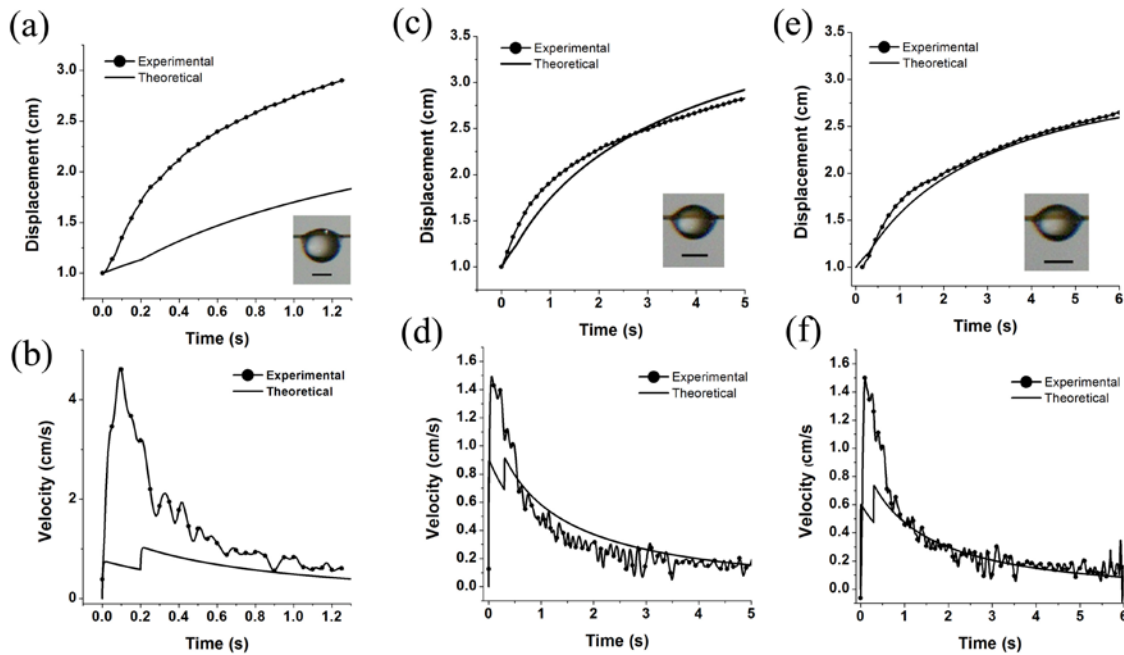


Figure 5.3. Typical displacement and velocity curves for three different drops of 100 cst silicone oil at the blowing speed of 8.9 m/s. (a-b) $R_i = 0.052$ cm, (c-d) $R_i = 0.042$ cm and (e-f) $R_i = 0.040$ cm. The insets show the drops on the filament for the respective trials. In the insets in panels (a), (c) and (e) scale bars are 0.5 mm.

In the case of a larger drop (Fig. 5.3a; $R_i = 0.052$ cm) the theoretical prediction underestimates the displacement, whereas in the case of smaller drops ($R_i = 0.042$ cm and $R_i = 0.040$ cm in Figs. 5.3c and 5.3e) the theoretical prediction is very close to the experimentally observed displacements. In all the cases the drop velocity increases initially at the beginning of motion and then decreases. The maximum velocity of the larger drop is underestimated compared to the experimental one (Fig. 5.3b, 5.3d and 5.3f). The eddies in the air flow and waves sustained by the drops are the primary sources of the fluctuations. Overall, in Figs. 5.3d and 5.3f the experimental velocity profiles follow the same trends as the predicted curves after $t = 0.5$ s.

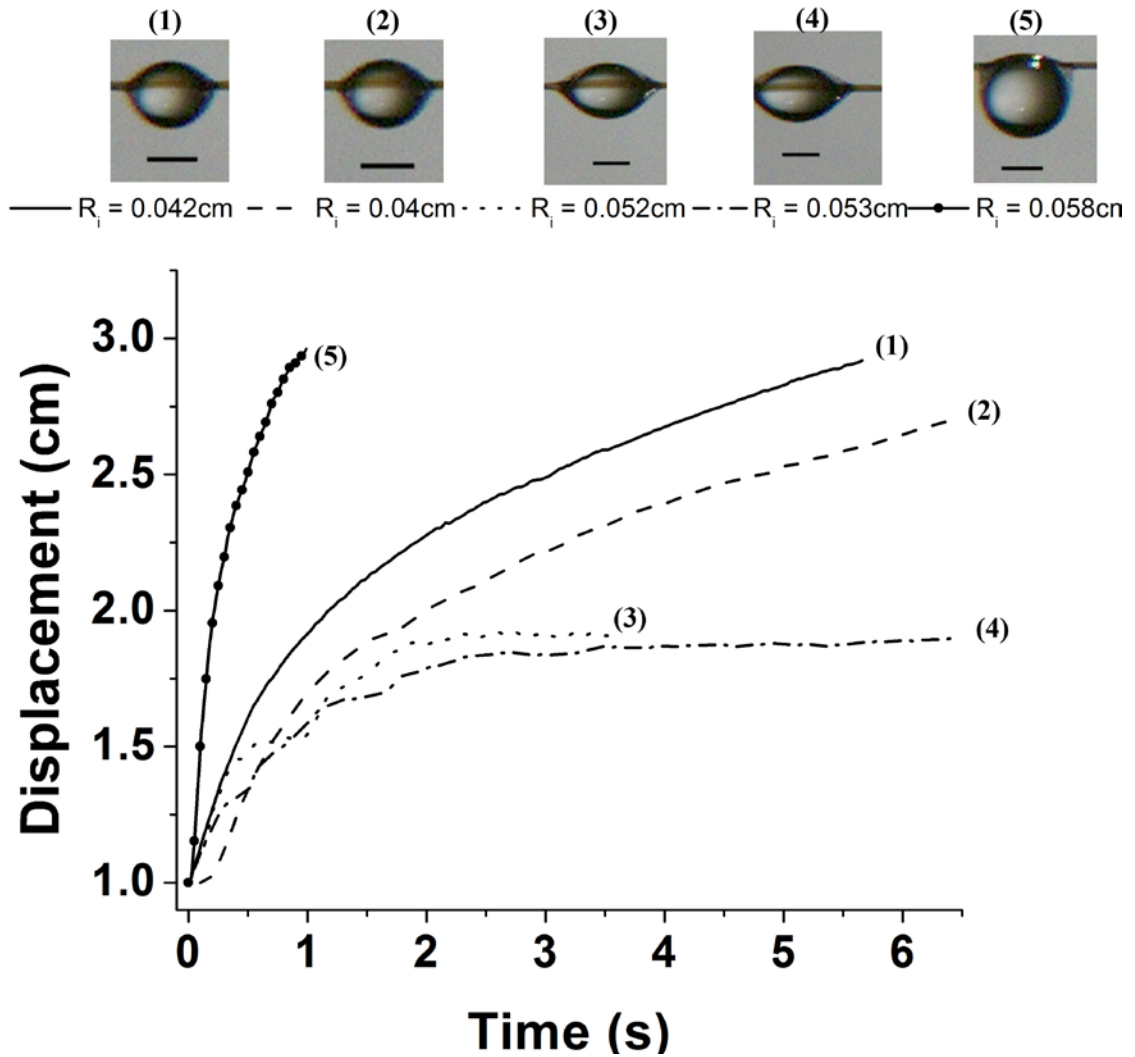


Figure 5.4. Typical experimental data for the displacement curves of different 100 cst silicone drops depicted in the insets which were submitted to the blowing speed of 8.9 m/s. Scale bars, 0.5 mm.

Figure 5.4 shows several typical experimental displacement curves of drops of different diameters and shapes. The drops depicted in the inset in the figure are ordered in the same order as in the legend above it. It is seen from the figure that drops with $R_i = 0.058\text{ cm}$, 0.053 cm and 0.052 cm show strikingly different displacement curves, although they have almost identical volume-equivalent radii R_i . The drop images shown in the inset in Fig. 5.4 could

explain this significant difference. It was observed that for the same volume-equivalent radius (or the same drop volume), drops could acquire different shapes on the filament. The capillary length $\sqrt{\sigma/\rho g}$ for the silicone oil used is ~ 1 mm. Gravity becomes a considerable factor when the drop diameter approaches the capillary length. Prediction of the drop shapes with diameters close or above the capillary length is difficult. On the other hand, smaller drops are similar to an axisymmetric barrel - a relatively easy shape for description. The inset in Fig. 5.4 shows that the drops with radii $R_i = 0.058$ cm, $R_i = 0.052$ cm and $R_i = 0.053$ cm possess different shapes on the filament which is the reason for the difference in their displacement curves.

Theoretical section 5.4.1 describes the model used to predict drop motion in Fig. 5.3. In brief, drop motion along the filament is determined by the following four forces: form drag, skin friction imposed by the air flow, force associated with the resistance due to dissipation close to the contact line, as well as viscous friction on the filament (cf. theoretical model 5.4.1). The drag coefficient, which includes the effects of both form drag and skin friction, was taken the same as for a volume-equivalent sphere. It is emphasized that this assumption can be a source of an inaccuracy for smaller drops since they are significantly deformed in the vicinity of the contact lines due to a small contact angle (see the inset in Fig. 5.4). Moreover, the viscous friction between the drop and the filament was approximated for a cylindrical body pulled over a filament. As the drop moves along the filament, a thin film is formed on the downstream side of the drop. This tail formation results in an unaccounted loss of drop volume which further reduces its velocity. It is believed that the above-mentioned approximations resulted in the deviations of the theoretical results from the experimental data in Fig. 5.3.

Similar experiments were conducted with the same fluid and filament at a reduced blowing pressure of 10 psi which corresponds to air velocity of 6.5 m/s at the nozzle exit. Figure 5.5 shows the displacement and velocity curves as a function of time for three drops of different diameters. The predicted results are also shown in Fig. 5.5. It was found that for drop radii $R_i = 0.05$ cm and $R_i = 0.047$ cm the theoretical predictions underestimate the displacements measured experimentally, whereas for the drop radius $R_i = 0.038$ cm the theoretical prediction overestimates the experimental results. In addition to the discrepancy sources discussed above, the approximation for the force associated with the resistance to the contact line motion might lead to some inaccuracies. Figure 5.6 shows the snapshots of a drop moving along the filament due to air blowing at speed of 6.5 m/s at several time moments. The change in the contact angle at the contact line on both sides of the droplet is evident from the figure. The value of the parameter K in Eq. (5.7) in theoretical section 5.4.1 responsible for the resistance due to the presence of the contact line was determined in each experiment using the contact angle values measured from the two first images of drops when they were just subjected to air blowing. It is evident from Fig. 5.6b that drop configuration near the contact line can change significantly as blowing begins. Only after such a drop moves to some distance, its equilibrium static shape is restored. This effectively means that the parameter K is changing. The magnitude of K was reduced by 30% compared to its initial value when drops acquired steady-state configurations in motion. This caused the discontinuity seen in the theoretically predicted velocity distributions seen in Figs. 5.3 and 5.5.

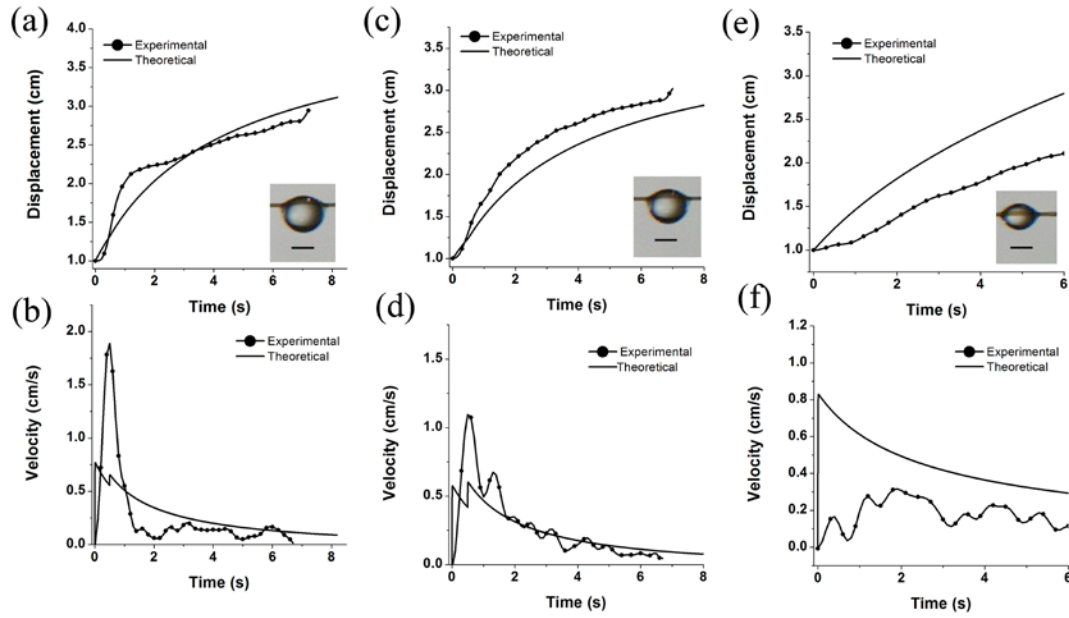


Figure 5.5. Displacement and velocity curves for three different drops of 100 cst silicone oil at the blowing speed of 6.5 m/s. (a-b) $R_i = 0.05$ cm; (c-d) $R_i = 0.047$ cm; (e-f) $R_i = 0.038$ cm. Scale bars in the insets in panels (a), (c) and (e) are 0.5 mm.

The drop with the volume-equivalent radius $R_i = 0.038$ cm (Fig. 5.6a) is deformed at the contact line. A low contact angle makes the drop more streamlined, and as a result, the form drag acting on it is lower than it is expected for the volume-equivalent spherical configuration. This result in an overestimate of the displacement and velocity of smaller drops with low contact angle in the numerical simulations compared to the experimental data (Fig. 5.5f).

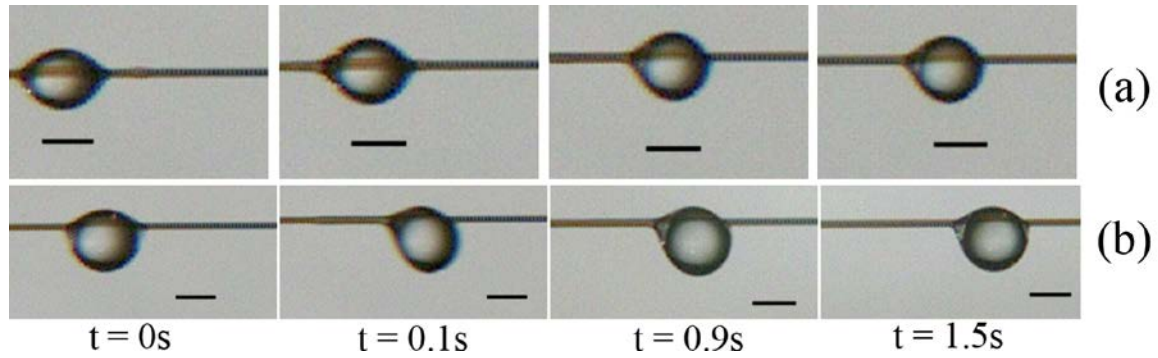


Figure 5.6. Snapshots of 100 cst silicone oil drop with (a) $R_i = 0.038$ cm, and (b) $R_i = 0.047$ cm moving along the filament at different time moments. The drops are moving due to air blowing with the speed of 6.5 m/s. Scale bars, 0.5 mm.

The measured displacement curves for drops of different volume-equivalent diameters subjected to the same air blowing velocity of 6.5 m/s are shown in Fig. 5.7. Two drops have the identical diameters ($R_i=0.047$ cm) but their displacement scenarios are absolutely different, as Fig. 5.7 shows. The difference in the displacement curves stems from the difference in the contact angles of the upper and lower parts of these drops on the filament. It appears that the same liquid on the same filament can form multiple drop shapes, with different asymmetry of the upper and lower part relative to the filament. Drops with identical radii but a larger difference in the contact angle (more suspended, barrel-shaped drops) move faster than those with smaller difference in the contact angle.

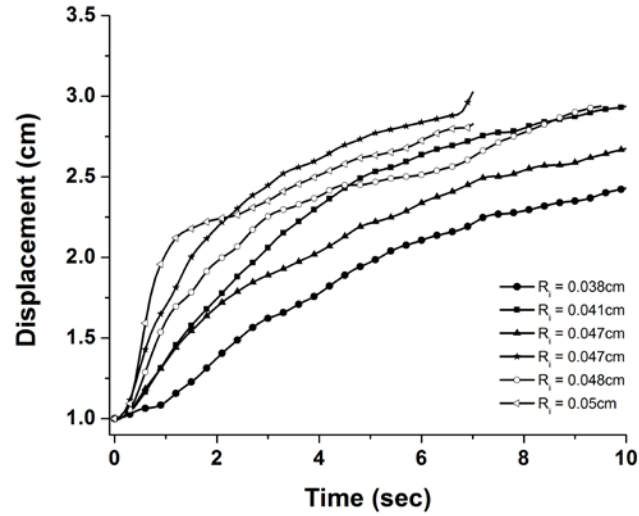


Figure 5.7. Measured displacement curves of 100 cst silicone oil drops subjected to the blowing speed of 6.5 m/s.

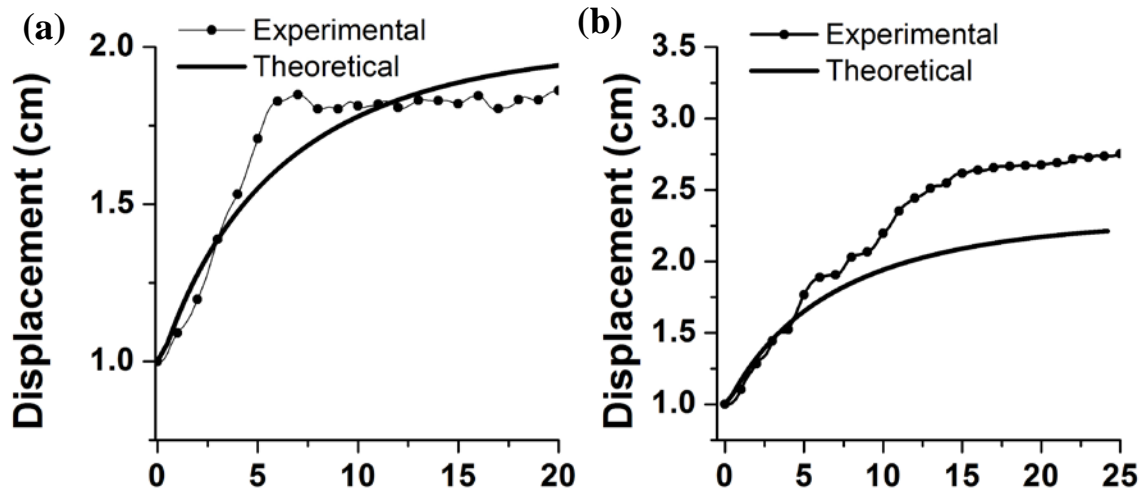


Figure 5.8. Displacement curves for two 100 cst silicone oil drops of different size at the blowing speed of 3.3 m/s. (a) $R_i = 0.05$ cm: in the range $5 \text{ s} < t < 20 \text{ s}$ the drop moves in a stick-slip manner; (b) $R_i = 0.055$ cm: in the range $2.5 \text{ s} < t < 13 \text{ s}$ the drop moves in a stick-slip manner.

At the lowest air blowing velocity of 3.3 m/s corresponding to 5 psi, it was observed that the predictions underestimated the measured displacement (Fig. 5.8b). In this case the stick-slip motion arises very frequently along with continuous drop oscillations (back and forth) as shown in Fig. 5.8a and 5.8b.

Figure 5.9 compares the maximum drop velocities obtained experimentally and predicted theoretically under different blowing speeds. The velocity magnitude decreases as the blowing speed decreases. The theoretically predicted values of the maximum drop velocity in Fig. 5.9 are in good agreement with the experimental data except the deviation found for very small and very large drops, as discussed before.

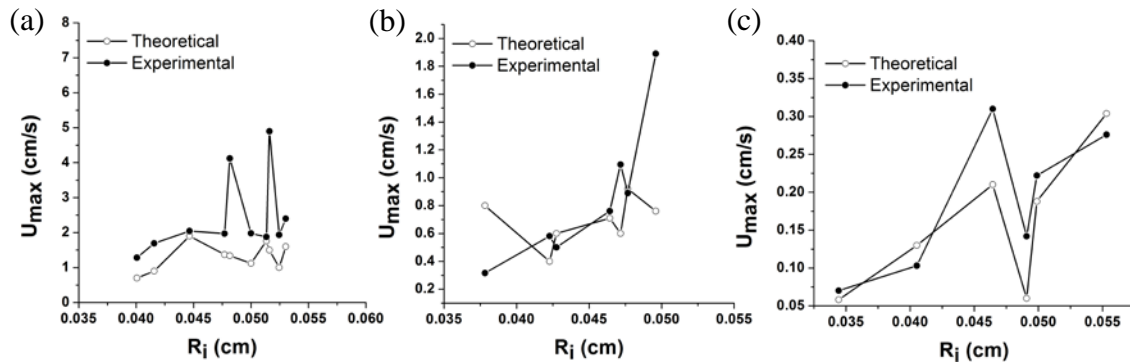


Figure 5.9. Comparison of the maximum velocity of the 100 cst silicone oil drops obtained experimentally and predicted theoretically for different drop radii and different blowing speeds: (a) $V_{\max} = 8.9$ m/s, (b) $V_{\max} = 6.5$ m/s and (c) $V_{\max} = 3.3$ m/s.

The experiments similar to those described above for 100 cst oil drops were also conducted with 50 cst and 20 cst silicone oil drops at identical blowing speeds to evaluate the effect of viscosity on drop motion along the filament. Figure 5.10 shows some typical displacement and velocity curves for three different 50 cst silicone oil drops. In the case of

larger drops (Figs. 5.10a and 5.10b) the theoretical predictions of the displacement overestimate the experimental data after $t = 0.6$ s due to the loss of mass from the drop as a thick tail on the filament forms. In the case of moderate size drops (Figs. 5.10c and 5.10d and Figs. 5.10e and 5.10f) the theoretical predictions are in good agreement with the experimental observations. The displacement and velocity curves of two different 50 cst drops at blowing speed of 6.5 m/s are shown in Fig. 5.11. The experimental displacement curves are underestimated due to the simplified approximations used in the theoretical simulations as discussed above.

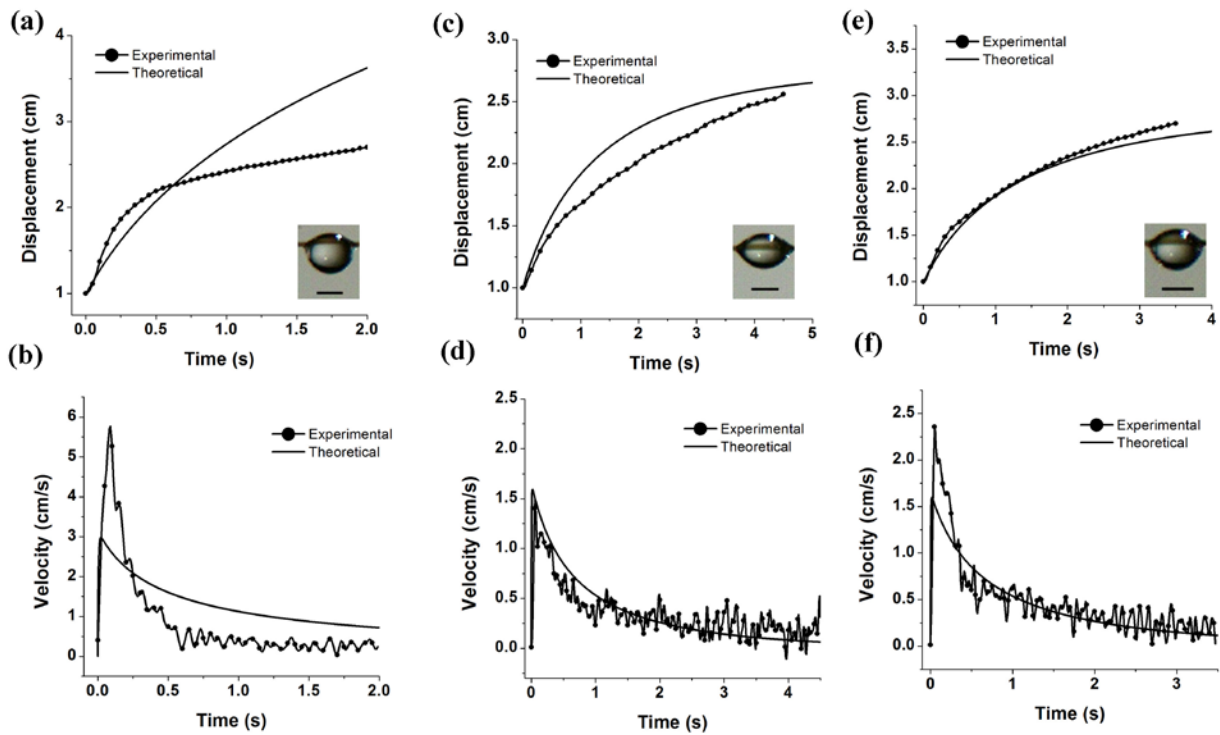


Figure 5.10. Typical displacement and velocity curves for three 50 cst silicone oil drops of different sizes at the blowing speed of 8.9 m/s. (a and b) $Ri = 0.045$ cm, (c and d) $Ri = 0.042$ cm, and (e and f) $Ri = 0.040$ cm. The insets show the drops on the filament. The scale bars are 0.5 mm.

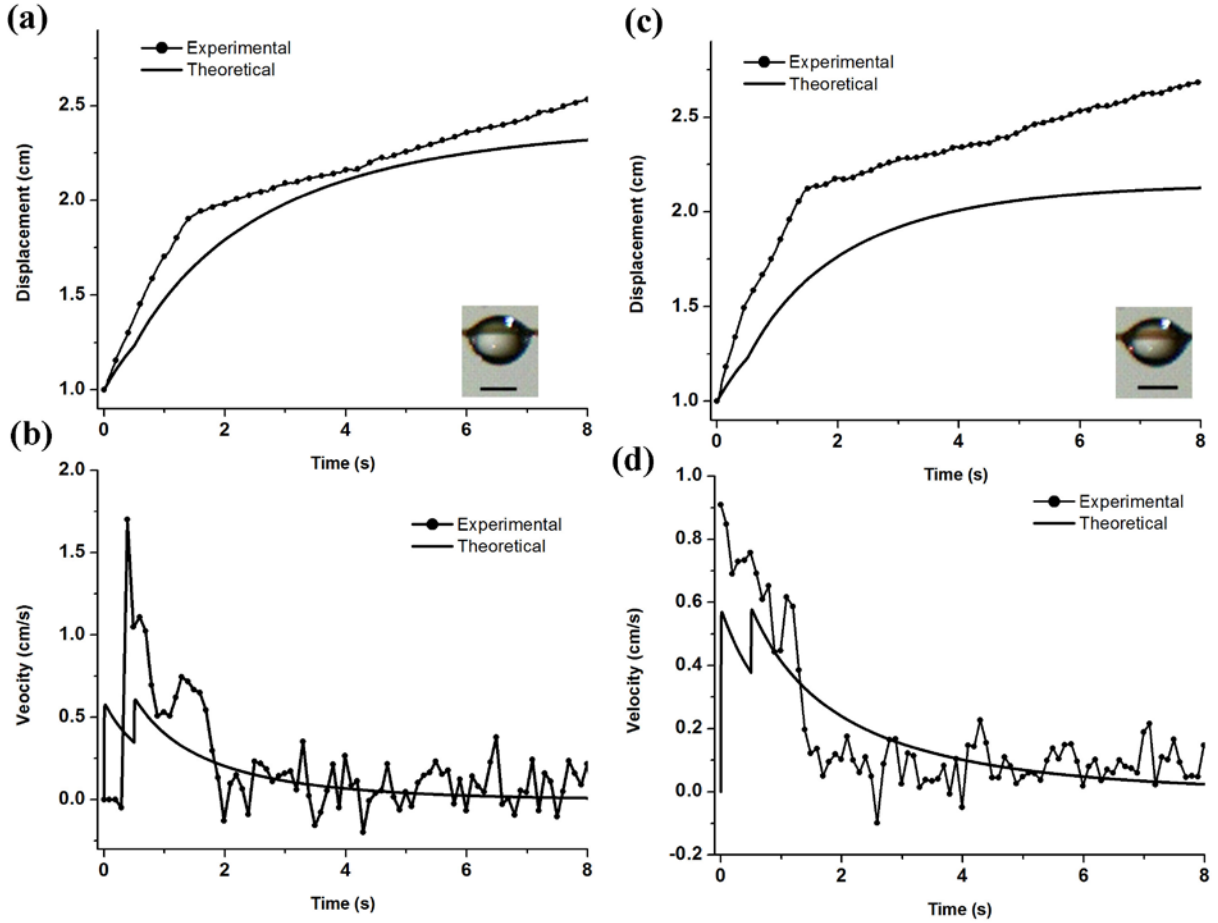


Figure 5.11. Typical displacement and velocity curves for two 50 cst silicone oil drops of different sizes at the blowing speed of 6.5 m/s. (a and b) $R_i = 0.041$ cm, and (c and d) $R_i = 0.037$ cm. The insets show the drops on the filament. The scale bars are 0.5 mm.

Then, silicone oil of a still lower viscosity of 20 cst was used. Drops were subjected to air blowing speed of 8.9 m/s and 6.5 m/s as before, and the results are shown in Figs. 5.12 and 5.13 and Fig. 5.14. In this case for larger drops (which hang under the filament) the theoretical prediction underestimates the data. On the other hand, for the barrel-shaped drops the theoretical predictions match the experimental observations for a few seconds, albeit deviate later on. The drop configurations become even more transient at the beginning of

blowing onto these low-viscosity drops compared to the higher-viscosity ones discussed before. Figure 5.14 shows several snapshots of 20 cst silicone oil drops of $R_i = 0.045$ cm at different moments after the beginning of blowing. It is seen that the initial deformation of the drop is very significant at $t = 0.01$ s, the fact which was accounted for in the evaluation of the value of K , as discussed above. The drop shape variation practically ceases at latter times, at $t = 0.15$ s to $t = 0.65$ s. It is emphasized that the theoretical predictions begin to deviate from the experimental data from the moment when the parameter K would start changing significantly, and so the value of K was reduced by 30% from its initial value.

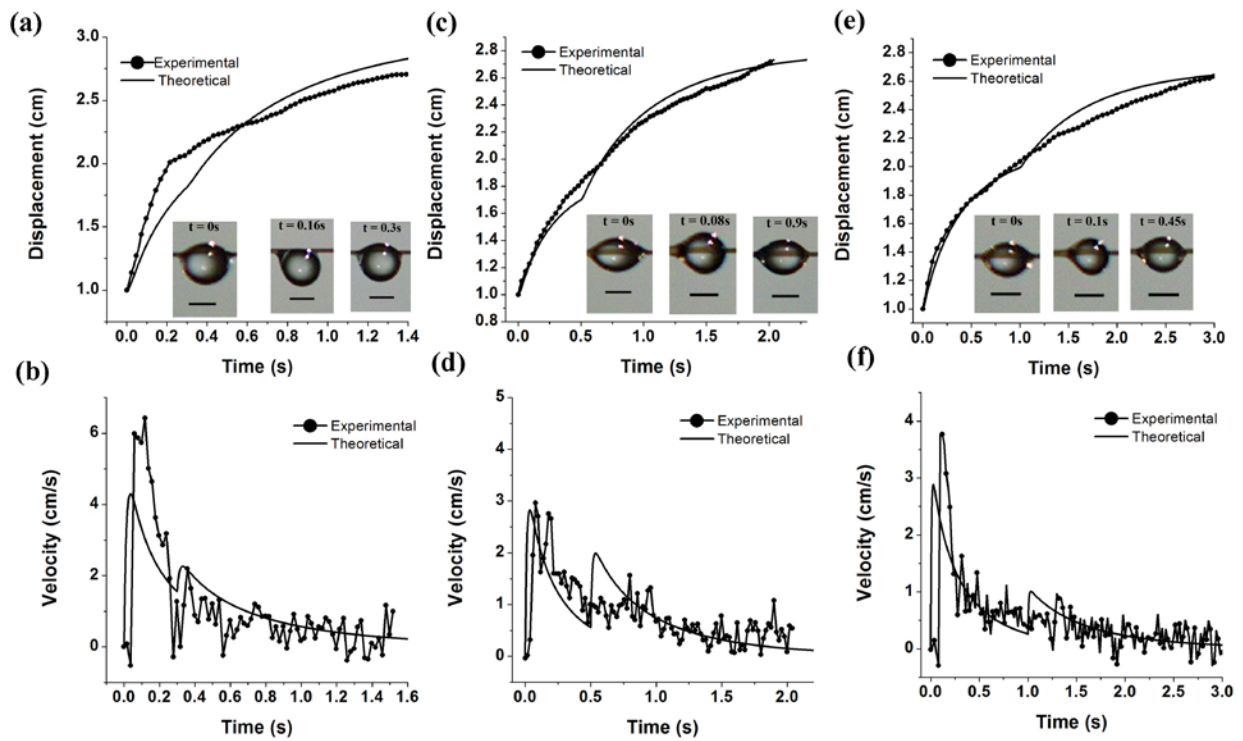


Figure 5.12. Typical displacement and velocity curves for three 20 cst silicone oil drops of different sizes at the blowing speed of 8.9 m/s. (a and b) $R_i = 0.047$ cm, (c and d) $R_i = 0.045$ cm, and (e and f) $R_i = 0.038$ cm. The insets show several snapshots of the drops on the filament; the scale bars are 0.5 mm.

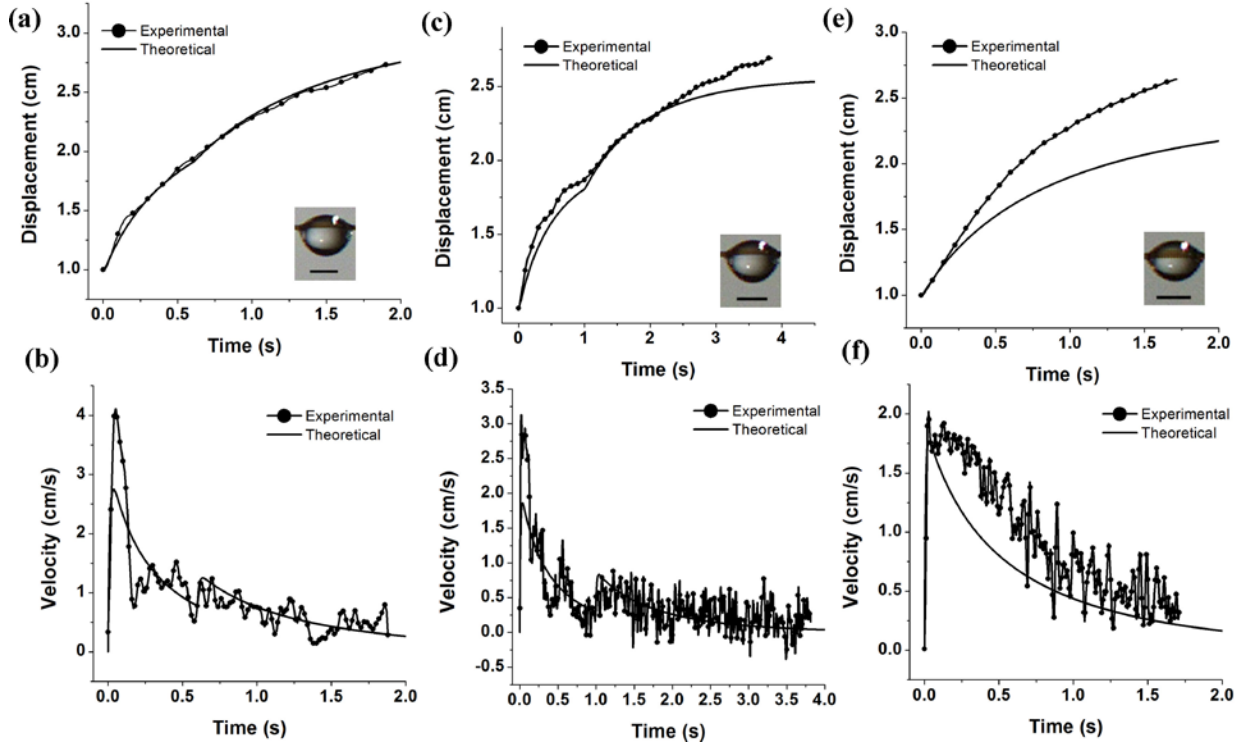


Figure 5.13. Displacement and velocity curves for three 20 cst silicone oil drops of different sizes at the blowing speed of 6.5 m/s. (a and b) $R_i = 0.044$ cm, (c and d) $R_i = 0.041$ cm, and (e and f) $R_i = 0.037$ cm. The insets show the drops on the filament. Scale bars are 0.5 mm.

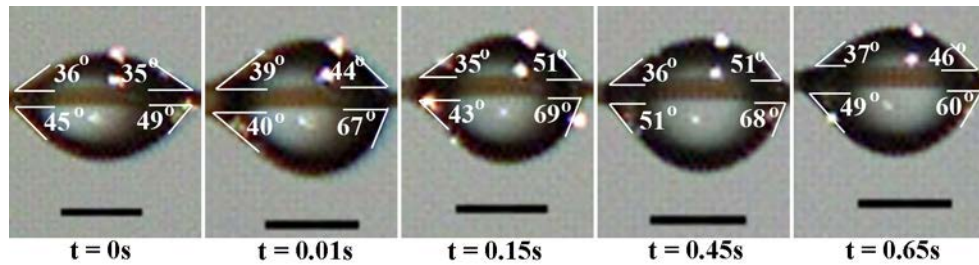


Figure 5.14. Snapshots of a 20 cst silicone oil drop of $R_i = 0.045$ cm on a filament at different time moments. The drop is moving due to air blowing at the speed of 8.9 m/s. Scale bars are 0.5 mm.

5.3.2 Instability of thin film and recoil motion of drops along the filament

As silicone oil drops move along the filament, a thin film is formed behind them. This situation is kindred to the classical withdrawal problem [Quere (1999) and Levich (1962)]. Thin liquid films formed on the filament are unstable as the surface tends to minimize the surface area, which results in film breakup into several droplets. The formation of the thin film on the filament is dependent on the capillary number and the equilibrium contact angle of the drop at rest on the filament. A theoretical estimate for the film formation is given in theoretical section 5.4.2. Equation (5.22) in theoretical section 5.4.2 yields the dimensionless velocity magnitude (the capillary number Ca) at which film formation is expected. Table 5.1 lists the values of the capillary number (the average values over several trials) measured for drops of different viscosity of silicone oil at different blowing speeds. In Table 5.1 the initial maximum velocity of the drop motion was used to calculate the capillary number. For typical values of the equilibrium contact angle, say, 45° , the right-hand side of Eq. (5.22) in theoretical section 5.4.2 is $\sim 0.7\varepsilon$, where ε is a dimensionless factor. Then, the value of ε should be of the order of 0.014, to have the inequality (5.22) fulfilled, since it was found experimentally that for all the cases described earlier the drops always formed tails on the filament. As drops move further from the nozzle exit, their velocity decreases significantly, since the blowing velocity diminishes due to viscous entrainment of the surrounding gas and friction over the filament and the drop surface, and no tail is formed any more. Correspondingly, the inequality in Eq. (5.22) theoretical section 5.4.2 stops holding.

Table 5.1 The average (over several trials) values of the capillary number of different silicone oil drops at various blowing speeds.

Viscosity of silicone oil	Ca ($V_{\max} = 8.9 \text{ m/s}$)	Ca ($V_{\max} = 6.5 \text{ m/s}$)	Ca ($V_{\max} = 3.3 \text{ m/s}$)
100 cst	0.14	0.04	0.01
50 cst	0.09	0.04	0.01
20 cst	0.06	0.04	0.01

Once the film is formed, it is subjected to capillary instability due to surface tension and breaks into smaller droplets. The thickness of the film formed on the filament could be theoretically estimated from the LLD theory according to Eq. (5.23) in theoretical section 5.4.2. For the typical values of the oil viscosity $\mu = 0.2 \text{ g/cm} \cdot \text{s}$, surface tension $\sigma = 20.9 \text{ g/s}^2$, the drop velocity relative to the filament $U = 4 \text{ cm/s}$, and the filament radius $a_f = 0.0045 \text{ cm}$, the film thickness calculated according to Eq. (5.23) is $\delta \sim 7 \text{ } \mu\text{m}$. It was also found experimentally using image processing that the thickness of the film formed on the filament was $\delta \sim 6.3 \text{ } \mu\text{m}$, which is in good agreement with the prediction. The film thickness increases with the liquid viscosity μ and drop velocity U . For $\mu = 1.0 \text{ g/cm} \cdot \text{s}$, $\sigma = 20.9 \text{ g/s}^2$, $U = 2 \text{ cm/s}$, and $a_f = 0.0045 \text{ cm}$, the theoretical estimate yields $\delta \sim 13 \text{ } \mu\text{m}$. The experimentally observed thickness of the thin film formed under these conditions was $\delta \sim 12 \text{ } \mu\text{m}$, also in close agreement with the prediction.

The wavelength of the fastest growing disturbance responsible for the instability of the thin film is $\lambda = 2\pi\sqrt{2}a_f$, [Yarin et al. (1993)] and the characteristic time of perturbation growth is predicted in Eq. (5.24) in theoretical section 5.4.2. Figure 5.15 illustrates the tail

instability and perturbation growth as a drop moves along the filament. At $t = 0.9$ s the growing perturbations become fully visible. As the drop moves further from the nozzle exit, its velocity decreases, which in turn, decreases the film thickness on the filament. If the drop velocity reduces to such an extent that the inequality in Eq. (5.22) of theoretical section 5.4.2 does not hold anymore, no film is observed. The film thickness decreases at $t = 3.9$ s and $t = 5.9$ s in Fig. 11 The wavelength of the fastest growing perturbation was theoretically found to be $400\text{ }\mu\text{m}$, whereas the experimentally measured distance between two droplets formed due to the film instability was $320\text{ }\mu\text{m}$ which is fairly close to the predicted value.

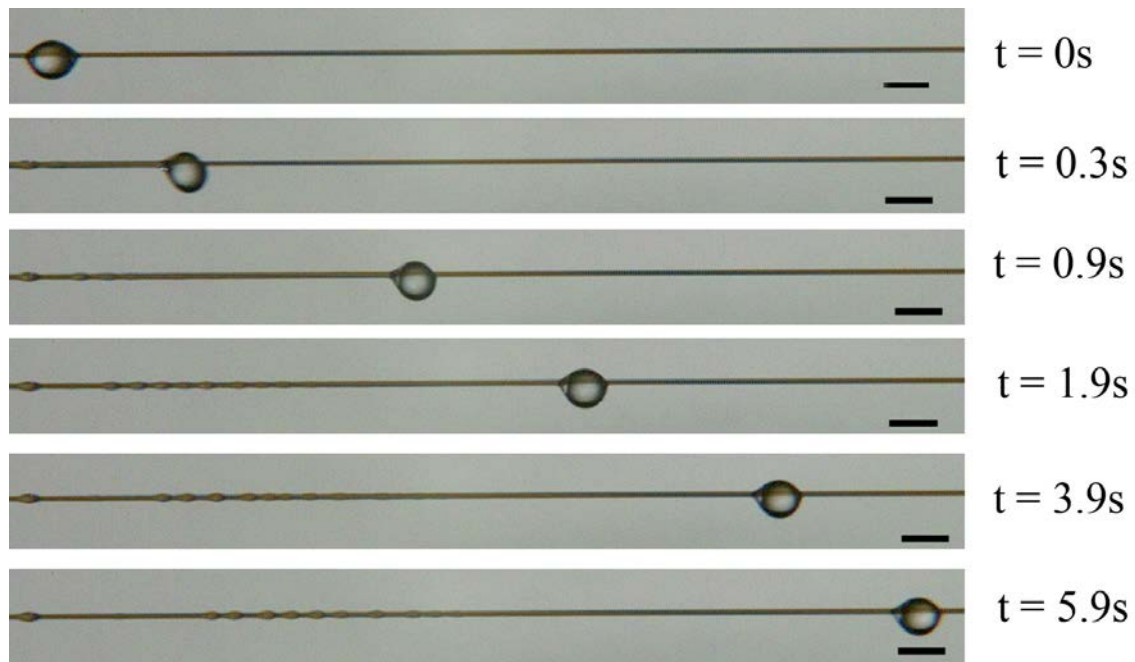


Figure 5.15. Development of the capillary instability of thin liquid film withdrawn from a drop moving along the filament. The drop of 100 cst silicone oil is subjected to blowing at the speed of 8.9 m/s at the nozzle exit. Blowing is from left to right. Scale bars are 0.5 mm .

As the film thickness decreases, the characteristic time of perturbation growth should increase according to Eq. (5.24) in theoretical section 5.4.2. At the beginning of the drop motion the film is comparatively thick, since the motion is fast. As a result, a thick tail is formed and perturbations grow fast and are visible in Fig. 5.15. As the drop is moving further over the filament, its velocity is decreasing, the tail becomes thinner, and does not develop visible perturbations as in Fig. 5.15.

Thin films formed on the filament behind the moving drops remain attached to them until the capillary instability fully develops. Surface tension pulls the drops back, against the direction of their motion. If air blowing has been stopped and a thin film on the filament still remains intact and attached to the drop, the latter is pulled back, and the recoil motion of the drop sets in. Figure 5.16a shows a drop during such recoil motion (from right to left). The drop was subjected to air blowing from left to right at a speed of 5.3 m/s, and the blowing was ceased after the drop moved away from the nozzle. During the recoil motion viscous friction in the droplet and its tail dissipate kinetic energy. It is seen in Fig. 5.16a that at $t = 1.2$ s after the cessation of blowing, the drop is moving from right to left and stops at $t = 5.2$ s when the thin film attached to it becomes to be visibly unstable and breaks into tiny droplets. The film thickness decreases as the drop moves to a larger distance from the nozzle and the pulling force also decreases.

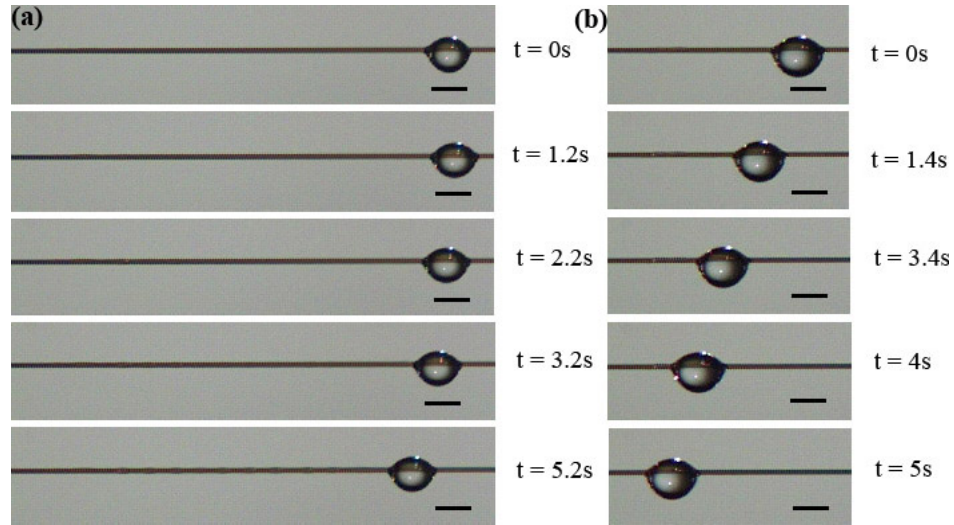


Figure 5.16. (a) Recoil motion of a 20 cst silicone oil drop after the cessation of air blowing. (b) Recoil motion of a 20 cst silicone oil drop. Air blowing was ceased earlier than in panel (a), and the drop recoils to a further distance, closer towards the nozzle. Scale bars, 1mm; $t=0$ corresponds to the moments of the cessation of air blowing.

Another set of recoil experiments was done, in which a drop was allowed moving to a shorter distance than in Fig. 5.16a before the cessation of air blowing. The speed of blowing and the initial position of the drop on the filament in Fig. 5.16b were the same as in Fig. 5.16a. As the thickness of the film attached to the drop in Fig. 5.16b is larger than that in Fig. 5.16a, the pulling force is also stronger and the drop recoils to a larger distance. The drop recoils back towards its starting point before the film completely breaks into several tiny droplets.

The forces involved in the recoil motion of drops are the pulling force due to the surface tension, viscous friction acting between the drop and the filament, as well as the viscous friction between the thin film and the filament. A theoretical estimate of the recoil velocity U_r and the distance travelled during recoil is obtained accounting for these forces, as

detailed in theoretical section 5.4.2. The recoil velocity is found from Eq. (5.25) in theoretical section 5.4.2. For the typical values of the parameters, say, $\mu = 0.3 \text{ g/cm}\cdot\text{s}$, $\sigma = 20.9 \text{ g/s}^2$, $a_f = 45 \text{ }\mu\text{m}$, and $R_i = 0.05 \text{ cm}$, the film thickness is calculated using Eq. (5.23) in theoretical section 5.4.2 taking the average drop velocity at the last stage before the cessation of blowing as 0.5 cm/s . The thickness is calculated as $\delta \sim 1.8 \text{ }\mu\text{m}$. The wavelength of the fastest growing perturbation is calculated as $\lambda \sim 0.04 \text{ cm}$. Using these values, the recoil velocity U_r is found to be 0.225 cm/s . The comparison of the predicted displacements of several 20 cst silicone oil drops during the recoil with the corresponding experimental data is shown in Fig. 5.17.

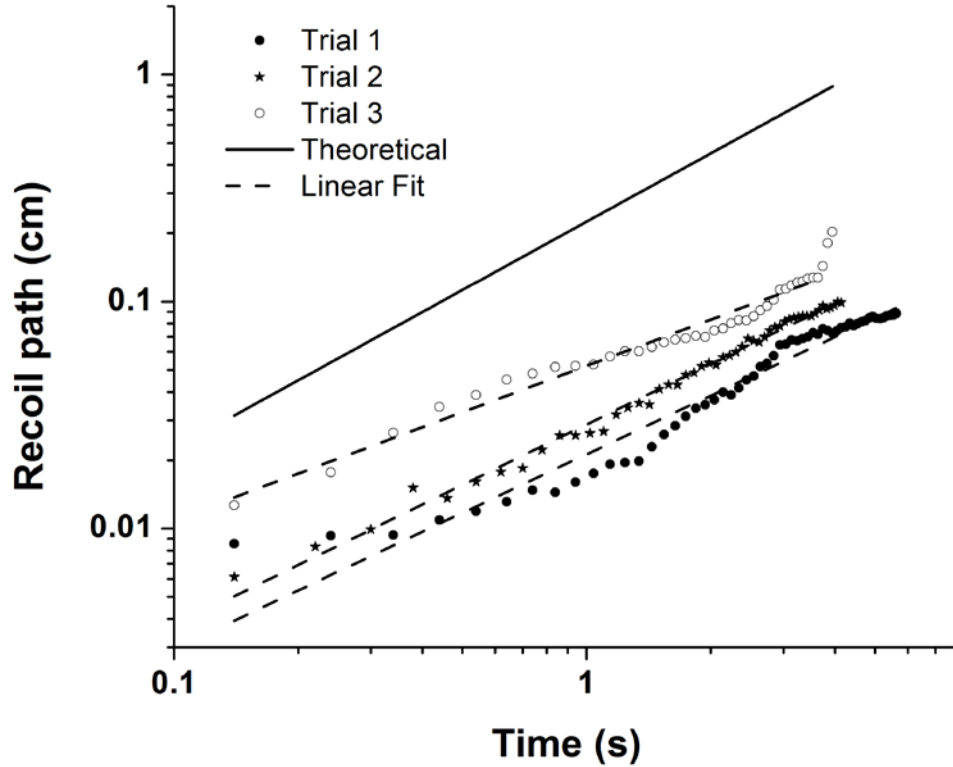


Figure 5.17. Recoil motion of three different 20 cst silicone oil drops along the filament. The experimental data are traced with dashed lines, the theoretical prediction is shown by solid line. The slopes of the linear fit to the recoil path were: 0.017 cm/s in trial 1, 0.024 cm/s in trial 2 and 0.03 cm/s in trial 3.

5.3.3 Stick-slip motion of drops on filament

The stick-slip motion of silicone oil drops was observed in some cases, predominantly at low blowing velocity of 3.3 m/s, as shown in Fig. 5.8b. In addition to the stick-slip motion, drop oscillations were also observed at some moments. The contact angle hysteresis of the drops on filaments is assumed to be one of the factors responsible for such stick-slip motion [Sharp et al. (2011); Mettu and Chaudhury (2011)]. To investigate the factors responsible for the drop oscillations, the blowing air flow field was visualized using smoke photography.

Figure 5.18 shows the instantaneous smoke pattern in air at the blowing speed of 3.3 m/s. It can be seen that the flow is laminar for a few centimeters from the nozzle, and after that it becomes intermittent, as transition to turbulence sets in. The large eddies emerging due to the flow intermittency contribute to drop oscillations.

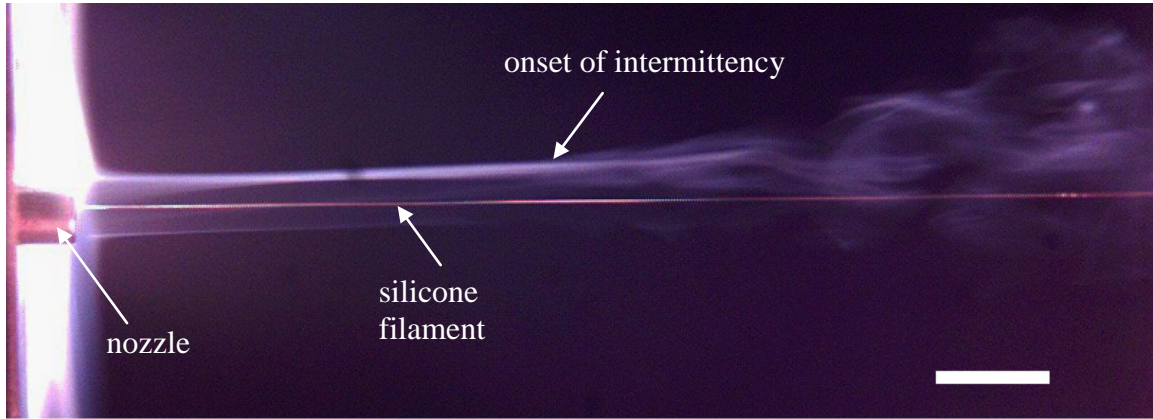


Figure 5.18. An instantaneous flow pattern in air issued from the nozzle at 3.3 m/s. The intermittency sets in at a distance of 2.7 cm from the nozzle. Flow visualization is done with smoke. Scale bar, 5mm.

A water droplet placed on the filament at a distance of 4.5 cm from the nozzle exit was subjected to blowing with the speed of 7.2 m/s at the nozzle exit. The lateral displacement of the drop apex was recorded at a sampling rate of 1 kHz, and the results are shown in Fig. 5.19a. The lateral displacement was processed using the Fast Fourier Transform (FFT). Note that even though the sampling was done at 1 kHz, it can only resolve frequencies up to 500 Hz. The corresponding absolute values of the Fourier coefficients obtained from the lateral displacement of the water drop apex in this experiment are shown in Fig. 5.19b. The negligibly small coefficient magnitudes beyond 200 Hz ensure the absence of important

frequencies beyond that range. The large eddies in air have sizes of the order of the distance from the nozzle exit to the drop, about $L = 4$ cm, and the maximum velocity at the nozzle exit V_0 is 7.2 m/s. Then, the corresponding frequency $\omega = V_0/L$ is 180 Hz. This frequency is of the same order of magnitude as the one observed experimentally (e.g. in the case shown in Fig. 5.19b the resonant frequency is of about 90 Hz).

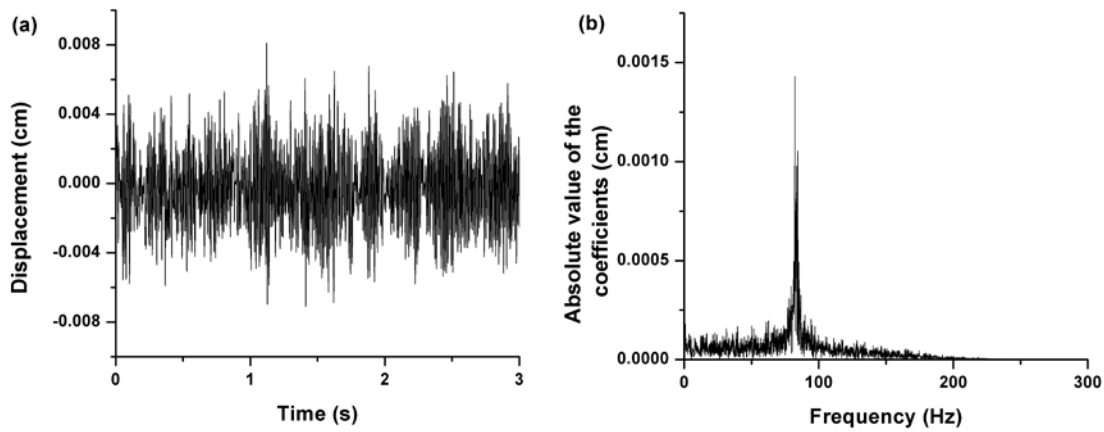


Figure 5.19. (a) Oscillations in the lateral displacement of water drop apex, and (b) the corresponding Fourier coefficients. The drop is positioned at a distance of 4.5 cm from the nozzle exit and the air blowing speed is 7.2 m/s. The standard deviation of the apex displacement measurement is about 0.0004 cm, i.e. close to 10% of the measured amplitude.

The values of the Reynolds number Re of the air flow were evaluated as $Re(x) = \rho_a V(x) 2R_i / \mu_a$, where $V(x)$ is the air velocity at the drop position, $2R_i$ is the volume-equivalent diameter of the drop, ρ_a and μ_a are the air density and dynamic viscosity, respectively. The values of Re were less than 200 in all the cases. No vortex shedding in flows past the spheres occurs at such low values of Re [Taneda (1956); Sakamoto and Haniu (1990); Kim and Durbin (1988)]. That means that the oscillations were merely caused by the

large eddies of the intermittent air flow. A comparison between the experimentally observed frequency of drop oscillations and the frequency of large eddies found in different experiments is shown in Fig. 5.20. Both frequencies are of the same order of magnitude, albeit the latter is typically higher than the former. Overall, the large eddies associated with air flow intermittency, along with the contact angle hysteresis, are responsible for the lateral oscillations of the drop and stick-slip motion. Therefore, the stick-slip motion of drops is always accompanied by the lateral oscillations of their apex.

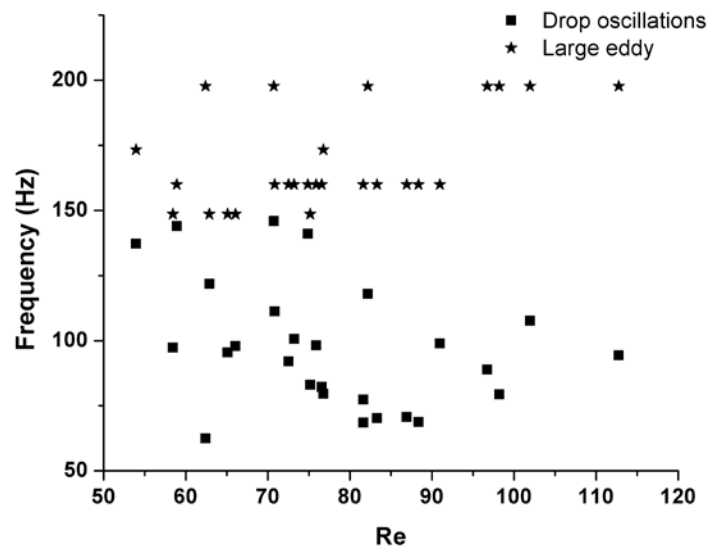


Figure 5.20. Frequency of lateral oscillations of water drop at different Reynolds numbers.

5.3.4 Drops on filament in cross-flow

The experiments were conducted with silicone oil drops of different viscosities (10 cst, 20 cst, 50 cst, and 100 cst) on filaments aligned perpendicularly to the air flow. The gas jet was issued at different pressures (5 psi to 30 psi in steps of 5 psi). The corresponding exit

velocity range was from 7.23 m/s to 22.7 m/s. The distance between the filament and the nozzle exit was kept constant at 1 cm. Silicone oil drops were placed on the filament and care was taken to keep them approximately against the nozzle center. Figure 5.21 shows the drop view with respect to the nozzle and filament from two different directions.

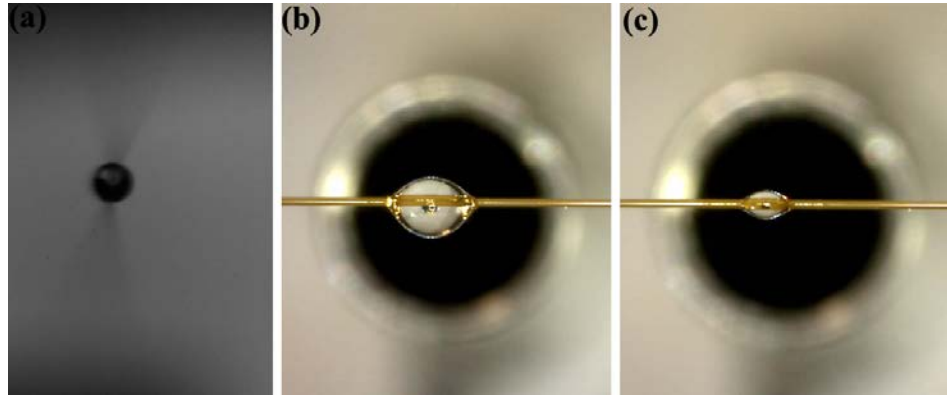


Figure 5.21. Position of the drop with respect to the filament and the nozzle exit. Panel (a) corresponds to the viewing direction A-A in Fig. 5.1c, and panels (b) and (c) correspond to the viewing direction B-B in Fig. 5.1c. The position and volume of the drop on the filament before and after blowing is illustrated in panels (c) and (d), respectively.

The breakup modes of drops located on a filament in gas cross-flow depend on the maximum air velocity at the nozzle exit. Different breakup modes were observed at different air velocities. At low air velocity a vibrational type breakup was observed. The vibrational type breakup refers to drop disintegration into large fragments comparable to the initial drop size. Three different types of the vibrational breakup were observed and referred to as V1, V2 and V3. Figure 5.22 shows the vibrational type breakup of type V1 of a silicone oil drop at $We = 2.8$ and $Oh = 0.07$. The initiation of the breakup process in the case of a drop on a filament is different from that of a freely falling or levitating one. The drop on a filament is

sometimes asymmetric depending on its volume and the contact angle. The friction forces acting at the contact surface between the drop and filament tend to counteract to the drop distortions due to the aerodynamic forces. Moreover, the drop on the filament is free to reshape itself still being attached to the surface. The initial configuration of the drop in Fig. 5.22 corresponds to $t = 0$ ms. As air blowing begins, the drop reshapes itself and becomes aligned along the direction of blowing with the shape resembling that of an inflated balloon as is seen in Fig. 5.22 at $t = 3$ ms and $t = 7.8$ ms. At low blowing velocities the drop does not immediately break up and is subjected to oscillations at its lowest eigenfrequency presumably associated with the inertia and surface tension. The theoretical eigenfrequency of drop oscillations is, thus evaluated as $f = (1/2\pi)(8\sigma/\rho R_i^3)^{1/2}$ [Landau and Lifshitz (1987)] and is compared to the measured one in Table 5.2. Then, practically the entire drop is blown off the filament at $t = 11.4$ ms. The effect of surface tension is predominant in the low viscosity cases, whereas the viscosity becomes the dominant factor for liquids of higher viscosity. After being blown off, the drop is swept by the gas flow with practically no further change in its shape, since the capillary waves are damped very rapidly ($t=25.2$ ms in Fig. 5.22).

Table 5.2 Oscillation frequencies of silicone oil and water drops in the direction of blowing. The experimental frequencies are an average taken over several trials.

Viscosity	10 cst	20 cst	50 cst	100 cst	Water
Experimental (Hz)	132.2	153.6	97	No oscillations	208
Theoretical (Hz)	184	184	184	184	339

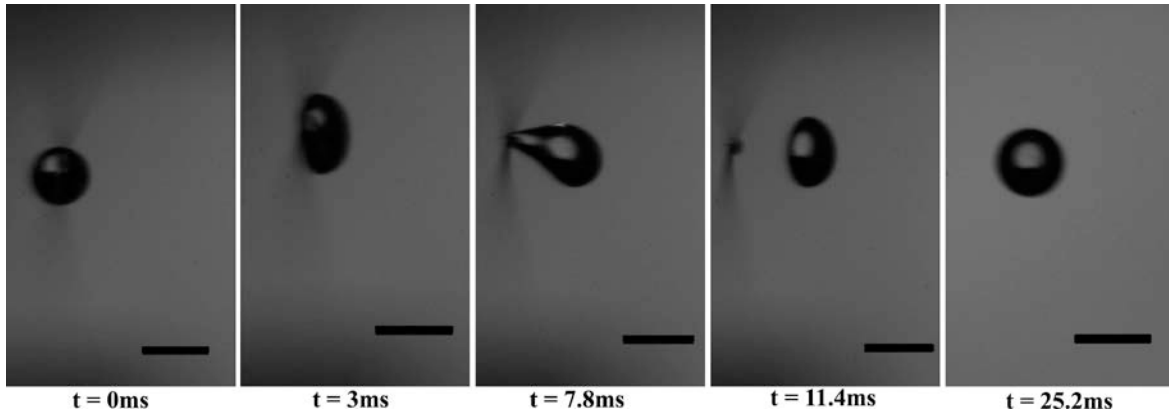


Figure 5.22. Several snapshots of drop blowing off in the vibrational type breakup of type V1. Silicone oil drop at $We = 2.8$ and $Oh = 0.07$ at different time moments. The direction of blowing is from left to right. The drop volume-equivalent diameter $2R_i = 0.9$ mm. Scale bars, 1 mm.

With an increase in the blowing velocity to 11.14 m/s ($We = 6.19$), the drop experiences a different mode of the vibrational breakup of type V2. In this case the drop initially aligns itself in the blowing direction and then is stretched to some extent as is shown in Fig. 5.23. A major portion of the drop is still attached to the filament with a liquid stem. The aerodynamic force is the origin of the stem stretching. At a later time moment the stem breaks off the filament presumably due to the capillary instability. Fragments of smaller radius originating from the stem breakup attains higher velocities than the larger fragments as could be seen from the positions of two fragments of different sizes at $t = 13.2$ ms and $t = 18.3$ ms. The aerodynamic form drag F scales with the fragment radius r as $F \propto r^2$. On the other hand, the fragment mass m scales as $m \propto r^3$. As a result, the acceleration increases as r decreases, and thus a higher velocity is attained. There is always a residual amount of liquid left on the filament after drop blowing off as is evident in Fig. 5.23 ($t = 18.3$ ms).

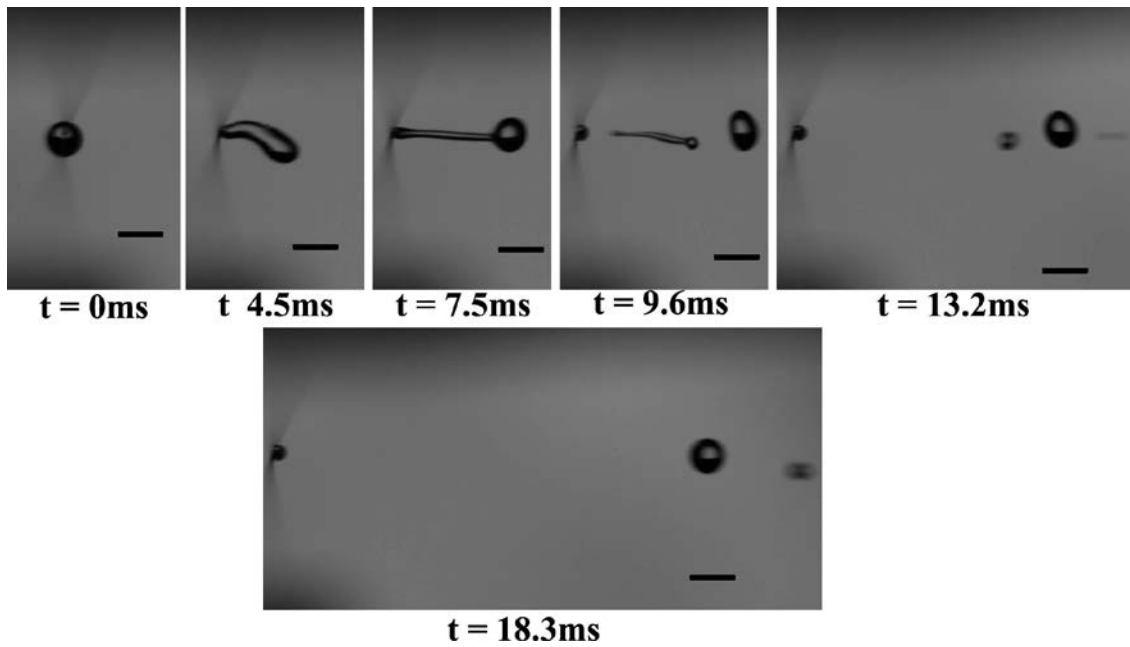


Figure 5.23. Several snapshots of drop blowing off corresponding to the vibrational breakup of type V2. Silicone oil drop at $We = 6.19$ and $Oh = 0.07$ at different time moments. The direction of blowing is from left to right. The volume-equivalent initial drop diameter $2R_i = 0.88$ mm. Scale bars, 1 mm.

At relatively low values of the Weber number We the drop does not detach from the filament but rather keeps oscillating being suspended on the stem. The threshold value of the Weber number to this pattern is the lower critical Weber number. It depends on the Ohnesorge number and the contact angle of the drop with the filament surface. At the same We , a liquid drop with a higher viscosity could keep oscillating without breaking off the filament, whereas a drop of a low viscosity liquid breaks off the filament.

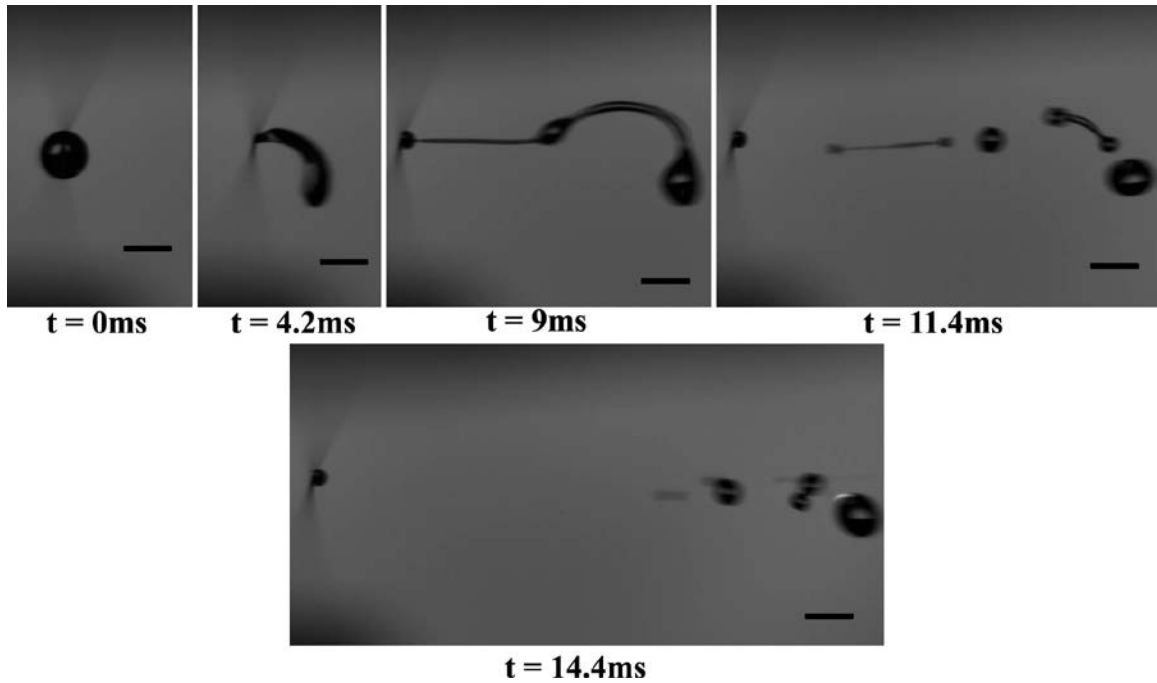


Figure 5.24. Several snapshots corresponding to the vibrational breakup of type V3. Silicone oil drop at $We = 7.39$ and $Oh = 0.07$ at different time moments. The direction of blowing is from left to right and the volume-equivalent initial drop diameter $2R_i = 1.1$ mm. Scale bars, 1 mm.

Another mode of the vibrational breakup of type V3, was observed at $We = 7.39$ as shown in Fig. 5.24. In this case the drop formed a long double-stem structure ($t = 9$ ms) which was then stretched in the blowing direction. The stems are subjected to the capillary instability and break up into smaller fragments. The fragment size resulting from the secondary stem (still attached to the filament at $t = 9$ ms in Fig. 5.24) is smaller than that from the primary thicker stem. As the We number is further increased together with the blowing velocity, the bag-stamen type breakup is observed as the upper critical Weber number is surpassed. Figure 5.25 shows the bag-stamen type breakup of a liquid drop at $We = 11.67$. The stamen is highlighted in Fig. 5.25 in the panel corresponding to $t = 5.1$ ms. It is

emphasized that the stamen is issued from the bag in the direction opposite to the direction of air blowing.

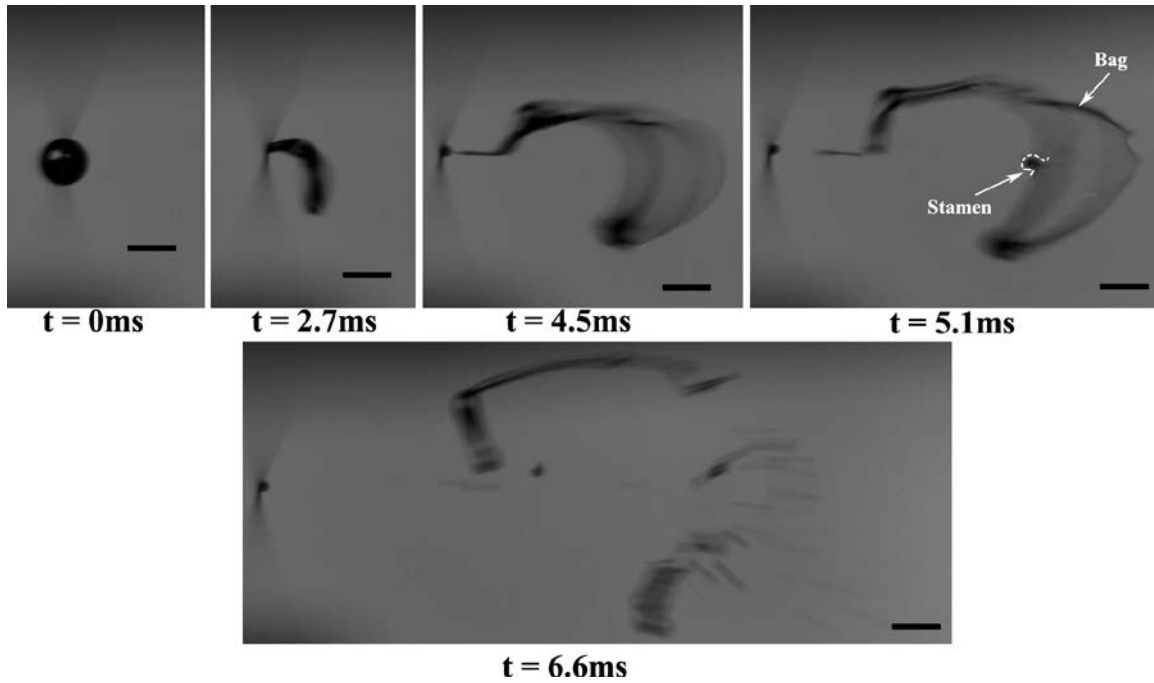


Figure 5.25. Snapshots of the bag-stamen type breakup of a silicone oil drop at $We = 11.67$ and $Oh = 0.07$ at different time moments. The blowing direction is from left to right and the volume-equivalent diameter of the initial drop $2R_i = 0.94$ mm. Scale bars, 1 mm.

With an increase in the Weber number We , the aerodynamic forces acting on the drop also increase in comparison to the capillary pressure, and the central part of the drop is thinned into a sheet surrounded by a rim at the periphery (Fig. 21, $t = 4.5$ ms). At $t = 5.1$ ms the central part of the bag-stamen structure is further increased in size. The rim of the bag developed surface waves (cf. Fig. 5.25 at $t = 5.1$ ms). Both, the bag and stamen then disintegrate into very small fragments.

Figure 5.26 shows the bag type breakup at $We = 17.17$. In distinction from the bag-stamen breakup in Fig. 5.25, there is no stamen present in this case. The instability of the bag is more evident in this case at $t = 4.5$ ms compared to the bag-stamen breakup in Fig. 5.25. The instability of the bag and its rim results in disintegration into smaller fragments than in the case of the vibrational breakup of type V3 in Fig. 5.24. The total time to breakup decreases as the Weber number We increases at a fixed Ohnesorge number as is evident in Figs. 5.22 - 5.26. The bag and bag-stamen types of breakup could switch with a slight difference in the blowing velocity.

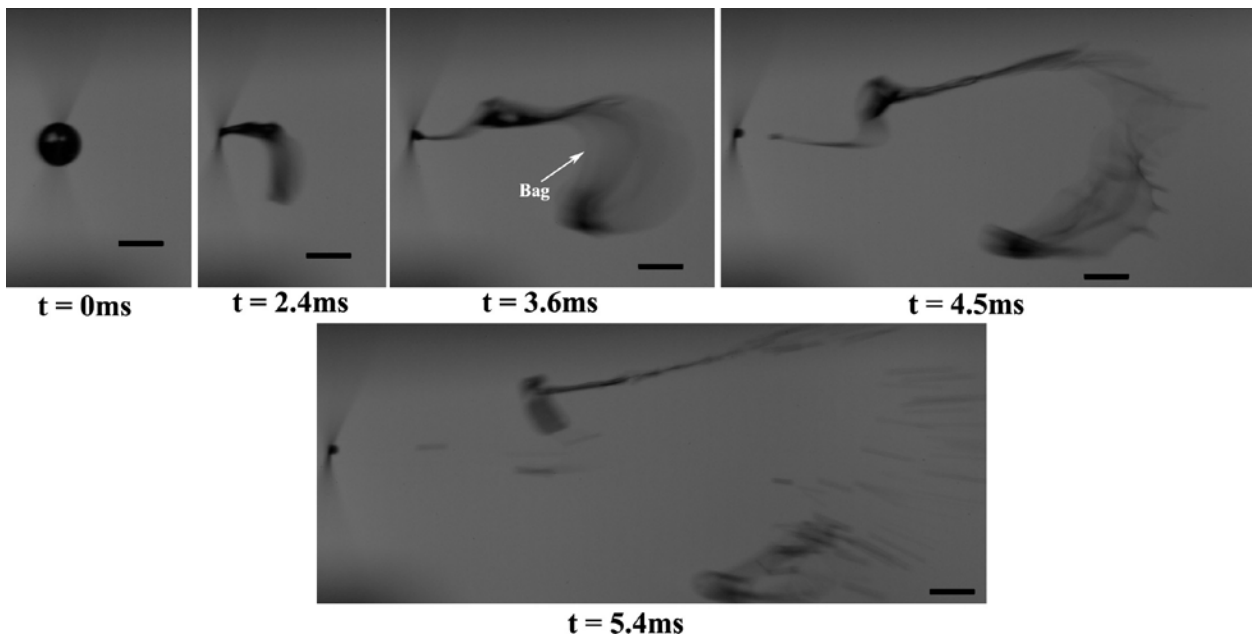


Figure 5.26. Snapshots of the bag type breakup of a silicone oil drop at $We = 17.17$ and $Oh = 0.07$ at different time moments. The direction of blowing is from left to right and the volume-equivalent diameter of the initial drop $2R_i = 1$ mm. No stamen is visible here. Scale bars, 1 mm.

As the Oh increases with the increase in viscosity, the energy dissipation also increases which thus reduces the drop deformation. Figure 5.27 shows the vibrational breakup of type V2 at $We = 17.73$ and $Oh = 0.13$. At same value of the Weber number We the drop of a lower viscosity liquid (of a lower Ohnesorge number $Oh=0.07$) undergoes the bag type breakup (Fig. 5.26) in distinction from the scenario in Fig. 5.27 for a higher liquid viscosity (a higher $Oh=0.13$).

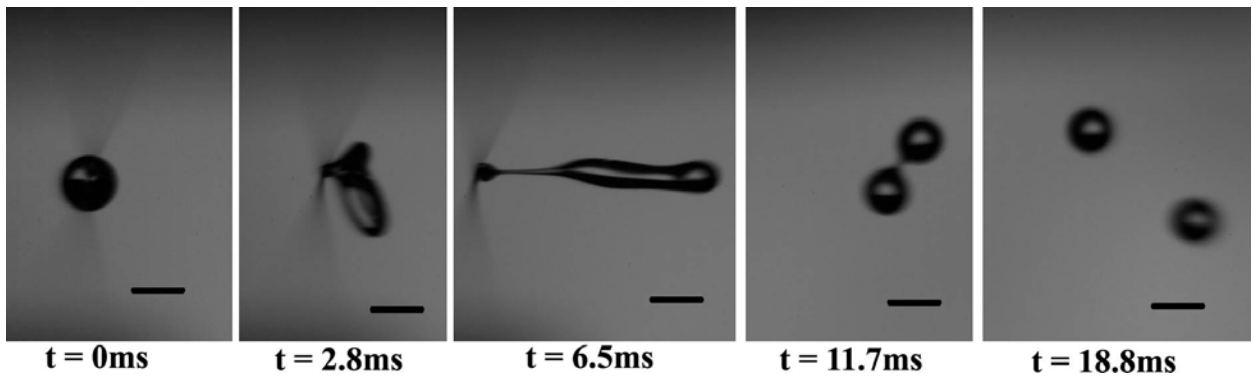


Figure 5.27. The vibrational breakup of type V2 of a silicone oil drop at $We = 17.73$ and $Oh = 0.13$ at different time moments. The direction of blowing is from left to right and the volume-equivalent diameter of the initial droplet $2R_i = 1$ mm. Scale bars, 1 mm.

Non-Newtonian viscoelastic polymer (PEO) solution was also tested. Figure 5.28 shows the breakup pattern of a PEO drop at a relatively low $We = 7.5$. The elastic nature of the polymer solution allows it to be significantly stretched under the action of the aerodynamic drag as is evident from Fig. 5.28 ($t = 37$ ms). The stem spanning the drop and filament continues stretching as its radius is shrinking. Moreover, the part of the drop which remains attached to the filament is depleted in time, which is similar to the tubeless viscoelastic siphon [Bird et al. (1987)]. Finally the stem breaks off the filament leaving no

PEO solution on the filament, in distinction from the Newtonian liquids where a portion of the initial drop is always left behind on the filament.

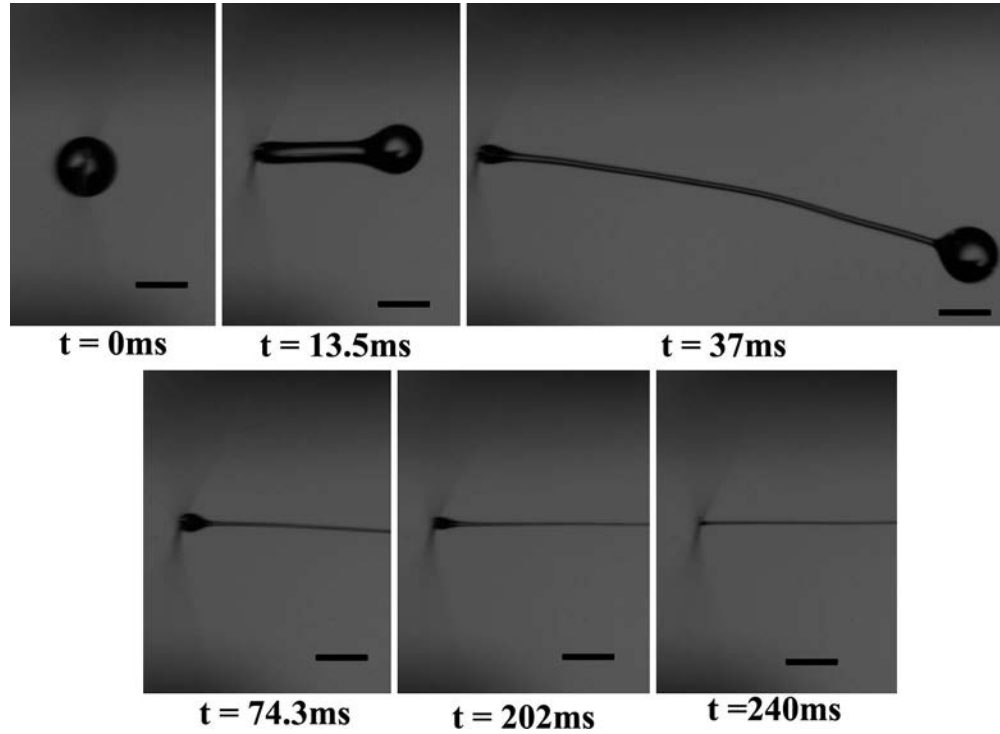


Figure 5.28. The breakup of 1 wt% aqueous solution of PEO ($M_w = 2000$ kDa) at $We = 7.5$ and $Oh = 0.25$ at different time moments. The direction of blowing is from left to right and the volume-equivalent diameter of the initial drop $2R_i = 1$ mm. Scale bars, 1 mm.

The We - Oh plane can be delineated into domains corresponding to different breakup modes as shown in Fig. 5.29. It is clear that at higher values of Oh the bag type breakup is delayed and the domain of the vibrational types of breakup increases, as the viscous dissipation diminishes deformation caused by the aerodynamic forces. The domain I corresponding to the vibrational type V1 possesses almost the same thickness at different

values of Oh , which expresses the fact that surface tension is dominant at lower values of We .

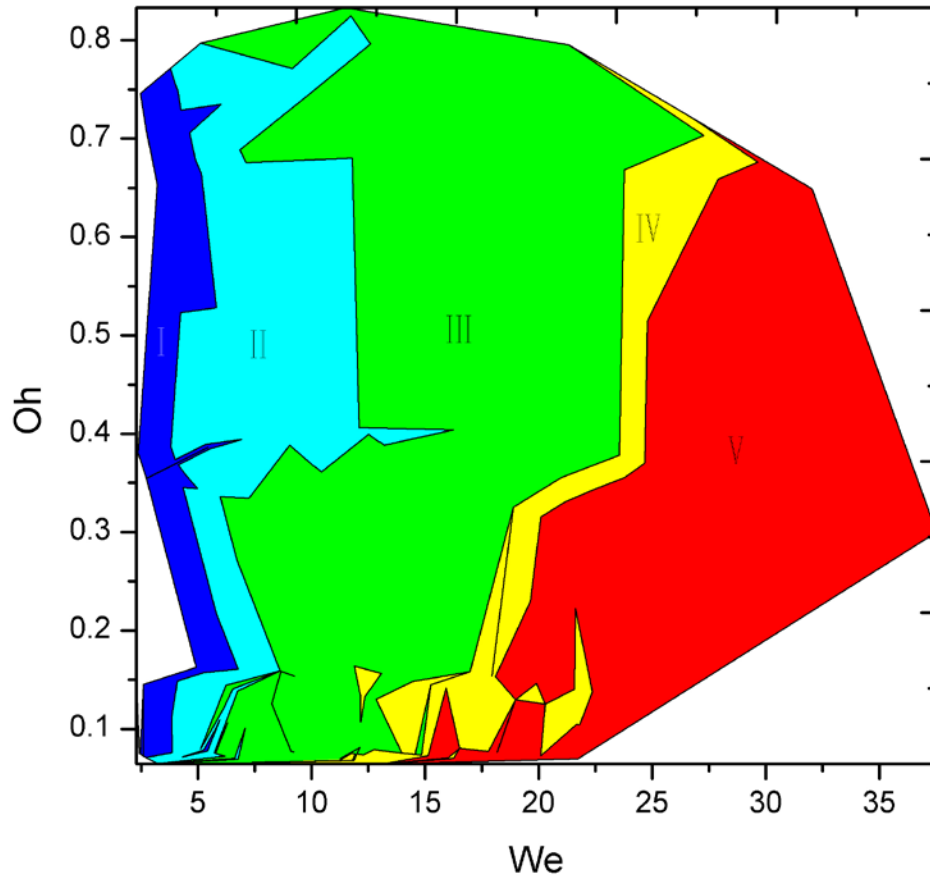


Figure 5.29. The We - Oh with the domains corresponding to different types of breakup of Newtonian liquid drops on filament in cross-flow: I- vibrational breakup of type V1; II- vibrational breakup of type V2; III- vibrational breakup of type V3; IV- bag-stamen type breakup; V- bag type breakup.

The breakup time t_b is defined as the time between the onset of the blowing and the detachment of a drop from the filament. The breakup time was measured using the experimental data for different blowing velocities (different We) and liquid viscosities. It

could be seen in Fig. 5.30 that at low values of the Weber number We the breakup time significantly increases as the viscosity increases. At higher We the increase in the breakup time with viscosity is insignificant and t_b becomes practically independent of viscosity.

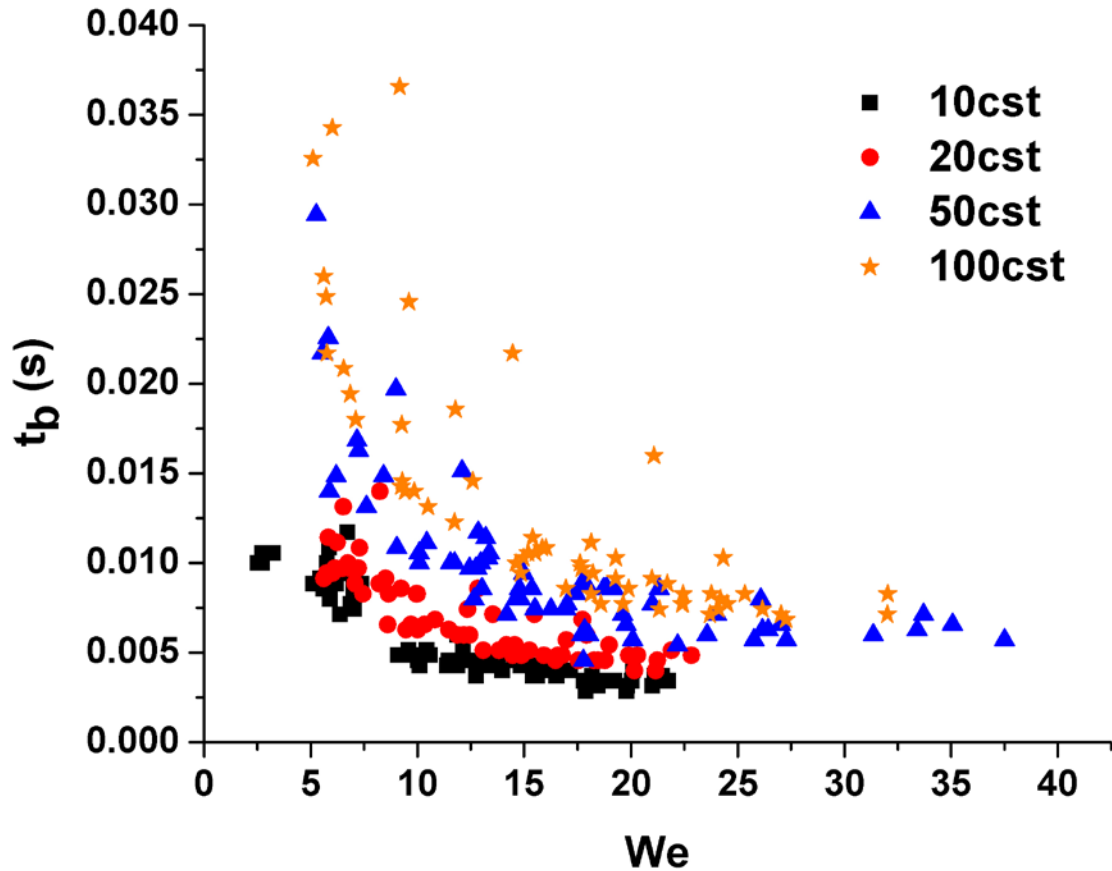


Figure 5.30. Breakup time versus the Weber number for different viscosities of silicone oils.

In the case of Newtonian silicone oils a part of a liquid drop always remains on the filament at the end of the blowing process after detachment of the main body. The volume-equivalent radius of the residual part left on the filament was calculated using Eq. (5.2) of theoretical section 5.4.1 and normalized with the initial drop radius. In the present section it is denoted as \bar{a} . Such data from multiple experiments was used to evaluate the probability

density function of the size of the residual part under different conditions. It is shown in Fig. 5.31 for four different air blowing velocities and four different viscosities of silicone oil. It was found that the normal distribution best fits the corresponding probability density functions. Figure 5.31d clearly shows

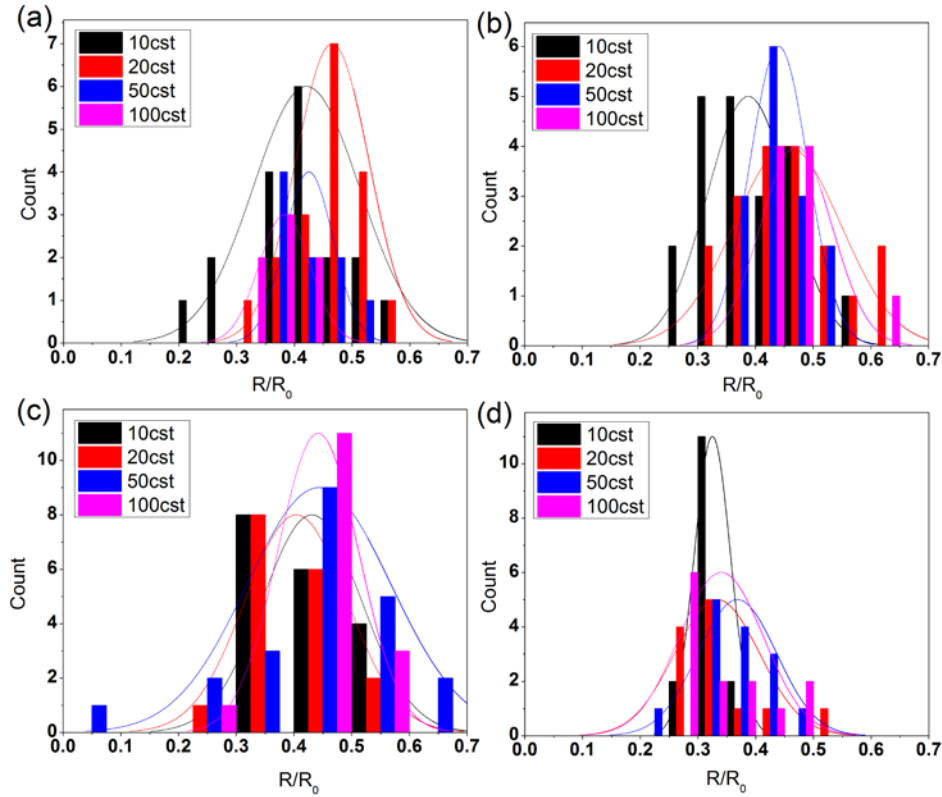


Figure 5.31. Probability density function of the size of the residual droplet left on the filament. (a) The blowing velocity $V_0=11.14$ m/s, (b) $V_0=14.43$ m/s, (c) $V_0=17.46$ m/s, (d) $V_0=20.13$ m/s. The lines spanning the bar charts are the corresponding normal distributions.

that the expected volume-equivalent radius of the residual drop left on the filament diminishes as the blowing velocity increases.

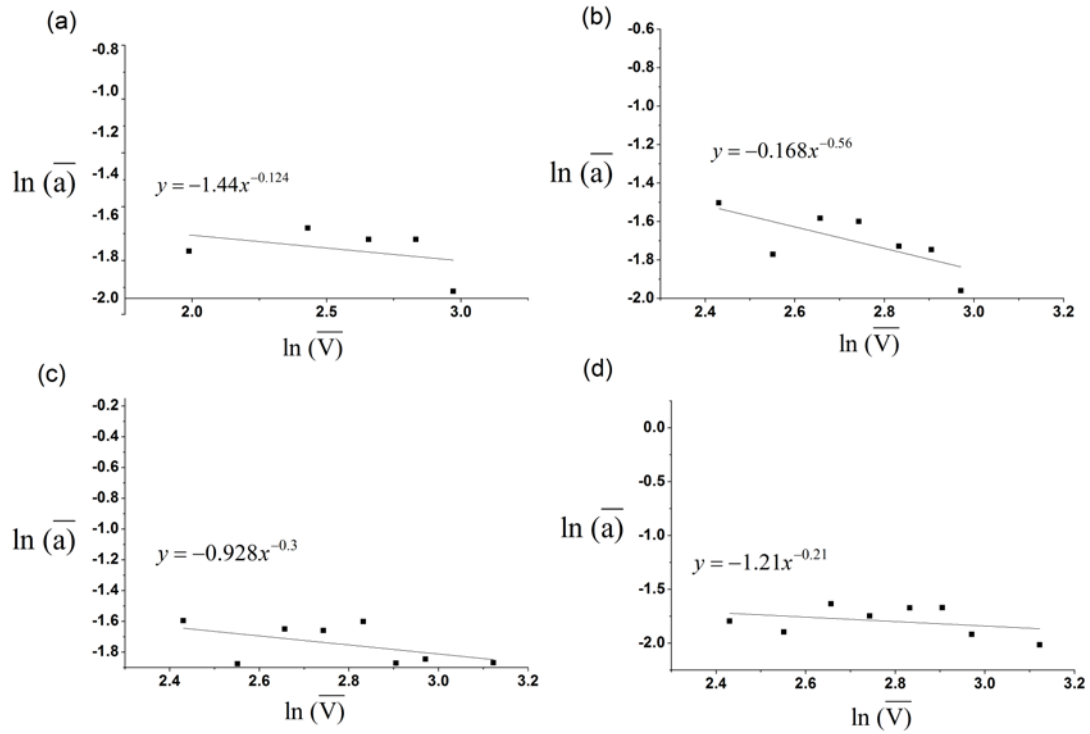


Figure 5.32. Normalized volume-equivalent radius of the residual droplet left on the filament versus the normalized air blowing velocity. Here the blowing velocity is rendered dimensionless by $V_* = 1$ m/s. Symbols represent the experimental data (the average taken over 20 trials for each point) spanned by a power-law fit written in each panel. (a) $\mu=10$ cst, (b) $\mu=20$ cst, (c) $\mu=50$ cst, (d) $\mu=100$ cst.

Two physical parameters of liquid could determine the size of the residual droplet left on the filament: the surface tension and/or the viscosity. The radius of the droplet which can withstand the aerodynamic drag (without being blown off) solely due to the surface tension is found as

$$a \sim \frac{\sigma}{C_d \rho_a V^2} \quad (5.1)$$

where C_d is the drag coefficient.

On the other hand, the radius of the droplet which can withstand the aerodynamic drag (without being blown off) solely due to the viscous dissipation is found as

$$a \sim \left(\frac{\mu a_f}{C_d \rho_a V} \right)^{1/2} \quad (5.2)$$

where a_f is the cross-sectional filament radius; cf. Eq. (5.3) in theoretical section 5.4.1 accounting for the fact that the radius of the residual droplet is close to that of the filament.

Equations (5.1) and (5.2) predict $a \sim V^{-2}$ and $a \sim V^{-1/2}$, respectively. These predictions can be compared to the experimental data in Fig. 5.32. The scaling predicted by Eq. (5.2) is closer to the data, albeit a good numerical agreement in the exponent value is found only in the case of $\mu=20$ cst in Fig. 5.32b.

5.3.5 Drop hopping across filaments

Silicone filaments were arranged parallel to each other at a distance of 2 mm in the basic case, as well as 1 mm for comparison. Figure 5.1c shows the details of the experimental setup in this case. The distance between the nozzle and the first filament was kept constant at 1 cm. The blowing direction was normal to the filament. Figure 5.33 shows how a drop of a Newtonian liquid, silicone oil, breaks off the first filament at the air blowing velocity of 11.14 m/s and gets intercepted by the filament placed next to the first one. The drop undergoes the vibrational breakup as is evident from the images corresponding to different time moments. A fraction of the original drop remains on the first filament. The drop intercepted at the second filament is also blown off from there leaving a small residual, and so on.

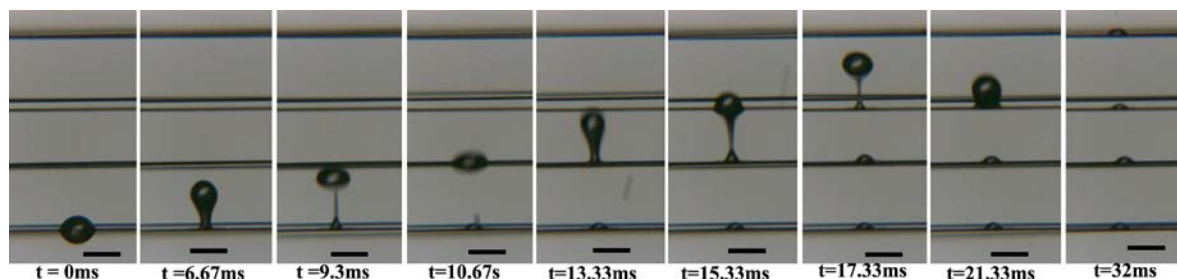


Figure 5.33. A 10 cst silicone oil drop hopping across parallel filaments which are perpendicular to the air blowing direction. The inter-filament distance is 2 mm. The blowing is from bottom to top of the image. $V_0 = 11.14$ m/s. Scale bars, 1 mm.

The hopping process at higher velocities of $V_0 = 14.43$ m/s and $V_0 = 17.46$ m/s are depicted in Figs. 5.34 and 5.35 respectively. At higher velocities the drop is stretched in the direction of blowing and is intercepted by the neighboring filament before breaking off from the previous one. A bridge-like network is formed between the filaments at times and the width of the bridge decreases as the drop proceeds further. The time it takes for a drop to hop over all four parallel filaments in the experiment decreases as the air blowing velocity increases, which is evident from the snapshots in Figs. 5.33, 5.34 and 5.35 in the ESI.

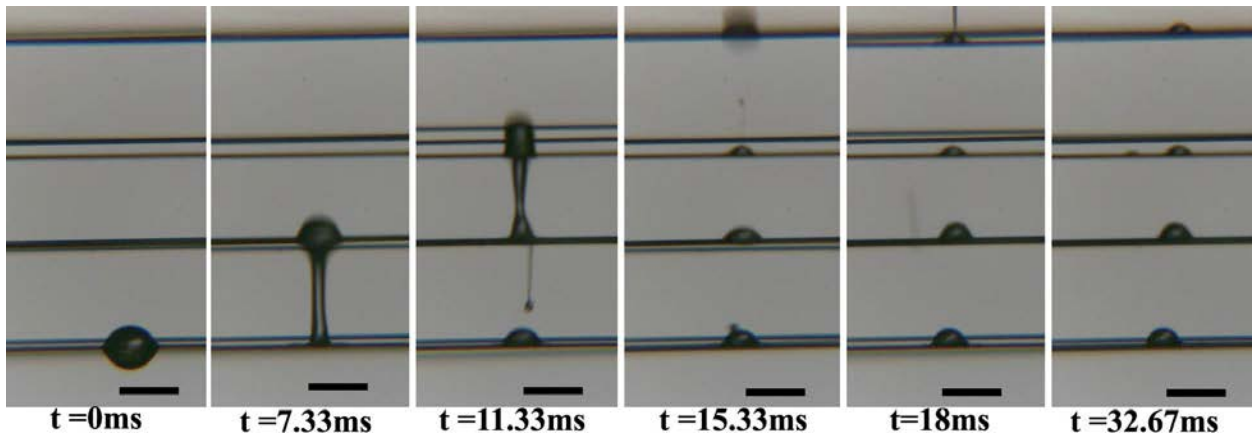


Figure 5.34 A 10 cst silicone oil drop hopping across parallel filaments which are perpendicular to the air blowing direction. The inter-filament distance is 2 mm. The blowing is from bottom to top of the image. $V_0 = 14.43$ m/s. Scale bars, 1 mm.

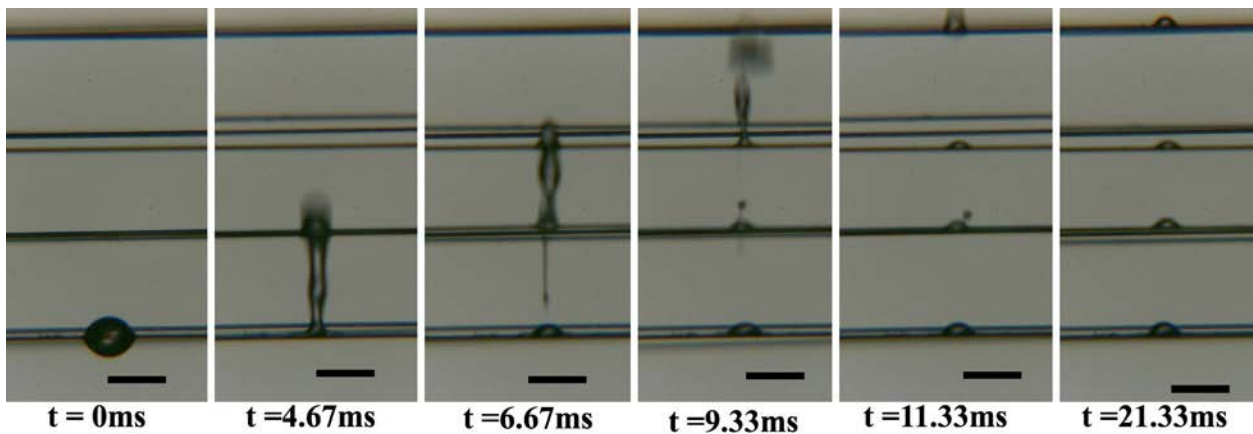


Figure 5.35 A 10 cst silicone oil drop hopping across parallel filaments which are perpendicular to the air flow. The inter-filament distance is 2 mm. The blowing direction is from bottom to top of the image. $V = 17.46$ m/s. Scale bars, 1 mm.

At a lower inter-filament distance of approximately 1 mm the drop forms a continuous bridge over all the filaments as shown in Fig. 5.36.

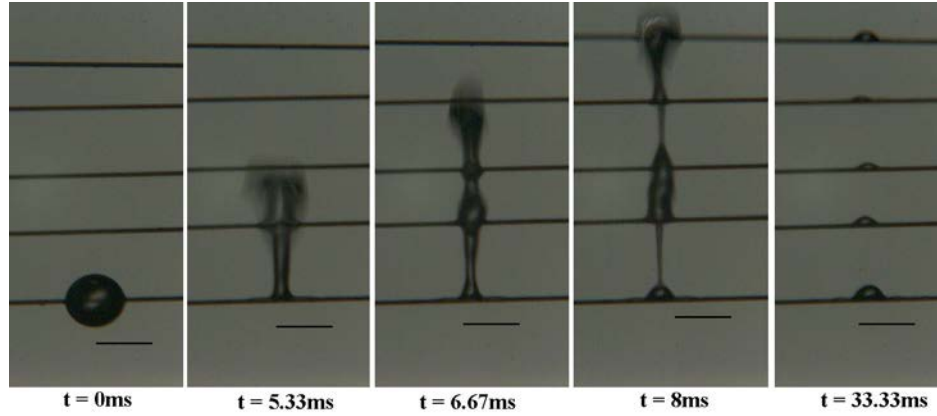


Figure 5.36. A 10 cst silicone oil drop bridging the filaments placed parallel to each other and perpendicular to the air flow. The inter-filament distance is 1 mm. The blowing direction is from bottom to top of the image. $V = 17.46$ m/s. Scale bars, 1 mm.

5.4 Theoretical model

5.4.1 Dynamics of drop motion along the filament

To predict drop motion along a thin filament under the action of parallel air stream, one has to account for the form drag, skin friction imposed by air, the force associated with the viscous resistance near the moving contact line, as well as the viscous friction at the filament surface. The form drag can be approximated by using the drag coefficient as

$$F_{\text{drag}} = C_d \frac{1}{2} \rho_a [V(x) - U(x)]^2 \pi (R_i^2 - a_f^2) \quad (5.3)$$

where the air density is denoted by ρ_a , the free stream velocity of air is $V(x)$, the drop velocity on the filament is $U(x)$, the drag coefficient C_d , and the drop volume-equivalent radius and the filament cross-sectional radius are denoted as R_i and a_f , respectively. The drag coefficient C_d includes the effects of form drag and skin friction imposed by air.

The drop was assumed to have a paraboloidal body of revolution and thus the volume-equivalent radius was thus calculated as

$$R_i = \left[l(a_m - a_f)(2a_m + 3a_f)/5 \right]^{1/3} \quad (5.4)$$

where ℓ is the drop length along the filament, a_m is the maximum radius of the drop, and a_f is the filament cross-sectional radius. These parameters were measured from the top view of the drop.

Viscous friction acting on a drop from a filament was evaluated in as [Yarin et al. (2002)]

$$F_{\text{viscous}} = -4\pi\mu R_i \frac{U}{\ln(R_i/a_f)}. \quad (5.5)$$

where the droplet viscosity is denoted by μ .

An additional resistive force is associated with viscous losses required to deform the free surface close to the moving contact line. The corresponding force per unit length required to pull the free surface in order to change the contact angle from its equilibrium value of θ_0 to θ is given as [Blake (1993)]

$$F_{\text{surf}} = \sigma(\cos\theta_0 - \cos\theta) \quad (5.6)$$

In the experiments it was observed that both the advancing and receding contact angles of moving drops change, and hence the net force associated with the resistance near the contact line can be expressed as

$$F_{\text{surf}} = \pi a_f \sigma K \quad (5.7)$$

where $K = \left[|\cos\theta_{11} - \cos\theta_{12}| + |\cos\theta_{21} - \cos\theta_{22}| + |\cos\theta_{31} - \cos\theta_{32}| + |\cos\theta_{41} - \cos\theta_{42}| \right]$, with θ_{11} , θ_{21} , θ_{31} , and θ_{41} being the equilibrium contact angles before blowing, while θ_{12} , θ_{22} , θ_{32} , and θ_{42} - the corresponding contact angles under blowing as sketched in Fig. 5.37.

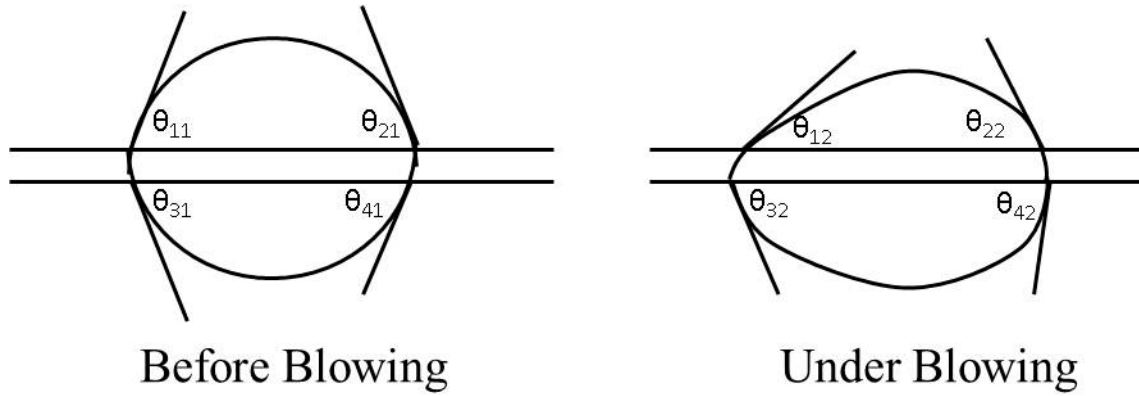


Figure 5.37. Schematic of the drop shape on a filament before blowing and during blowing.

The Reynolds number of the blowing based on the nozzle diameter is of the order of $Re = 100$ (with the blowing speed of the order of 10^2 cm/s, and the nozzle diameter $d=0.22$ cm). Therefore, such jet-like flow is expected to be transitional/turbulent. Considering the air stream blown from the nozzle as an axisymmetric submerged jet, we approximate the air velocity along the filament (in the direction of x , with $x=0$ corresponding to the nozzle) as [Loitsyanskii (1966)]

$$V(x) = \frac{3}{8\pi\kappa} \sqrt{\frac{J_0}{\rho_a}} \frac{1}{x} \left[1 - \frac{1}{16\sqrt{\pi\kappa}} \frac{d}{x} \right] \quad (5.8)$$

where the empirical constant $\kappa = 0.021$, the momentum flux $J_0 = \pi d^2 \rho_a V_0^2 / 4$ and V_0 is the maximum velocity at the nozzle exit. Since the locations where drop moves correspond to $x \gg d$, the second term in the parentheses could be neglected and Eq. (5.8) takes the form

$$V(x) = 5V_0 \frac{d}{x} \quad (5.9)$$

The second law of Newton for drop motion combining all the above-mentioned forces reads

$$\rho \frac{4}{3} \pi R_i^3 \frac{dU}{dt} = C_d \frac{1}{2} \rho_a [V(x) - U]^2 \pi (R_i^2 - a_f^2) - 4\pi \mu R_i \frac{U}{\ln(R_i / a_f)} - \pi a_f \sigma K \quad (5.10)$$

where ρ is the liquid density.

The dynamic equation (5.10) is supplemented by the kinematic equation

$$\frac{dx}{dt} = U \quad (5.11)$$

Render Eqs. (5.10) and (5.11) dimensionless using the following scales

$$\bar{x} = \frac{x}{R_i}; \quad \bar{t} = \frac{t}{R_i^2/\nu}; \quad \bar{U} = \frac{U}{V_0} \quad (5.12)$$

(with ν being the kinematic viscosity of liquid in the drop), and introduce the dimensionless length scale ratio

$$k = \frac{R_i}{a_f} \quad (5.13)$$

Then, also using Eq. (5.9), we reduce Eqs. (5.10) and (5.11) to the following dimensionless form

$$\frac{d\bar{U}}{d\bar{t}} = \frac{3}{8} C_d (1 - k^{-2}) \text{Re} \frac{\rho_a}{\rho} \left[\frac{C}{\bar{x}} - \bar{U} \right]^2 - \frac{3}{\ln(k)} \bar{U} - \frac{3K}{4k \text{Oh}^2 \text{Re}} \quad (5.14)$$

$$\frac{d\bar{x}}{d\bar{t}} = \text{Re} \bar{U} \quad (5.15)$$

where the factor $C = 5(d / R_i)$, $\text{Re} = V_0 R_i / \nu$ is the Reynolds number, and $\text{Oh} = \mu / \sqrt{\rho \sigma R_i}$ is the Ohnesorge number. As in the present case $\text{Re} < 1000$, the drag coefficient is given by the Schiller and Neumann formula [Schiller and Naumann (1935)]

$$C_d = \frac{24}{\text{Re}} \left(1 + 0.15 \text{Re}^{0.687} \right) \quad (5.16)$$

The system of Eqs. (5.14) - (5.16) is solved numerically using the Kutta-Merson method.

5.4.2 Tail formation and instability; recoil motion of drops

Drop motion along the filament can be seen as a withdrawal problem where the filament is pulled out from a pool of liquid. As a drop is moving along the filament, it can form a withdrawn tail. Consider the filament surface $Y=0$ in Fig. 5.38 as it is pulled beneath the drop with velocity U to the right. In parallel, the contact line resists the deformation of the drop surface and slips along the filament with velocity U_s to the left. The strain due to the slip velocity is thus

$$\frac{d\theta}{dt} = \frac{\partial u}{\partial y} \approx - \frac{U_s}{R_i} \quad (5.17)$$

where t is time.

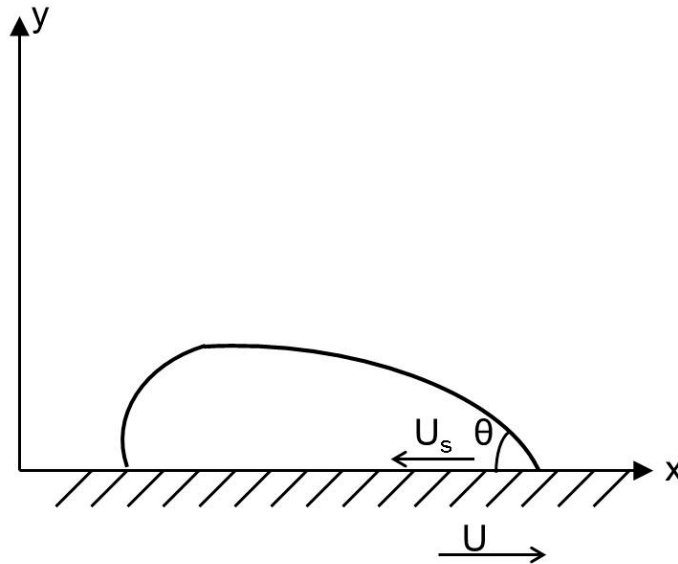


Figure 5.38. Schematic of the drop deformation in the process of tail formation due to the filament motion along the x-axis.

Therefore, the power dissipated due to the sliding motion of the tail over the length L_s can be expressed as

$$P_d \approx \mu \left(\frac{U_s}{R_i} \right)^2 2\pi a_f L_s R_i \quad (5.18)$$

The drop surface is tending to return the contact angle θ to its equilibrium value θ_0 ($\theta < \theta_0$), with the power [cf. Eq. (5.6)]

$$P_c \approx 2\pi a_f \sigma (\cos\theta - \cos\theta_0) U_s \quad (5.19)$$

In the inertialess approximation $P_c = P_d$. Using Eqs. (5.17) - (5.19) and the Taylor series expansion for $(\cos\theta - \cos\theta_0)$, i.e. assuming θ to be close to θ_0 , yields the following expression for the slip length

$$L_s = \frac{\sigma}{\mu} \sin\theta_0 t \quad (5.20)$$

On the other hand, the entrainment length of the drop due to the filament motion is

$$L = Ut \quad (5.21)$$

A tail can only be formed if $L > L_s$. Using Eqs. (5.20) and (5.21), the condition corresponding to the formation of a tail can be evaluated as

$$Ca > \varepsilon \sin\theta_0 \quad (5.22)$$

where $Ca = U\mu/\sigma$ is the capillary number, and ε is a constant dimensionless factor.

The condition (5.22) implies that the tail is formed if the filament (or drop motion) velocity U is sufficiently large for a given equilibrium contact angle. If the velocity is too low, no tail should be formed.

The thickness of the tail δ can be obtained from the Landau-Levich-Deryaguin (LLD) theory as [Levich (1962) and Ruckenstein (2002)]

$$\delta = 1.34a_f Ca^{2/3} \quad (5.23)$$

The tail formed on the filament is subjected to the capillary instability as discussed in Yarin et al. (1993), and the wavelength of the capillary breakup of the tail is given as $\lambda = 2\pi\sqrt{2}a_f$. The time of perturbation growth on the tail corresponding to its breakup into secondary droplets is expressed as [Yarin et al. (1993)]

$$t = \frac{12\mu a_f^4}{\sigma \delta^3} \quad (5.24)$$

As soon as air blowing is ceased, the tail formed on the filament tends to pull the drop back in order to reduce the free surface energy, which facilitates the recoil motion. The viscous friction between the drop and filament, as well as between the tail attached to the drop and filament, dissipates kinetic energy of recoil motion.

The force balance in the recoil motion is expressed as [cf. Eq. (5.5)]

$$2\pi(a_f + \delta)\sigma = 4\pi\mu R_i \frac{U_r}{\ln(R_i/a_f)} + \mu \frac{U_r}{\delta} 2\pi(a_f + \delta)2\lambda \quad (5.25)$$

where U_r is the recoil velocity.

5.5 Conclusion

In the experiments of the present work both axisymmetric barrel-shaped and asymmetric clamshell-shaped silicone oil drops were observed on filaments subjected to air blowing. In the first set of experiments drops were driven by parallel air jet along a polyamide-coated filament. The experiments elucidated the effect of drop viscosity and the speed of air blowing. It was found that the drop motion in some case resembles stick-slip motion. The stick-slip motion is accompanied by the oscillations of the drop shape. It is

shown that the stick-slip motion appears due to the interplay between the probable contact angle hysteresis and the large eddies generation in the intermittent air jet.

Drops moving along the filament in parallel air flow issue an axisymmetric tail-like film surrounding the filament behind the drop. This tail-like film is subjected to the capillary instability and can breakup into a train of tiny droplets. An intact tail imposes capillary force pulling moving drops back, which causes receding motion at some distances along the filament.

Droplets of Newtonian silicone oils blown off filaments by air cross-flow normal to the filament revealed the following five different subsequent types of breakup as the Weber number increases: three different vibrational types of breakup [the balloon-like (V1), single-stamen (V2) and double-stamen (V3)], followed by the bag-stamen type of breakup, and the bag type of breakup. Viscoelastic drop of poly(ethylene oxide) solution demonstrated vibrational type of breakup, albeit very different from those for Newtonian liquids.

Being blown off a filament in a cross-flow, silicone oil (Newtonian liquid) drops leave residual parts on the filament. Their size seemingly is governed by viscous forces more than by surface tension, and their size distribution is normal. In distinction, viscoelastic drops ultimately pulled all liquid from the filament by the mechanism recembling that of tubeless viscoelastic siphon.

Hopping of drops between parallel filaments in cross-flow was also observed, with residual parts left on all filaments. At low inter-filament distances, drops can bridge several filaments simultaneously.

The simplified models developed in the present work are helpful in elucidating the physical origin of the experimental observations. A detailed quantitative description would

require fully three-dimensional time-dependent direct numerical simulations of the mutually-interacting intermittent gas flow and a deformable drop on a solid filament, with a wide range of length and time scales involved.

6. IMPACT OF AQUEOUS SUSPENSION DROPS ONTO NON-WETTABLE POROUS MEMBRANES: HYDRODYNAMIC FOCUSING AND PENETRATION OF NANOPARTICLES

6.1 Introduction

The impacts and dynamic penetration of nanoparticle suspension drops into porous filter membranes are studied experimentally and theoretically. This type of penetration is associated with hydrodynamic focusing and is radically different from the wettability-driven imbibition. In the case of hydrodynamic focusing water can penetrate into a non-wettable porous medium at very low values of the dynamic pressure associated with drop impact. Two types of membranes are used in the experiments: (i) glass fiber filter membrane wettable by the carrier fluid (water), and (ii) Polytetrafluoroethylene (PTFE) depth filter membrane, non-wettable by the carrier fluid. The nanoparticle entrainment and deposition inside the membrane bulk is used to mostly visualize the ultimate penetration fronts by observing the cut cross-sections of the membranes, albeit also provide an insight into innovative applications like circuit printing on nonwovens. The deposition patterns inside the membranes are also linked to the drop splashing patterns at their front surfaces. The experimental results confirm that during the dynamic focusing water can penetrate into a non-wettable porous medium (PTFE). Water also penetrates by the same hydrodynamic focusing mechanism into the wettable glass fiber membrane, where it additionally spreads on a much longer time scale due to the wettability-driven flow. A theory explaining hydrodynamic focusing penetration of liquid into porous medium after drop impact is proposed. It is used to explain and predict water penetration into the non-wettable filter

medium after drop impact, and the results are compared with the experimental data. Also the critical thickness of non-wettable membranes determined by dissipation of the kinetic energy in flow inside membrane is evaluated and compared with the experimental data.

6.2 Materials and methods

6.2.1 Materials

Glass fiber filter (1 mm thick and 47 mm in diameter) with 2.7 μm pores and Polytetrafluoroethylene (PTFE) depth filter (1 mm thick, 47 mm in diameter) with 10 μm pores were purchased from Cole-Parmer and used as received. Glass fiber membrane is wettable with water, whereas PTFE is non-wettable. The surfaces of the membranes were observed using optical microscope Olympus BX-51 (Fig. 6.1). They are nonwoven fibrous materials. The glass fiber filter reveals distinct pores and fibers (Fig. 6.1a-c), whereas the PTFE filter reveals some film-like structures with open pores attached to fibers (Fig. 6.1d-f). The pore size is determined by the particle size that will be retained with 100% efficiency under specified conditions. The pore size of the membranes used in the present work was specified by the supplier as 2.7 μm for the glass fiber filter (wetable) and ≤ 10 μm for the PTFE membrane (non-wettable). The pore size at the surfaces of both membranes seems to be larger because the lower lying fibers which block pores are out of focus and thus are practically invisible.

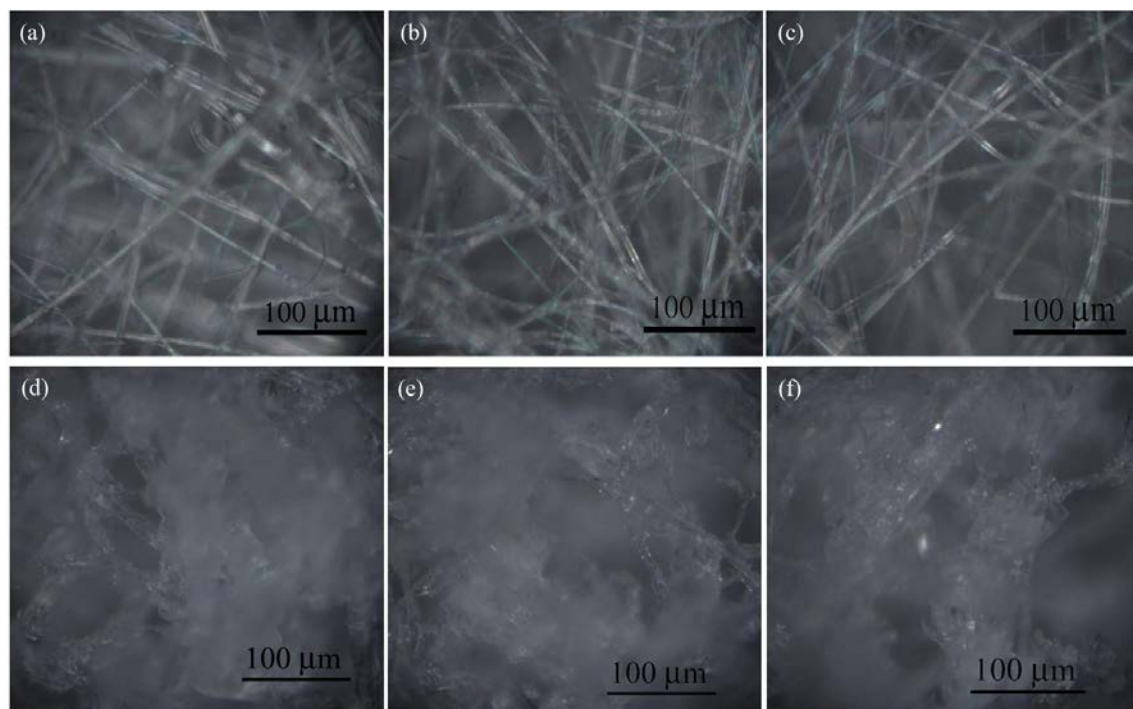


Figure 6.1. Optical microscope images of glass fiber filter (a-c) and PTFE membrane (d-f) showing the fibers and the pore sizes.

The surface roughness is approximately equal to the fiber diameter in the membrane. The roughness of the glass fiber filter $R_a = 2\text{-}4\text{ }\mu\text{m}$, and that of the PTFE membrane is $R_a = 5\text{-}8\text{ }\mu\text{m}$. The contact angle of water on the PTFE membrane was measured as 160° (in the superhydrophobic range), as is seen from an image of a softly deposited water drop (Fig. 6.2). On the other hand, it was impossible to measure the contact angle of water drop on the glass fiber filter as it spreads immediately as it comes in contact with the wettable filter.

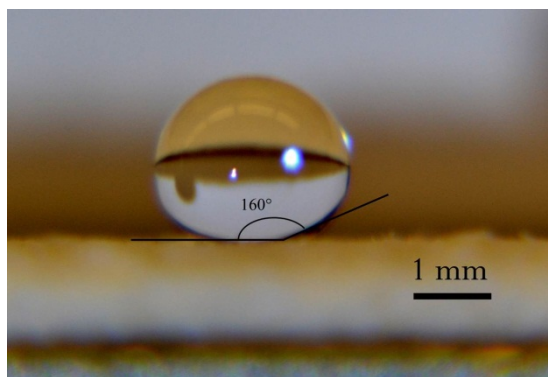


Figure 6.2. Contact angle of water drop on the PTFE membrane.

Black titanium nanoparticles (60-80 nm) were purchased from Skyspring Nanomaterials, Inc. Nanoparticle suspension was prepared by adding 0.1 g of nanoparticles to 20 g of water (0.5 wt %). Surface tension and viscosity of such aqueous suspension are practically indistinguishable from those of water. The suspension was then sonicated using probe sonicator (QSonica Q500) for 1 min to make it homogeneous. Sonication was applied to prevent nanoparticle cluster formation and sedimentation. Fresh suspension drops were used in drop impact experiments right after the sonication.

6.2.2 Experimental setups

Drops of nanoparticle suspension were dripped onto porous membranes using the experimental setup similar to that of Sahu et al. (2012) sketched in Fig. 6.3. The setup included an adjustable platform, a syringe pump, a high speed CCD camera (Phantom Miro 4), an external light source, a computer and a stand assembly. Samples of the membranes were located centrally on the adjustable platform which can be moved in the horizontal direction.

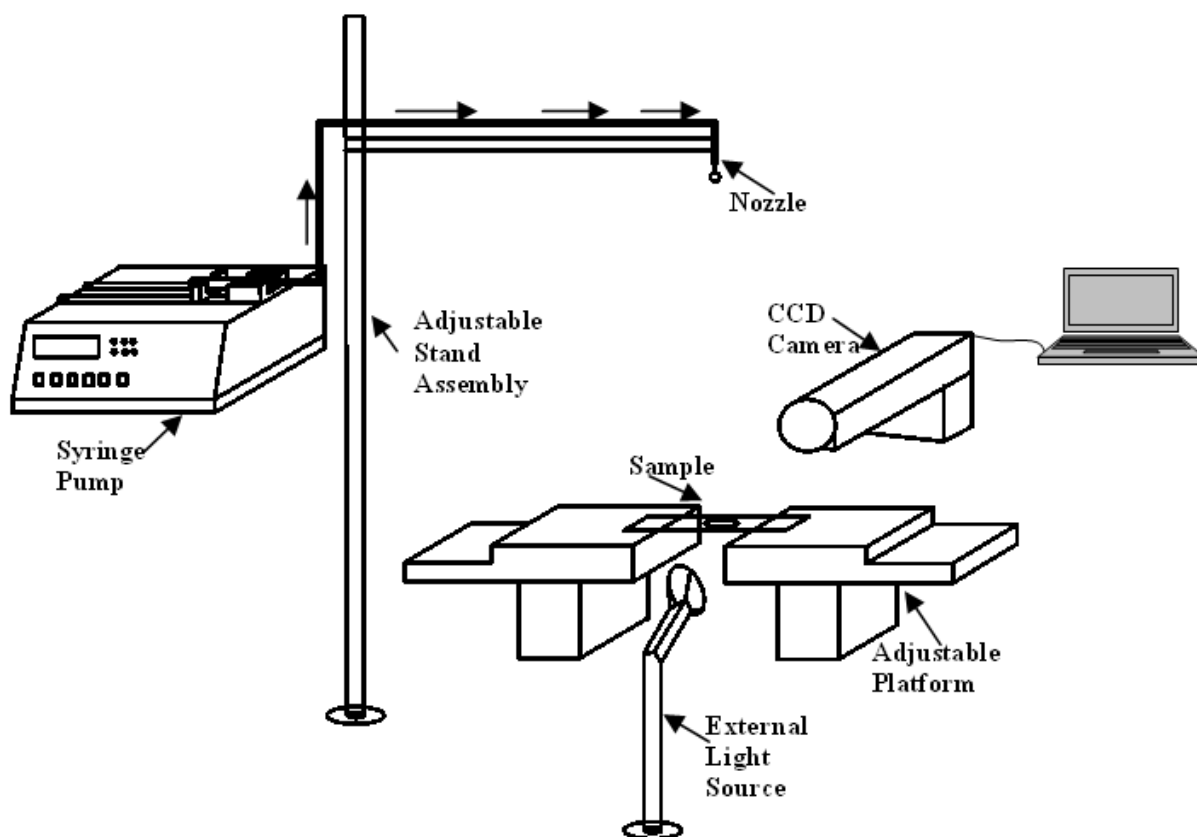


Figure 6.3. Schematic of the experimental setup used to drip nanoparticle suspension drops onto porous membranes.

Suspension drops were released from 18G and 14G needles. Their impact velocity V_0 was measured at the impact moment using the high-speed imaging. The drops (17 μl , formed from 18G needle with the inner and outer diameters of 0.838 mm and 1.27 mm, respectively; and 26 μl , formed from 14G needle with the inner and outer diameters of 1.6 mm and 2.108 mm, respectively) were released onto glass fiber membrane from the heights h from 0 cm (soft deposition) to 70 cm (the gravity-driven impact). The measured impact velocities are listed in Table 6.1. In addition similar drops from 14G needle were released from impact heights of 180 cm and higher onto glass fiber and PTFE membranes, with the measured impact velocity of 5.32 m/s and higher.

After an impact of suspension drop, the porous membranes were left to dry for a few hours and then were mounted on the setup shown in Fig. 6.4. The setup in Fig. 6.4 included two high-performance low-profile ball-bearing linear stages placed orthogonally to each other. A sharp razor blade was attached to the stage translating in the vertical direction (the Y axis). The sample was placed horizontally (the horizontal plane includes the X axis). The cross-section A-A corresponded to the viewing direction of the camera (Nikon D3100) with respect to the sample. Namely, after a nanoparticle-seeded drop dripped onto a sample of a porous membrane and the latter was completely dried, the nanoparticles would be embedded inside if water penetrates the pores. Then, the porous membrane was sliced by the razor blade in several locations along the X-axis (Fig. 6.4), and the camera was used to observe the nanoparticle distribution in the cut cross-sections of the sample. The images of nanoparticles in the cut cross-sections of the membranes were taken for the slices produced after every translation of 0.5 mm along the X-axis. After that, the images were processed using ImageJ, Matlab and Adobe Photoshop CS2.

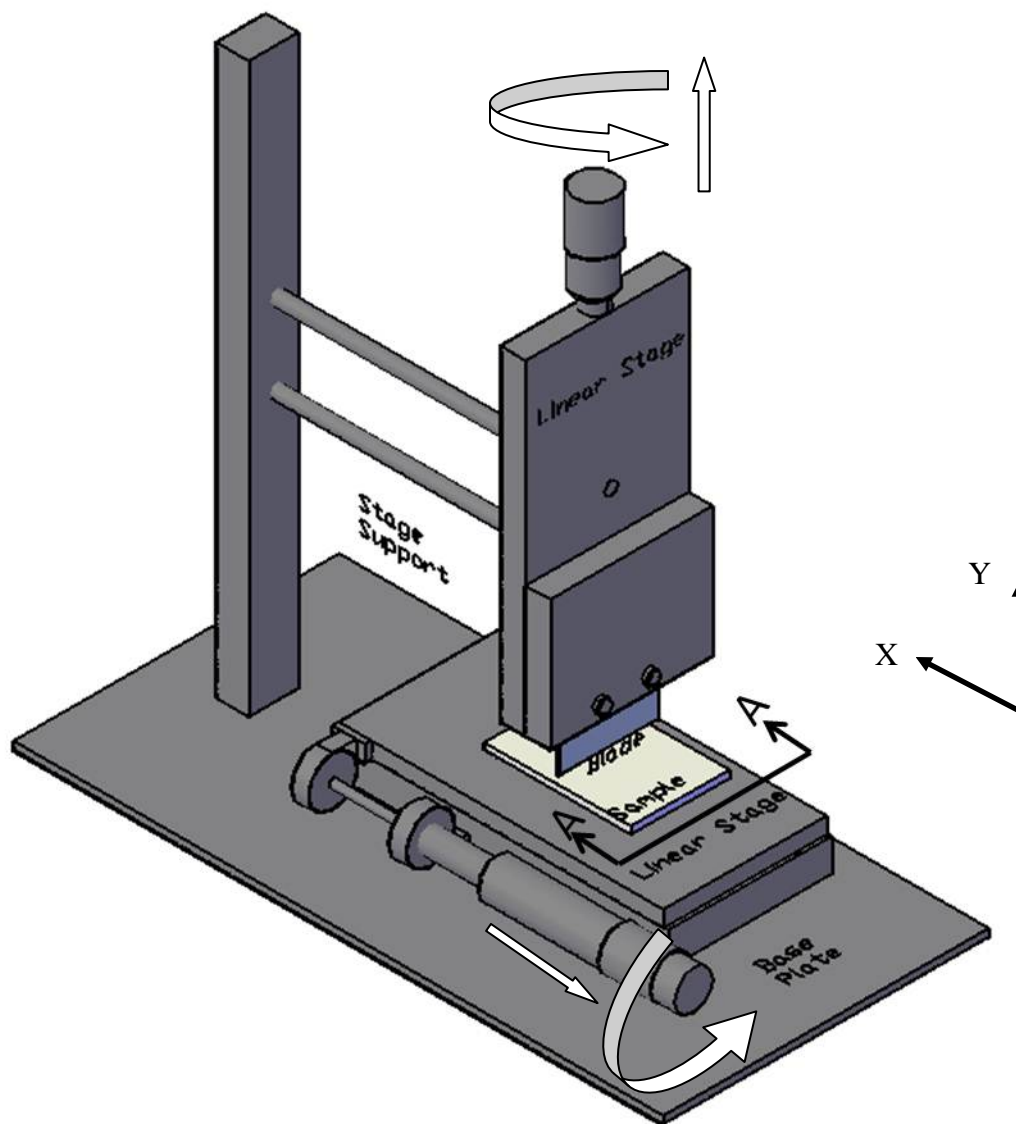


Figure 6.4. Schematic of the experimental setup for cutting sample membranes to detect nanoparticles embedded inside (if any).

6.3 Experimental results: penetration into pores

The top view of the dried glass fiber membrane and the side view of its cut cross-section at the location where the penetration depth was maximal (Fig. 6.5) reveal the nanoparticle deposition domain. After a drop impacts onto the front surface of the membrane,

it spreads over it, as well as some part of the suspension penetrates into the pores. Nanoparticles are entrained by the solvent flow until they are intercepted by the glass fibers in the membrane. The entire domains with the deposited nanoparticles and their boundaries are clearly visible at the front surface of the membrane and in its depth. It should be emphasized that the characteristic time of nanoparticle entrainment by flow evaluated as $\tau = 2\rho_{\text{part}} a_{\text{part}}^2 / 9\mu$ (with ρ_{part} being particle density, a_{part} its radius, and μ being liquid viscosity) is of the order of 10^{-9} s. Compared to the penetration time of the order of 10-100 μs , it shows that our nanoparticles were fully entrained by liquid flow inside the membrane until they ultimately touch the pore wall and were intercepted there.

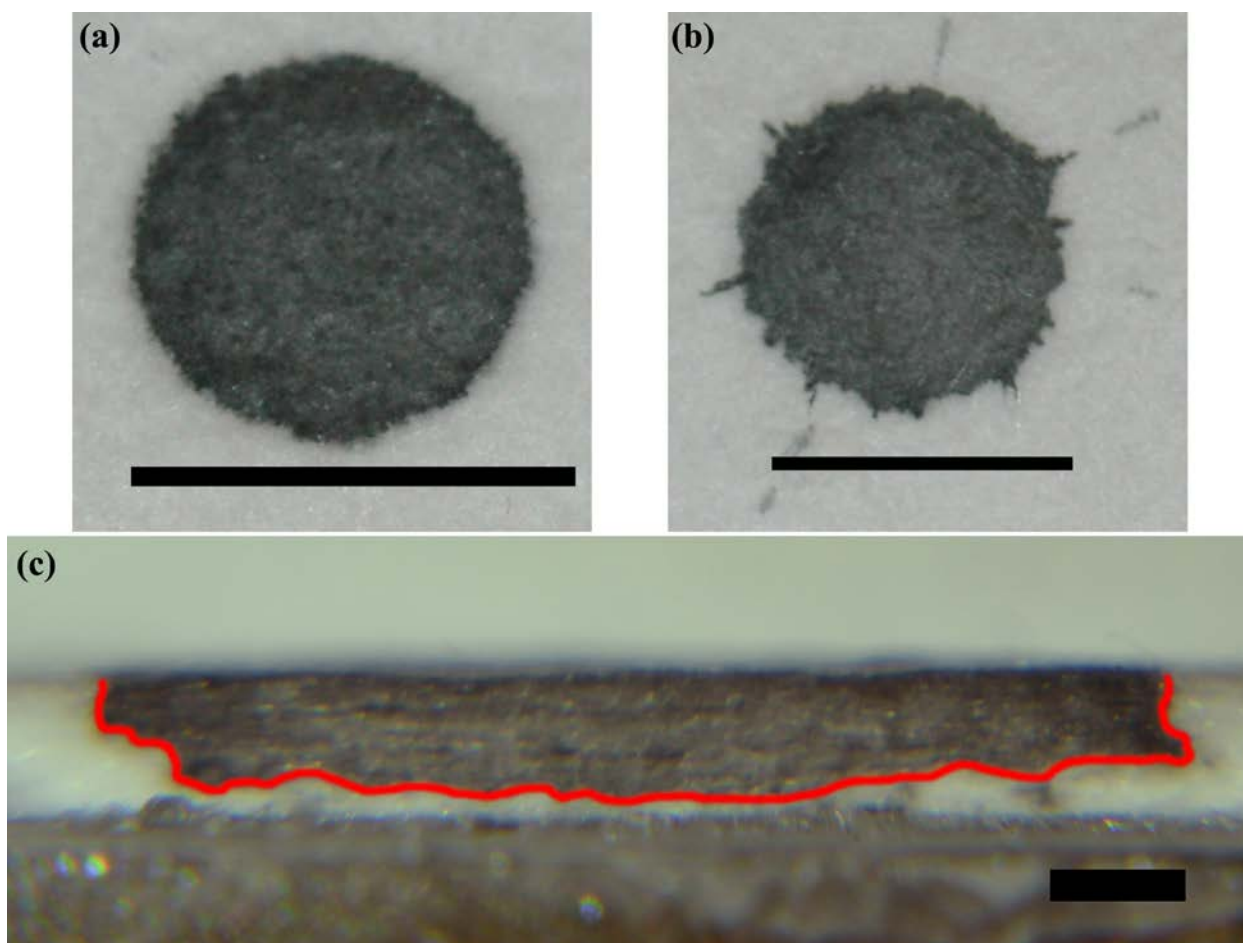


Figure 6.5. Top views of the glass fiber membrane after drop impact at 1.4 m/s [panel (a)] and 3.49 m/s [panel (b)]: the final domains of the nanoparticle deposition at the membrane surface. The impact velocities were measured at the impact moment. Drops were formed using a 14G needle. Scale bars: 1cm. (c) The side view of the cut cross-section of the membrane corresponding to the maximum penetration depth of a drop which impacted at 1.4 m/s: the nanoparticle distribution in depth. The lower boundary of the deposition domain is traced by the red line. Scale bar: 1mm. In all the images the membrane domains with no nanoparticles deposited look white, while those with the deposited nanoparticles look black. In panel (c) the dark strip under the membrane is the supporting Aluminum plate.

A partial bouncing and splashing after a drop impact is characteristic of non-wettable membranes. Figure 6.6 compares the outcome of the suspension drop impact onto a non-wettable PTFE membrane with that of the impact onto a wettable glass fiber membrane. The splashing patterns seen from the top are drastically different in these cases, with splashing on the non-wettable PTFE membrane being much more pronounced. However, it has been shown earlier [Sahu et al. (2012)], that above a certain threshold impact velocity, the static wettability of the surface does not play any significant role in penetration of water drops into porous media due to the hydrodynamic focusing. In the present case, there was no visible penetration of water into the non-wettable PTFE membrane in the 0-100 cm range of the impact heights, in distinction from the glass fiber membrane. However, when the impact height was 180 cm, a central fraction of the primary drop indicated in Fig. 6.6a by arrow at the frame corresponding to $t = 8$ ms penetrated through the non-wettable PTFE membrane.

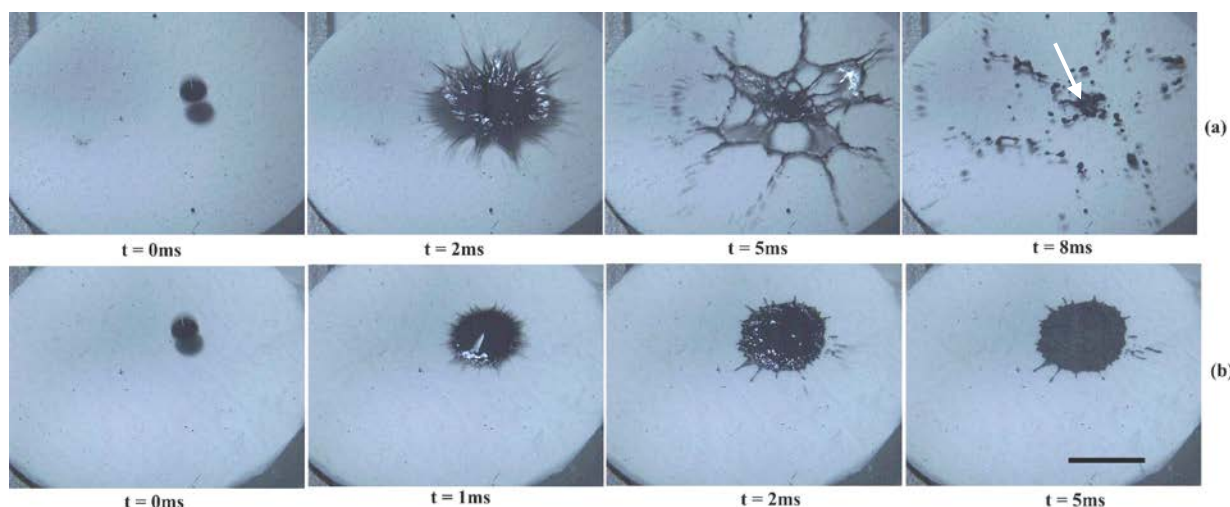


Figure 6.6. Sequence of images of drops of aqueous suspensions of nanoparticles impacting onto: (a) PTFE membrane, and (b) glass fiber membrane. The drops were issued from a 14G needle at the height of 180 cm, and had the impact velocity of 5.32 m/s (measured at the impact moment). Scale bar is 1cm.

Drop penetration visualized by nanoparticle entrainment into non-wettable PTFE membranes is the main aim of the present work. Five different impact velocities of 5.32 m/s, 5.64 m/s, 6.05 m/s, 6.47 m/s and 6.8 m/s where drop penetration happens were employed, and at each of them six trials were done. After the experiments the samples were cut in two different directions: (i) beginning from the drop impact surface, and (ii) in the opposite direction (see Figs. 6.7a and 6.7b, respectively). It was observed that the cutting direction affects the depth of the area of nanoparticle deposition inside the membrane, which means that the membrane material with the attached nanoparticles can be shifted to some extent by the razor blade. Overall, the experiments demonstrated that the seeding nanoparticles suspended in liquid drops can penetrate to a significant depth into non-wettable PTFE membranes being entrained by water flux.

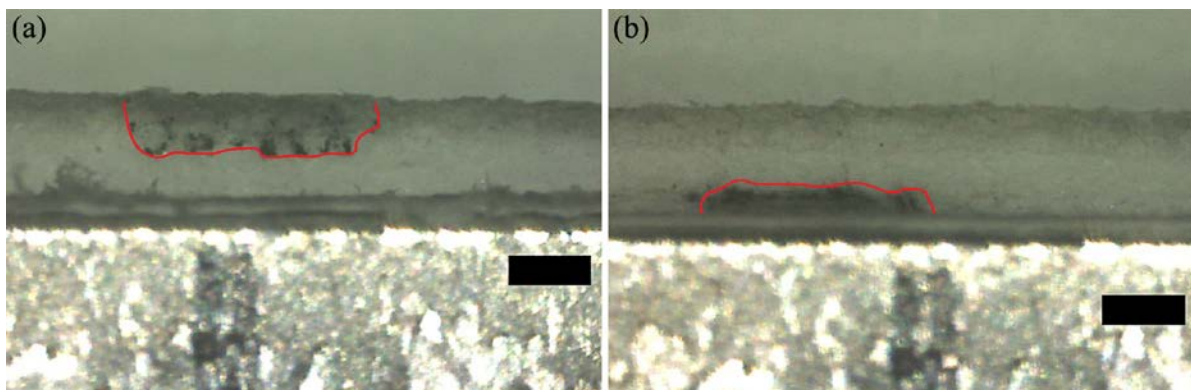


Figure 6.7. The side view of the cut cross-section of PTFE depth membranes at the locations corresponding to the maximal penetration depth. Panel (a) corresponds to the case when the membrane was cut beginning from the surface where the drop impact took place, whereas panel (b) shows the cut done in the opposite direction. The drops were issued from a 14G needle from the height of 180 cm, and had the impact velocity of 5.32 m/s (measured at the impact moment). The boundaries of the nanoparticle domains are traced by the red lines. Scale bars are 1 mm.

To minimize the effect of the cutting direction on the measured ultimate penetration depth, the average profiles found in the cuts beginning from the drop impact surface, and in the opposite direction are used further on for comparison with the theoretical predictions (see Figs. 6.8 and 6.9).

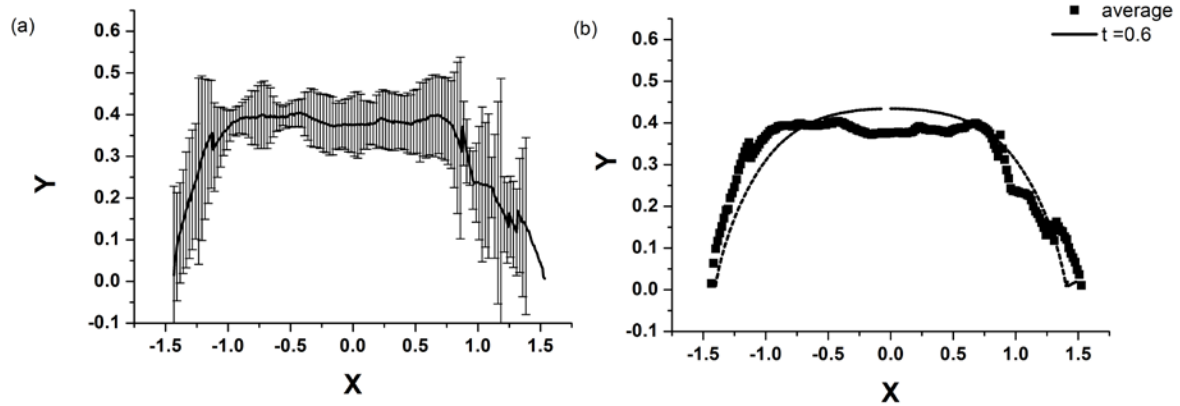


Figure 6.8. (a) The experimentally measured ultimate penetration front into PTFE depth membrane is shown by symbols with the error bars corresponding to variance within different samples. (b) The predicted penetration front corresponding to the dimensionless time $t=0.6$. The drops were issued from a 14G needle. The impact height was 180 cm and the corresponding impact velocity was 5.32 m/s. The coordinates are rendered dimensionless using the membrane thickness h . As discussed in detail in section 6.5, time is rendered dimensionless by h/U_p ; $b=0.8$ (this value of b corresponds to a 26 μl drop impacting onto a membrane of thickness $h=0.1$ cm, with liquid penetrating with $\bar{a} = 0.435$).

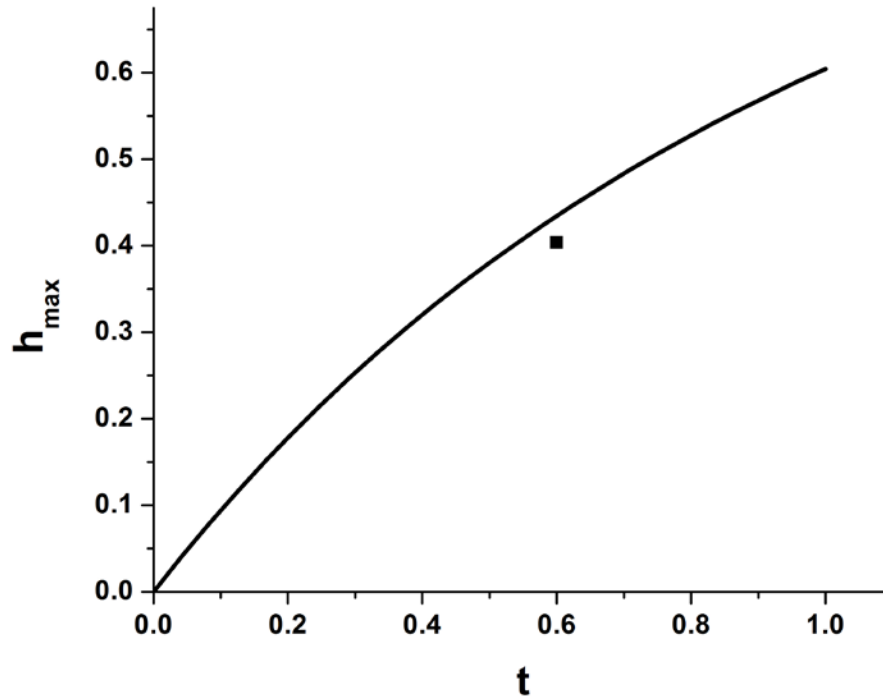


Figure 6.9. The ultimate point of nanoparticle deposition corresponding to the results of Fig. 8 is shown by the symbol (PTFE depth membrane). The predicted locations of the tip of the water propagating front are shown by line, which is extended beyond the visible ultimate deposition of nanoparticles. Time is rendered dimensionless by h/U_p .

The three-dimensional reconstruction of the domain where nanoparticles were deposited inside the non-wettable membrane by penetrating water is shown in Fig. 6.10. The data was acquired using 7 different cuts across the drop stain at the surface, as shown in the inset in Fig. 6.10.

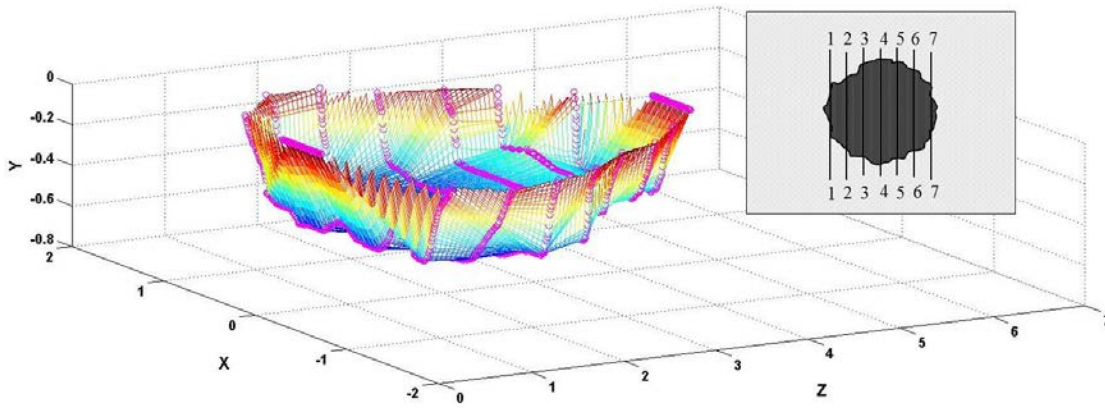


Figure 6.10. Three-dimensional reconstruction of the penetration domain in PTFE membrane seeded by nanoparticles using data acquired from different sections of the drop impact surface. The drops were issued from a 14G needle, and cuts were done from the drop impact surface. The impact height was 180 cm and the corresponding impact velocity was 5.32 m/s. The inset shows a sketch of the cuts used in the reconstruction. The colors signify the depth at various points and correspond to the y-axis.

It should be emphasized that in the present case the dynamic pressure in liquid at the moment of impact (the ambient pressure is obviously not important) is less than the capillary pressure. Indeed, in the present case $\rho V_0^2 = 2.83 \times 10^5 \text{ g}/(\text{cm s}^2)$, and $4\sigma/d \geq 2.88 \times 10^5 \text{ g}/(\text{cm s}^2)$, whereas the static penetration condition requires ρV_0^2 to be sufficiently larger than $4\sigma/d$ [Bazilevsky et al. (2008)]. Therefore, water penetration into the PTFE membrane illustrated in Figs. 6.7-6.9 is clearly due to the hydrodynamic focusing, exactly as in [Lembach et al. (2010); Sahu et al. (2012); Sinha-Ray et al. (2011); Weickgenannt et al. (2011a) and Weickgenannt et al. (2011b)], where velocities and pore sizes were even smaller, and ρV_0^2 was much less than $4\sigma/d$.

For comparison consider the results of numerical modeling of drop impact onto a system of parallel, not interconnected capillaries, which was studied as a model of porous medium in [Ding and Theofanous (2012)] (cf. Fig. 20 there). If water is implied as the liquid in the drop, the dimensionless Reynolds and Weber numbers corresponding to Fig. 20 in [Ding and Theofanous (2012)] reveal the impact velocity of $V_0=388.3$ cm/s and the drop radius of 0.028 cm, as the parameters studied. Figure 20 in [Ding and Theofanous (2012)] also shows 3 capillaries per drop, which yields the capillary diameter d as $d=0.0187$ cm. In this case the drop diameter $D=0.056$ cm is pretty close to that of the capillary size, therefore this is definitely not the case where the hydrodynamic focusing is expected. However, since in Fig. 20 in [Ding and Theofanous (2012)] the value of $\rho V_0^2 = 1.51 \times 10^5$ g/(cm s²), whereas $4\sigma/d = 1.54 \times 10^4$ g/(cm s²), i.e. $\rho V_0^2 \gg 4\sigma/d$, and in addition capillaries are rather wettable, water penetration is possible without the effect of hydrodynamic focusing. It should be emphasized that water penetration into porous medium after drop impact is definitely possible if $\rho V_0^2 \gg 4\sigma/d$, however, under the conditions of the hydrodynamic focusing (when drop diameter D is much larger than the pore diameter d) water penetration is also possible when $\rho V_0^2 < 4\sigma/d$, an unexpected fact from the perspective of the static penetration condition. This fact is also corroborated by the remarkable experimental results in [Brunet et al. (2009)] where the threshold values corresponding to water penetration after drop impact onto a grid revealed that penetration is possible when $\rho V_0^2 / (4\sigma/d) \approx 0.05$.

The part of the primary drop which does not penetrate into the membrane forms secondary droplets which roll off the upper surface of the PTFE membrane. In the case of the glass fiber membrane, splashing at the upper surface is diminished, as well as a wider puddle of water penetrates through the membrane, as is seen in Fig. 6.5b. The latter, however,

cannot be completely attributed to the dynamic penetration (the hydrodynamic focusing), since the slower wettability-driven flow of nanoparticle suspension inside the membrane is sustained for a long time after the impact.

The dynamic spreading of a drop over porous media is different from that over the impermeable substrates [Yarin (2006) and Weickgenannt et al. (2011b)]. The impact velocity, surface tension, solvent viscosity, surface roughness, pore size, wettability and permeability of the porous medium affect the flow resulting from drop impact. Drop spreading over the impermeable surfaces is usually characterized by the spread factor [Yarin (2006)] with the following empirical relation widely used [Scheller and Bousfield (1995)]

$$\zeta = 0.61(\text{Re}^2 \text{Oh})^{0.166} = 0.61 \left(\frac{\text{We}}{\text{Oh}} \right)^{0.166} \quad (6.1)$$

where $\zeta = 2R_{\max}/D$, with R_{\max} being the ultimate spreading radius, D the drop volume-equivalent diameter, and the Reynolds, Ohnesorge and Weber numbers given by

$$\text{Re} = \frac{\rho D V_0}{\mu}, \quad \text{Oh} = \frac{\mu}{(\rho \sigma D)^{1/2}}, \quad \text{We} = \frac{\rho D V_0^2}{\sigma} \quad (6.2)$$

In Eq. (6.2) the impact velocity is denoted as V_0 , and the density, viscosity and surface tension of liquid are ρ , μ and σ , respectively. Then, the dimensional expression for the spreading diameter is $2R_{\max} = \rho^{0.249} D^{1.249} V_0^{0.332} \sigma^{-0.083} \mu^{0.166}$. It should be emphasized that the empirical Eq. (6.1) is fully confirmed by the numerical and theoretical predictions of the more recent work [Eggers et al. (2010)]. Indeed, the maximal drop spreading which determines the spread factor ζ available according to the numerical and modeling results in Fig. 9 in [Eggers et al. (2010)] reveals the value of $\zeta \approx 3.2$ for $\text{We}=\text{Re}=800$. This is exactly the value which is found from Eq. (6.1) with $\text{We}=\text{Re}=800$. Similarly, the recent experiments

in Fig. 3 in [Lagubeau et al. (2012)] revealed for $We=214$ and $Re=2690$ the value of $\zeta \approx 3.5-3.6$, whereas Eq. (6.1) yields $\zeta \approx 3.53$.

The values of the spread factor ζ in the present experiments with drop impacts onto the porous glass fiber membrane where splashing was minimal could be easily established. They are contrasted in Table 6.1 with those predicted by Eqs. (6.1) and (6.2) for an impermeable medium. It is clearly seen that Eqs. (6.1) and (6.2) significantly overestimate the measured values of the spread factor. In the experiments the spread factor is diminished due to liquid penetration into the pores [Starov et al. (2003)]. It should be emphasized that the experimental values of the spread factor at $V_0=0$ m/s correspond to purely wettability-driven spreading, for which no comparable value can be obtained using Eqs. (6.1) and (6.2).

Table 6.1. Spread factor measured for drop impact onto the glass fiber membrane at different impact velocities. The experimental results listed in the table are the averages of two duplicate experiments.

Needle gauge	Impact velocity V_0 (m/s)	Weber Number (We)	Spread factor ζ (experimental, on porous medium)	Spread factor ζ [by Eqs. (1) and (2) corresponding to an impermeable surface]	δ	Drop volume (μl)
14G	0	0	2.21	-		26
	1.45	107.3	2.37	3.53	1.49	
	2.64	355.5	2.78	4.31	1.55	
	3.5	624.9	2.91	4.73	1.63	
18G	0	0	1.87	-		17
	1.47	95.4	2.25	3.42	1.52	
	2.95	384.0	2.61	4.31	1.65	
	3.92	678.1	2.70	4.74	1.76	

Table 6.1 shows that for 26 μl drops the ratio δ of the calculated spread factor for the impermeable surface [Eqs. (6.1) and (6.2)] to the one measured experimentally increases from 1.49 to 1.63 as the impact velocity increases from 1.45 m/s to 3.5 m/s, and for 17 μl drops from 1.52 to 1.76 in the 1.47 m/s to 3.92 m/s velocity range. This clearly is associated with liquid penetration into the membrane. The data in Table 6.1 show that the spread factor

measured at the same impact velocity is higher for the larger drops compared to the smaller ones. Note also, that the spread factor on the porous medium in the range $2.21 < \zeta < 2.7$ measured in the experiments of the present work (Table 6.1) is close to the prediction $\zeta \approx 2.6$ in Fig. 4 in the numerical simulations in [Reis Jr et al. (2008)].

For the non-wettable PTFE membrane, splashing is so significant (Fig. 6.6a) that reliable measurements of the spread factor ζ are impossible.

6.4 Theoretical model

6.4.1 Drop impact and penetration into a single pore

In the experiments on drop impact onto surfaces coated with electrospun nanofiber mats drop sizes are typically of the order of $D \sim 10^{-2} - 10^{-1} \text{ cm}$, the pore sizes are of the order of $d \sim 2 \times 10^{-3} \text{ cm}$, and the impact velocity $V_0 \sim 1-3 \text{ m/s}$ (the present experiments and Sinha-Ray et al. (2011); Weickgenannt et al. (2011a) and Weickgenannt et al. (2011b)). Drop impact onto a single pore can be considered as an abrupt impact of a solid wall with a gap (orifice) in the middle onto a semi-circular liquid domain (Fig. 6.11, where the planar case is assumed for simplicity). The assumption of a semi-circular liquid domain at the beginning of water penetration is an approximation, albeit a realistic one, according to the experimental observations of [Brunet et al. (2009)], and the numerical modeling of [Ding and Theofanous (2012)], since sheet jetting below the impacting drop is extremely fast (on the scale of $10 \text{ } \mu\text{s}$). Moreover, it should be emphasized that as Eq. (6.18) obtained below in the present work shows, a detailed shape of liquid over a pore (semi-circular or a half-plane) makes practically no difference in the initial rate of water penetration when the drop size D is much larger than the pore size d , as in the present case.

Note also, that the expected dynamic effects in the present case are so dominant according to Lembach et al. (2010); Sahu et al. (2012); Sinha-Ray et al. (2011); Weickgenannt et al. (2011a) and Weickgenannt et al. (2011b), that surface tension at the liquid front penetrating into the pore would be negligible, and the situation under consideration is radically different from the one in [Lorencean and Quere (2003)] where the dynamic effects were relatively weak, while surface tension determined the penetration threshold.

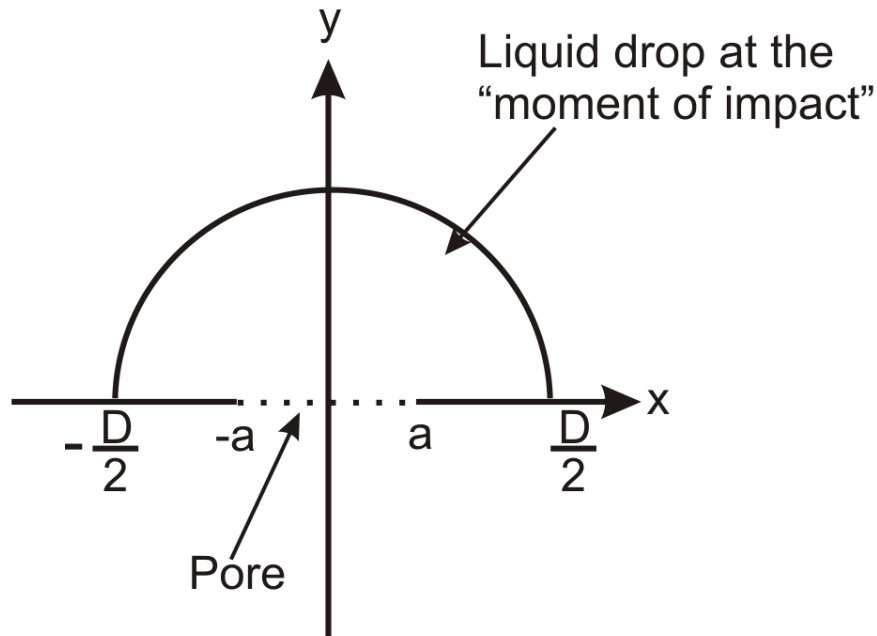


Figure 6.11. Sketch of drop impact onto a single pore.

The initial flow development after the impact is determined by the pressure impulse

$$\Pi = \lim_{\substack{\tau \rightarrow 0 \\ \Delta p \rightarrow \infty}} \int_0^{\tau} \Delta p dt \quad (\text{where the overpressure } \Delta p \rightarrow \infty, \text{ and the impact duration } \tau \rightarrow 0). \quad \text{The}$$

pressure impulse is of the order of one [Lembach et al. (2010)]. The pressure impulse is applied to the drop at $-D/2 < x \leq -a$, $y = 0$ and $a \leq x < D/2$, $y = 0$. The arising flow is

potential, with the flow potential $\varphi = -\Pi/\rho$ being a harmonic function, i.e. satisfying the Laplace equation [Batchelor (1981)]

$$\frac{\partial^2 \varphi}{\partial x^2} + \frac{\partial^2 \varphi}{\partial y^2} = 0 \quad (6.3)$$

The value of the pressure impulse was evaluated as [Lembach et al. (2010)] $\Pi \approx \rho V_0 D$.

In Eq. (6.3) and hereinafter the coordinates x and y and the pore half-width are rendered dimensionless by the drop radius $D/2$ (with the dimensionless $\bar{a} = 2a/D$), and the potential φ – by $V_0 D$. Below the bars over the dimensionless parameters are omitted for brevity. Therefore, the dimensionless boundary conditions imposed on the solution of Eq. (6.3) in the present case read

$$\varphi(x, y=0) = \varphi_0 = -1 \text{ over } -1 \leq x \leq -a \text{ and over } a \leq x \leq 1 \quad (6.4)$$

$$\varphi(x, y=0) = 0 \text{ over } -a < x < a \quad (6.5)$$

$$\varphi(x, y) = 0 \text{ at } x^2 + y^2 = 1, y > 0 \quad (6.6)$$

In particular, the boundary condition (6.5) implies that at the opening there is no impulse transmitted to the impacted liquid, i.e. the overpressure there is equal to zero. It is easy to see that the interior of the semi-circle corresponding to the liquid domain in the complex plane $z=x+iy$ in Fig. 6.12a is conformally mapped onto the upper half-plane $\omega = \xi + i\eta$ (with i being the imaginary unit) in Fig. 6.12b by the following mapping function (which is easy to see by the boundary correspondence) [Mathews and Howell (2006)]

$$\omega = \left(\frac{1+z}{1-z} \right)^2 \quad (6.7)$$

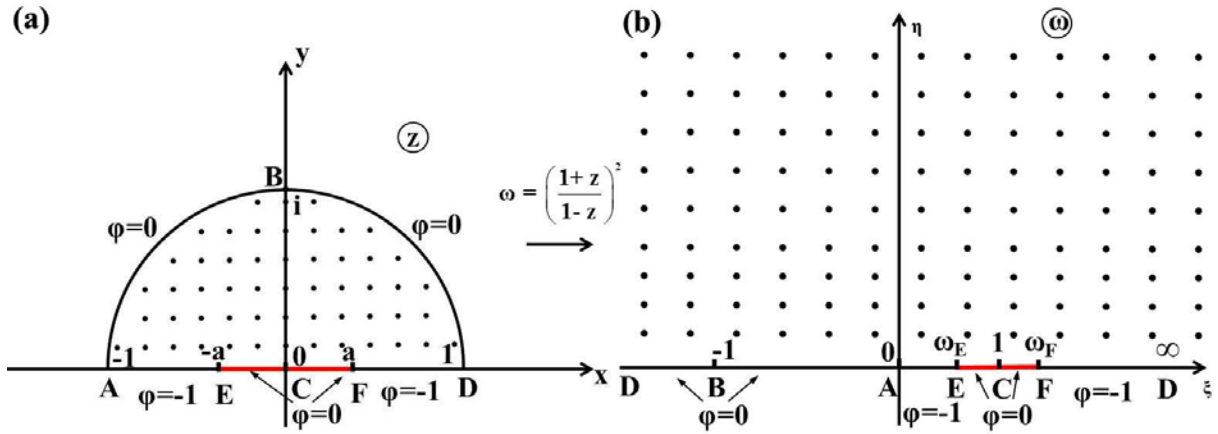


Figure 6.12. Conformal mapping onto the upper half-plane.

Accordingly, the boundary conditions (6.4)-(6.6) take the following form in the ω -plane

$$\varphi = 0 \text{ at } -\infty \leq \xi < 0 \quad (6.8)$$

$$\varphi = -1 \text{ at } 0 \leq \xi < \xi_E \quad (6.9)$$

$$\varphi = 0 \text{ at } \xi_E \leq \xi < \xi_F \quad (6.10)$$

$$\varphi = -1 \text{ at } \xi_F \leq \xi < \infty \quad (6.11)$$

where the mapped ξ -coordinates of points E and F are given by

$$\xi_E = \left(\frac{1-a}{1+a} \right)^2, \quad \xi_F = \left(\frac{1+a}{1-a} \right)^2 \quad (6.12)$$

The field of the harmonic potential $\varphi(\xi, \eta)$ in the upper half-plane with the boundary conditions imposed at the real axis (6.8)-(6.11) is given by Poisson's integral formula for the upper half-plane [Polya and Latta (1974)]

$$\varphi(\xi, \eta) = \frac{\eta}{\pi} \int_{-\infty}^{\infty} \frac{\varphi(\kappa, 0)}{(\kappa - \xi)^2 + \eta^2} d\kappa \quad (6.13)$$

where κ is a dummy (real) variable.

The integral in Eq. (6.13) is evaluated using Eqs. (6.8) - (6.11), and the resulting flow potential needed to calculate the initial flow through the pore is found as

$$\varphi(\xi, \eta) = -\frac{1}{\pi} \left[\arctan\left(\frac{\xi_E - \xi}{\eta}\right) + \arctan\left(\frac{\xi}{\eta}\right) + \frac{\pi}{2} - \arctan\left(\frac{\xi_F - \xi}{\eta}\right) \right] \quad (6.14)$$

The expression for the potential $\varphi(\xi, \eta)$ (6.14) is recast into $\varphi(x, y)$ using the fact that the conforming mapping (6.7) is identical to the following coordinate transformation

$$\xi = \frac{(1 - x^2 - y^2)^2 - 4y^2}{[(1 - x)^2 + y^2]^2}, \quad \eta = \frac{4y(1 - x^2 - y^2)}{[(1 - x)^2 + y^2]^2} \quad (6.15)$$

The corresponding velocity vector is $\mathbf{v} = \nabla\varphi$. Therefore, the dimensionless y-component of \mathbf{v} over the pore $-a < x < a$ is found as

$$v_{\text{pore}}(x) = \left. \frac{\partial\varphi}{\partial y} \right|_{y=0} = -\frac{4(1 - x^2)}{\pi(1 - x)^4} \left[-\frac{1}{(\xi_E - K)} - \frac{1}{K} + \frac{1}{(\xi_F - K)} \right], \quad K = \frac{(1 - x^2)^2}{(1 - x)^4} \quad (6.16)$$

The latter shows that at the center of the pore entrance the dimensionless y-component of velocity

$$v_{\text{pore}} \Big|_{x=0; y=0} = -\frac{2(1 - a)^2}{\pi a} \quad (6.17)$$

The corresponding dimensional velocity component toward the pore at its center is

$$U_p = -\frac{4D}{\pi d} V_0 \left(1 - \frac{d}{D} \right)^2 \quad (6.18)$$

It should be emphasized that this penetration velocity U_p is much larger than the drop impact velocity V_0 , since the ratio $D/d \gg 1$ ($d=2a$). Equation (6.18) is also in agreement with the result of Lembach et al. (2010) where the impacting drop was considered as a complete upper half-plane rather than the semi-circle of Fig. 6.12a. In particular, Eq. (6.18) recovers the result of Lembach et al. (2010) in the limit $D/d \rightarrow \infty$, $U_p = -(4D/\pi d)V_0$. Also, as in Lembach et al. (2010), the y-component of velocity diverges at the sharp edges of the pore, i.e. according to Eq. (6.16)

$$v|_{x=\pm a} = -\infty \quad (6.19)$$

On the other hand, at the contact line of the drop it acquires high positive vertical velocity, since according to Eq. (6.16)

$$v|_{x=\pm 1} = \infty \quad (6.20)$$

Note that in reality the singular velocity values will be restricted by viscosity as was discussed previously [Lembach et al. (2010)]. It should be emphasized that in the case of a drop impact onto porous media, liquid can penetrate into about 100 pores simultaneously [Sahu et al. (2012)]. Then, $2a$ should be considered as an effective penetration area and $a < 1$ ($d < D$), rather than $a \ll 1$ ($d \ll D$). An additional illustration of the potential distribution (6.14) in the drop after the impact onto a wall with a pore at the center is shown in Figs. 6.13a-c. Since the pressure values are related to $-\phi$, the regions with high pressure correspond to the deep-blue domains near the wall in these figures.

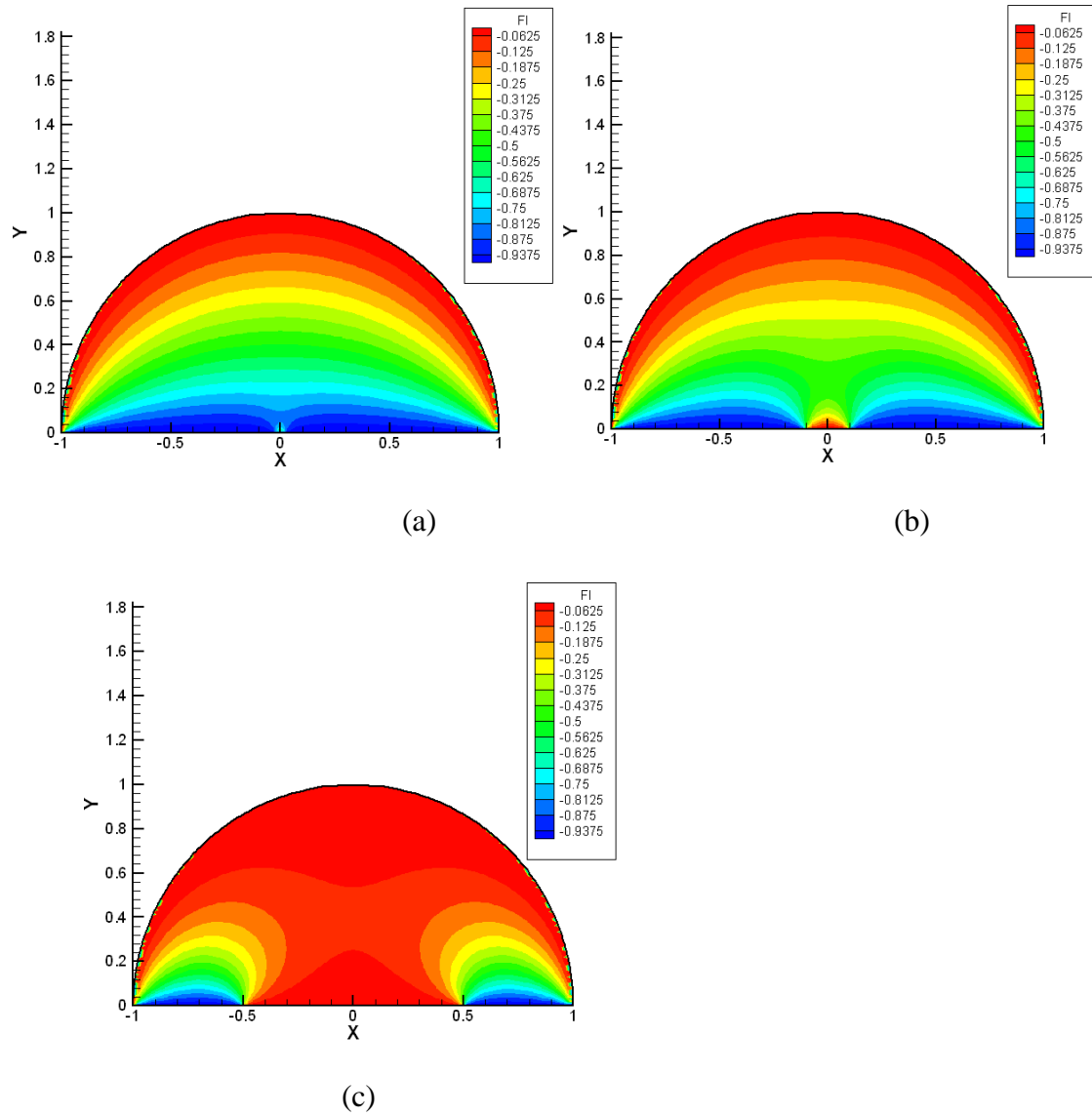


Figure 6.13. Potential distribution at the moment of impact. (a) $a = 0.01$, (b) $a = 0.1$, (c) $a = 0.5$ (remind that here a stands for the dimensionless \bar{a}).

The sharp pressure loss at the orifice at the moment of impact revealed by the results in Fig. 6.13 should produce a narrow liquid jet entering the pore at high speed. Such jets, indeed, were observed by the present group in the experiments with drop impact on

suspended membranes in [Sahu et al. (2012)], where Fluorinert fluids with very low surface tension were used to prevent jet merging at the rear side of the membrane. One of the experimental images of this type is shown in Fig. 6.14.

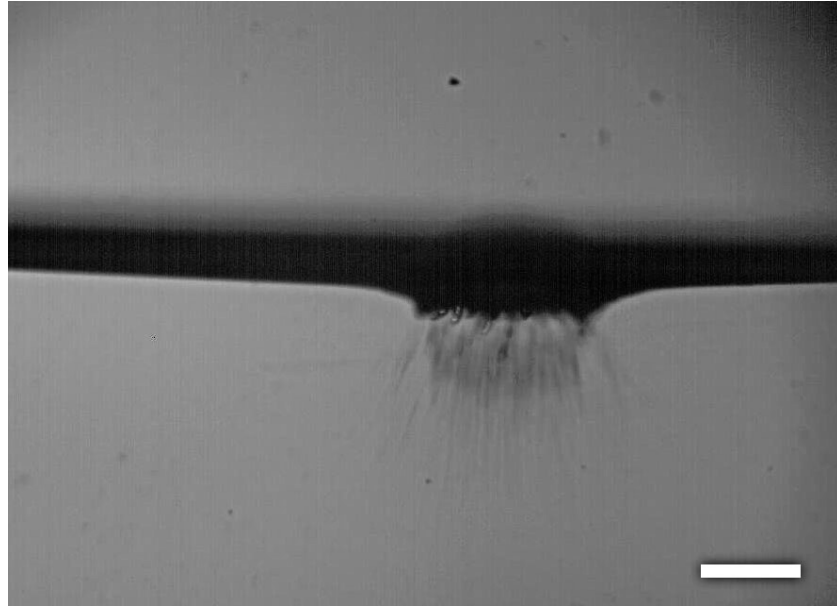


Figure 6.14. Impact of a drop of Fluorinert fluid FC 7500 onto a Nylon membrane with the impact velocity of 2.64 m/s. Scale bars, 1mm.

When a high pressure is applied to a diminishing mass of liquid near the contact line, there should be a propensity to a prompt splash in the form of liquid rising from the wall [Yarin (2006)] near the contact line, which is clearly expressed by the infinite vertical velocity there as per Eq. (6.20) (in reality restricted by viscosity). This phenomenon is similar to a finite impulse propagating over a whip near its edge: without energy losses the whip edge velocity would be infinite (since mass of the affected edge tends to zero); in reality there are energy losses, but the velocity is still very high and expresses itself as a whistle of the whip in air. The entire velocity distribution predicted by Eq. (6.16) at the drop bottom is depicted in Fig.

6.15. It shows that over almost the entire pore, the velocity is practically uniform and close to the central value given by Eqs. (6.17) and (6.18). The infinite velocity values at the pore edges, inevitable in the inviscid formulation, will be smoothened in reality by viscous shear stresses, as mentioned above [Lembach et al. (2010)].

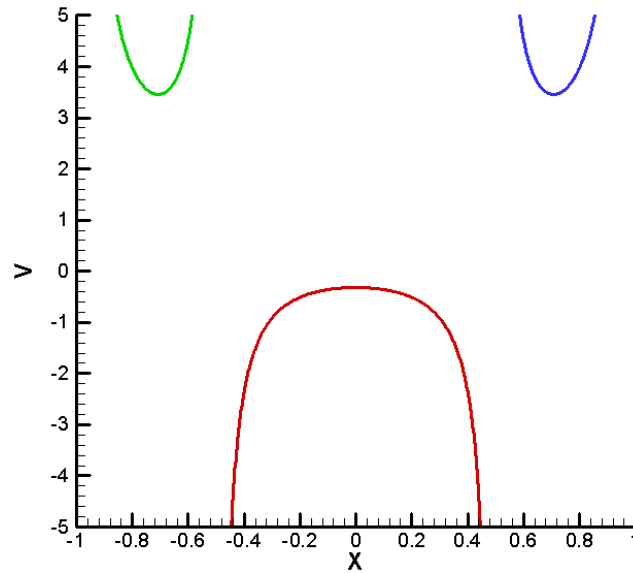


Figure 6.15. Velocity distribution at the drop bottom for a pore with $a = 0.5$. The red part corresponds to the pore, the green and blue parts – to the wall.

6.4.2 Forced liquid filtration inside membrane

After penetration into the inter-fiber pores in the membrane, liquid from the impacting drop is spreading according to Darcy's law, and its velocity \mathbf{v} possesses a potential φ related to pressure p as [Barenblatt et al. (1989) and Loitsyanskii (1966)]

$$\mathbf{v} = \nabla\varphi, \quad \varphi = -\frac{k}{\mu}p \quad (6.21)$$

where k is the permeability, and μ is the liquid viscosity.

According to Eq. (6.18), liquid can penetrate into porous medium with the velocity magnitude close to U_p given by the following expression

$$U_p = \frac{4}{\pi} \frac{D}{d} V_0 \quad (6.22)$$

Taking for the estimate $D=10^{-1}$ cm, $d=10$ μ m, and $V_0=1$ m/s, we find the initial penetration rate into a single pore as $U_p \approx 100$ m/s. The effective average filtration velocity v through tortuous pores in the porous medium involved in Darcy's law is defined as the volumetric flow rate divided by total (pores and solid fibers) cross-sectional area. It would be much less than the initial flow velocity along a single straight pore, approximately of the order of $v=1$ m/s (Sahu et al. (2012), evaluated by the velocities of the jets issued from the membranes). Then, the filtration Reynolds number $Re_{\text{filtration}} = \rho v d / \mu \approx 10$. Note, that on the depth scale of about 10-100 μ m it will rapidly diminish to the level of about $Re_{\text{filtration}} = 1$ due to the dissipation of the kinetic energy inside the pores [Sahu et al. (2012)]. Darcy's law is known to be applicable in the $Re_{\text{filtration}} \leq 10$ range [Charbeneau (2006)].

Consider a membrane sketched in Fig. 6.16. In the present case it is convenient not to use the complex potential $\chi(z) = \phi(x,y) + i\psi(x,y)$, with ψ being the stream function related to the

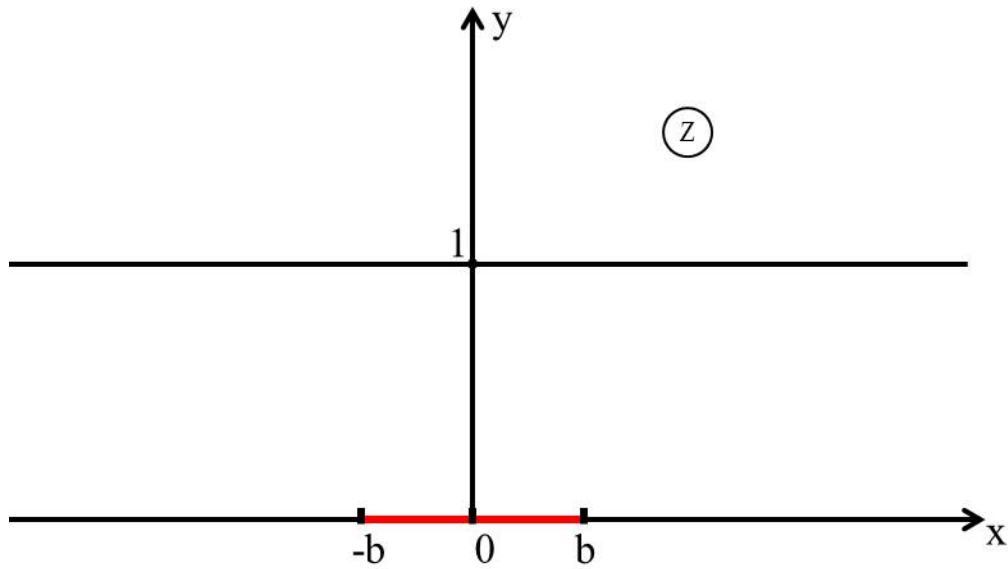


Figure 6.16. Sketch of the membrane which is impacted by a drop from below. The bottom of the spread-out drop corresponds to $-b \leq x \leq b$, $y = 0$. The coordinates x and y , as well as b are rendered dimensionless by the membrane thickness h . This means, in particular, that the dimensionless effective penetration width of liquid after drop impact $2\bar{a}$ of subsection 6.4.1 now becomes $2b = \bar{a}(D/h)$.

hydrodynamic potential ϕ by the Cauchy-Riemann conditions, but rather to employ another function of complex variable associated with the conjugate velocity $\bar{V} = d\chi/dz$, namely

$$i\bar{V}(z) = v + iu \quad (6.23)$$

where u and v are the x - and y -velocity components, respectively.

The real part of $i\bar{V}$ satisfies the following boundary conditions at the membrane surfaces

$$v|_{y=0} = U_p \quad \text{for } |x| \leq b \quad (6.24)$$

$$v|_{y=0} = 0 \quad \text{for } |x| > b \quad (6.25)$$

$$v|_{y=1} = 0 \quad (6.26)$$

In the domain shown in Fig. 6.16 the function $i\bar{V}(z)$ can be found from the boundary conditions for its real part at the surfaces using the Palatini formula which follows from the Schwartz formula for a disk [Henrici (1974) and Lavrentiev and Shabat (1973)]. The general solution thus obtained reads

$$i\bar{V}(z) = -\frac{i}{2} \int_{-\infty}^{\infty} v(\kappa, y=0) \coth \frac{\pi(\kappa-z)}{2} d\kappa + \frac{i}{2} \int_{-\infty}^{\infty} v(\kappa, y=1) \tanh \frac{\pi(\kappa-z)}{2} d\kappa \quad (6.27)$$

where κ is a dummy (real) variable over the entire x -axis. It should be emphasized that if z is located at any of the domain surfaces, the first integral in Eq. (6.27) is evaluated in the Sochocki-Plemelj sense.

Note that the velocity field (6.27) corresponds to the situation where liquid has already spread throughout the entire domain of a thin membrane. However, it is tempting to use it to predict the liquid front propagation, since the membranes of interest are thin.

Substituting the boundary conditions (6.24)-(6.26) into Eq. (6.27), we arrive at

$$i\bar{V}(z) = -\frac{iU_p}{2} \int_{-b}^b \coth \frac{\pi(\kappa-z)}{2} d\kappa \quad (6.28)$$

which yields inside the domain

$$i\bar{V}(z) = U_p - \frac{iU_p}{\pi} \ln \left\{ \frac{\sinh[\pi(b-z)/2]}{\sinh[\pi(b+z)/2]} \right\} \quad (6.29)$$

Correspondingly, the velocity components u and v rendered dimensionless by U_p are given by the following dimensionless expressions inside the domain

$$u(x, y) = \operatorname{Re} \left(-\frac{1}{\pi} \ln \left\{ \frac{\sinh [\pi(b-z)/2]}{\sinh [\pi(b+z)/2]} \right\} \right) \quad (6.30)$$

$$v(x, y) = 1 + \operatorname{Im} \left(\frac{1}{\pi} \ln \left\{ \frac{\sinh [\pi(b-z)/2]}{\sinh [\pi(b+z)/2]} \right\} \right) \quad (6.31)$$

with $\operatorname{Re}(\bullet)$ and $\operatorname{Im}(\bullet)$ denoting the real and imaginary parts, respectively.

Then, the liquid front propagation is tracked by the following kinematic equations

$$\frac{dX(s)}{dt} = u[X(s), Y(s)] \quad (6.32)$$

$$\frac{dY(s)}{dt} = v[X(s), Y(s)] \quad (6.33)$$

where s is the Lagrangian parameter of a liquid element at the filtration front at $t=0$, and X and Y are the current x and y coordinates of this element, respectively, which satisfy the following initial conditions

$$t = 0, \quad X = s \text{ with } -b \leq s \leq b, \quad Y \rightarrow 0 \quad (6.34)$$

Time t is rendered dimensionless by h/U_p where h is the membrane thickness, and X , Y and s are rendered dimensionless by h .

It should be emphasized that, as it was mentioned above, the potential distribution in the complete half-plane or a semi-circle, produce an almost identical potential (and thus flow) fields near the impact surface, as the comparison of the present results based on the conformal mapping (6.7) depicted in Fig. 6.12 and those of Lembach et al. (2010) showed. This corroborates the idea to use the flow field (6.30) and (6.31) even at the early stages of the filtration front propagation as is implied by Eqs. (6.32)-(6.34).

The system of Eqs. (6.32) and (6.33) with the velocity components from Eqs. (6.30) and (6.31) and the boundary conditions (6.34) was integrated numerically using the Kutta-Merson method. Some representative results are shown in Fig. 6.17. It should be emphasized that as $t \rightarrow \infty$ the filtration front would continue to widen after it has reached the rear side of the strip. The reason for that is that the boundary condition (6.24) implies that water pumping into membrane will continue forever. In the experiments with drop impact, however, water is supplied through the membrane boundary only on the scale of $t=0.6$ (see Fig. 6.8b and section 5.1 below). Therefore, water spreading outside the filtration front corresponding to $t=0.6$ in Fig. 6.17 is impossible in the non-wettable membranes used in the present work. Note also that the flow velocity in the mat rapidly becomes very small due to viscous dissipation discussed in detail in section 5.2 below. That, implies, as the experimental data show (see section 5.1 below), that the nanoparticle transport ceases at $t=0.6$, and the furthest boundary marked by the nanoparticles visualizes an effective ultimate filtration front. A detailed comparison of such predictions with the experimental data is shown in Figs. 6.8 and 6.9 and is discussed in the following section.

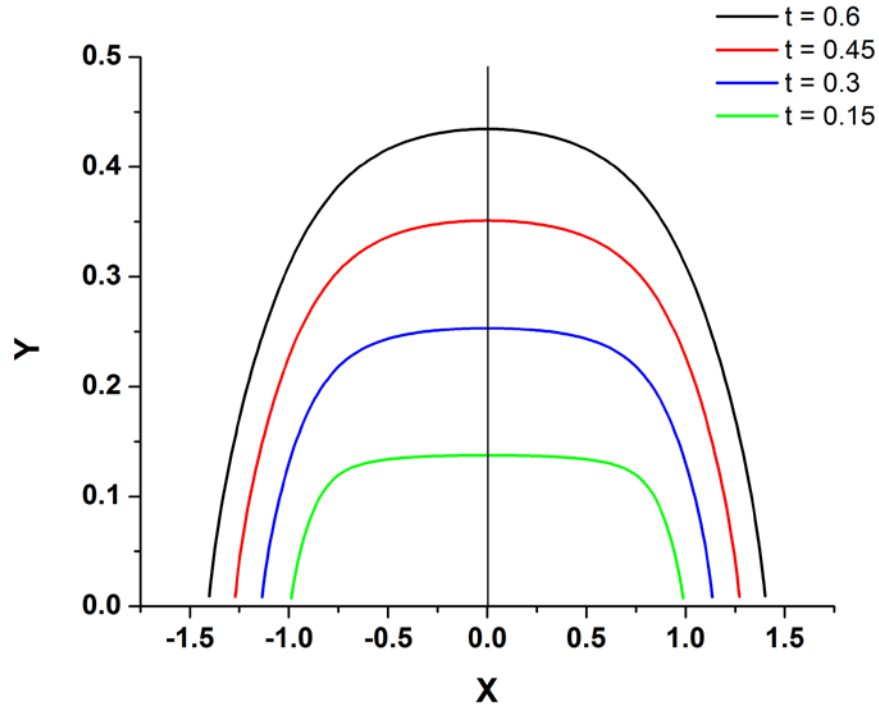


Figure 6.17. Filtration front configurations at the dimensionless time moments shown in the inset. Time shown in the inset is rendered dimensionless by h/U_p . In the present case $b=0.8$.

6.5 Discussion: theory versus experiment

6.5.1 Penetration fronts

The liquid which filtrates through the membrane after a suspension drop impact is seeded with nanoparticles which are gradually intercepted by the pore walls. Therefore, the outer boundaries of the visible nanoparticle domains in the cut cross-sections observed experimentally (cf. Fig. 6.5c and Figs. 6.7a, 6.7b, 6.8 and 6.10) visualize the filtration fronts where water flow was already so weak (due to viscous dissipation) that it could not move or pull nanoparticles more. Such a front is termed the ultimate filtration front.

The predicted configurations of the filtration fronts at different time moments similar to those in Fig. 6.17 were compared to the experimentally measured configurations shown in Figs. 6.8 and 6.9 for the PTFE membranes, which are unaffected by wettability-driven flow. In Fig. 6.8 the measured ultimate penetration front inside the PTFE membrane is compared to the predicted front at time moment $t=0.6$. The predicted penetration front is sufficiently close to the experimentally observed front. This front thus corresponds to the dimensional time moment $t = 0.6h / U_p$. Taking for the estimate $h=0.1$ cm and $U_p \approx 10^2$ m/s, we find that the ultimate front has been reached in 6 μ s. The result is plausible, since according to Fig. 2 in Ref. 4, liquid spreading inside thin porous membranes ceases on the 100 μ s scale.

6.5.2. Viscous dissipation inside pores and the critical thickness of PTFE membrane

In Lembach et al. (2010), Weickgenannt et al. (2011a) and Eqs. (6.18) and (6.22) it was shown that liquid penetration into pores of size d after drop impact of size D at velocity V_0 proceeds with the initial velocity U_p

$$U_p \approx V_0 \frac{D}{d} \quad (6.35)$$

which is much higher than V_0 in the cases where $D/d \gg 1$, which manifests the hydrodynamic focusing effect. In particular, in the present case $D \approx 0.1$ cm, whereas $d \approx 10^{-3}$ cm for the PTFE membrane used. Given $V_0 \approx 1$ m/s, the hydrodynamic focusing can result in the initial velocities of water penetration of the order of $U_p \approx 100$ m/s. This analysis can be extended, in principle, to the case where drop penetrates into several pores simultaneously, which will diminish the value of U_p .

The estimate below follows that of Sahu et al. (2012). The kinetic energy of the penetrating water is rapidly dissipated by viscous friction at the pore walls. At a certain critical mat thickness the entire initial kinetic energy will be dissipated, which means that the maximum penetration depth is reached.

Namely, the kinetic energy E_k of water penetrating into the pores is of the order of

$$E_k \approx \rho U_p^2 D^3 \approx \rho \left(V_0 \frac{D}{d} \right)^2 D^3 \quad (6.36)$$

In the hydrodynamic focusing process the only resistance to flow in the pores is associated with viscous friction at the pore walls, since the resistance associated with surface tension would be negligibly small. Accordingly, the viscous shear stress S can be estimated as

$$S \approx \mu \frac{U_p}{d} \approx \frac{\mu}{d} \left(V_0 \frac{D}{d} \right) \quad (6.37)$$

The length of a tortuous pore would be of the order of the drop size D , which means that the pore surface area is of the order of dD , while the viscous friction force acting on water in a single pore is about SdD . The number of pores through which water is penetrating is of the order of $(D/d)^3$. Therefore, the total viscous force is of the order of $SdD(D/d)^3$. The estimate of the number of pores takes account of the pores in all the directions. Accordingly, the work done by viscous forces while water has penetrated a membrane of thickness h is of the order of $SdD(D/d)^3 h$, which is the total viscous dissipation E_d . Using Eq. (6.37), we find that

$$E_d \approx \frac{\mu}{d} \left(V_0 \frac{D}{d} \right) dD \left(\frac{D}{d} \right)^3 h \quad (6.38)$$

When the entire kinetic energy of water is fully dissipated at the critical mat thickness, $E_k \approx E_d$. Then, according to Eqs. (6.36) and (6.38) the critical membrane thickness is found as

$$h = \frac{\rho V_0 d^2}{\mu} \quad (6.39)$$

It should be emphasized that the critical thickness of a non-wettable membrane is understood as the minimal thickness which can never be penetrated by water. Evaluating it by the tip of nanoparticle-deposition domain, i.e. using the ultimate penetration fronts as it is done below, is a slight underestimate in the experimental data.

Equation (6.39) means that

$$\frac{h}{D} = \text{const} \times \frac{\text{We}}{\text{Ca}} \left(\frac{d}{D} \right)^2 \quad (6.40)$$

where $\text{Ca} = \mu V_0 / \sigma$ is the capillary number, and the Weber number is $\text{We} = \rho V_0^2 D / \sigma$, where σ is the surface tension.

Equation (6.40) can be transformed as

$$\Omega = C \times \text{We} \quad (6.41)$$

where $\Omega = (h/D) / \left[\text{Ca}^{-1} (d/D)^2 \right]$, which can be found from the experimental data (i.e. measured), and C is a constant to be found by fitting this equation to the experimental data.

The measured values of Ω obtained by observing the ultimate penetration fronts are plotted in Fig. 6.18 versus the Weber number, and also fitted by a linear fit expected according to Eq. (6.41). This is done for the five different impact velocities of 5.32, 5.64 m/s, 6.05 m/s, 6.47 m/s and 6.8 m/s.

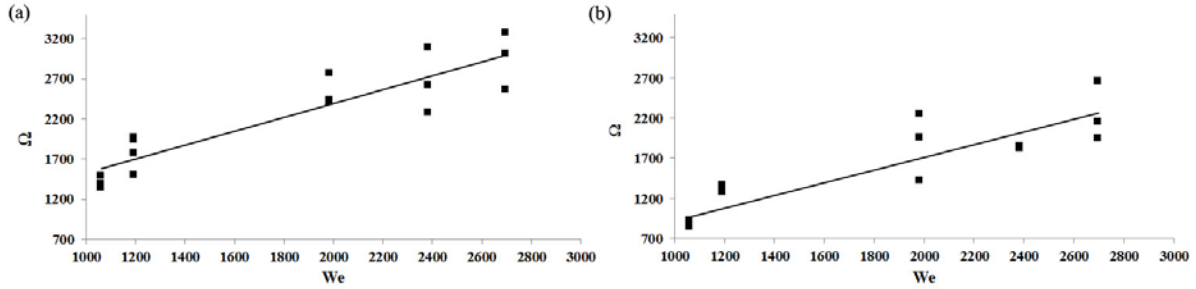


Figure 6.18. Normalized penetration depth Ω versus the Weber number. Straight lines are the linear fits according to Eq. (6.41). Panel (a) corresponds to the case where the PTFE membrane was cut beginning from the drop impact surface, whereas panel (b) corresponds to the case where the PTFE membrane was cut in the opposite direction. The value of C for panel (a) is 0.864 and for panel (b) is 0.791.

6.6 Conclusion

In the dynamic process accompanying water drop impact onto non-wettable membranes, water can penetrate into the interconnected pores to a significant depth, in distinction from penetration due to significant overpressure. In such dynamic penetration process hydrodynamic focusing plays the dominant role, while wettability and surface tension are secondary. Note that water penetration into porous medium after drop impact under significant overpressure is obviously possible if $\rho V_0^2 \gg 4\sigma/d$, however, due to the hydrodynamic focusing (when drop diameter D is much larger than the pore diameter d) water penetration is also possible when $\rho V_0^2 < 4\sigma/d$, which is much less obvious.

It should be emphasized that in comparison with the planar solution constructed in the present case, in the axisymmetric case penetration velocity of drops even increases by the factor of $\pi/2$, as the results of Lembach et al. (2010); Weickgenannt et al. (2011a) showed.

Therefore, the hydrodynamic focusing should become even more pronounced in the axisymmetric case. In the experiments, the seeding nanoparticles were entrained and deposited inside non-wettable porous membranes, which underlines the results associated with hydrodynamic focusing and dynamic wettability. Note in addition, that nanoparticle entrainment is beneficial not only as a research tool for the liquid front visualization, but also is of interest for printing microelectronics on textiles and for some other technological processes. The proposed theory is capable of qualitatively explaining the observed phenomena and yields their plausible quantitative evaluation, including the critical penetration depth determined by viscous dissipation in flow inside membranes.

7. EFFECT OF DROP EVAPORATION ON SUSPENDED NANOFIBER MAT

7.1 Introduction

The present section aims at the evaporation of water drops on a suspended nanofiber mat. Drop evaporation on polycarbonate and PTFE sheets were also studied to compare the outcome with that on the suspended nanofiber mat. Void formation was observed after the drop evaporation on suspended nanofiber mats. Nanofibers are normally used on a supportive filter media. However, even on such supported nanofibers, which are much smaller than the filter pores, are freely suspended over them. These suspended nanofiber mats can form voids due to liquid evaporation and effectively increase the pore size of the compound filter.

7.2. Experimental materials and methods

7.2.1 Materials

Polyacrylonitrile (PAN-molecular weight – 150 kDa) was obtained from Polymer Inc. N-N, Dimethyl Formamide (DMF) anhydrous 99.8%, was obtained from Sigma Aldrich. Aluminum sheets were purchased from McMaster-Carr.

7.2.2 Experimental method and setup

Aluminum sheet (1'' x 1'' x 0.025') with a hole of diameter 0.5'' at the center was used as the surface for collecting electrospun nanofibers. The nanofiber mats were electrospun from polyacrylonitrile. To keep the nanofibers collected over the hole in the aluminum sheet untouched, a supportive collector was made as shown in Fig. 1. Fibers were deposited for a very short time (60 s) to form moderately rarefied mats. Water drops possess

contact angle of 30-40° on cast PAN [Lembach et al. (2010)]. A water drop approximately 2 mm in diameter was softly deposited and left to evaporate on a freely suspended PAN nanofiber mat. The aluminum sheet with the drop on the suspended nanofiber mat was placed in a closed chamber to avoid any significant air current affecting drop evaporation. Temperature and humidity within the chamber were recorded and found to be almost constant within the time span of drop evaporation. The images of the evaporating drops were taken both from the side, using a DSLR camera (Nikon 3100), and also from the top, using the handheld microscope (Dino-Lite). It should be emphasized that a footprint of a single drop leans on hundreds of nanofibers and the interfiber pores. In another experiment a drop was placed under an optical microscope Olympus BX-51 and the drop and fibers underneath and around it were continuously observed. The network of the fiber mat formed after electrospinning before drop deposition was then compared to that after the drop evaporation. The images were processed using ImageJ, MatLab and Photoshop.

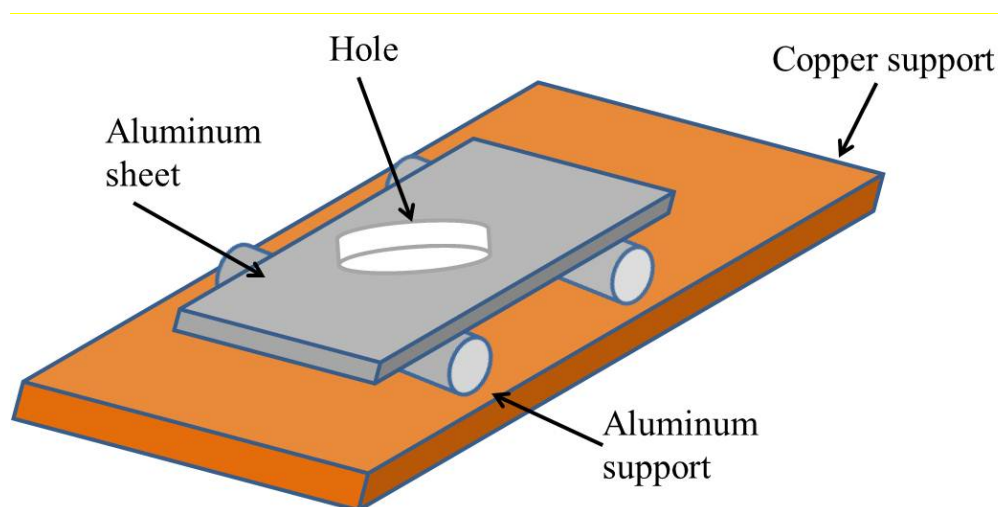


Figure 7.1. Schematic of the collector used to form suspended nanofiber mats.

7.3. Results and discussions

7.3.1 Evaporation of a sessile drop

In the preliminary experiment water drops were gently deposited onto a polycarbonate sheet, PTFE sheet and suspended nanofiber mat. Figure 7.2 shows the drop located on different surfaces at the instant when they had been gently deposited onto them. The initial contact angles and the contact diameters of the drops on different surfaces were found to be different. The experiment was conducted in a chamber with the temperature and humidity control as described above.

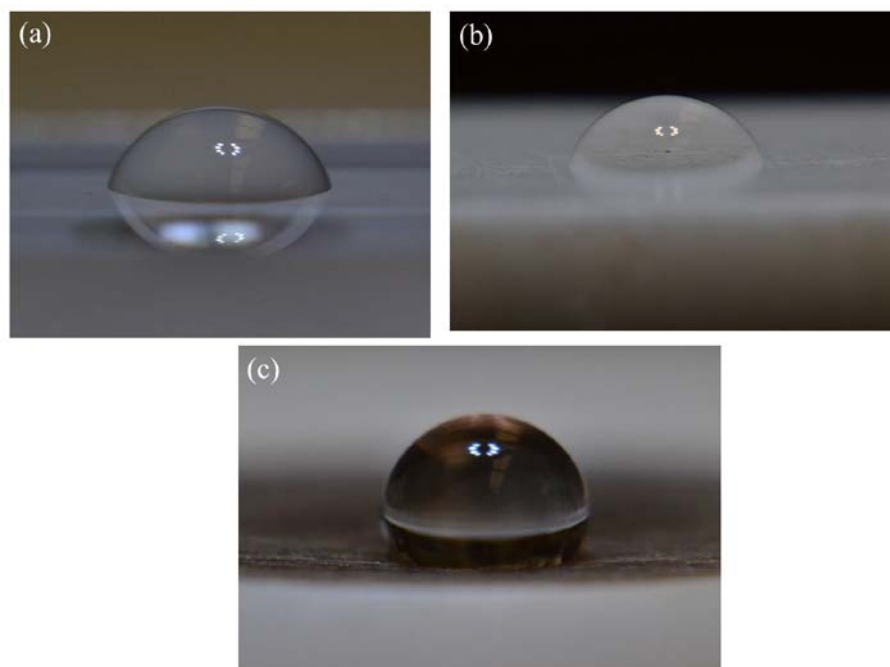


Figure 7.2. Water drops gently deposited onto: (a) polycarbonate sheet, (b) PTFE sheet, and (c) suspended PAN nanofiber mat. Time $t = 0$, i.e. the images correspond to the deposition moment.

The images were taken at an interval of 2 min both from the top and the side, and the contact angle (θ), the height of the drop (h), and the contact diameter of the drop (D) were measured. Different stages of drop evaporation were observed according to Fig. 7.3, which shows the change in the contact angle, the drop height, and the contact diameter during the evaporation process. The polycarbonate sheet is partially wettable and so the initial contact angle is less than 90° . The temperature and relative humidity within the chamber were 22°C and 59%, respectively. At the very beginning of evaporation, the contact diameter did not change and remained constant as is evident from Fig. 7.3(b), whereas the contact angle and the drop height were decreasing with time.

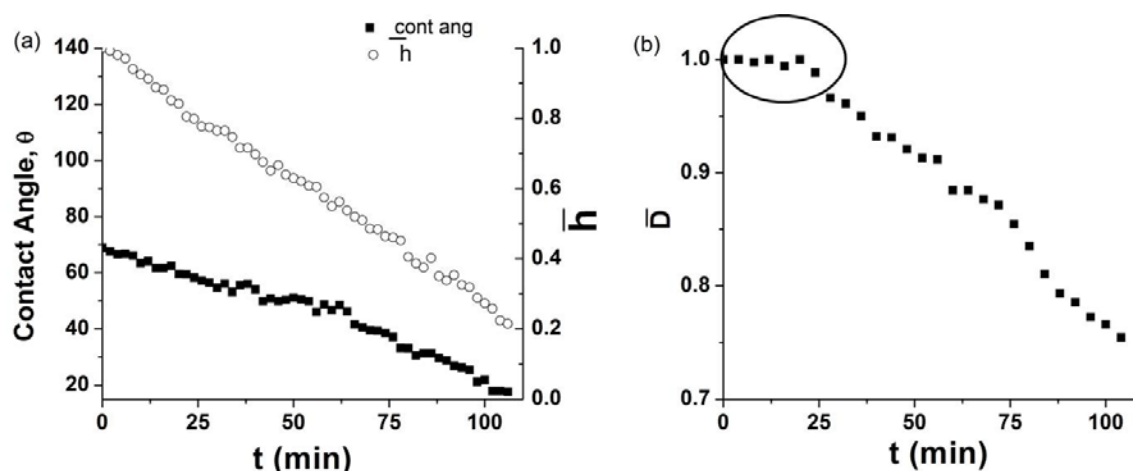


Figure 7.3. Drop parameters during evaporation on a polycarbonate sheet. (a) Change in the contact angle and the dimensionless height. The height is rendered dimensionless by the initial height of the drop at $t=0$. (b) Change in the dimensionless contact diameter of the drop during evaporation. The contact diameter was rendered dimensionless by the initial contact diameter at $t=0$. The encircled area corresponds to the regime of constant area at the first stage of drop evaporation.

Similar observations were made with drop evaporating on the PTFE surfaces. In this case the drop evaporates faster than the one on the polycarbonate sheet, since the volume of the former was less than the volume of the latter. Different stages of the evaporation process observed on the PTFE surface are shown in Fig. 7.4. At the first stage of evaporation the contact diameter remains constant, whereas the contact angle and the drop height were decreasing. At the following stage of drop evaporation the contact diameter, contact angle and the drop height were decreasing simultaneously.

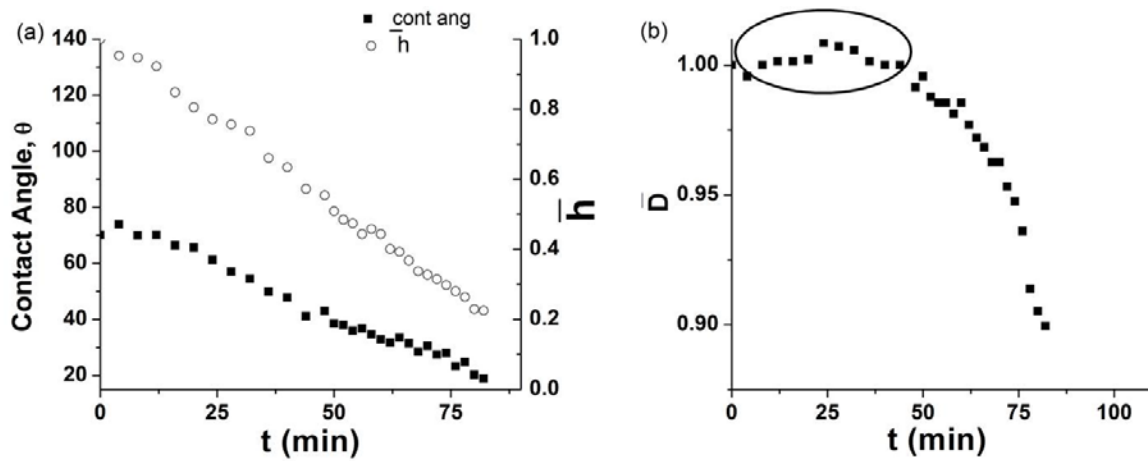


Figure 7.4. Drop parameters during evaporation on the PTFE sheet. (a) Change in the contact angle and the dimensionless height. The height is rendered dimensionless by the initial height of the drop at $t=0$. (b) Change in the dimensionless contact diameter of the drop during evaporation. The contact diameter was rendered dimensionless by the initial contact diameter at $t=0$. The encircled area corresponds to the regime of constant area at the first stage of drop evaporation.

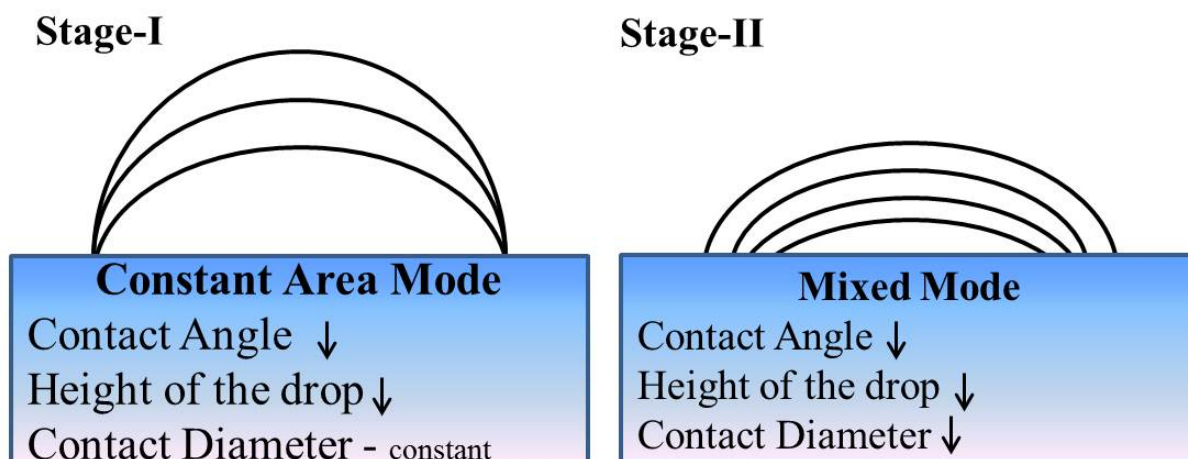


Figure 7.5. Different stages of drop evaporation observed on the solid surfaces.

Different stages of drop evaporation observed on the cast polycarbonate and PTFE sheets are summarized in Fig. 7.5.

Drop evaporation on suspended nanofiber mats is different from the process observed on the intact solid surfaces discussed above. A water drop forms a large contact angle of 125° after being softly deposited on the nanofiber mat as shown in Fig. 7.2(c). The contact diameter could not be measured from the top, as it is overshadowed by the bulged median diameter of the drop. However, it was observed that the drop gets pinned on the nanofiber mat as soon as it makes contact with it, as it was reported earlier by Lembach et al. (2010). The contact angle and the contact diameter do not change at the first stage of drop evaporation and only the drop height changes. At the latter stage of evaporation the contact angle begins to change. The temperature and relative humidity during the evaporation process were 21°C and 69 %, respectively. The measurement of the contact diameter was subjected to some inaccuracies due to the depth of field of the lens used resulting in some

fluctuations in the data in Fig. 7.6b. Overall, the contact diameter did not change significantly for a longer period of time in comparison to that on the polycarbonate and PTFE sheets. The evaporation process was slower than that on the intact solid surfaces. At the very end of the evaporation process different small films were formed over the interfiber pores within several small nanofiber pockets. These films continued evaporating and eventually formed voids visible at the nanofiber mat surface.

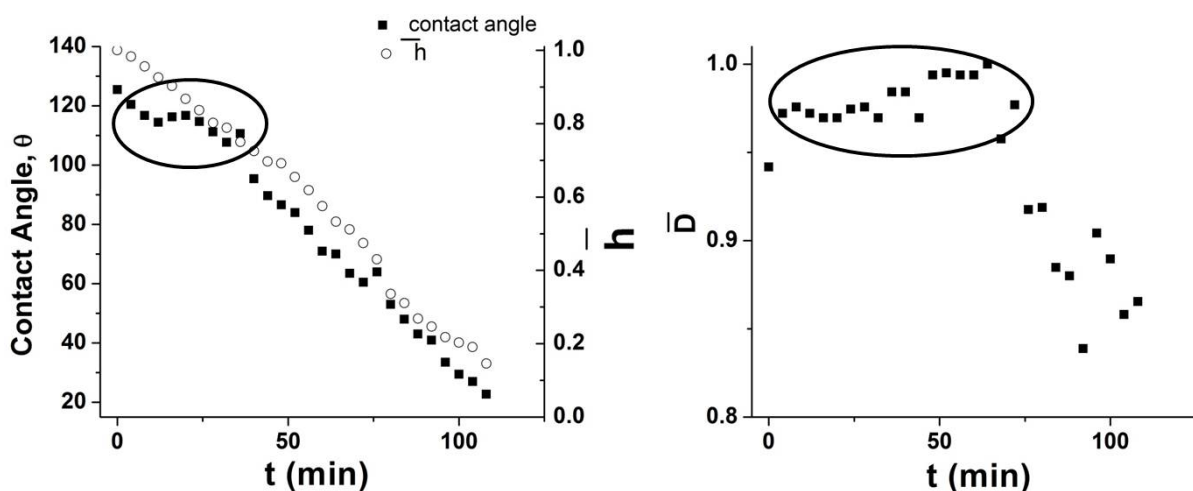


Figure 7.6. Drop parameters during evaporation on the PAN nanofiber mat. (a) Change in the contact angle and the dimensionless height. The height is rendered dimensionless by the initial height of the drop at $t=0$. (b) Change in the dimensionless contact diameter of the drop during evaporation. The contact diameter was rendered dimensionless by the initial contact diameter at $t=0$. The encircled area corresponds to the regime of constant area at the first stage of drop evaporation.

7.3.2 Void formation during drop evaporation on nanofiber mats

In the case of drop evaporation on a porous and flexible nanofiber mat, when a thin water film is left over an interfiber pore, its contact line attached to the surrounding nanofibers tends to shrink to minimize the surface area of the liquid lens. As a result, it subjects the surrounding nanofibers to a certain pulling force. Figure 7.7 shows a sequence of images of the second phase of water drop evaporation on the PAN nanofiber mat. It is evident that the nanofibers adjacent to the contact line are deformed during the evaporation process. Figure 7.8 depicts a superposition of two images of the same place near the contact line taken before water had evaporated and after that. The darker fibers are located at the positions before water evaporation has been completed (at the onset of the second stage). On the other hand, the brighter fibers are located at the final positions after the evaporation process has been completed. The white arrows show the displacements of the individual nanofiber elements during liquid evaporation. It should be emphasized that on dense nanofiber mats contact line motion was precluded during the entire evaporation process, since the contact line was unable to generate force sufficient for relocation of many nanofibers at once. In such cases drops evaporate in a fully spread-out state with no shrinkage, in agreement with the previous observations [Srikar et al. (2009); Sinha-Ray et al. (2011); Weickgenannt et al. (2011)].

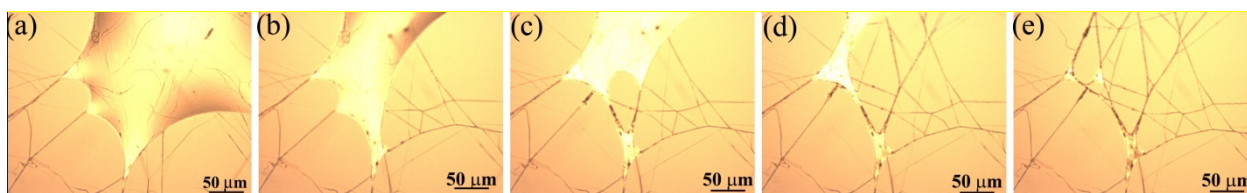


Figure 7.7. Water drop evaporation on a rarefied PAN nanofiber mat. The nanofibers surrounding the contact line are pulled and deformed by liquid. The time interval between two neighboring images is 1 s.

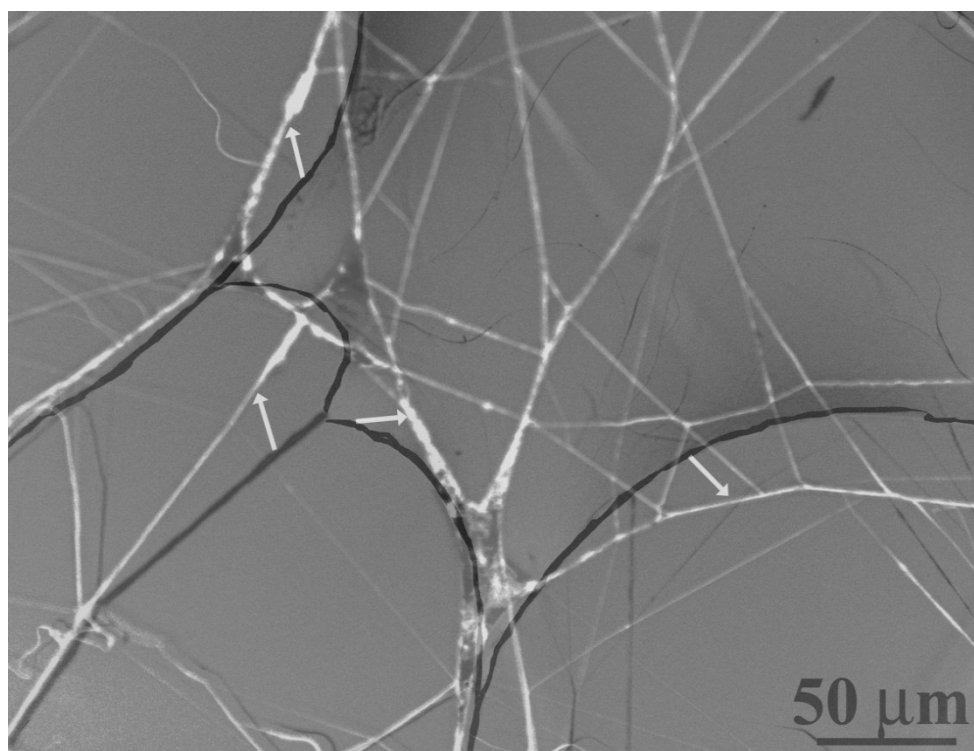


Figure 7.8. Superimposed images of the same nanofibers which were initially surrounding the contact line of a residual of an evaporating drop (dark fibers) and their locations after evaporation had been finished (light fibers). The arrows indicate displacement of the individual fiber elements.

Figure 7.9 shows the effect of water evaporation on the PAN nanofibers located in a wetted area inside the contact line. The mat used in Fig. 7.9 is denser than those in Figs. 7.7 and 7.8. In Fig. 7.9 the nanofibers in direct contact with the contact line do not show any relocation, whereas those inside the wetted domain move. As a result, several voids appear inside the wetted area.

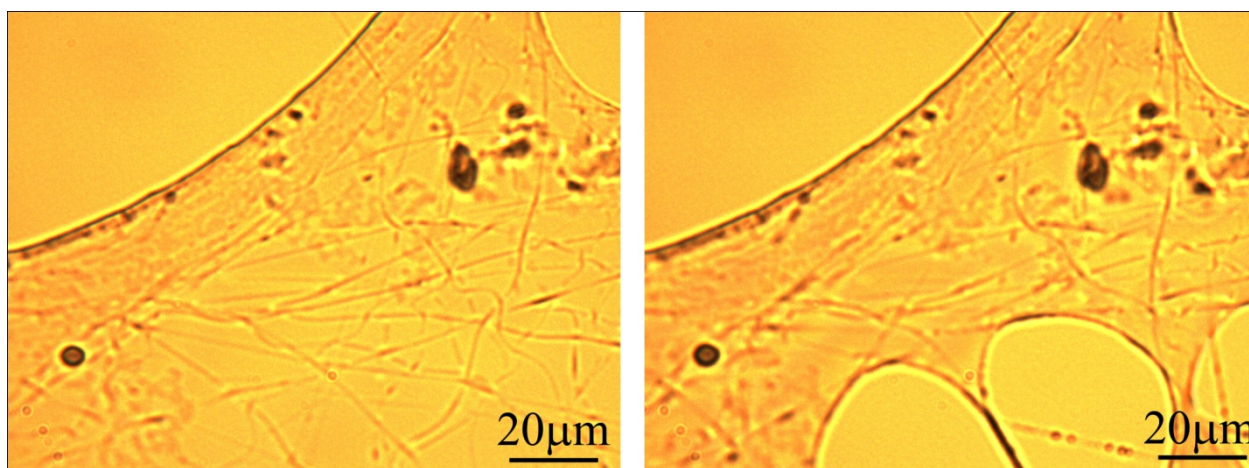


Figure 7.9. Relocation of nanofibers inside the wetted area of a denser nanofiber mat. The fibers adjacent to the contact line do not move.

The area of the nanofiber mat, where the water drop was deposited was observed under the optical microscope both before and after its evaporation. Several samples of thin and thick nanofiber mats were prepared. Figure 7.10 shows the optical images of both thin and thick nanofiber mats before the drop evaporation. The drop was then deposited at the very center of the suspended nanofiber mat. Several images at different locations were taken to cover the area covered by the drop so that a comparison could be made of the images taken

before and after drop evaporation. For that purpose, after drop evaporation another set of images was taken within the evaporation zone of the mat.

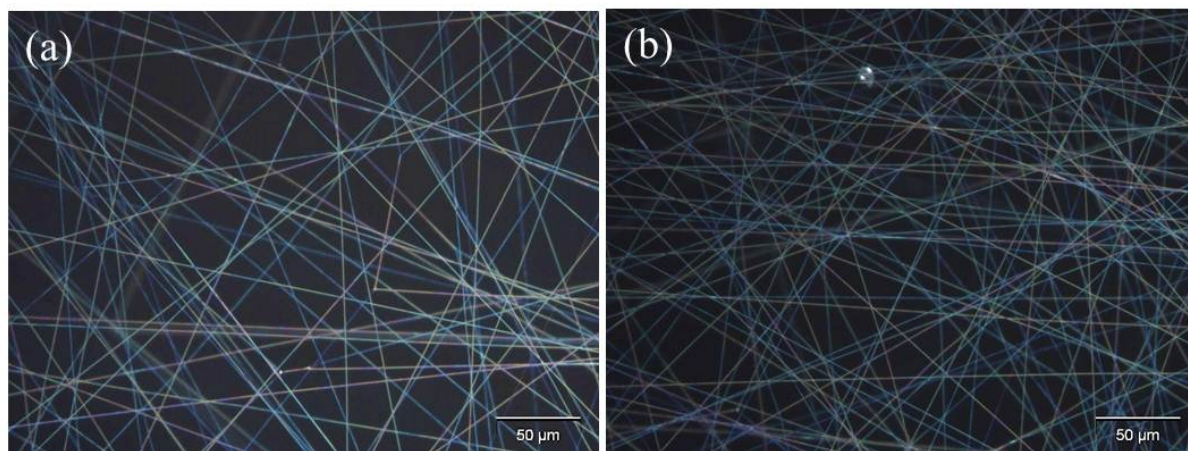


Figure 7.10. Thin and thick nanofiber mats collected on the aluminium plates for different times of electrospinning. The images were taken before drop evaporation.

Figure 7.11 shows the optical images of the nanofiber mat after drop evaporation on the same samples as in Fig. 7.10. The emergence of voids is evident from the images in Fig. 7.11. Some layers of the nanofibers merge together leaving voids. During the electrospinning process nanofibers are collected layer-by-layer and there is always an air gap between neighboring layers of nanofibers due to electrostatic repulsion of still-charged layers. As soon as a water drop is deposited, the electrical charge is immediately discharged and different layers of nanofibers tend to merge together and reduces the air gap between them. The pore size in the nanofiber mat increases after drop evaporation.

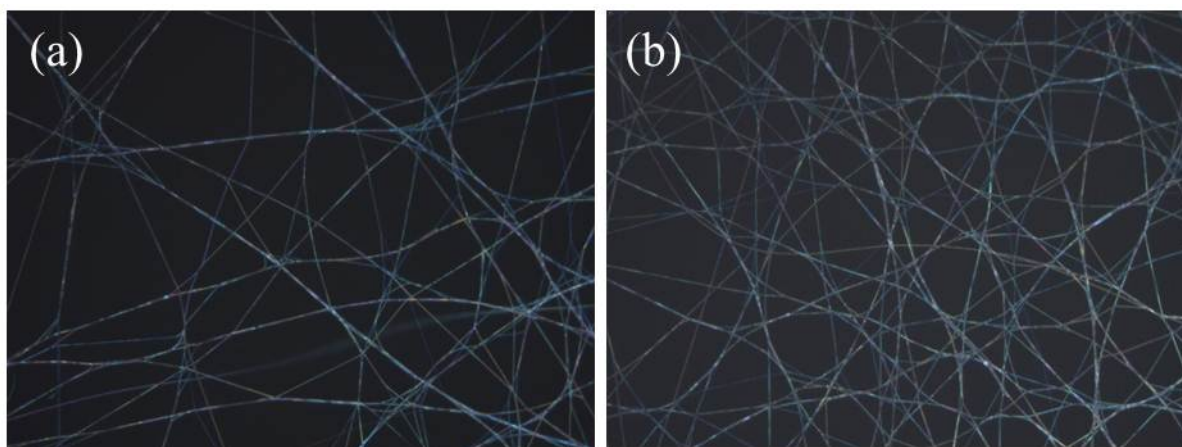


Figure 7.11. Thin and thick nanofiber mats collected on the aluminium plates for different times of electrospinning. The images were taken after drop evaporation.

7.3.3 Effect on porosity of nanofiber mats

The optical microscope images shown in Figs. 7.10 and 7.11 were subjected to various image analysis methods using the MatLab program. The effective sizes ℓ of the visible interfiber pores were derived from their measured areas S as $\ell = \sqrt{S}$. Once an image was loaded into MatLab, the unfocused fibers or objects in the background of the image were subtracted from the foreground, narrowing the depth of field of the image and thus sharpening it. Next, the image was converted from RGB to a grayscale image. The fibers were then distinguished from the background by a threshold value (the background being darker and the fibers being lighter than this value), thus the image was converted into a binary image. Once the image showed a white background with black fibers, a median filter was applied to sharpen the edges of the fibers and the area analysis began.

The frequencies of finding the effective lengths in the range $\ell + d\ell$ were found and used to plot the corresponding probability density functions of an individual nanofiber mat before and after evaporation. Figure 7.12a reveals the presence of pores of up to the effective length of $4.77 \mu\text{m}$. After the drop evaporates the length scale of the pores increases to a mean value of $9.57 \mu\text{m}$ as is evident from Fig. 7.12(b).

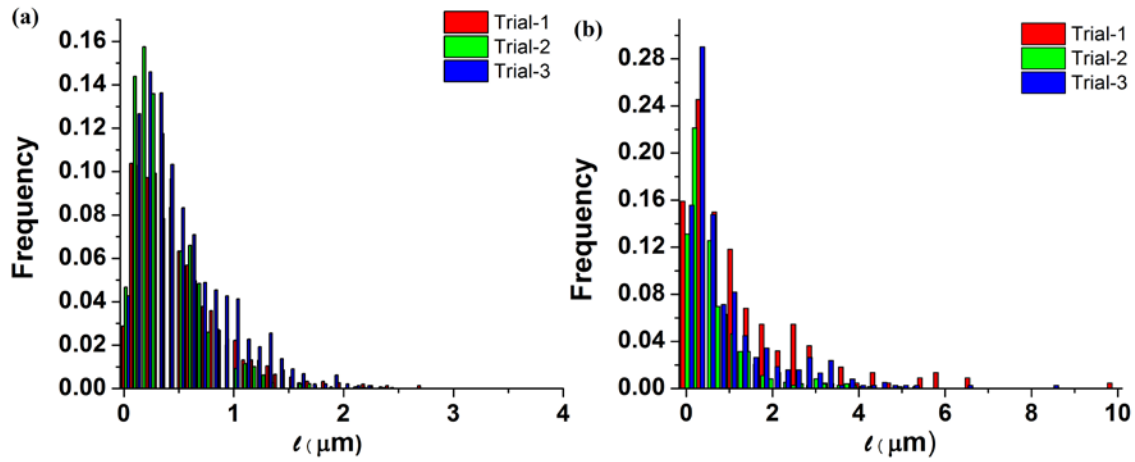


Figure 7.12 Frequency distribution of void sizes: (a) before, and (b) after drop evaporation.

The formation of circular arcs occurs mostly over the span of multiple cell areas, where apparently many fibers have been collapsed into one strand. The straight fiber cells occupying the space between the arced fibers indicate a lack of formation of large voids in this case.

7.3.4 Theoretical Model

The diameters of the nanofibers are of the order of several hundred nanometers. Therefore, their bending stiffness is negligibly small. A thin filament can be considered as an elastic undergoing bending due to the thin liquid film attached to it. A schematic of two nanofibers bent due to the attached liquid film is shown in Fig. 7.13a. The liquid film attached to the fibers tends to minimize its surface area, whereas the fiber attached to the film is bent in the form of an arc.

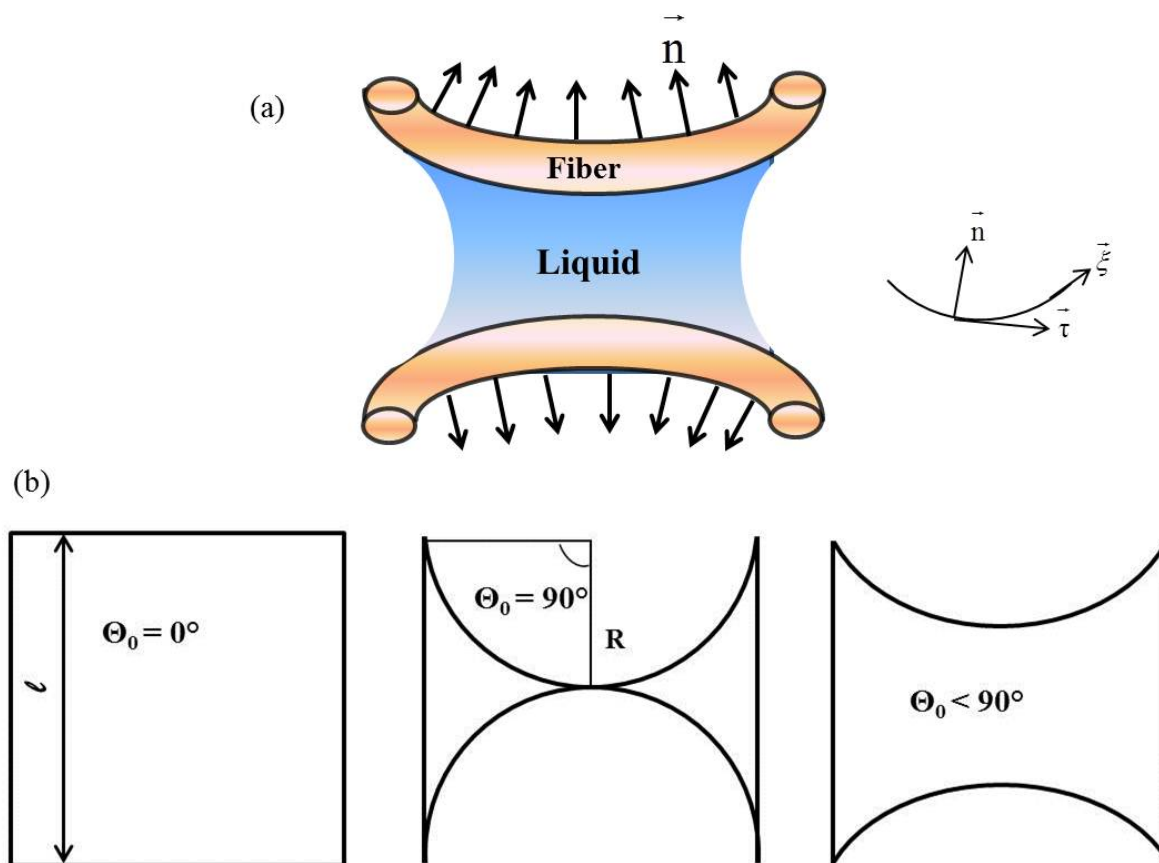


Figure 7.13 Schematic of the fiber deformation due to the evaporation of water film spanning the fibers. (a) Bending of nanofibers by the attached film and (b) different possible film configurations that might arise as a result of fiber bending.

The momentum balance equation for a fiber reads

$$\frac{d}{d\xi}(P\boldsymbol{\tau}) + \mathbf{q} = 0; \quad \mathbf{q} = -2\sigma\mathbf{n} \quad (7.1)$$

where P is the total force acting in the nanofiber cross-section, \mathbf{q} is the distributed force applied to a unit length of the fiber due to the surface tension, and σ is the surface tension coefficient. The normal unit vectors are shown in Fig. 7.13.

Using the Frenet-Serret formula, Eq. (7.1) is rearranged to the following form

$$\frac{dP}{d\xi}\boldsymbol{\tau} + P\kappa\mathbf{n} - 2\sigma\mathbf{n} = 0 \quad (7.2)$$

where κ is the curvature. The projections of Eq. (7.2) show that $dP/d\xi = 0$, and

$$P\kappa - 2\sigma = 0; \quad \kappa = \frac{2\sigma}{P} \quad (7.3)$$

It is seen that the curvature is constant, which means that the fiber shape is a circular arc.

Therefore, the radius of the circular arc is found as

$$R = \frac{P}{2\sigma} \quad (7.4)$$

Assume that strains are small and nanofibers follow Hooke's law

$$\sigma_{\tau\tau} = E\varepsilon_{\tau\tau} \quad (7.5)$$

where $\sigma_{\tau\tau}$ is the longitudinal stress, E is Young's modulus, and $\varepsilon_{\tau\tau}$ is the strain.

Then, the force acting in the nanofiber cross-sections is

$$P = E\pi a^2 \varepsilon_{\tau\tau} \quad (7.6)$$

where a is the cross-sectional radius which is of the order of 300 nm.

The fibers bend in the form of an arc, and the radius of the arc can be alternatively expressed in terms of the length ℓ of the equivalent square representing a cell in the fiber mat as

$$R = \frac{L}{2\sin\theta_0} \quad (7.7)$$

The strain in the nanofiber due to the bending can thus be calculated from the deformation shown in Fig. 7.13b

$$\varepsilon_{\tau\tau} = \frac{\theta_0 - \sin\theta_0}{\sin\theta_0}; 0 < \theta_0 < 90^\circ \quad (7.8)$$

where θ_0 is the angle subtended by the center of the arc and the edge of the square, as shown in Fig. 7.13b.

Substituting Eq. (7.7) and (7.8) into Eq. (7.4), one obtains

$$\frac{\sigma L}{E\pi a^2} = \theta_0 - \sin\theta_0 \quad (7.9)$$

The optical microscope images of the nanofiber mat both before and after drop evaporation shown in Figs. 7.10 and 7.11 were processed in MatLab, and individual cells were isolated and the characteristic lengths ℓ of each cell were calculated. For the estimates, the following values of the parameters are used: the Young's modulus of the nanofibers as $E=5$ GPa, the surface tension coefficient $\sigma = 72$ g/s², and the fiber radius $a = 300$ nm. The value of θ_0 was then evaluated for each individual cell. Ten optical images were taken for each sample of the suspended nanofiber mat and an average of all was thus used to construct the probability density function corresponding to the cell-size distribution shown in Fig. 7.14. The tails corresponding to bigger cells (holes) are highlighted as the encircled areas on the curves.

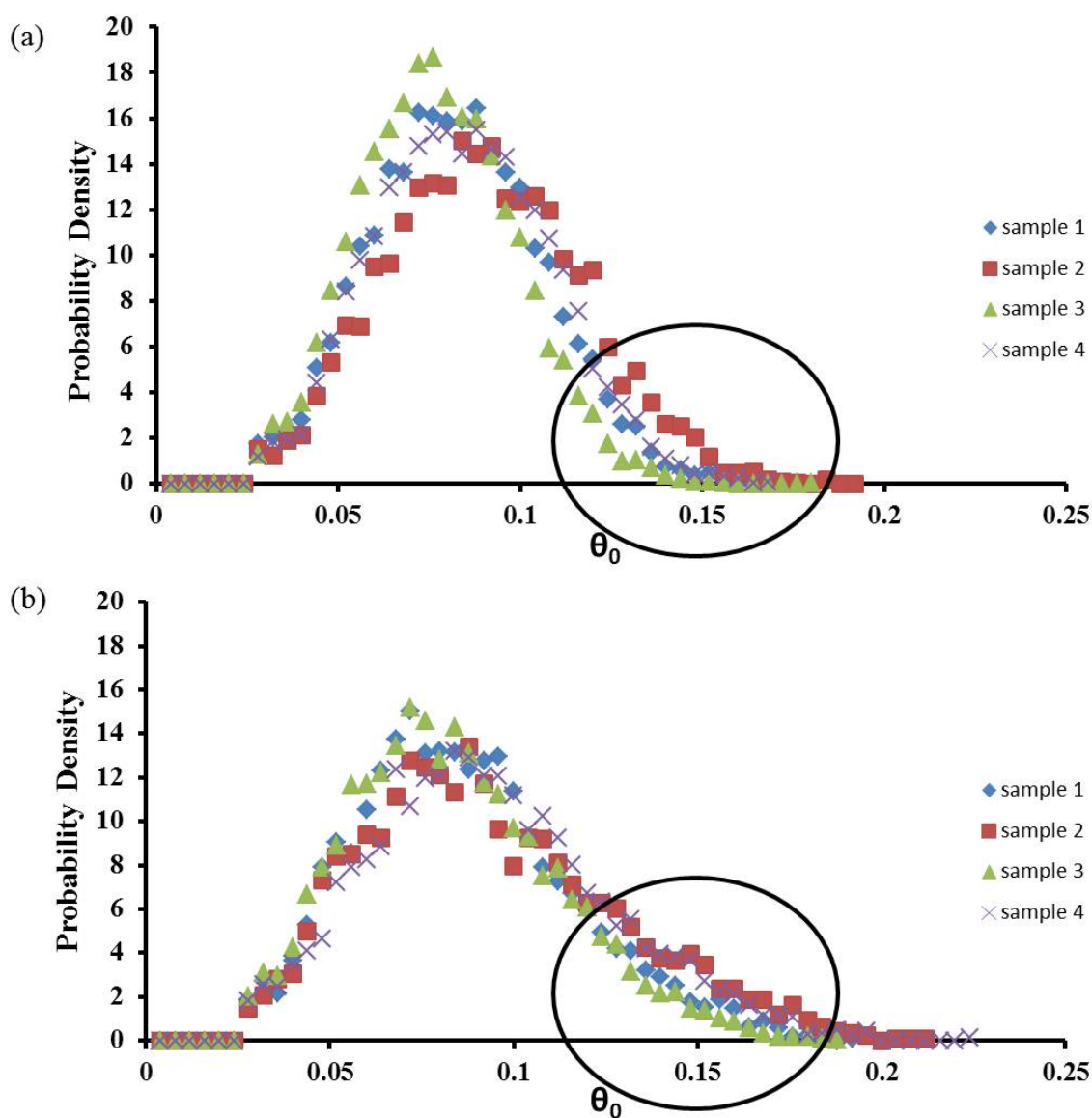


Figure 7.14 Probability density function versus θ_0 constructed using data acquired for four different nanofiber samples. Panel (a) corresponds to the results before drop evaporation, and panel (b) - after drop evaporation. The probability density function of each sample is an average of ten different images taken over the area where the footprint of a gently deposited drop was located. The encircled area in panel (b) shows formation of large pores, which is expressed by an increase in their frequency.

The random enlargement of the open cells formed by the network of nanofibers during the drop evaporation is studied in the framework of the percolation theory. Each cell is considered as an individual site and the network of cells is considered as a group of clusters. As the drop evaporation proceeds, the sites (wet cells) burst leading to the formation of an infinite cluster (a big hole). The critical value of the percolating threshold for the site percolation in 2D for a square lattice is $p_c = 1/2$ [Essam et al. (1983)]. The transition of the percolation threshold as described by the renormalization group theory is shown in Fig. 7.15. The probability of an open cell in the network $p > 1/2$ inevitably results in formation of an infinite cluster.

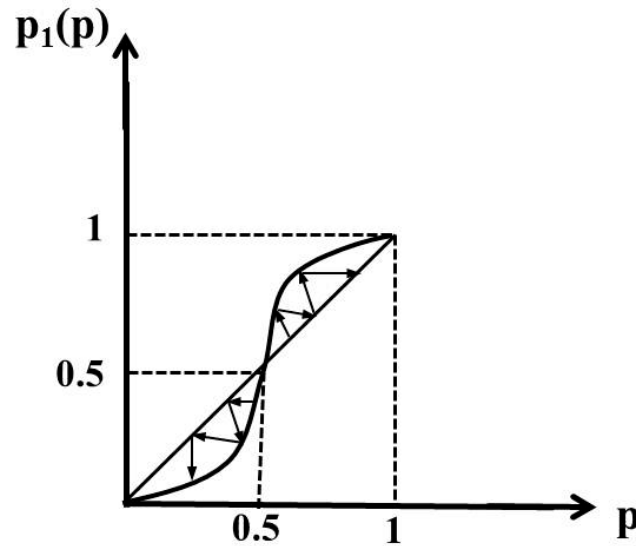


Figure 7.15 Threshold transition described by the renormalization group theory in 2D.

The probabilities of the hole emergence were calculated for four different samples both before and after drop evaporation using the probability density functions of Fig. 7.14 and choosing the value $\theta_{0b}=0.088$ as the one corresponding to burst of liquid film spanning two bent nanofibers (see the utmost right image in Fig. 7.13b). The results for these calculated probabilities are shown in Fig. 7.16. Those calculated using the data acquired before drop evaporation, predominantly belong to the range $p < 1/2$, whereas those after the evaporation, predominantly belong to the range $p > 1/2$. This results points out at formation of a percolation cluster of holes, i.e. formation of big holes in the nanofiber mat as a result of drop evaporation.

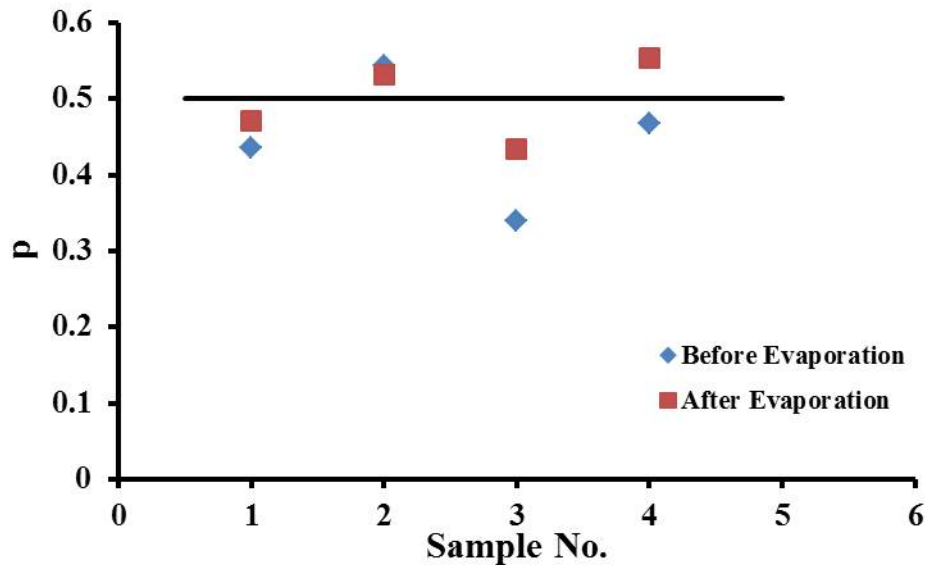


Figure 7.16 Probability p of hole formation as a result of water evaporation and shrinkage of water films spanning neighboring nanofibers.

7.4 Conclusion

Differences in the drop evaporation modes were observed between the intact solid surfaces (polycarbonate and PTFE sheets) and suspended nanofiber mats. The deflection of nanofibers by the contact line of the spanning wetted spot was observed. An increase in the effective cell size in the nanofiber mat after drop evaporation was found. Using the percolation theory, it was shown that formation of big cluster of holes is expected in accordance with the experimental data.

8. CONCLUSION

The present work dealt with different key aspects of coalescing filter operation on the physical level. The main stages involved in separation of airborne liquid drops brought by a gas flux onto a coalescing filter were studied experimentally and theoretically. Several novel experimental setups were designed for conducting these experiments and theoretical modeling was used to explain, rationalize and predict the observations. Several new phenomena were observed during the initial short-time time interaction of the oncoming liquid drops with a filament in a filter medium. The existing ideology of preparing a superhydrophobic porous membrane which would completely prevent water penetration has been completely discarded. It was shown that superhydrophobicity does not prevent water from being delivered into a filter if the impact velocity surpasses a threshold value of the order of 3 m/s, and the hydrodynamic focusing becomes important. In addition, the existence of a critical thickness of a fibrous mat was predicted and demonstrated experimentally, which is sufficient for complete dissipating of the kinetic energy, and thus preventing water droplet to leave the filter on the rear side.

Different types of drop behavior inside fibrous mats were uncovered. Drop motion along and across fibers driven by air flow was studied, and different modes of drop evolution were delineated on the Weber-Ohnesorge number plane. Drop hopping between the fibers was also observed.

In addition, propagation of liquid fronts associated with drop boundaries inside non-wettable nonwovens was studied experimentally and theoretically, as well as the entrainment of nanoparticles by such fronts.

Usage of nanofibers in the filtration industry is steadily increasing. The mechanically-driven rearrangement of nanofiber membranes under the action of drop evaporation at the front surface was also addressed in the experiments of the present work. Void formation was uncovered and quantitatively described.

The findings of the present work reported are useful for development of novel coalescing filters and proper understanding of their operation.

9. CITED LITERATURE

A. Marmur, The equilibrium contact angle. The Springer Handbook of Experimental Fluid Mechanics; (eds. Tropea, C.; Yarin, A.L.; Foss, J.) Springer: Berlin 2007; Section 3.3.1, 106.

Agarwal, S., von Arnim, V., Stegmaier, T., Planck, H., & Agarwal, A. (2013). Role of surface wettability and roughness in emulsion separation. *Separation and Purification Technology*, 107, 19-25.

Alleborn, N., & Raszillier, H. (2004). Spreading and sorption of droplets on layered porous substrates. *Journal of colloid and interface science*, 280(2), 449-464.

Arcoumanis, C., Whitelaw, D. S., & Whitelaw, J. H. (1996). Breakup of droplets of Newtonian and non-Newtonian fluids. *Atomization and Sprays*, 6(3).

Asai, A., Shioya, M., Hirasawa, S., & Okazaki, T. (1993). Impact of an ink drop on paper. *The Journal of imaging science and technology*, 37(2), 205-207.

Barenblatt, G. I., Entov, V. M., & Ryzhik, V. M. (1989). *Theory of fluid flows through natural rocks*, Kluwer, Dordrecht.

Barhate, R. S., & Ramakrishna, S. (2007). Nanofibrous filtering media: filtration problems and solutions from tiny materials. *Journal of Membrane Science*, 296(1), 1-8.

Batchelor, G. K. (2000). *An introduction to fluid dynamics*. Cambridge university press.

Bazilevsky, A. V., Yarin, A. L., & Megaridis, C. M. (2008). Pressure-driven fluidic delivery through carbon tube bundles. *Lab on a Chip*, 8(1), 152-160.

Bhardwaj, R., Longtin, J. P., & Attinger, D. (2007). A numerical investigation on the influence of liquid properties and interfacial heat transfer during microdroplet deposition onto a glass substrate. *International Journal of Heat and Mass Transfer*, 50(15), 2912-2923.

Bird, R. B., Hassager, O., Armstrong, R. C., & Curtiss, C. F. *Dynamics of polymeric liquids- Kinetic theory*. Vol. 2. 1987.

Birdi, K. S., Vu, D. T., & Winter, A. (1989). A study of the evaporation rates of small water drops placed on a solid surface. *The Journal of physical chemistry*, 93(9), 3702-3703.

Birkhoff, G., MacDougall, D. P., Pugh, E. M., & Taylor, G. (1948). Explosives with lined cavities. *Journal of Applied Physics*, 19(6), 563-582.

Birouk, M., Stäbler, T., & Azzopardi, B. J. (2003). An experimental study of liquid jets interacting with cross airflows. *Particle & Particle Systems Characterization*, 20(1), 39-46.

Bitten, J. F. (1970). Coalescence of water droplets on single fibers. *Journal of colloid and interface science*, 33(2), 265-271.

Blake, T. D. (1993). Dynamic contact angles and wetting kinetics. *Wettability*, 49, 251-309.

Borhan, A., & Rungta, K. K. (1993). An experimental study of the radial penetration of liquids in thin porous substrates. *Journal of colloid and interface science*, 158(2), 403-411.

Bormashenko, E., Musin, A., & Zinigrad, M. (2011). Evaporation of droplets on strongly and weakly pinning surfaces and dynamics of the triple line. *Colloids and Surfaces A: Physicochemical and Engineering Aspects*, 385(1), 235-240.

Brown, R. C. (1993). *Air filtration: an integrated approach to the theory and applications of fibrous filters* (Vol. 650). Oxford: Pergamon press.

Brunet, P., Lapierre, F., Zoueshtiagh, F., Thomy, V., & Merlen, A. (2009). To grate a liquid into tiny droplets by its impact on a hydrophobic microgrid. *Applied Physics Letters*, 95(25), 254102.

Cao, X. K., Sun, Z. G., Li, W. F., Liu, H. F., & Yu, Z. H. (2007). A new breakup regime of liquid drops identified in a continuous and uniform air jet flow. *Physics of Fluids* (1994-present), 19(5), 057103.

Carroll, B. J. (1986). Equilibrium conformations of liquid drops on thin cylinders under forces of capillarity. A theory for the roll-up process. *Langmuir*, 2(2), 248-250.

Carroll, B. J. (1986). Equilibrium conformations of liquid drops on thin cylinders under forces of capillarity. A theory for the roll-up process. *Langmuir*, 2(2), 248-250.

Charbeneau, R. J. (2006). *Groundwater hydraulics and pollutant transport*. Waveland Press.

Chou, T. H., Hong, S. J., Liang, Y. E., Tsao, H. K., & Sheng, Y. J. (2011). Equilibrium phase diagram of drop-on-fiber: Coexistent states and gravity effect. *Langmuir*, 27(7), 3685-3692.

Chou, W. H., Hsiang, L. P., & Faeth, G. M. (1997). Temporal properties of drop breakup in the shear breakup regime. *International journal of multiphase flow*, 23(4), 651-669.

Clarke, A., Blake, T. D., Carruthers, K., & Woodward, A. (2002). Spreading and imbibition of liquid droplets on porous surfaces. *Langmuir*, 18(8), 2980-2984.

Contal, P., Simao, J., Thomas, D., Frising, T., Callé, S., Appert-Collin, J. C., & Bémer, D. (2004). Clogging of fibre filters by submicron droplets. Phenomena and influence of operating conditions. *Journal of Aerosol Science*, 35(2), 263-278.

Cooley, J. F. (1902). U.S. Patent No. 692,631. Washington, DC: U.S. Patent and Trademark Office.

Dawar, S., & Chase, G. G. (2010). Correlations for transverse motion of liquid drops on fibers. *Separation and Purification Technology*, 72(3), 282-287.

Dawar, S., Li, H., Dobson, J., & Chase, G. G. (2006). Drag correlation of drop motion on fibers. *Drying technology*, 24(10), 1283-1288.

Delbos, A., Lorenceau, E., & Pitois, O. (2010). Forced impregnation of a capillary tube with drop impact. *Journal of colloid and interface science*, 341(1), 171-177.

Denesuk, M., Smith, G. L., Zelinski, B. J. J., Kreidl, N. J., & Uhlmann, D. R. (1993). Capillary penetration of liquid droplets into porous materials. *Journal of colloid and interface science*, 158(1), 114-120.

Ding, H., & Theofanous, T. G. (2012). The inertial regime of drop impact on an anisotropic porous substrate. *Journal of Fluid Mechanics*, 691, 546-567.

Duprat, C., Bick, A. D., Warren, P. B., & Stone, H. A. (2013). Evaporation of drops on two parallel fibers: influence of the liquid morphology and fiber elasticity. *Langmuir*, 29(25), 7857-7863.

Duprat, C., Protiere, S., Beebe, A. Y., & Stone, H. A. (2012). Wetting of flexible fibre arrays. *Nature*, 482(7386), 510-513.

Eggers, J., Fontelos, M. A., Josserand, C., & Zaleski, S. (2010). Drop dynamics after impact on a solid wall: theory and simulations. *Physics of Fluids (1994-present)*, 22(6), 062101.

Eral, H. B., de Ruiter, J., de Ruiter, R., Oh, J. M., Semprebon, C., Brinkmann, M., & Mugele, F. (2011). Drops on functional fibers: from barrels to clamshells and back. *Soft Matter*, 7(11), 5138-5143.

Erbil, H. Y., McHale, G., & Newton, M. I. (2002). Drop evaporation on solid surfaces: constant contact angle mode. *Langmuir*, 18(7), 2636-2641.

Erbil, H. Y., McHale, G., Rowan, S. M., & Newton, M. I. (1999). Determination of the receding contact angle of sessile drops on polymer surfaces by evaporation. *Langmuir*, 15(21), 7378-7385.

Essam, I. W., Gaunt, D. S., & Guttmann, A. J. (1978). Percolation theory at the critical dimension. *Journal of Physics A: Mathematical and General*, 11(10), 1983

Faeth, G. M., Hsiang, L. P., & Wu, P. K. (1995). Structure and breakup properties of sprays. *International Journal of Multiphase Flow*, 21, 99-127.

Filatov, Y., Budyka, A., & Kirichenko, V. (2007). Electrospinning of micro-and nanofibers: fundamentals in separation and filtration processes. *J. Eng. Fibers Fabrics*, 3, 488.

Formhals, A. (1934). U.S. Patent No. 1,975,504. Washington, DC: U.S. Patent and Trademark Office.

Frising, T., Thomas, D., Bémer, D., & Contal, P. (2005). Clogging of fibrous filters by liquid aerosol particles: Experimental and phenomenological modelling study. *Chemical Engineering Science*, 60(10), 2751-2762.

Funk, C. S., Winzer, B., & Peukert, W. (2014). Correlation between shape, evaporation mode and mobility of small water droplets on nanorough fibres. *Journal of colloid and interface science*, 417, 171-179.

Gao, L., & McCarthy, T. J. (2009). Wetting $101^\circ\ddagger$. *Langmuir*, 25(24), 14105-14115.

Gilet, T., Terwagne, D., & Vandewalle, N. (2009). Digital microfluidics on a wire. *Applied Physics Letters*, 95(1), 014106.

Gilet, T., Terwagne, D., & Vandewalle, N. (2010). Droplets sliding on fibres. *The European Physical Journal E: Soft Matter and Biological Physics*, 31(3), 253-262.

Goren, S. L. (1962). The instability of an annular thread of fluid. *Journal of Fluid Mechanics*, 12(02), 309-319.

Guildenbecher, D. R., López-Rivera, C., & Sojka, P. E. (2009). Secondary atomization. *Experiments in Fluids*, 46(3), 371-402.

Gunde, A. C., Bera, B., & Mitra, S. K. (2010). Investigation of water and CO₂ (carbon dioxide) flooding using micro-CT (micro-computed tomography) images of Berea sandstone core using finite element simulations. *Energy*, 35(12), 5209-5216.

Guo, Z. G., & Liu, W. M. (2007). Sticky superhydrophobic surface. *Applied physics letters*, 90(22), 223111.

Han, D., & Steckl, A. J. (2009). Superhydrophobic and oleophobic fibers by coaxial electrospinning. *Langmuir*, 25(16), 9454-9462.

Henrici, P. (1993). *Applied and computational complex analysis, discrete Fourier analysis, Cauchy integrals, construction of conformal maps, univalent functions* (Vol. 3). John Wiley & Sons. p. 102-104 & 224

Hinze, J. O. (1955). Fundamentals of the hydrodynamic mechanism of splitting in dispersion processes. *AIChE Journal*, 1(3), 289-295.

Hirahara, H., & Kawahashi, M. (1992). Experimental investigation of viscous effects upon a breakup of droplets in high-speed air flow. *Experiments in Fluids*, 13(6), 423-428.

Howell, R. W., & Mathews, J. H. (2006). *Complex Analysis for Mathematics and Engineering*. NY: Jones & Bartlett Publ., p. 413.

Hoyt, J. W., & Taylor, J. J. (1977). Waves on water jets. *Journal of Fluid Mechanics*, 83(01), 119-127.

Inamura, T., Yanaoka, H., & Kawada, T. (2009). Visualization of airflow around a single droplet deformed in an airstream. *Atomization and Sprays*, 19(7).

Jiang, L., Zhao, Y., & Zhai, J. (2004). A Lotus-Leaf-like Superhydrophobic Surface: A Porous Microsphere/Nanofiber Composite Film Prepared by Electrohydrodynamics. *Angewandte Chemie*, 116(33), 4438-4441.

Joseph, D. D., Beavers, G. S., & Funada, T. (2002). Rayleigh–Taylor instability of viscoelastic drops at high Weber numbers. *Journal of Fluid Mechanics*, 453, 109-132.

Jung, Y. C., & Bhushan, B. (2008). Wetting behaviour during evaporation and condensation of water microdroplets on superhydrophobic patterned surfaces. *Journal of microscopy*, 229(1), 127-140.

Kamo, J., Hirai, T., & Kamada, K. (1992). Solvent-induced morphological change of microporous hollow fiber membranes. *Journal of membrane science*, 70(2), 217-224.

Kim, H. J., & Durbin, P. A. (1988). Observations of the frequencies in a sphere wake and of drag increase by acoustic excitation. *Physics of Fluids* (1958-1988), 31(11), 3260-3265.

Kim, T. I., & Suh, K. Y. (2009). Unidirectional wetting and spreading on stooped polymer nanohairs. *Soft Matter*, 5(21), 4131-4135.

Krzeczkowski, S. A. (1980). Measurement of liquid droplet disintegration mechanisms. *International Journal of Multiphase Flow*, 6(3), 227-239.

Kulkarni, P. S., Patel, S. U., & Chase, G. G. (2012). Layered hydrophilic/hydrophobic fiber media for water-in-oil coalescence. *Separation and Purification Technology*, 85, 157-164.

Kumar, A., & Hartland, S. (1988). Shape of a drop on a vertical fiber. *Journal of colloid and interface science*, 124(1), 67-76.

Kumar, S. M., & Deshpande, A. P. (2006). Dynamics of drop spreading on fibrous porous media. *Colloids and Surfaces A: Physicochemical and Engineering Aspects*, 277(1), 157-163.

Kwak, M. K., Jeong, H. E., Kim, T. I., Yoon, H., & Suh, K. Y. (2010). Bio-inspired slanted polymer nanohairs for anisotropic wetting and directional dry adhesion. *Soft Matter*, 6(9), 1849-1857.

Lagubeau, G., Fontelos, M. A., Josserand, C., Maurel, A., Pagneux, V., & Petitjeans, P. (2012). Spreading dynamics of drop impacts. *Journal of Fluid Mechanics*, 713, 50-60.

Landau, L. D., & Lifshitz, E. M. (2013). *Fluid Mechanics: Landau and Lifshitz: Course of Theoretical Physics (Vol. 6)*. Elsevier.

- Langmuir, I. (1918). The evaporation of small spheres. *Physical review*, 12(5), 368.
- Lavrent'ev, M. A., & Shabat, B. V. (1973). *Methods of the Theory of Functions of a Complex Variable*.
- Lee, J. B., & Lee, S. H. (2011). Dynamic wetting and spreading characteristics of a liquid droplet impinging on hydrophobic textured surfaces. *Langmuir*, 27(11), 6565-6573.
- Lembach, A. N., Tan, H. B., Roisman, I. V., Gambaryan-Roisman, T., Zhang, Y., Tropea, C., & Yarin, A. L. (2010). Drop impact, spreading, splashing, and penetration into electrospun nanofiber mats. *Langmuir*, 26(12), 9516-9523.
- Levich, V. G. (1962). *Physicochemical hydrodynamics* (Vol. 689). Englewood Cliffs, NJ: Prentice-Hall.
- Liew, T. P., & Conder, J. R. (1985). Fine mist filtration by wet filters—I. Liquid saturation and flow resistance of fibrous filters. *Journal of aerosol science*, 16(6), 497-509.
- Link, D. R., Anna, S. L., Weitz, D. A., & Stone, H. A. (2004). Geometrically mediated breakup of drops in microfluidic devices. *Physical Review Letters*, 92(5), 054503.
- Liu, Z., & Reitz, R. D. (1997). An analysis of the distortion and breakup mechanisms of high speed liquid drops. *International journal of multiphase flow*, 23(4), 631-650.
- Loitsyanskii, L. G. (1966). *Mechanics of liquids and gases* (p. 151). Oxford: Pergamon Press.
- Lorenceau, É., & Quéré, D. (2003). Drops impacting a sieve. *Journal of colloid and interface science*, 263(1), 244-249.
- Lorenceau, É., & Quéré, D. (2004). Drops on a conical wire. *Journal of Fluid Mechanics*, 510, 29-45.
- Lorenceau, É., Clanet, C., & Quéré, D. (2004). Capturing drops with a thin fiber. *Journal of colloid and interface science*, 279(1), 192-197.
- Lushnikov, A. (1997). Igor' Vasilievich Petryanov-Sokolov (1907–1996). *Journal of Aerosol Science*, 28(4), 545-546.
- Mark, J., Kamm, R. D., & Hoi, L. W. (1991). The nonlinear growth of surface-tension-driven instabilities of a thin annular film. *J. Fluid Mech*, 233, 141-156.
- Marmur, A., & Cohen, R. D. (1997). Characterization of porous media by the kinetics of liquid penetration: the vertical capillaries model. *Journal of colloid and interface science*, 189(2), 299-304.
- Maxwell, J. C. (1890). *The Scientific Papers of James Clerk Maxwell..* (Vol. 2). J. Hermann.

McHale, G., & Newton, M. I. (2002). Global geometry and the equilibrium shapes of liquid drops on fibers. *Colloids and Surfaces A: Physicochemical and Engineering Aspects*, 206(1), 79-86.

McHale, G., Aqil, S., Shirtcliffe, N. J., Newton, M. I., & Erbil, H. Y. (2005). Analysis of droplet evaporation on a superhydrophobic surface. *Langmuir*, 21(24), 11053-11060.

McHale, G., Newton, M. I., & Carroll, B. J. (2001). The shape and stability of small liquid drops on fibers. *Oil & Gas science and technology*, 56(1), 47-54.

Mead-Hunter, R., Bredin, A., King, A. J., Larcher, A. V., Becker, T., & Mullins, B. J. (2012). The influence of soot nanoparticles on the micro/macro-scale behaviour of coalescing filters. *Chemical Engineering Science*, 84, 113-119.

Mead-Hunter, R., King, A. J., & Mullins, B. J. (2014). Aerosol-mist coalescing filters—A review. *Separation and Purification Technology*.

Mettu, S., & Chaudhury, M. K. (2011). Motion of liquid drops on surfaces induced by asymmetric vibration: role of contact angle hysteresis. *Langmuir*, 27(16), 10327-10333.

Moffat, J. R., Sefiane, K., & Shanahan, M. E. (2009). Effect of TiO₂ Nanoparticles on Contact Line Stick–Slip Behavior of Volatile Drops. *The Journal of Physical Chemistry B*, 113(26), 8860-8866.

Mullins, B. J., Agranovski, I. E., Braddock, R. D., & Ho, C. M. (2004). Effect of fiber orientation on fiber wetting processes. *Journal of colloid and interface science*, 269(2), 449-458.

Mullins, B. J., Braddock, R. D., Agranovski, I. E., & Cropp, R. A. (2006). Observation and modelling of barrel droplets on vertical fibres subjected to gravitational and drag forces. *Journal of colloid and interface science*, 300(2), 704-712.

Mullins, B. J., Braddock, R. D., Agranovski, I. E., Cropp, R. A., & O'Leary, R. A. (2005). Observation and modelling of clamshell droplets on vertical fibres subjected to gravitational and drag forces. *Journal of colloid and interface science*, 284(1), 245-254.

Nguyen, T. A., Nguyen, A. V., Hampton, M. A., Xu, Z. P., Huang, L., & Rudolph, V. (2012). Theoretical and experimental analysis of droplet evaporation on solid surfaces. *Chemical Engineering Science*, 69(1), 522-529.

Nhung Nguyen, T. P., Brunet, P., Coffinier, Y., & Boukherroub, R. (2010). Quantitative testing of robustness on superomniphobic surfaces by drop impact. *Langmuir*, 26(23), 18369-18373.

Noblin, X., Buguin, A., & Brochard-Wyart, F. (2004). Vibrated sessile drops: Transition between pinned and mobile contact line oscillations. *The European Physical Journal E: Soft Matter and Biological Physics*, 14(4), 395-404.

Noblin, X., Buguin, A., & Brochard-Wyart, F. (2009). Vibrations of sessile drops. *The European Physical Journal-Special Topics*, 166(1), 7-10.

Park, M., Im, J., Shin, M., Min, Y., Park, J., Cho, H., ... & Kim, K. (2012). Highly stretchable electric circuits from a composite material of silver nanoparticles and elastomeric fibres. *Nature nanotechnology*, 7(12), 803-809.

Pezron, I., Bourgain, G., & Quéré, D. (1995). Imbibition of a fabric. *Journal of Colloid and Interface Science*, 173(2), 319-327.

Pich, J. (1966). Theory of aerosol filtration by fibrous and membrane filters. *Aerosol science*, 223-285.

Picknett, R. G., & Bexon, R. (1977). The evaporation of sessile or pendant drops in still air. *Journal of Colloid and Interface Science*, 61(2), 336-350.

Pilch, M., & Erdman, C. A. (1987). Use of breakup time data and velocity history data to predict the maximum size of stable fragments for acceleration-induced breakup of a liquid drop. *International Journal of Multiphase Flow*, 13(6), 741-757.

Piroird, K., Clanet, C., Lorenceau, É., & Quéré, D. (2009). Drops impacting inclined fibers. *Journal of colloid and interface science*, 334(1), 70-74.

Pittoni, P. G., Chang, C. C., Yu, T. S., & Lin, S. Y. (2013). Evaporation of water drops on polymer surfaces: pinning, depinning and dynamics of the triple line. *Colloids and Surfaces A: Physicochemical and Engineering Aspects*, 432, 89-98.

Polya, G., & Latta, G. (1974). *Complex variables*, Wiley, New York, p. 245

Quéré, D. (1999). Fluid coating on a fiber. *Annual Review of Fluid Mechanics*, 31(1), 347-384.

Ranger, A. A., & Nicholls, J. A. (1969). Aerodynamic shattering of liquid drops. *Aiaa Journal*, 7(2), 285.

Raynor, P. C., & Leith, D. (2000). The influence of accumulated liquid on fibrous filter performance. *Journal of Aerosol Science*, 31(1), 19-34.

Reis Jr, N. C., Griffiths, R. F., & Santos, J. M. (2008). Parametric study of liquid droplets impinging on porous surfaces. *Applied Mathematical Modelling*, 32(3), 341-361.

Reneker, D. H., Yarin, A. L., Zussman, E., & Xu, H. (2007). Electrospinning of nanofibers from polymer solutions and melts. *Advances in applied mechanics*, 41, 43-346.

Rosenfeld, J. I., & Wasan, D. T. (1974). Coalescence of drops in a liquid-liquid dispersion by passage through a fibrous bed. *The Canadian Journal of Chemical Engineering*, 52(1), 3-10.

Roshko, A. On the development of turbulent wakes from vortex streets, National Advisory Committee for Aeronautics, 1954. Technical Note 1191.

Rowan, S. M., Newton, M. I., & McHale, G. (1995). Evaporation of microdroplets and the wetting of solid surfaces. *The Journal of Physical Chemistry*, 99(35), 13268-13271.

Ruckenstein, E. (2002). Scaling analysis of coating of a plate or a fiber. *Journal of Colloid and Interface Science*, 246(2), 393-400.

Sahu, R. P., Sinha-Ray, S., Yarin, A. L., & Pourdeyhimi, B. (2012). Drop impacts on electrospun nanofiber membranes. *Soft Matter*, 8(14), 3957-3970.

Sahu, R. P., Sinha-Ray, S., Yarin, A. L., & Pourdeyhimi, B. (2013). Blowing drops off a filament. *Soft Matter*, 9(26), 6053-6071.

Sakamoto, H., & Haniu, H. (1990). A study on vortex shedding from spheres in a uniform flow. *Journal of Fluids Engineering*, 112(4), 386-392.

Sareen, S. S., Rose, P. M., Gudesen, R. C., & Kintner, R. C. (1966). Coalescence in fibrous beds. *AIChE Journal*, 12(6), 1045-1050.

Scheffler, R., Bell, N. S., & Sigmund, W. (2010). Electrospun Teflon AF fibers for superhydrophobic membranes. *Journal of Materials Research*, 25(08), 1595-1600.

Scheller, B. L., & Bousfield, D. W. (1995). Newtonian drop impact with a solid surface. *AIChE Journal*, 41(6), 1357-1367.

Schiller, L., & Naumann, Z. (1935). A drag coefficient correlation. *Vdi Zeitung*, 77(318), 51.

Schönfeld, F., Graf, K. H., Hardt, S., & Butt, H. J. (2008). Evaporation dynamics of sessile liquid drops in still air with constant contact radius. *International Journal of Heat and Mass Transfer*, 51(13), 3696-3699.

Shanahan, M. E. R., & Bourges, C. (1994). Effects of evaporation on contact angles on polymer surfaces. *International journal of adhesion and adhesives*, 14(3), 201-205.

Sharp, J. S., Farmer, D. J., & Kelly, J. (2011). Contact angle dependence of the resonant frequency of sessile water droplets. *Langmuir*, 27(15), 9367-9371.

Sherony, D. F., Kintner, R. C., & Wasan, D. T. (1978). Coalescence of secondary emulsions in fibrous beds. *Surface and Colloid Science*, 10, 99-161.

Shin, C., & Chase, G. G. (2004). Water-in-oil coalescence in micro-nanofiber composite filters. *AIChE journal*, 50(2), 343-350.

Shin, C., Chase, G. G., & Reneker, D. H. (2005). Recycled expanded polystyrene nanofibers applied in filter media. *Colloids and Surfaces A: Physicochemical and Engineering Aspects*, 262(1), 211-215.

Shin, D. H., Lee, S. H., Choi, C. K., & Retterer, S. (2010). The evaporation and wetting dynamics of sessile water droplets on submicron-scale patterned silicon hydrophobic surfaces. *Journal of Micromechanics and Microengineering*, 20(5), 055021.

Shin, D. H., Lee, S. H., Jung, J. Y., & Yoo, J. Y. (2009). Evaporating characteristics of sessile droplet on hydrophobic and hydrophilic surfaces. *Microelectronic Engineering*, 86(4), 1350-1353.

Sinha-Ray, S., Zhang, Y., & Yarin, A. L. (2010). Thorny devil nanotextured fibers: the way to cooling rates on the order of 1 kW/cm². *Langmuir*, 27(1), 215-226.

Sivakumar, D., Katagiri, K., Sato, T., & Nishiyama, H. (2005). Spreading behavior of an impacting drop on a structured rough surface. *Physics of Fluids (1994-present)*, 17(10), 100608.

Song, H., Chen, D. L., & Ismagilov, R. F. (2006). Reactions in droplets in microfluidic channels. *Angewandte chemie international edition*, 45(44), 7336-7356.

Spalding, D. B. (1953, December). The combustion of liquid fuels. In *Symposium (international) on combustion (Vol. 4, No. 1, pp. 847-864)*. Elsevier.

Spielman, L. A., & Goren, S. L. (1972). Theory of coalescence by flow through porous media. *Industrial & Engineering Chemistry Fundamentals*, 11(1), 66-72.

Srikanth, R., Gambaryan-Roisman, T., Steffes, C., Stephan, P., Tropea, C., & Yarin, A. L. (2009). Nanofiber coating of surfaces for intensification of drop or spray impact cooling. *International Journal of Heat and Mass Transfer*, 52(25), 5814-5826.

Starov, V. M., Zhdanov, S. A., Kosvintsev, S. R., Sobolev, V. D., & Velarde, M. G. (2003). Spreading of liquid drops over porous substrates. *Advances in colloid and interface science*, 104(1), 123-158.

Strouhal, V. (1878). Ueber eine besondere Art der Tonerregung. *Annalen der Physik*, 241(10), 216-251.

Strutt, J. W., & Rayleigh, L. (1878). On the instability of jets. *Proc. London Math. Soc*, 10, 4-13.

Tadmor, R. (2011). Approaches in wetting phenomena. *Soft Matter*, 7(5), 1577-1580.

Tadmor, R., Bahadur, P., Leh, A., N'guessan, H. E., Jaini, R., & Dang, L. (2009). Measurement of lateral adhesion forces at the interface between a liquid drop and a substrate. *Physical review letters*, 103(26), 266101.

- Taneda, S. (1956). Experimental investigation of the wake behind a sphere at low Reynolds numbers. *Journal of the Physical Society of Japan*, 11(10), 1104-1108.
- Theofanous, T. G., & Li, G. J. (2008). On the physics of aerobreakup. *Physics of Fluids* (1994-present), 20(5), 052103.
- Thoroddsen, S. T. (2002). The ejecta sheet generated by the impact of a drop. *Journal of Fluid Mechanics*, 451, 373-381.
- Thoroddsen, S. T., Etoh, T. G., & Takehara, K. (2008). High-speed imaging of drops and bubbles. *Annu. Rev. Fluid Mech.*, 40, 257-285.
- Tien. C. (1989). *Granular Filtration of Aerosols and Hydrosols*, Butterworths: Boston.
- Tsai, P., CA van der Veen, R., van de Raa, M., & Lohse, D. (2010). How micropatterns and air pressure affect splashing on surfaces. *Langmuir*, 26(20), 16090-16095.
- Tsai, P., Pacheco, S., Pirat, C., Lefferts, L., & Lohse, D. (2009). Drop impact upon micro-and nanostructured superhydrophobic surfaces. *Langmuir*, 25(20), 12293-12298.
- Voyutskii, S. S., Akl'yanova, K. A., Panich, R., & Fodiman, N. (1953). Mechanism of separation of the disperse phase of emulsions during filtration. In *Dokl. Akad. Nauk SSSR* (Vol. 91, pp. 1155-1158).
- Weickgenannt, C. M., Zhang, Y., Lembach, A. N., Roisman, I. V., Gambaryan-Roisman, T., Yarin, A. L., & Tropea, C. (2011a). Nonisothermal drop impact and evaporation on polymer nanofiber mats. *Physical Review E*, 83(3), 036305.
- Weickgenannt, C. M., Zhang, Y., Sinha-Ray, S., Roisman, I. V., Gambaryan-Roisman, T., Tropea, C., & Yarin, A. L. (2011b). Inverse-Leidenfrost phenomenon on nanofiber mats on hot surfaces. *Physical Review E*, 84(3), 036310.
- Weiss, D. A., & Yarin, A. L. (1999). Single drop impact onto liquid films: neck distortion, jetting, tiny bubble entrainment, and crown formation. *Journal of Fluid Mechanics*, 385, 229-254.
- Wierzba, A. (1990). Deformation and breakup of liquid drops in a gas stream at nearly critical Weber numbers. *Experiments in Fluids*, 9(1-2), 59-64.
- Wilcox, J. D., June, R. K., Brown, H. A., & Kelley, R. C. (1961). The retardation of drop breakup in high-velocity airstreams by polymeric modifiers. *Journal of Applied Polymer Science*, 5(13), 1-6.
- Wu, X. F., & Dzenis, Y. A. (2005). Elasticity of planar fiber networks. *Journal of applied physics*, 98(9), 093501.

Wu, X. F., & Dzenis, Y. A. (2006). Droplet on a fiber: geometrical shape and contact angle. *Acta mechanica*, 185(3-4), 215-225.

Wu, X. F., & Dzenis, Y. A. (2007). Collapse analysis of nanofibres. *Nanotechnology*, 18(28), 285702.

Yarin, A. L. (2006). Drop impact dynamics: splashing, spreading, receding, bouncing.... *Annu. Rev. Fluid Mech.*, 38, 159-192.

Yarin, A. L., Chase, G. G., Liu, W., Doiphode, S. V., & Reneker, D. H. (2006). Liquid drop growth on a fiber. *AIChE journal*, 52(1), 217-227.

Yarin, A. L., Liu, W., & Reneker, D. H. (2002). Motion of droplets along thin fibers with temperature gradient. *Journal of applied physics*, 91(7), 4751-4760.

Yarin, A. L., Oron, A., & Rosenau, P. (1993). Capillary instability of thin liquid film on a cylinder. *Physics of Fluids A: Fluid Dynamics* (1989-1993), 5(1), 91-98.

Zhao, H., Liu, H. F., Cao, X. K., Li, W. F., & Xu, J. L. (2011). Breakup characteristics of liquid drops in bag regime by a continuous and uniform air jet flow. *International Journal of Multiphase Flow*, 37(5), 530-534.

10. APPENDIX

The following are the statements from the Publisher granting permission to use previously published articles of the present author in this thesis. Permission granted by the Royal Society of Chemistry addresses the work on drop impact onto electrospun nanofiber membrane from sections 2.1 and 3.1, as well as Chapter 4, and also for the work on blowing drops off a filament from sections 2.2 and 3.2, as well as Chapter 5. These sections are reproduced by permission of The Royal Society of Chemistry and the link of the papers is as follows:

<http://pubs.rsc.org/en/Content/ArticleLanding/2012/SM/c2sm06744g#!divAbstract>

<http://pubs.rsc.org/en/Content/ArticleLanding/2013/SM/c3sm50618e#!divAbstract>

Acknowledgements to be used by RSC authors

Authors of RSC books and journal articles can reproduce material (for example a figure) from the RSC publication in a non-RSC publication, including theses, without formally requesting permission providing that the correct acknowledgement is given to the RSC publication. This permission extends to reproduction of large portions of text or the whole article or book chapter when being reproduced in a thesis.

The acknowledgement to be used depends on the RSC publication in which the material was published and the form of the acknowledgements is as follows:

- For material being reproduced from an article in *New Journal of Chemistry* the acknowledgement should be in the form:
 - [Original citation] - Reproduced by permission of The Royal Society of Chemistry (RSC) on behalf of the Centre National de la Recherche Scientifique (CNRS) and the RSC
- For material being reproduced from an article *Photochemical & Photobiological Sciences* the acknowledgement should be in the form:
 - [Original citation] - Reproduced by permission of The Royal Society of Chemistry (RSC) on behalf of the European Society for Photobiology, the European Photochemistry Association, and RSC
- For material being reproduced from an article in *Physical Chemistry Chemical Physics* the acknowledgement should be in the form:
 - [Original citation] - Reproduced by permission of the PCCP Owner Societies
- For material reproduced from books and any other journal the acknowledgement should be in the form:
 - [Original citation] - Reproduced by permission of The Royal Society of Chemistry

The acknowledgement should also include a hyperlink to the article on the RSC website.

The form of the acknowledgement is also specified in the RSC agreement/licence signed by the corresponding author.

Except in cases of republication in a thesis, this express permission does not cover the reproduction of large portions of text from the RSC publication or reproduction of the whole article or book chapter.

A publisher of a non-RSC publication can use this document as proof that permission is granted to use the material in the non-RSC publication.

11. CURRICULUM VITAE

NAME: Rakesh Prasad Sahu

EDUCATION: Bachelor of Mechanical Engineering, Jadavpur University, Kolkata, West Bengal, India, 2010

Ph.D., Mechanical Engineering, University of Illinois at Chicago, Chicago, Illinois, USA, 2014

TEACHING: Teaching Assistant in the Department of Mechanical and Industrial Engineering, University of Illinois at Chicago, Illinois: Fluid Mechanics (ME 211), Fluid Mechanics Lab (ME 211).

HONORS: Faydor Litvin Graduate Award, University of Illinois at Chicago, 2013

Student Presenter Award, University of Illinois at Chicago

Graduate Student Council Travel Award, University of Illinois at Chicago, 2013

Chancellor's Student Service and Leadership Award, University of Illinois at Chicago, 2014.

PROFESSIONAL MEMBERSHIP: Materials Research Society
American Physical Society
American Society of Mechanical Engineers

PUBLICATIONS: 1. Sinha-Ray, S., Sahu, R. P., & Yarin, A. L. (2011). Nano-encapsulated smart tunable phase change materials. *Soft Matter*, 7(19), 8823-8827.

2. Sahu, R. P., Sinha-Ray, S., Yarin, A. L., & Pourdeyhimi, B. (2012). Drop impacts on electrospun nanofiber membranes. *Soft Matter*, 8(14), 3957-3970.

3. Pelot, David D., et al. "Strong squeeze flows of yield-stress fluids: The effect of normal deviatoric stresses." *Journal of Rheology* (1978-present) 57.3 (2013): 719-742.

4. Sahu, R. P., Sinha-Ray, S., Yarin, A. L., & Pourdeyhimi, B. (2013). Blowing drops off a filament. *Soft Matter*, 9(26), 6053-6071.

5. Chaudhari, R. R., Sahu, R. P., Ghosh, S., Mukhopadhyay, A., & Sen, S. (2013). Flame color as a lean blowout predictor. *International Journal of Spray and Combustion Dynamics*, 5(1), 49-66.

6. Sett, S., Sahu, R. P., Sinha-Ray, S., & Yarin, A. L. (2014). Superspreaders Versus “Cousin” Non-Superspreaders: Disjoining Pressure in Gravitational Film Drainage. *Langmuir*, 30(10), 2619-2631.
7. Sahu, R. P., Chatterjee, S., Biswas, N., Mukhopadhyay, A., & Sen, S. (2014, in press). Experimental investigation of the effect of jet inclination on bifurcation of laminar jets. *International Journal of Heat and Fluid Flow*.
8. Sahu, R. P., Sett, S., Yarin, A. L., & Pourdeyhyimi, B. Impact of Aqueous Suspension Drops onto Non-Wettable Porous Membranes: Hydrodynamic Focusing and Penetration of Nanoparticles. *Colloids and Surfaces A: Physicochemical and Engineering Aspects*, under review.